UNIVERSITY OF SOUTHAMPTON

FACULTY OF ENGINEERING AND THE ENVIRONMENT

Institute of Sound and Vibration Research

IMPROVED TURBOFAN INTAKE LINER DESIGN AND OPTIMIZATION

by

Prateek Mustafi

Thesis for the degree of Doctor of Philosophy

February 12, 2013

UNIVERSITY OF SOUTHAMPTON

ABSTRACT

FACULTY OF ENGINEERING AND THE ENVIRONMENT
Institute of Sound and Vibration Research

Doctor of Philosophy

IMPROVED TURBOFAN INTAKE LINER DESIGN AND OPTIMIZATION

by Prateek Mustafi

In modern turbofan engines, fan noise is one of the principle noise sources due to increased bypass ratio of the engines. Acoustic liners in the intake and bypass sections of the engine are effective in mitigating noise generated by the fan. They also play an important role in reducing fan blade instabilities by minimizing low-frequency acoustic reflections within the intake. Any damage on the lined surface has the potential to compromise the effectiveness of the liner; especially, its noise suppressing capabilities. The research presented in this thesis explores these areas on a much wider scale and aims to obtain an improved design of turbofan liners. The work performed ranges from developing an efficient strategy to optimize intake liners automatically to reduce both community noise and low-frequency acoustic reflections, to investigating the effects of liner damage and repair on the performance of zero-splice intake liners.

Computational Aero-Acoustic (CAA) models have been used to predict radiated noise from a turbofan intake and the results have been validated against Rolls-Royce rig and engine test data. Adjustments have been made to the linear predictions to account for non-linear propagation effects which are significant at high fan speeds. Intake liners have been optimised to mitigate radiated noise in the far-field by using the CAA code within automated optimisation routines. The cumulative process time of these automated techniques seems to be within the acceptable limit by the industry.

The acoustic effects of liner damage and repair on liner performance have been assessed by using analytical and computational prediction models. The effects of the extent and the location of the damage or the repaired surface on the overall performance of the liner is assessed. Some preliminary rules and guidelines have also been proposed in order to quantify the acoustic effects of the damage.

The acoustic impact of different intake liners on low-frequency reflections have been investigated by using computational models. The results show that high resistance liners are more effective in minimizing acoustic reflections within the intake.

Contents

List of Figures

List of Tables

DECLARATION OF AUTHORSHIP

I, PRATEEK MUSTAFI, declare that this thesis titled,

IMPROVED TURBOFAN INTAKE LINER DESIGN AND OPTIMIZATION

and the work presented in the thesis are both my own, and have been generated by me as the result of my own original research. I confirm that:

- this work was done wholly or mainly while in candidature for a research degree at this University;
- where any part of this thesis has previously been submitted for a degree or any other qualification at this University or any other institution, this has been clearly stated;
- where I have consulted the published work of others, this is always clearly attributed;
- where I have quoted from the work of others, the source is always given. With the exception of such quotations, this thesis is entirely my own work;
- I have acknowledged all main sources of help;
- where the thesis is based on work done by myself jointly with others, I have made clear exactly what was done by others and what I have contributed myself;
- parts of this work have been published as:

P. Mustafi, R. J. Astley, R. Sugimoto "*A computational study of the effects of liner damage on zero-splice turbofan intake liners*", 18th AIAA/CEAS Aeroacoustics Conference, Colorado Springs, USA, 4-6 June 2012, AIAA-2012-2152.

P. Mustafi, R. J. Astley, R. Sugimoto and A. J. Kempton "*Validation of CAA predictions for forward-arc fan noise, and intake liner optimisation*", 15th CEAS-ASC Workshop on Acoustic Liners and Associated Propagation Techniques, Lausanne, Switzerland, 13-14 October 2011.

R. J. Astley, R. Sugimoto and P. Mustafi "*The effect of hard patches on zero-splice turbofan intake liners, computational study*", Inter-noise, Osaka, Japan, 4-7 September 2011, Paper 450164.

R. J. Astley, R. Sugimoto and P. Mustafi "*Computational aero-acoustics for fan duct propagation and radiation. Current status and application to turbofan liner optimisation*", Journal of Sound and Vibration, Vol. 330, Issue 16, 3832-3845.

R. J. Astley, R. Sugimoto, P. Mustafi, M. F. Kewin and I. M. Achunche "*Applying Computational Aero-Acoustics (CAA) to turbofan liner optimisation*", 20th International Congress on Acoustics, Sydney, Australia, 23-27 August 2010, Paper 354.

R. J. Astley, R. Sugimoto and P. Mustafi "*The application of computational Aero-acoustics (CAA) to automated liner optimisation of turbofan ducts*", 17th International Congress on Sound and Vibration (ICSV), Cairo, Egypt, 18-22 July 2010, Paper 817.

R. J. Astley, R. Sugimoto, P. Mustafi, M. F. Kewin and I. M. Achunche "*Liner optimisation for turbofan ducts - towards a fully automated procedure*", 16th AIAA/CEAS Aeroacoustics Conference, Stockholm, Sweden, 7-9 June 2010, AIAA-2010-3826.

R. J. Astley, R. Sugimoto, I. M. Achunche, M. F. Kewin, P. Mustafi and E. P. Deane "*A review of CAA for fan duct propagation and radiation, with application to liner optimisation*", Procedia Engineering, IUTAM Symposium on Computational Aero-Acoustics for Aircraft Noise Prediction, Southampton, UK, 29-31 March 2010, Vol. 6, 143-152.

Signed: _____

Date: _____

Acknowledgements

Firstly, I would gratefully acknowledge the financial support for my PhD study provided jointly by Engineering and Physical Sciences Research Council (EPSRC) and by Rolls-Royce plc through a Dorothy Hodgkin postgraduate Award (DHPA). I am thankful to the Rolls-Royce University Technology Centre in Gas Turbine Noise at ISVR to provide me an opportunity to contribute to an industrially focussed research, something which I always wanted to do.

I am very grateful to my academic supervisors, Prof. Jeremy Astley and Dr. Rie Sugimoto, for their advice and immense support in my research. Under their guidance and attention to details, I gained invaluable experience both academically and personally. I would also like to thank my industrial supervisor Dr Andrew Kempton (Rolls-Royce UK) for providing me an opportunity to work on many industrial projects and to increase my learning curve in the field of aero-acoustics.

The research was greatly benefitted from useful interactions with many individuals. In particular, I would like to thank: Steeve Laldjee (FFT) for the development of PHOENIX and for his support with ACTRAN/TM; Brian Tester (ISVR) for his advise on using the Cargill code; Dr. Alan McAlpine (ISVR) for his advice on non-linear propagation theory; Christoph Richter (Rolls-Royce Deutschland) for providing the data on liner damage study and Iansteel Achunche (Rolls-Royce UK) for his advice on using SOFT.

During the course of three years, I had an opportunity to meet many friendly people. Here are a few to list: Iansteel Achunche, Feargus Kewin, Eugene Deane, Vincent Blandeau, Samuel Sinayoko, Martina Dieste, Mattieu Gruber, Adriana Salgado, Mahdi Azarpeyvand, Jack Lawrence, Albert Prinn, Hessam Alavi, Prathiban Sureshkumar, Zbigniew Rarata, Paul Rodga, Luis Tafur, Jon Stone, Upol Islam and the list goes on...

Last but not the least, I would like to thank my mom, my dad and my sister for for their priceless love and support during my PhD study. Even though they were continents apart, I felt that they were always with me here in Southampton.

Prateek Mustafi,
February 12, 2013.

Abbreviations

ACARE	Advisory Council for Aeronautics Research
ANPRORAD	ANalysis for PROpagation and RADiation
ARMOGA	Adaptive Range Multi-Objective Genetic Algorithm
BB	Broadband noise source
BEM	Boundary Element Method
BPF	Blade Passing Frequency
BR	Bypass Ratio
B-induct	Bypass induct analysis
CAA	Computational Aero-Acoustics
CFD	Computational Fluid Dynamics
DDOF	Double Degree Of Freedom
DoF	Design of Experiments
DGM	Discontinuous Galerkin Method
DHC	Dynamic Hill Climbing
DNS	Direct numerical simulation
DoE	Design of Experiment
EIPM	Equal Intensity Per Mode source
EO	Engine Order
EPNL	Effective Perceived Noise Level
FDNS	Frequency Domain Numerical Simulation
FE	Finite Element
FEM	Finite Element Method
FFT	Free Field Technologies
GA	Genetic Algorithm
GUI	Graphical User Interphase
HBR	High Bypass Ratio
HW	Hard-Walled
ICAO	International Civil Aviation Organization
IE	Infinite Element
IHI	Ishikawajima-Harima Heavy Industries
IL	Intensity Level
ISVR	Institute of Sound and Vibration Research

LEE	Linearised Euler Equation(s)
MM	Multi-Mode noise source model
ND	Nodal Diameter
NL	Non-Linear
OFS	Outer Fixed Structure
OGV	Outlet Guide Vane
Optimtool	Optimisation Toolbox
PHOENIX	Parametric mesHing and analysis of aerOENgine Intakes and eXhausts
PNL	Perceived Noise Level
POA	Percentage Open Area (porosity)
PWL	PoWer Level
RBF	Radial Basis Function
RSM	Response Surface Modelling
SDOF	Single Degree Of Freedom
SM	Single-Mode noise source model
SOFT	Smart Optimisation For Turbomachinery
SPL	Sound Pressure Level
SW	Soft Wall

Symbols

(r, θ, ψ)	Spherical coordinate system
(r, θ, z)	Cylindrical coordinate system
(x, y, z)	Cartesian coordinate system
(x, y, z)	Cartesian coordinate system
$(\hat{i}, \hat{j}, \hat{k})$	Cartesian unit vector notations
$\hat{n}$	unit vector perpendicular to a surface
S	denotes surface
V	denotes volume
ϵ	error
C_P	specific heat capacity at constant pressure
C_V	specific heat capacity at constant volume
γ	ratio of specific heats (C_P/C_V)
ω	angular frequency
ω_{mn}^{co}	modal cut-off frequency
t	time
i	$\sqrt{-1}$
f	frequency
λ	wavelength
c	speed of sound; *no subscript*: acoustic component, *no subscript*: $_0$ mean flow component, $_T$ total
k	acoustic wavenumber
M	Mach number; *subscript*: $_t$ fan-tip Mach number, $_a$ fan-plane axial Mach number, $_{rel}$ relative Mach number at the fan ($= \sqrt{M_a^2 + M_t^2}$)
m	azimuthal mode order
n	radial mode order
a	radius of a cylindrical duct or fan radius of a turbofan intake
D	duct diameter or fan diameter
B	number of fan blades
I	acoustic intensity
W, w	FE weighting function or test function
$\mathbf{C}$	damping term
$\mathbf{F}$	forcing term

$\mathbf{K}$	acoustic stiffness term
$\mathbf{M}$	acoustic mass term
Z, z	specific acoustic impedance of the acoustic liner
R	specific liner resistance
X, χ	specific liner reactance
l	liner mass inertance
d	liner cell depth
β	coefficient of nonlinearity ($= \frac{\gamma+1}{2}$)
σ	linear attenuation rate of an acoustic wave
ρ	density; *no subscript* or *superscript*: * acoustic component, *subscript*: $_0$ mean flow component
p	pressure; *no subscript* or *superscript*: * acoustic component, *subscript*: $_0$ mean flow component, $_s$ shock strength of a non-linear wave
$\mathbf{u}$	particle velocity; *no subscript* or *superscript*: * acoustic component, *subscript*: $_0$ mean flow component
ϕ	velocity potential; *superscript*: * acoustic component, *subscript*: $_0$ mean flow component, $_i$ at element node
A_{mn}, B_{mn}	modal wave amplitude; *superscript*: + wave travelling in positive z-direction, - wave travelling in negetive z-direction
N_{mn}	modal nomalisation factor
k_{mn}^{co}	modal cut-off wavenumber
$k_z, k_{z,mn}$	axial wavenumber; *superscript*: + wave travelling in positive z-direction, - wave travelling in negetive z-direction
$k_{r,mn}$	radial wavenumber
Ω	angular velocity

Chapter 1

Introduction

1.1 Background

Over the last decade, the commercial air traffic has increased significantly across the globe (ICAO) [1]. This has posed serious concerns about the impact of the increasing aircraft noise on the people residing close to the airports. As a result, stringent regulations on noise restrictions have been implemented by government organisations [1–3]. Such noise legislations encourage research which aim at the reduction of aircraft noise. A target of a 10dB reduction in the total aircraft noise to be achieved in 2020 starting from a datum level in 2000 (see figure 1.1) has been set by the Advisory Council of Aeronautics Research in Europe (ACARE) [4]. The reduction of aircraft noise is therefore a vital factor in the development of new aircrafts. This requires that the different sources of aircraft noise to be identified and novel noise reduction techniques to be developed in order to target these noise sources.

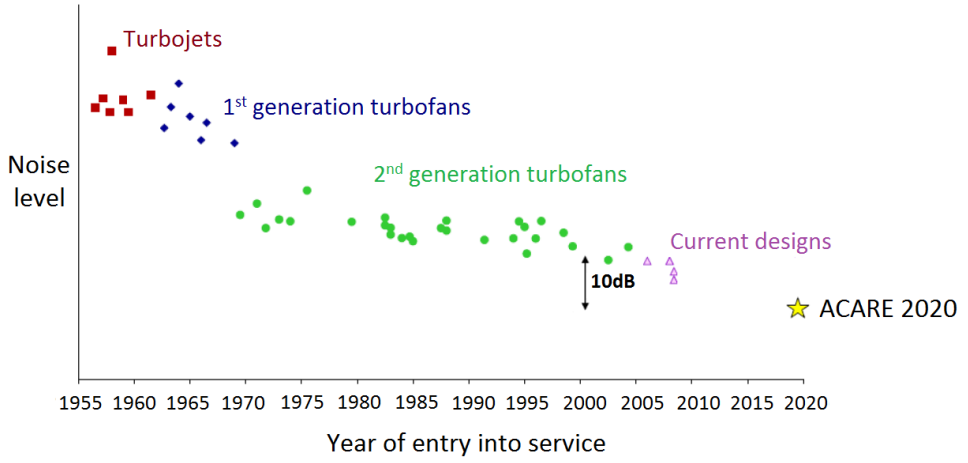

FIGURE 1.1: Time history of noise reduction in aero-engines [3]

1.2 Aircraft noise sources

Total aircraft noise can be broadly subdivided into two categories - airframe noise and engine noise [5–7](figure 1.2). Airframe noise is generated by unsteady flow interacting with the airframe itself (high lift devices, landing gears, etc.). Engine noise constitutes a wide variety of noise sources for which the frequency spectra vary drastically at different shaft rotational speeds of the engine. These sources include noise from the jet, fan, compressor, combustor and turbine.

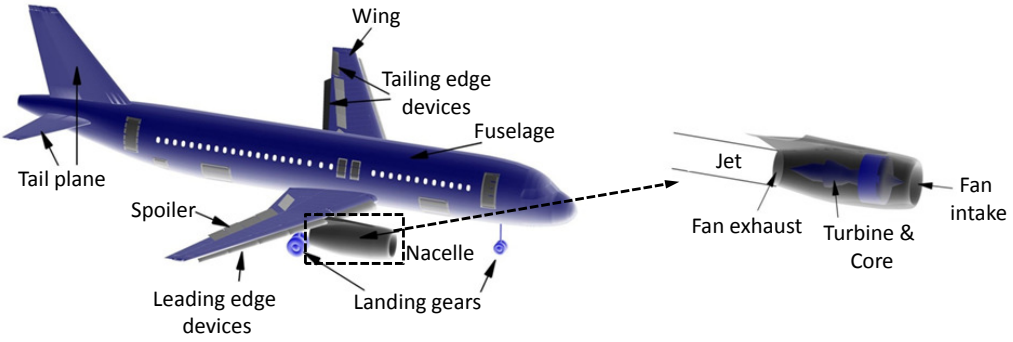

FIGURE 1.2: Aircraft noise sources [8]

In early jet engines, much of the audible noise was generated by the hot exhaust gases mixing with the surrounding air at the rear of the engine [3, 7]. By introducing a fan at the front of the engine, most of the thrust is produced by the air bypassed around the core. This allowed a lower jet core velocity in turn reducing jet noise. The noise emitted by modern commercial aircrafts is substantially less than that produced by designs fifty years ago (figure 1.3). However, the introduction of a large fan in modern turbofan engines has led to fan noise overtaking the jet as the dominant noise source. Unlike jet noise, the fan noise is radiated both forward of the engine through the intake (or inlet) and rearward through the bypass duct as shown in figure 1.4. Fan noise can be subdivided into broadband (continuous frequency range) and tonal (at discrete frequencies) noise.

Broadband noise is generated when a turbulent flow interacts with stationary or moving solid surfaces, primarily the leading and trailing edges of the rotor and Outlet Guide Vanes (OGVs). In order to model this noise source in terms of duct acoustic modes, it is generally represented as an ensemble of all the uncorrelated cut-on modes at the fan plane [10–14].

Tonal noise can be classified as tones produced at the harmonics of the Blade Passing Frequency (BPF) and the Engine Order (EO) tones. BPF tones can be generated by the rotating pressure field on the fan plane locked to the rotor (rotor-locked tones) or

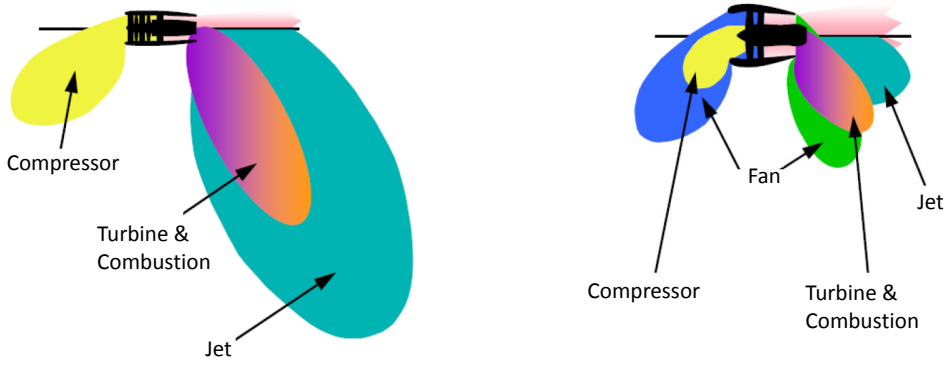

(a) Typical 1960s design (b) Typical modern design

FIGURE 1.3: Magnitude and directivity of the radiated sound power of different engine noise sources for a typical 1960s and a modern design [7]

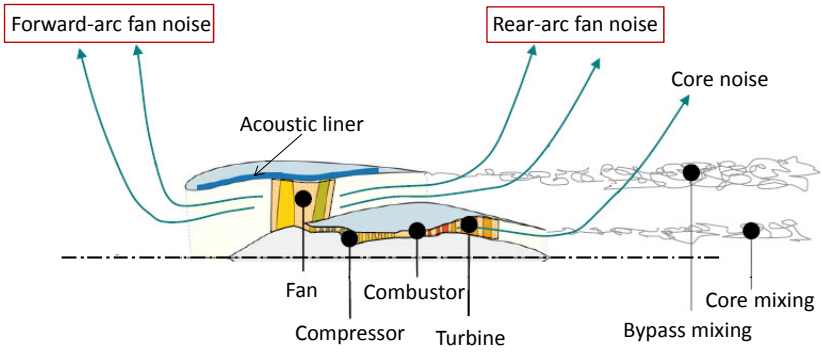

FIGURE 1.4: Fan noise radiation through intake and bypass sections of a modern turbofan engine [9]

by the periodic interactions of the rotor wakes with the OGVs (rotor-stator interaction tones) or by flow distortion effects (distortion tones) [7]. Rotor-locked tones are generated only at high fan operating conditions when the fan-tip speed is supersonic. In terms of duct acoustic modes, the rotor-locked tones are modelled as modes with azimuthal orders which are integer multiples of the number of fan blades. Engine order or "Buzz-saw" tones occur in the intake at 'engine orders' (integer multiples of shaft rotational frequency). They exist only when the fan-tip speed is supersonic and are generated due to small variations in fan blade stagger angles. [15].

A key method to control fan noise is the use of acoustic treatment in the intake and bypass sections of the engine (figure 1.4). They are typically formed from single or double layers of honeycomb material, separated from the mean flow by a porous facing sheet,

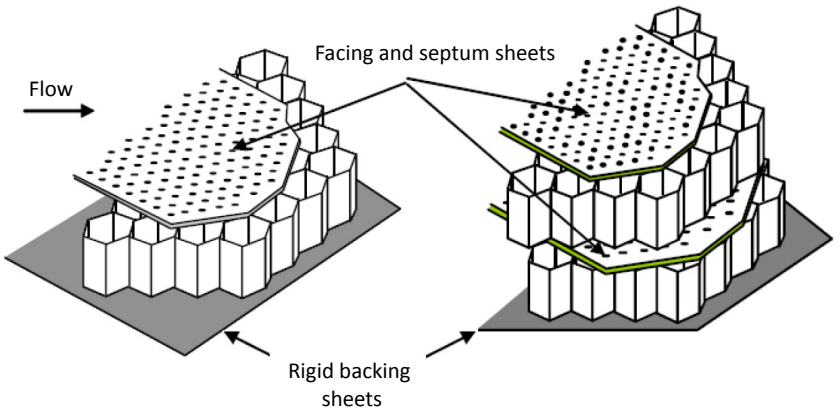

FIGURE 1.5: Single layer and double layer liner constructions [16]

and fixed to a rigid backing plate (figure 1.5). The design of this acoustic treatment depends on the desired Effective Perceived Noise Level (EPNL) [6] to be achieved. EPNL is an ISO standard for measuring aircraft noise that takes into account the frequency, noise content and duration of the event. There are three noise certification points set by ICAO to calculate EPNL. Two of which are at take-off (sideline and cutback) and one during landing (approach) [3, 7]. The engine is at the maximum power setting during sideline engine condition. Cut-back condition refers to a reduced power setting after the initial climb. The engine is at a low power setting during landing and is said to operate at the approach condition. This means that the acoustic treatment must have the appropriate attenuation characteristics at these certification conditions, within the limit of its specified length and weight.

1.3 Aims, motivation and original contributions

The research presented in this thesis has been performed in close collaboration with Rolls-Royce plc. The objective of the research is to provide an improved turbofan liner design capable of reducing community noise and low-frequency reflections at the fan which trigger fan blade instabilities. The research also aims at investigating the effects of liner damage and repair on the performance of zero-splice liners to establish some preliminary guidelines for liner damage/repair limit. The scope of this research is limited only to the intake section of a turbofan engine.

Computational Aero-Acoustic (CAA) methods are well developed for predicting propagation of sound on subsonic flows [9] and using such methods in place of measured data is highly beneficial since the acquisition of the latter is costly and time consuming. In order to use a CAA method confidently for predicting turbofan noise, a thorough assessment and validation of the method is required. In this thesis, a commercial

Finite/Infinite Element (FE/IE) code ACTRAN/TM is used to predict noise propagation in turbofan intakes and radiation into the far-field. The code is also validated against the measured data. The capabilities of ACTRAN/TM have been exploited extensively both for predicting far-field radiated noise and acoustic reflections at low frequencies.

ACTRAN/TM is however based on a linear theory and cannot model the propagation of high amplitude tones which are strongly excited at supersonic fan-tip speeds. An analytical model devised by Morfey and Fisher [17] and Fisher *et al.* [18] and later extended by McAlpine *et al.* [15, 19] is used to predict the propagation of tones at such speeds.

The original contributions of this thesis are listed below:

I. A methodology is developed to apply non-linear adjustments by using 'Morfey-Fisher model' to the results obtained by linear prediction models to correctly determine the attenuation of tones at supersonic fan-tip speeds.

II. Far-field noise predictions are validated against turbofan rig and engine test data by using complex noise source models directly derived from hard-walled in-duct and far-field measurements, in addition to the conventional 'equal-energy' source models.

III. ACTRAN/TM shell codes like ANPRORAD and PHOENIX (detailed in chapter 2) are used within automated optimisation routines to perform liner optimisation to reduce far-field radiated noise. The optimisation study is performed for realistic geometries and noise source models at two different engine conditions including non-linear corrections to the attenuation of BPF tones.

IV. The effects of size and location of linear damage on the noise attenuation by zero-splice intake liners are investigated at different fan speeds by an existing analytical asymptotic model. The results are compared to ACTRAN/TM. The study is extended for realistic intake geometries with non-uniform flow profiles by using ACTRAN/TM with the aim to predict the effects of liner patches on far-field noise directivities. The study provides some essential guidelines for the size and the location of liner damage/repair limit.

V. The acoustic impact of different liner configurations on the amplitude of low-frequency acoustic reflections from low order incident modes are assessed by using ACTRAN/TM (both axisymmetric and 3D intake models).

1.4 Report overview

The research work presented in this thesis is broad in context focussing on varied topics which are closely related. They range from the development of a fully automated procedure to optimise intake liners to reduce community noise and low-frequency acoustic reflections, to the investigation of the effects of liner damage to the noise reducing capabilities of a zero-splice liner. Since this thesis covers a wide range of topics, the literature review for each topic is presented separately.

This thesis consists of 9 chapters. Chapter 2 describes the CAA tool ACTRAN/TM used to predict fan noise propagation and radiation from turbofan intakes. This is followed by a description of the non-linear propagation model in chapter 3.

In chapter 4, The far-field Sound Pressure Level (SPL) predictions are validated against measured data for the available source information and liner details. In chapter 5, ACTRAN/TM is embedded within optimisation routines to develop fully-automated optimization schemes to optimize intake liners to reduce far-field radiated noise at approach and sideline engine conditions. Non-linear adjustments are applied to high-amplitude tones at sideline condition.

In chapter 6, an analytical asymptotic model is used as a benchmark to investigate the acoustic effects of liner damage and repair on the performance of a zero-splice intake liner. The study performed in this chapter is a precursor to comprehensive CAA modelling in chapter 7. In chapter 7, ACTRAN/TM is used to predict the effects of liner damage on noise attenuation in a realistic intake geometry and non-uniform mean flow. A number of models with different degree of simplification of the intake geometry are used to investigate the influence of such simplifications on the results.

In chapter 8, different liner configurations are analyzed for reducing low frequency acoustic reflections at the fan. The liner is also optimised to minimize these reflection by using the automated optimisation routine used in chapter 5.

Finally in chapter 9, overall conclusions and recommendations for future work are presented.

1.5 Planning and progress

An overview of the work plan is shown in figure 1.6 indicating the tasks which were undertaken in the course of three years.

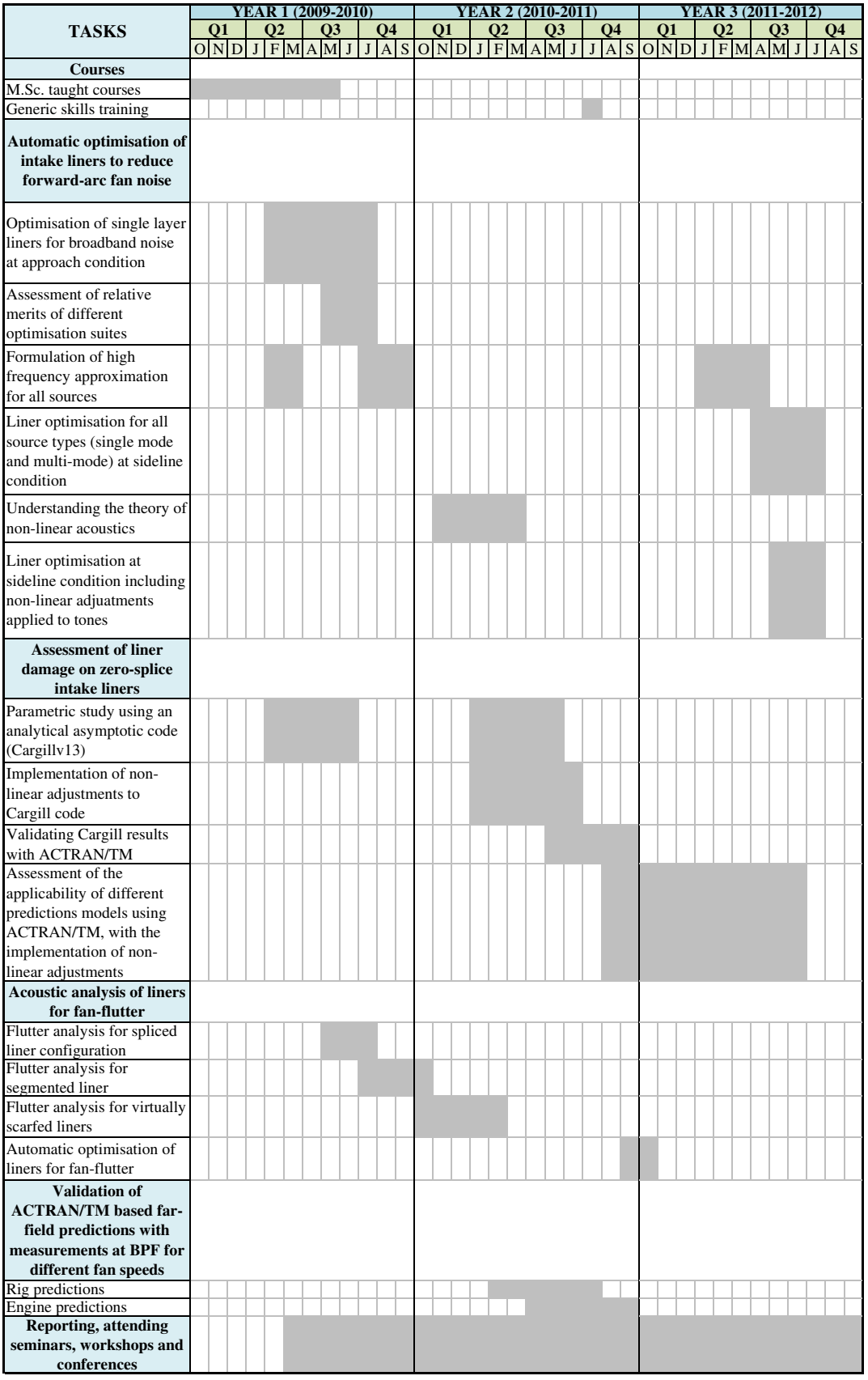

FIGURE 1.6: Work plan

Chapter 2

Linear prediction method for fan noise propagation and radiation

2.1 Introduction

Accurate estimates of Effective Perceived Noise Level (EPNL) for commercial aircraft are required for noise certification and for assessing compliance with local community noise regulations. Noise data from rig and engine tests provide the most reliable basis for such predictions. However, such data are costly to acquire and cannot always be extrapolated in a straightforward way to new configurations. Accurate prediction schemes to predict noise propagation and radiation from the engine are therefore crucial in the preliminary engine design stage. This chapter describes the prediction method based on linear propagation theory, which is used in this thesis to model the propagation of sound in intake ducts and radiation to the far field.

2.2 Literature Review

Analytic methods to predict sound propagation in turbofan ducts were developed by many authors in the past but were applicable only to uniform cylindrical and annular duct. An overview of some of these methods is given by Eversman [20]. Sound field which can be represented in terms of the duct modes [21] forms the basis for most analytical and semi-analytical methods. They include hard-wall eigenvalue solutions for sound absorption in ducts of regular geometry, mode matching codes and sound radiation models for cylindrical and annular ducts.

Unlike the eigenvalues calculated for a hard-wall duct, determination of eigenvalues for a lined duct is not a straight-forward task due to the complexity involved in solving the transcendental equations [20]. One of the first attempts in this field was presented by

Morse and Ingard [22] who dealt with a no-flow problem, producing charts relating the wall impedance to the eigenvalues without actually solving the eigenvalue equation explicitly. Later, Eversman [20] developed an integration scheme to solve the eigenvalue equation in presence of a mean flow. The scheme used a fourth-order Runge-Kutta integration with a variable step size, and a Newton-Raphson routine for refining the solution. Brooks [23] used the same scheme to track the lined eigenvalues for an acoustically lined rectangular duct by using the hard-wall eigenvalues as the initial values to the integration scheme.

To calculate the acoustic field in ducts with axial discontinuities in liner impedance, McAlpine *et al.* [24] developed a mode-matching code which involves the matching of acoustic modes in different lined segments of a uniform duct, in terms of acoustic pressure and axial particle velocity. Later, Astley *et al.* [25] proposed an alternative mode matching formulation in which the matching was based on continuity of mass and axial momentum at the liner discontinuities, as opposed to pressure and velocity matching.

With regards to estimating sound radiation into the far-field from aero-engine ducts, Rice [26, 27] established a relationship between the the peak in far-field directivity patterns and duct mode cut-off ratio. It was shown that a nearly cut-off mode would radiate predominantly at 90^o from the duct axis while the well propagating modes radiate nearer to the axis. Gabard and Astley [28] derived an exact solution to predict the sound field radiated from an axisymmetric annular duct with infinite center body including a bypass shear layer. This work was an extension to the study performed by Munt [29] who considered a problem of circular jet with bypass shear layer, and to Rienstra [30] for a semi-infinite duct with an infinite centre body, using Wiener-Hopf technique.

However, the analytical models cannot capture the effects of a realistic geometry and flow. Numerical methods are therefore important to assess the effect of the realistic geometry and mean flow. Over the last decade, Computational Aero-Acoustics (CAA) methods have been developed to study propagation of sound on subsonic flows and have been used extensively by many authors in the past. Methods that are widely used for modelling of sound propagation from turbofan ducts include Boundary Element (BE) methods [31], Finite and Infinite Element (FE/IE) models [32–34] and other Computational Aero-Acoustics (CAA) methods, based on the solution of the full [35] or Linearised Euler Equations (LEE) [36, 37]. The solutions of full Euler equations are important in modelling non-linear propagation effects due to large acoustic perturbations. For flows where non-linear effects are less significant, schemes which solve LEEs are generally used. Although LEEs omit the viscous effects, they can deal with sheared or rotational flows if the mean flow is solved by using Reynolds Averaged Navier Stokes (RANS) solvers [36, 37]. This makes them suitable especially for bypass and exhaust flow problems. BE and FE/IE models solve a convected wave equation in the frequency

domain and are applicable only when the mean flow is irrotational. A detailed review of some of these computational methods can be found in references [9, 38].

The computational tool used in this study for predicting noise propagation in turbofan ducts and radiation into the far-field is the commercial FE/IE code, ACTRAN/TM, developed by Free Field Technologies (FFT), Belgium. This chapter explores the acoustic propagation model used in ACTRAN/TM. The FE formulation and the IE model used in ACTRAN/TM have been outlined. The shell codes, ANPRORAD and PHOENIX, used in this thesis to perform ACTRAN/TM predictions in turbofan intakes are also described.

2.3 Acoustic propagation model

Viscous effects are generally neglected in the modeling of sound propagation from turbofan ducts since such losses are significant only over large propagation distances. Therefore, Euler equations form the starting point for most computational models [9], and in most instances they are simplified by linearising the small amplitude unsteady perturbations on the steady mean flow. The resulting equations are given by

$$\frac{\partial \rho^*}{\partial t} + \nabla \cdot (\rho^* \mathbf{u_0} + \rho_\mathbf{0} \mathbf{u}^*) = 0, \tag{2.1}$$

and

$$\rho_0 \left(\frac{\partial}{\partial t} + \mathbf{u_0} \cdot \nabla \right) \mathbf{u}^* + \rho_\mathbf{0} \left(\mathbf{u}^* \cdot \nabla \right) \mathbf{u_0} + \rho^* \left(\mathbf{u_0} \cdot \nabla \right) \mathbf{u_0} + \nabla p^* = \mathit{0}. \tag{2.2}$$

Equations 2.1 and 2.2 are the linearized Euler equations for continuity and momentum respectively, where ρ, p and $\mathbf{u}$ denote density, pressure and velocity respectively. Mean flow quantities are denoted by the subscript $_0$, and unsteady perturbations quantities are denoted by the superscript *. For isentropic mean flow, there exist a simple relationship between the unsteady pressure and density perturbations [39–41]:

$$p^* = c_0^2 \rho^*. \tag{2.3}$$

In Equation 2.3, c_0 is the local speed of sound in the mean flow. The problem reduces to the solution of equations 2.1 and 2.2 for variables p^* (or ρ^*) and $\mathbf{u}^*$. Further simplification can be made if the flow is irrotational in the perturbed velocity $\mathbf{u}^*$ can be written in terms of an acoustic velocity potential ϕ^*, as $\mathbf{u}^* = \nabla\phi^*$. The linearized continuity and momentum equations can then be expressed as [9]

$$\frac{\partial \rho^*}{\partial t} + \nabla \cdot (\rho^* \mathbf{u_0} + \rho_\mathbf{0} \nabla\phi^*) = 0, \tag{2.4}$$

and

$$p^* = c_0^2 \rho^* = -\rho_0 \left(\frac{\partial}{\partial t} + \mathbf{u_0} \cdot \nabla \right) \phi^*. \tag{2.5}$$

Time-harmonic versions of these equations are obtained by rewriting $\phi^*(\mathbf{x}, t)$ as $\phi(\mathbf{x})\mathbf{e}^{\mathbf{i}\omega\mathbf{t}}$, where $\omega(= 2\pi f)$ is the radian frequency and ϕ is the complex amplitude. Using equations 2.4 and 2.5, the convected Helmholtz equation can be obtained [39].

$$(i\omega + \nabla \cdot \mathbf{u_0} + \mathbf{u_0} \cdot \nabla) \left[\frac{\rho_0}{c_0^2} (\mathbf{i}\omega + \mathbf{u_0} \cdot \nabla) \phi \right] - \nabla \cdot (\rho_0 \nabla \phi) = \mathbf{0}. \tag{2.6}$$

The problem now reduces to the solution of a single unknown parameter, the acoustic velocity potential ϕ. To obtain a solution of acoustic field by using equation 2.6, boundary conditions of the surrounding body or surfaces must be defined.

2.3.1 Impedance boundary conditions

The boundary condition on all rigid surfaces is that of zero normal particle velocity giving $\nabla\phi^* \cdot \hat{\mathbf{n}} = \mathbf{0}$, where $\hat{\mathbf{n}}$ is a unit vector perpendicular to the surface. For a duct lined with a locally reacting liner, the relationship between the acoustic pressure p^* and normal component of the acoustic particle velocity $\mathbf{u}^*$ at the duct wall in the absence of mean flow [20, 41], is given by

$$\mathbf{u}^* \cdot \hat{\mathbf{n}} = \frac{p^*}{Z}, \tag{2.7}$$

where, Z is the specific acoustic impedance of the liner. For a hard-walled duct $\mathbf{u}^*$ is zero at the wall and $|Z| = \infty$ (from equation 2.7). In presence of a uniform flow $\mathbf{U_0}$, an infinitely thin boundary layer is assumed to be present at the impedance surface, giving Eversman's [42] implementation of Myers [43] boundary condition:

$$\mathbf{u}^* \cdot \hat{\mathbf{n}} = \frac{p^*}{Z} + \mathbf{U_0} \cdot \nabla \left(\frac{p^*}{\mathbf{i}\omega Z} \right) - \frac{p^*}{\mathbf{i}\omega Z} \hat{\mathbf{n}} \cdot (\hat{\mathbf{n}} \cdot \nabla \mathbf{U_0}). \tag{2.8}$$

2.3.2 Sound propagation in a uniform duct with uniform mean flow

Consider a uniform cylindrical duct with circular cross section (an idealised form of a turbofan intake duct) of radius a (figure 2.1). In case of a uniform mean flow of Mach number M along the duct axis z, the convected Helmholtz equation (equation 2.6) simplifies to

$$\nabla^2 \phi - M^2 \frac{\partial^2 \phi}{\partial z^2} - 2ikM \frac{\partial \phi}{\partial z} + k^2 \phi = 0, \tag{2.9}$$

where $k(=\omega/c_0)$ ia the free-field wavenumber of the acoustic wave. In cylindrical coordinates (r, θ, z), equation 2.9 can be written as

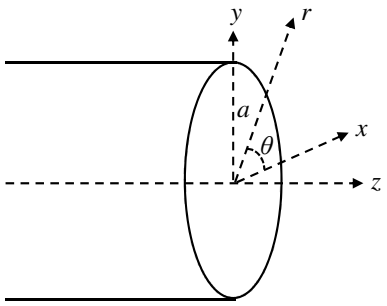

FIGURE 2.1: Cylindrical duct of circular cross-section of radius a

$$\frac{\partial^2\phi}{\partial r^2} + \frac{1}{r}\frac{\partial\phi}{\partial r} + \frac{1}{r^2}\frac{\partial^2\phi}{\partial\theta^2} - (1-M^2)\frac{\partial^2\phi}{\partial z^2} - 2ikM\frac{\partial\phi}{\partial z} + k^2\phi = 0. \tag{2.10}$$

The general solution of equation 2.10 for the acoustic velocity potential can be expressed in terms of a summation of all the duct modes [12, 39].

$$\phi_{mn}(r,\theta,z) = \sum_{m=-\infty}^{\infty}\sum_{n=1}^{\infty} J_{|m|}(k_{r,mn}r)e^{im\theta}\left(B^{+}_{mn}e^{-ik^{+}_{z,mn}z} + B^{-}_{mn}e^{-ik^{-}_{z,mn}z}\right), \tag{2.11}$$

where m is the azimuthal mode order, n is the radial mode order, B_{mn} is the modal amplitude of the acoustic velocity potential for mode (m, n), $J_{|m|}$ is the Bessel function of order $|m|$, $k_{r,mn}$ is the radial wavenumber and $k_{z,mn}$ is the axial wavenumber for mode (m, n). Superscripts '$+$' and '$-$' denote the quantities for the modes propagating in the positive and negative z directions respectively. Equivalently, using equation 2.5, the solution can be obtained in terms of acoustic pressure

$$p_{mn}(r,\theta,z) = \sum_{m=-\infty}^{\infty}\sum_{n=1}^{\infty} J_{|m|}(k_{r,mn}r)e^{im\theta}\left(A^{+}_{mn}e^{-ik^{+}_{z,mn}z} + A^{-}_{mn}e^{-ik^{-}_{z,mn}z}\right), \tag{2.12}$$

where A_{mn} is the modal amplitude of the acoustic pressure for mode (m, n), and is related to B_{mn} by the relation

$$A_{mn} = -i\rho_0 c_0 B_{mn}(k - Mk_{z,mn}). \tag{2.13}$$

The axial and the radial numbers are related by the dispersion relationship

$$k^{\pm}_{z,mn} = \frac{-kM \pm \sqrt{k^2 - (1-M^2)k^2_{r,mn}}}{(1-M^2)}. \tag{2.14}$$

The radial wavenumber $k_{r,mn}$ can be obtained by imposing the impedance boundary condition at the duct wall. In the presence of a uniform axial flow, the equation 2.8 simplifies to

$$\frac{\partial \phi}{\partial r} = -\frac{\rho_0 c_0}{Z}\left(ik\phi + M\frac{\partial \phi}{\partial z}\right) - \left(\frac{1}{ik}\right) M \frac{\partial}{\partial z}\left(\frac{\rho_0 c_0}{Z}\left(ik\phi + M\frac{\partial \phi}{\partial z}\right)\right). \tag{2.15}$$

The hard-wall boundary condition at the duct wall is obtained by setting $|Z| = \infty$, which gives $\partial\phi/\partial r = 0$ at $r{=}a$. Therefore, substituting equation 2.11 into equation 2.15 and setting $Z(\omega) = \infty$, gives

$$J'_{|m|}(k_{r,mn}a) = 0, \tag{2.16}$$

where J' is the derivative of the bessel function with respect to the radial distance r. Similarly, the boundary condition for an acoustically lined duct of liner impedance Z at the duct wall ($r{=}a$), is given by

$$k_{r,mn}\frac{J'_{|m|}(k_{r,mn}a)}{J_{|m|}(k_{r,mn}a)} = \frac{\rho_0 i\omega}{Z}\left(1 - \frac{Mk_{z,mn}}{k}\right)^2. \tag{2.17}$$

Equation 2.12 is a general solution for acoustic pressure within a cylindrical duct with circular cross-section. A similar expression can be obtained for an annular duct with inner and outer radius b and a respectively, which is given by

$$p_{mn}(r,\theta,z) = \sum_{m=-\infty}^{\infty}\sum_{n=1}^{\infty}\left(J_{|m|}(k_{r,mn}r) + CY_{|m|}(k_{r,mn}r)\right)e^{im\theta} \left(A^{+}_{mn}e^{-ik^{+}_{z,mn}z} + A^{-}_{mn}e^{-ik^{-}_{z,mn}z}\right), \tag{2.18}$$

where $Y_{|m|}$ is the Neumanns function of order $|m|$ and C is given by [39]

$$C = -\frac{J'_{|m|}(k_{r,mn}a)}{Y'_{|m|}(k_{r,mn}a)}.$$

2.3.2.1 Cut-on frequency

The cut-on frequency in a hard-wall duct is the minimal frequency at which a given acoustic mode (m, n) starts to propagate. From the dispersion relationship (equation 2.14), one can see that if the value of $k^2 - (1 - M^2)k_{r,mn}^2$ is positive, then the axial wavenumber $k_{z,mn}$ is entirely real, in which case the mode is 'cut-on' and it propagates along the duct. But, if the value of $k^2 - (1 - M^2)k_{r,mn}^2$ is negative, then the axial wavenumber $k_{x,mn}$ is has an imaginary part, in which case the mode is 'cut-off' and it represents decaying or evanescent waves. Therefore, for a given mode (m, n), the cut-on wavenumber is given by [39]

$$k_{mn}^{co} = k_{r,mn}\sqrt{1 - M^2}. \tag{2.19}$$

However, for a lined duct mode, the term 'cut-on' has no meaning as all the modes decay as they propagate along the duct. All the modes decay at different rates which depends on the magnitude of the imaginary part of the axial wave number $(Im(k_{z,mn}))$

2.4 CAA prediction tool - ACTRAN/TM

The CAA tool used in this thesis is a frequency domain, commercial FE/IE code ACTRAN/TM [39]. It is based on the convected Helmholtz formulation for the acoustic velocity potential (equation 2.6). Within this application, the acoustic source at the source plane is defined in terms of a modal boundary condition where the incident acoustic field is defined in terms of rigid-wall duct modes (equation 2.12 for circular ducts and equation 2.18 for annular ducts). The reflected modes at this modal boundary are obtained as part of the solution. The impedance boundary condition (equation 2.8) is applied in terms of liner admittance for acoustically lined duct walls. ACTRAN analysis can be performed for both two-dimensional (2D) or axisymmetric geometries and three dimensional (3D) non-axisymmetrical geometries.

For radiation problems, ACTRAN/TM uses an FE/IE model of the type proposed by Astley [32, 33]. The model is based on a partitioned approach in which the inner acoustic domain is modelled by Finite Elements and the outer acoustic domain which extends to infinity, is modelled using a layer of Infinite Elements (IE).

2.4.1 The FE formulation

The FE method is based on variational formulation which seeks to obtain an approximate solution of the convected wave equation such that the weighted average of the error is zero. This is known as the weighted residual technique [44] and is applied to

the continuity equation (equation 2.4). Considering time-harmonic dependence of the acoustic variables, equation 2.4 and can be written as

$$i\omega\rho + \nabla \cdot (\rho \mathbf{u_0} + \rho_0 \nabla\phi) = 0. \tag{2.20}$$

If ρ_a and ϕ_a are considered to be approximate solutions of equation 2.20, then

$$i\omega\rho_a + \nabla \cdot (\rho_a \mathbf{u_0} + \rho_0 \nabla\phi_a) = \epsilon \neq 0, \tag{2.21}$$

where ϵ is the error or residual. The approximate solutions ρ_a and ϕ_a are sought by ensuring that the average of the weighted residual is zero over the computational domain of volume V, which gives

$$\int_V W(i\omega\rho_a + \nabla \cdot (\rho_a \mathbf{u_0} + \rho_0 \nabla\phi_a))dV = 0, \forall W, \tag{2.22}$$

where W is the weighting or test function. By using the divergence theorem, equation 2.22 can be rearranged to give

$$\int_V (\nabla W \cdot (\rho_a \mathbf{u_0} + \rho_0 \nabla\phi_a) - W i\omega\rho)\, dV = \int_S W \cdot (\rho_a \mathbf{u_0} + \rho_0 \nabla\phi_a) \cdot \mathbf{n} dS, \tag{2.23}$$

where S is the bounding surface of the computational domain and $\mathbf{n}$ is a unit vector normal to the surface pointing into the domain. Equation 2.23 is required to hold true for all possible weighting function W.

Substituting the approximate solutions ρ_a and ϕ_a into equation 2.5 and considering time-harmonic dependence, it gives

$$\rho_a = -\frac{\rho_0}{c_0^2} \left(i\omega + \mathbf{u_0} \cdot \nabla\right) \phi_a. \tag{2.24}$$

Substituting equation 2.24 into equation 2.23 results in the variational formulation for the convected wave equation:

$$\int_V \frac{\rho_0}{c_0^2}\left(c_0^2\nabla W\cdot\nabla\phi_a-(\mathbf{u_0}\cdot\nabla\phi_a)(\mathbf{u_0}\cdot\nabla W)\right)dV$$
$$+\int_V \frac{\rho_0}{c_0^2}\left(i\omega\phi_a\left(W(\mathbf{u_0}\cdot\nabla\phi_a)-(\mathbf{u_0}\cdot\nabla W)\right)-\omega^2W\phi_a\right)dV$$
$$=\int_S \frac{\rho_0}{c_0^2}\left(c_0^2W\nabla\phi_a-\mathbf{u_0}W(\mathbf{u_0}\cdot\nabla\phi_a)-\mathbf{i}\omega\mathbf{u_0}W\phi_a\right)\cdot\mathbf{n}dS. \tag{2.25}$$

For a hard wall boundary, both $\mathbf{u_0}\cdot\mathbf{n}$ and $\phi_a\cdot\mathbf{n}$ are equal to zero. The right hand side of equation 2.25 is then zero. For a lined wall however, only $\mathbf{u_0}\cdot\mathbf{n}$ is zero and the Myers boundary condition is implemented for $\phi_a\cdot\mathbf{n}$. At the source and exit planes of the duct, $\phi_a\cdot\mathbf{n}$ is prescribed in terms of duct modes.

In the FE formulation, the entire computational domain is discretised into a number of sub-volumes called finite elements. Nodes are defined at the element vertices. For quadratic elements, nodes are also located at the mid-point of the element sides. The approximate solution ϕ_a is calculated at each node. Equation 2.25 now transforms into a summation of the volume and surface integrals for each element in the entire domain. The velocity potential ϕ_a within the entire computational domain can be expressed as

$$\phi_a=\sum_{i=1}^{N}N_i\phi_i, \tag{2.26}$$

where N is the total number of nodes. N_i is the element shape function associated with node i, which is defined by the topology of the associated element [39]. ϕ_i is the value of the velocity potential corresponding to node i, which is an unknown quantity. The weighting function associated with each node is chosen to be equal to shape function

$$W_i=N_i. \tag{2.27}$$

Substituting equations 2.26 and 2.28 into equation 2.25 results in a matrix equation of the form

$$\left(\mathbf{K}+\mathbf{i}\omega\mathbf{C}-\omega^2\mathbf{M}\right)\Phi=\mathbf{F}, \tag{2.28}$$

where Φ is a vector which contains the unknown values of velocity potential at each nodal point in the computational domain. $\mathbf{K}$, $\mathbf{C}$, $\mathbf{M}$ and $\mathbf{F}$ are the stiffness, damping and mass matrices and forcing vector respectively. These are determined solely by the shape functions and boundary conditions prescribed at the surfaces of the domain. Equation 2.28 is solved in ACTRAN/TM and nodal values of acoustic velocity potential are obtained.

2.4.2 Infinite elements

When modelling free-field radiation problems, the entire unbounded acoustic domain may not be discretised by using FE mesh for obvious reasons. Infinite element scheme [45–47] is used in ACTRAN/TM to deal with such problems. In this scheme, the exterior domain in not truncated but is represented by using elements of infinite extent. The sound field within infinite elements is represented as outwardly propagating wave-like solutions such that the wave field satisfies Sommerfeld radiation condition in the far-field. This condition requires that

$$r\left(\frac{\partial p}{\partial r} + ikp\right) \to 0 \quad \text{as } r \to \infty \tag{2.29}$$

where r is the radial distance from the source. A wave field satisfying equation 2.29 can be represented as an infinite series of 'multipole' terms of the form

$$p(r,\theta,\phi,k) = e^{-ikr}\sum_{\nu=1}^{\infty}\frac{\alpha_\nu(\theta,\phi)}{r^\nu}. \tag{2.30}$$

However for computational purposes, the summation is truncated after N terms;

$$p(r,\theta,\phi,k) = e^{-ikr}\sum_{\nu=1}^{N}\frac{\alpha_\nu(\theta,\phi)}{r^\nu}. \tag{2.31}$$

The maximum number of terms N is the infinite element radial interpolation order. This value has to be chosen meticulously in order to prevent spurious reflection back into the computational domain. A study on the determination of the infinite element order is presented in Appendix B.

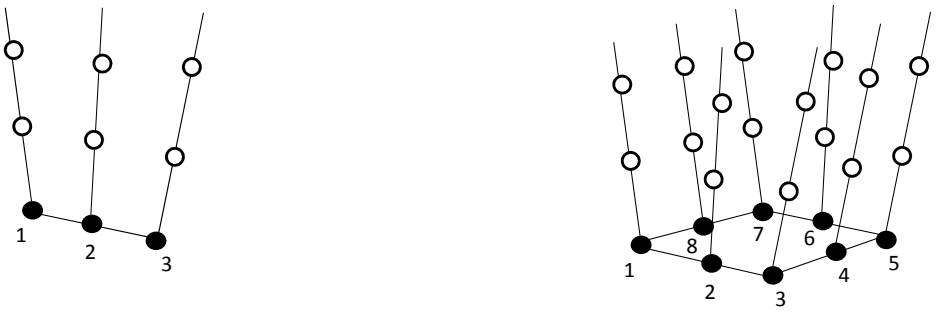

(a) 2D or axisymmetric problems

(b) 3D problems

FIGURE 2.2: Infinite elements (unfilled dots) extruded from the primary nodes (filled dots) at the free external face of the FE mesh [39].

In the FE/IE model used in ACTRAN/TM, the acoustic field near the intake geometry is discretised using finite elements. To model sound radiation beyond the FE domain, a layer of infinite elements is compatibly matched along the free external faces of the FE mesh (shown in Figure 2.2). The infinite elements thus impose an exponential decay on the solutions obtained from the FE mesh.

2.5 Shell codes to perform intake predictions

In this thesis, ACTRAN/TM is mostly used within proprietary shell codes namely ANPRORAD and PHOENIX. These shell codes automatically generates the FE mesh and executes the necessary ACTRAN/TM jobs over a specified range of azimuthal orders and frequencies. They are used to performs both near and far-field acoustic analysis of sound propagation and radiation from turbofan intakes. In the following sections, the axisymmetric versions of these codes are briefly described. These versions of the shell code generate an axisymmetric ACTRAN/TM model in which the geometry is meshed in a plane of rotation and each azimuthal order is treated as a separate computation.

2.5.1 ANPRORAD

ANPRORAD (ANalysis for PROpagation and RADiation) [48] was developed at ISVR in partnership with IHI Corporation. By providing the key geometric data of the turbofan intake in co-ordinate form, ANPRORAD creates the entire intake geometry using B-spline interpolation. Figure 2.3 shows the axisymmetrized model of a High-Bypass Ratio (HBR) intake created by ANPRORAD. The computational domain is divided into a near field region V_{NF} which is modelled by finite elements and an external region V_{FF} modelled using by infinite elements. The FE domain is defined by an ellipsoid with a centre (c,0) with c being the distance from the fan plane and a and b as the major and minor axis respectively (figure 2.3).

The FE domain is compatibly matched to a layer to infinite elements. The remaining boundaries of the domain consists of the fan plane Γ_F, the lined surfaces Γ_L and the remaining hard-walled surfaces Γ_H which includes the spinner and remaining parts of the nacelle. Since ANPRORAD is used to perform noise predictions only in the forward-arc of an intake duct, the rear of the nacelle is represented in a non-realistic manner.

In order to mesh the FE domain, the number of nodes per wavelength in the axial direction N_z and the number of elements in the radial direction at the source plane need to be specified in the ANPRORAD input file 'inputfile.txt' [48]. N_z is usually

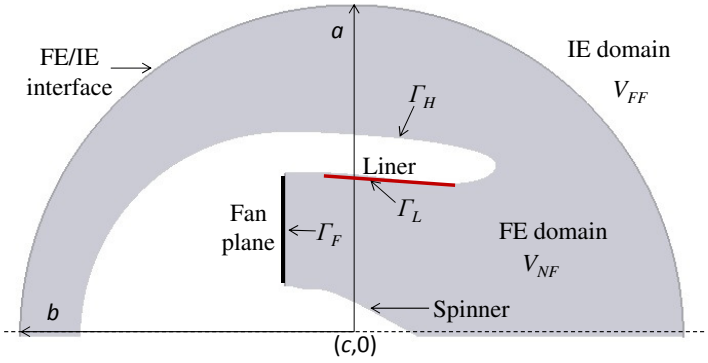

FIGURE 2.3: FE ellipsoid domain with centre $(c,0)$ and major and minor axes a and b respectively

specified in terms of the effective wavelength at the fan plane λ^*_{FP} to account for the wave shortening effect and is expressed as

$$\lambda^*_{FP} = \lambda_{FP}\left(1 - M_{FP}\right), \tag{2.32}$$

where λ_{FP} is the local wavelength at the fan plane and is expressed as

$$\lambda_{FP} = \frac{c_{stag}}{f\sqrt{1 + \left(\frac{\gamma-1}{2}\right) M^2_{FP}}}, \tag{2.33}$$

where c_{stag} is the stagnation value of sound speed and M_{FP} is the Mach number at the fan plane.

The number of elements in the radial direction is decided in a way such that the elements are square-shaped at the source plane. If the model is three-dimensional, the number of elements in the circumferential direction also needs to be specified at the source plane. The number of circumferential elements is chosen in a manner such that the highest azimuthal mode order is effectively resolved. A low resolution axisymmetric ANPRORAD mesh is shown in figure 2.4. A mesh resolution of five quadratic elements per effective wavelength is used to discretise the FE domain.

In order simulate a desired engine condition in ANPRORAD, the flow field boundary condition is specified in terms of Mach number at the fan plane and the ambient flow Mach number. These conditions can also be specified in ANPRORAD in terms of mass flow rate. The mean flow is calculated by using a compressible Euler solver embedded in the code. An example of mean flow solution for approach engine condition (specifications listed in table A.1) produced by ANPRORAD is shown in figure 2.5.

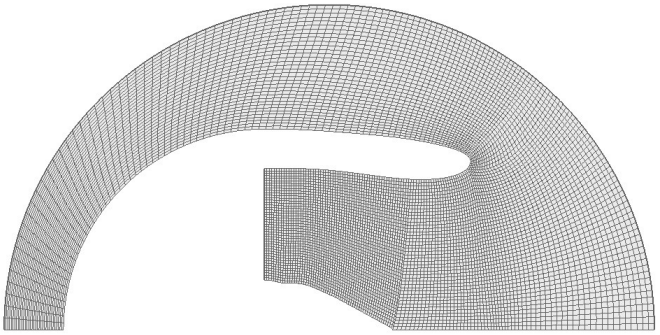

FIGURE 2.4: FE mesh generated by ANPRORAD for acoustic computation at 1kHz

ANPRORAD is however designed to perform the acoustic analysis for a single azimuthal mode. In order to use it for multiple azimuthal modes, another program 'multi-m' has been developed by Sugimoto [49] which executes ANPRORAD for multiple azimuthal orders. By providing an information of all incident modes, 'multi-m' produces an output file containing the far-field SPL values at field points specified in ANPRORAD.

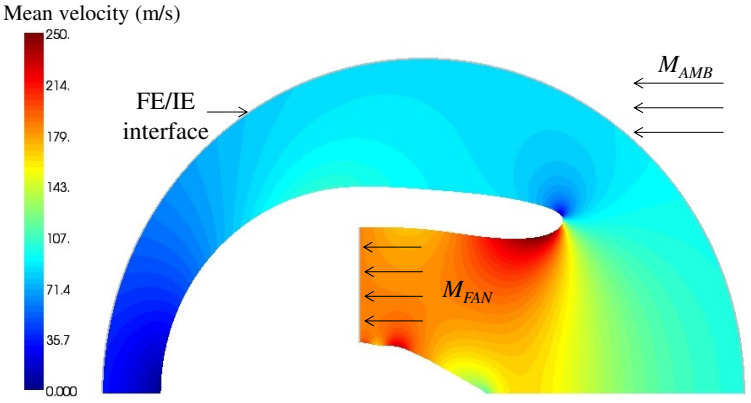

FIGURE 2.5: Mean flow velocity Contours calculated using the Euler flow solver in ANPRORAD

2.5.2 PHOENIX

PHOENIX (Parametric mesHing and analysis of aerOENgine Intakes and eXhausts) [50] is another ACTRAN/TM shell code which automates the procedures for noise prediction in both intake and bypass sections of a turbofan engine. It was developed at ISVR in partnership with Free Field Technologies (FFT), Belgium. Like ANPRORAD, PHOENIX also generated a FE mesh and runs ACTRAN/TM computations over a desired range of incident acoustic modes and/or frequencies specified by the

user. The shell code creates the intake or bypass geometry by using key geometric data provided by the user. In this thesis, the axisymmetric version of this code is used.

For intake predictions, the computational domain is divided into a near field region modelled by using finite elements and an external region modelled using by infinite elements. PHOENIX generates a circular FE domain with a centre (c,0) radius r (figure 2.6).

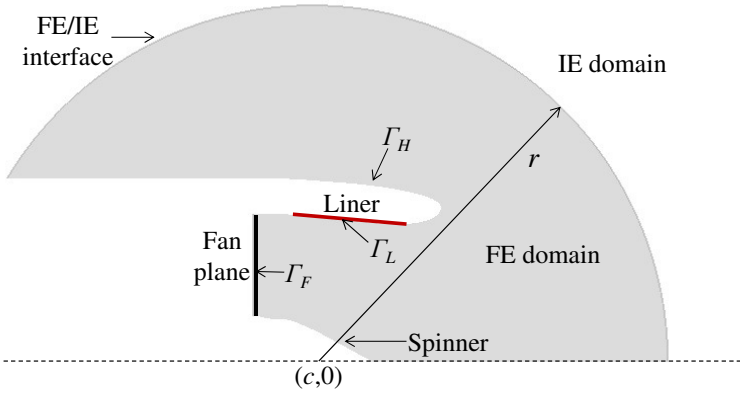

FIGURE 2.6: Circular FE domain with centre (c,0) and radius r

The FE domain is descritised by using unstructured mesh consisting of quadratic elements. The mesh is generated automatically by using either GMSH or ICEM CFD meshing tools. The target elements size in the FE mesh is decided by three factors:

I. $ACOUS\_FACTOR$: It defines the number of quadratic elements per effective axial wavelength

II. $RADIAL\_FACTOR$: It is used to refine the mesh near the source plane. It defines the number of quadratic elements on the radial direction at the source plane.

III. $CURV\_FACTOR$: It drives the mesh refinement on the curved section of the geometry like the intake lip.

The user also has the liberty to generate the FE mesh using other meshing tools as long as the mesh can be exported in an ACTRAN supported format. An example of FE mesh generated by GMSH is shown in figure 2.7.

The mean flow is calculated by using an Euler flow solver within ACTRAN/TM. Unlike ANPRORAD, the mean flow is not computed by using the acoustic mesh but on a separate mesh generated on a larger domain as shown in figure 2.8(a) The flow field boundary condition can specified in terms of axial velocity, Mach number or mass flow rate at the fan plane and the far field. The detail on the specification of the flow

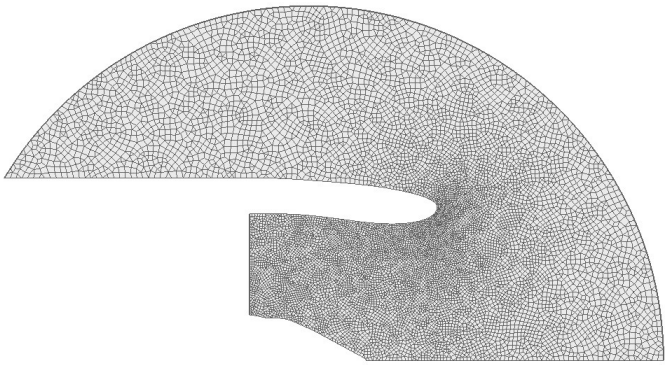

FIGURE 2.7: FE mesh generated by PHOENIX for acoustic computation at 1kHz

boundary condition can be found in the manual [50]. Figure 2.8(b) shows an example of mean flow solution produced by PHOENIX for the same flow condition used in figure 2.5.

The mean flow solution is then interpolated on the acoustic mesh. Figure 2.9 shows the interpolated flow.

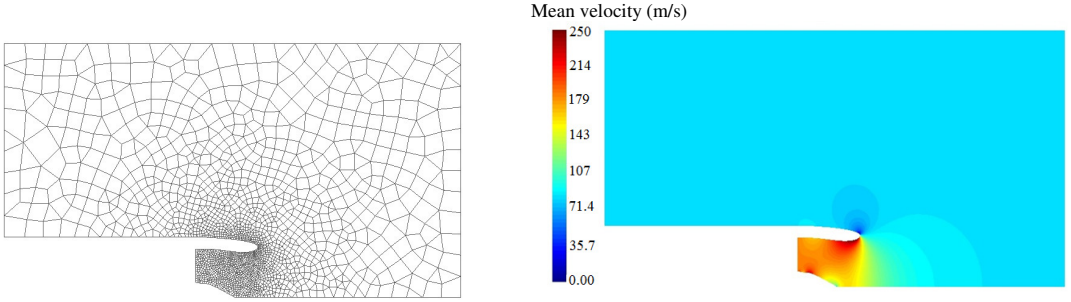

(a) FE mesh for mean flow computation

(b) Mean flow solution

FIGURE 2.8: An example of mean flow computation in PHOENIX

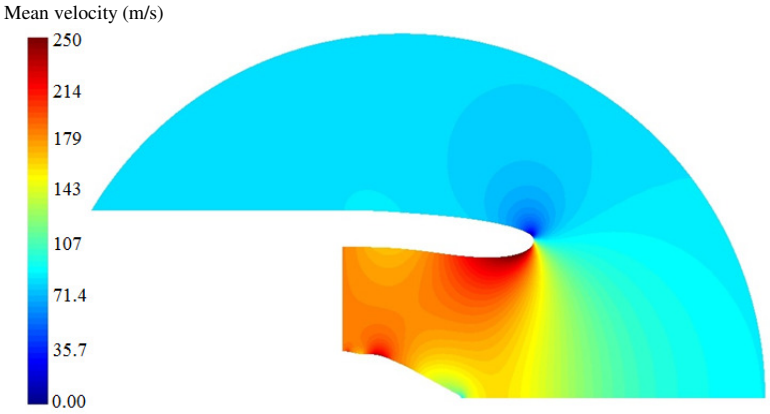

FIGURE 2.9: Mean flow solution interpolated on the acoustic mesh

PHOENIX uses a more recent version of ACTRAN as compared to ANPRORAD. Moreover, PHOENIX can easily generate reasonably fine FE meshes at very high frequencies whereas ANPRORAD fails to do so. In this thesis however, ANPRORAD is used more extensively than PHOENIX as the latter was very recently developed at ISVR.

2.5.3 Comparison of PHOENIX and ANPRORAD intake predictions

Both PHOENIX and ANPRORAD employ ACTRAN/TM to perform the acoustic computation but the solvers used for mean flow computation are different. In PHOENIX, the compressible mean flow is computed by Euler flow solver available within ACTRAN/TM whereas ANPRORAD uses an independent Euler solver. It is therefore important to check whether the results obtained by the two shell codes agree with each other.

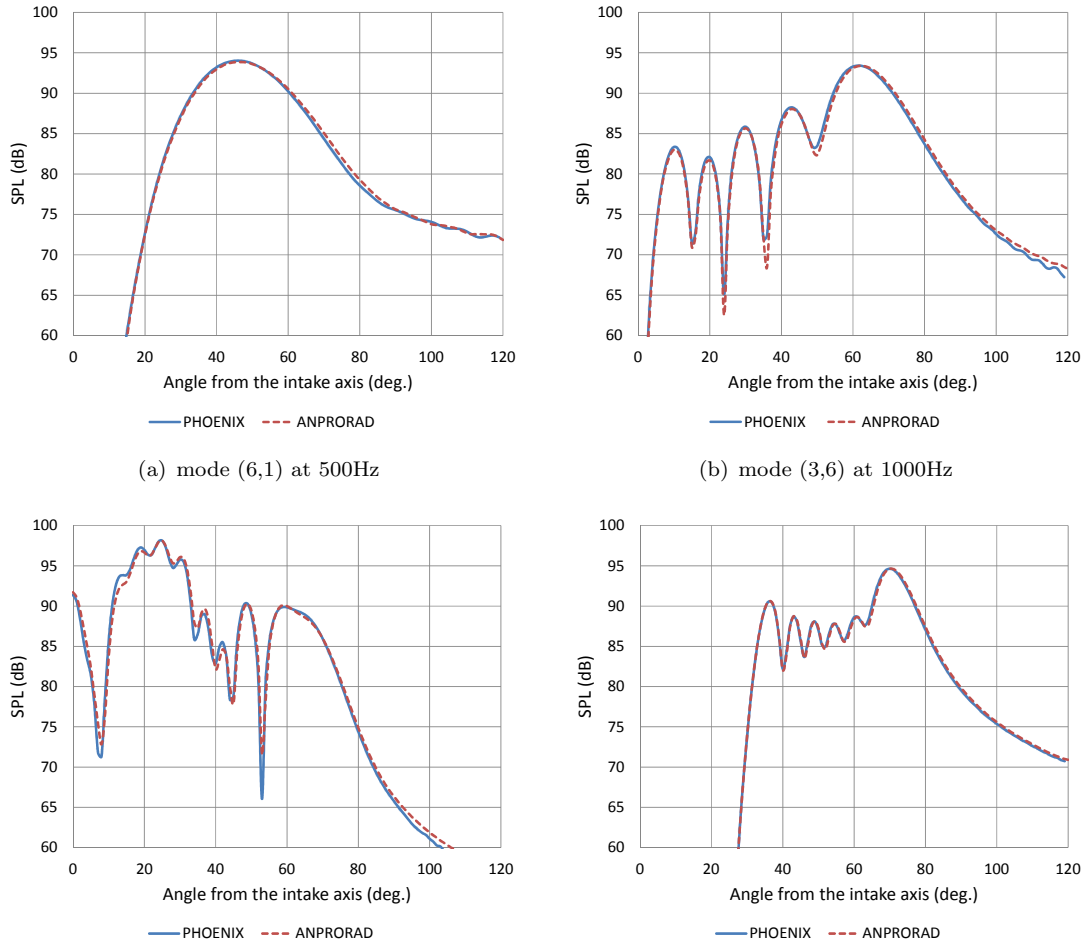

(a) mode (6,1) at 500Hz

(b) mode (3,6) at 1000Hz

(c) mode (0,11) at 2000Hz

(d) mode (40,6) at 3150Hz

FIGURE 2.10: Far-field SPL directivities obtained by ANPRORAD and PHOENIX

The far-field results obtained by ANPRORAD and PHOENIX are compared in this section for the approach engine condition (specifications listed in table A.1). The mean flow solutions produced by the two shell codes for the approach condition are shown in figures 2.5 and 2.9. Figure 2.10 shows the far-field SPL directivities of some randomly selected modes at four third octave centre frequencies. The results clearly indicate that the solutions obtained by ANPRORAD and PHEONIX are in good agreement.

2.6 Summary

In this chapter, a brief description of the commercial CAA tool ACTRAN/TM has been provided, which is used extensively in this thesis. The code solves the convected Helmholtz equation for the acoustic velocity potential and is therefore computationally less demanding. It can be used to solve acoustic propagation and radiation problems in a realistic turbofan intake within acceptable time frames. Two shell codes, ANPRORAD and PHOENIX which automatically generates FE mesh and runs ACTRAN/TM jobs with the prescribed set of conditions provided by the user, have also been briefly described. PHOENIX has a special advantage over ANPRORAD as the former can easily generate reasonably fine FE meshes even at very high frequencies.

ACTRAN/TM is however based on a linear theory and cannot deal with non-linear propagation of high amplitude tones at engine conditions when the fan-tip speed is supersonic. Such effects cannot be neglected to obtain accurate predictions at high fan operating conditions. A procedure to model non-linear propagation effects of high amplitude tones is presented in the next chapter.

Chapter 3

Non-linear propagation of shock waves in turbofan intakes

3.1 Introduction

Non-linear acoustics is a branch of acoustics which deals with waves of amplitude high enough that linear theory is violated. Detailed theoretical description of the non-linear phenomenon in acoustics can be found in references [51–54]. In turbomachinery applications, non-linear theory is very important to study noise propagation at high fan speeds, especially at locations close to the fan [15, 19, 55]. At high supersonic fan-tip speeds, the rotor-locked tones are strongly cut-on and have very high amplitudes. It is due to this reason that the propagation of these BPF tones cannot be predicted using linear theory. Hence, a non-linear prediction tool needs to be implemented to study the non-linear effects of these high amplitude acoustic waves. In this chapter, an analytical model devised by Morfey and Fisher [17] and Fisher *et al.* [18] is emphasized in detail with its application to the non-linear propagation of BPF tones.

At sideline engine condition when the fan tip speed exceeds sonic velocity, the pressure waveform close to the duct wall consists of a series of shock and Prandtl-Meyer expansion waves which are locked to the rotor [15, 19, 55]. These shock and expansion waves are located very close to the leading edge of the fan blade and they propagate by spiralling upstream of the fan in the intake of a turbofan engine. For a fan with identical blades and consistent stagger angle, the pressure waveform along the axis perpendicular to the shock waves resembles a regular saw-tooth (or N-wave) as shown in figure 3.1. The shocks propagate upstream of the intake at an undisturbed speed of sound relative to the axial oncoming flow and subsequently, their strength decays non-linearly with the axial distance upstream of the fan. In the frequency spectrum, a regular saw-tooth is a superposition of tones at BPF and its harmonics [15, 19]. The

energy from tones at lower harmonics gets distributed over the higher harmonics as a result of non-linear dissipation of BPF tones.

The theory of non-linear attenuation of a regular saw-tooth described in references [15, 17–19, 55] is revised in this chapter to study non-linear propagation effects of BPF tones at high supersonic fan tip speeds. Finally, a methodology is described to model non-linear propagation effects in an approximate way within the linear predictions.

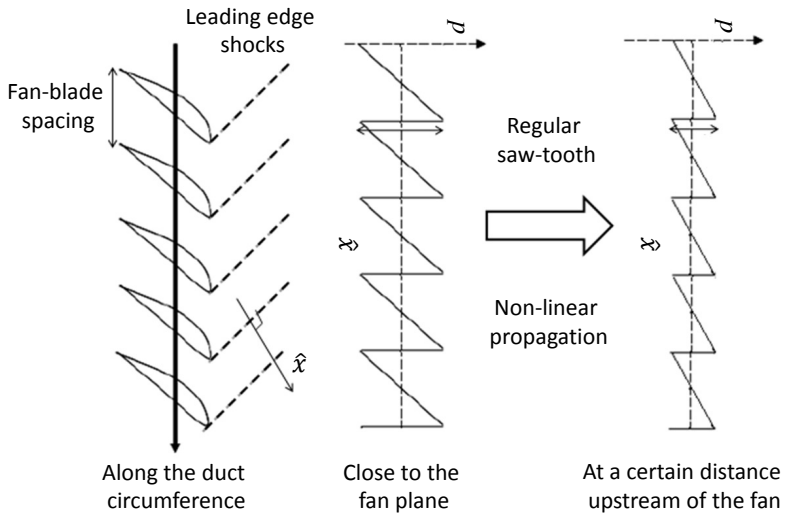

FIGURE 3.1: Generation and non-linear propagation of shock waves by a supersonic ducted fan; $\hat{x}$ is the axis perpendicular to the shock waves

3.2 Literature Review

In the past, the non-linear propagation of high amplitude sound waves in uniform ducts was studied by Mendousse [56] and Rudnick [57]. In 1970, Morfey and Fisher [17] derived the non-linear attenuation of regular saw-tooth based on the weak shock theory. It was assumed that the shock system propagates in a purely one dimensional manner and the attenuation was calculated in terms of the total time the spiralling wavefront takes to reach a fixed axial location upstream of the inlet. This time was referred as the 'time of flight' which was shown to be linearly dependent on the axial distance upstream of the intake. However, the analytical model did not include any absorbtion term to account for sound absorbed by the acoustic liners. In 1998, Fisher, Tester and Schwaller [18] extended the model by including an absorbtion term which was independent of modes and frequency. This model was used as the first approximation to determine the non-linear attenuation of the waveform in acoustically lined turbofan intakes. It was assumed that all the BPF harmonics decay at the same rate, which

can be argued as a crude approximation since the liner's performance will be frequency dependent.

A recent series of papers by McAlpine and Fisher [15, 19] emphasized on the non-linear attenuation of BPF tones to predict buzz-saw noise. In practice, the fan blades of the rotor are non-identical and have slight variations in stagger angles. As a result, the pressure signature near the fan looks like an irregular saw-tooth [15]. The frequency spectrum of such a waveform contains energy not only at the BPFs but also at the engine order (EO) tones occurring at the harmonics of shaft rotation frequency. Buzz-saw noise is predominantly caused due to the non-linear decay of rotor-locked pressure field as it propagates upstream of the intake. The key step in these papers was that the non-linear propagation models are transformed into modal/frequency domain allowing the absorbtion term to be frequency and mode dependent. A numerical scheme termed as Frequency Domain Numerical Solution (FDNS) was developed by McAlpine to predict the amplitudes of the EO tones which dominate 'buzz-saw' noise in hard-walled and acoustically lined ducts.

In all the non-linear study performed in this thesis, it is assumed that the saw-tooth waveform generated near the fan at supersonic fan-tip speeds is regular, that is, the fan blades are identical and have consistent stagger angles. In other words, the frequency spectrum consists of BPF tones only. Hence, the analytical models developed by Morfey and Fisher [17] and Fisher, Tester and Schwaller [18] for hard-walled and acoustically lined ducts are used to predict the non-linear propagation of rotor-locked BPF tones. The simplicity of the model encourages easy post-processing of the results obtained from CAA models like ACTRAN, which is detailed later in this chapter. However, it is important to note that such a model may be considered as a weak model as it neglects the buzz-saw noise components at supersonic regime. Although the BPF tones are really protrusive at the fan section, the presence of the EO tones can influence the variation of the BPF energy in the duct [55], which the model does not take into account.

3.3 Non-linear wave equation

When the non-linear terms in the conservation equations of continuity, momentum and energy are retained, these equations are much harder to solve. However, consideration of special cases reduces the mathematical difficulty [54]. Assuming a lossless perfect gas, the Euler equations in conservative form [58, 59] are expressed as

i) **Continuity** :

$$\frac{D\rho}{Dt} + \rho\nabla \cdot \mathbf{u} = \mathbf{0}, \tag{3.1}$$

ii) **Momentum** :

$$\rho \frac{D\mathbf{u}}{Dt} + \nabla p = 0, \tag{3.2}$$

ii) **Energy** (isentropic condition):

$$\frac{p}{p_0} = \left(\frac{\rho}{\rho_0}\right)^{\gamma}, \tag{3.3}$$

iii) **Equation of state** :

$$p = \rho RT, \tag{3.4}$$

iv) **Speed of sound** :

$$c^2 = \frac{Dp}{D\rho}, \tag{3.5}$$

which using equation 3.3 becomes

$$c^2 = \frac{\gamma p}{\rho}. \tag{3.6}$$

In equations 3.1 to 3.6, the symbols have their usual meaning and denote the total quantities and the subscript $_0$ denotes their static values. The operator D/Dt ($=\partial/\partial t + \mathbf{u}\cdot\nabla$) is the substantial derivative [59]. For non-linear waves, the speed of sound c is not constant [54] and p and ρ can be expressed in terms of c using equations 3.3 and 3.6:

$$p = p_0 \left(\frac{c}{c_0}\right)^{\frac{2\gamma}{\gamma-1}} \tag{3.7}$$

$$\rho = \rho_0 \left(\frac{c}{c_0}\right)^{\frac{2}{\gamma-1}} \tag{3.8}$$

Substituting equations 3.7 and 3.8 in equations 3.1 and 3.2, we get

Non – linear Continuity :

$$\frac{Dc}{Dt} + \frac{\gamma-1}{2} c\nabla\cdot\mathbf{u} = \mathbf{0} \tag{3.9}$$

Non – linear Momentum :

$$\frac{D\mathbf{u}}{Dt} + \frac{2}{\gamma-1} c\nabla c = 0 \tag{3.10}$$

Assuming unidirectional plane flow, $\mathbf{u} = (u, 0, 0)$, equations 3.9 and 3.10 simplify to one-dimensional non-linear continuity and momentum equations:

$$\frac{\partial c}{\partial t} + u\frac{\partial c}{\partial x} + \frac{\gamma - 1}{2}c\frac{\partial u}{\partial x} = 0 \tag{3.11}$$

$$\frac{\partial u}{\partial t} + u\frac{\partial u}{\partial x} + \frac{2}{\gamma - 1}c\frac{\partial c}{\partial x} = 0 \tag{3.12}$$

In order to solve this second-order system of equations, we seek to find a relationship between c and u that makes both the equations same [54]. If such a relationship exists, then

$$\frac{\partial c}{\partial t} = \frac{\partial c}{\partial u}\frac{\partial u}{\partial t} \tag{3.13}$$

$$\frac{\partial c}{\partial x} = \frac{\partial c}{\partial u}\frac{\partial u}{\partial x} \tag{3.14}$$

Substituting equations 3.13 and 3.14 in equations 3.11 and 3.12, we get

$$\frac{\partial u}{\partial t} = \left(u + \frac{\gamma - 1}{2}\frac{c}{\frac{\partial c}{\partial u}}\right)\frac{\partial u}{\partial x} \tag{3.15}$$

$$\frac{\partial u}{\partial t} = \left(u + \frac{2}{\gamma - 1}c\frac{\partial c}{\partial u}\right)\frac{\partial u}{\partial x} \tag{3.16}$$

Equations 3.15 and 3.16 are similar only if $\partial c/\partial u = \pm(\gamma - 1)/2$. On choosing the positive sign for forward traveling waves and using the condition that $c = c_0$ at $u = 0$, we get

$$c = c_0 + \frac{\gamma - 1}{2}u, \tag{3.17}$$

which on substitution in either 3.11 or 3.12, gives

$$\frac{\partial u}{\partial t} + (c_0 + \beta u)\frac{\partial u}{\partial x} = 0, \tag{3.18}$$

where β $(= (\gamma + 1)/2)$ is termed as the coefficient of non-linearity. To apply equation 3.18 to a shock system which propagates with the speed of sound c_0 in a purely one-dimensional manner, the co-ordinate x is expressed as $x = \hat{x} + c_0 t$, where $\hat{x}$ co-ordinate normal to the shocks moving with the speed of sound c_0 as shown in figure 3.1. Expressing equation 3.18 in terms of the moving co-ordinate $\hat{x}$, we get [51]

$$\frac{\partial u}{\partial t} + \beta u \frac{\partial u}{\partial \hat{x}} = 0. \tag{3.19}$$

Equation 3.19 is derived from Euler equation as the starting point which assumes a lossless medium. But if the medium is not lossless, a dissipative term similar to the viscous dissipative term ($\nu \nabla^2 u$) in Navier-Stokes equation can be included on the right. Equation 3.19 can, therefore, be modified as

$$\frac{\partial u}{\partial t} + \beta u \frac{\partial u}{\partial \hat{x}} = \varepsilon \frac{\partial^2 u}{\partial \hat{x}^2}, \tag{3.20}$$

where ε is the dissipation coefficient (for viscous dissipation, ε is the coefficient of viscosity, generally denoted as ν). For a plane progressive wave ($u = p/\rho c$), equation 3.20 can be solely expressed in term of p.

$$\frac{\partial p}{\partial t} + \frac{\beta}{\rho_0 c_0} p \frac{\partial p}{\partial \hat{x}} = \varepsilon \frac{\partial^2 p}{\partial \hat{x}^2}. \tag{3.21}$$

3.4 Non-linear attenuation of a regular saw-tooth-type shock waveform - analytical model

Morfey and Fisher [17] developed an analytical expression to calculate the non-linear attenuation of regular saw-tooth in hard-walled duct based on the weak shock theory. It was based on the fact that different points on the pressure waveform travel with different speeds in which a point ahead of the shock travels with speed $c < c_0$ and points behind the shock travel with speed $c > c_0$. Hence, all the points on the waveform where $p < p_0$ travel slower, and points where $p > p_0$ travel faster than the shock. Fisher *et al.* [18] used the same model including an absorbtion term to predict the non-linear attenuation in lined ducts.

The same analytical model was re-derived by McAlpine and Fisher [19] using the non-linear Burgers equation (equation 3.21) by expressing the regular saw-tooth in terms of a complex fourier series. This derivation is revised in detail in this section.

Rewriting equation 3.21 in terms of non-dimensional variables,

$$T = \frac{t}{\frac{c_0}{\lambda}} \tag{3.22}$$

$$X = \frac{2\pi \hat{x}}{B\lambda} \tag{3.23}$$

$$P = \frac{\gamma + 1}{2\gamma} \frac{p}{p_0} \tag{3.24}$$

where λ is the inter-shock spacing or the wavelength of the regular saw-tooth (N-wave) and B is the number of fan blades (see figure 3.2), we get

$$\frac{\partial P}{\partial T} + \frac{2\pi}{B} P \frac{\partial P}{\partial X} = \frac{\varepsilon}{B^2} \frac{\partial^2 P}{\partial X^2}. \tag{3.25}$$

Dropping the dissipative term by assuming a lossless medium, we have

$$\frac{\partial P}{\partial T} + \frac{2\pi}{B} P \frac{\partial P}{\partial X} = 0. \tag{3.26}$$

The pressure signature along $\hat{x}$ is assumed to be a regular saw-tooth which can be expressed in terms of a complex fourier series [19],

$$P(X,T) = \sum_{m=-\infty}^{\infty} C_m(T) e^{imX}, \tag{3.27}$$

where C_m are the complex coefficients and m is the azimuthal order of the modes which constitute the regular saw-tooth waveform in frequency domain. Since the waveform is a superposition of all the BPF tones, m allows only the integer multiples of B. In the study performed by McAlpine and Fisher [19], it was assumed that the rotor-locked pressure field is localized very close to the wall and therefore all the energy is assumed to be concentrated in modes with radial order n=1. The complex Fourier coefficients C_m can be determined for a regular N-wave with shocks positioned at $X = ((2k-1)\pi)/B$, where $k = 1, 2, 3...B$; [19]

$$C_m = \frac{iBP_s}{2\pi m} cos\left(\frac{m\pi}{B}\right), \tag{3.28}$$

where P_s is the non-dimensional shock strength or the amplitude of pressure waveform. By using equation 3.27 and 3.28, equation 3.26 can be transformed into a simple differential equation.

$$\frac{dP_s}{dT} = -P_s^2. \tag{3.29}$$

Equation 3.29 can be modified by including a linear damping term to predict the non-linear attenuation of the saw-tooth in an acoustically lined duct [19] to give

$$\frac{dP_s}{dT} = -P_s^2 - \sigma P_s, \tag{3.30}$$

where σ is the linear attenuation rate due to the liner. In order to solve equation 3.30 analytically, σ is assumed to be constant (independent of frequency and mode number), that is, all the BPF harmonics decay at the same rate. This is a crude assumption in prediction of non-linear attenuation in lined ducts. However, appropriate predictions can be obtained by choosing a reasonable value of σ, which is explained in detail in the next section. Integrating equations 3.29 and 3.30 provides an analytical model to predict the non-linear attenuation of a regular saw-tooth type pressure waveform in hard-walled and acoustically lined ducts:

Without linear attenuation:

$$p_s(T) = \frac{p_0 s}{\left[1 + \frac{\gamma+1}{2\gamma} T s\right]} \tag{3.31}$$

With linear attenuation:

$$p_s(T) = \frac{p_0 s e^{-\sigma T}}{\left[1 + \frac{\gamma+1}{2\gamma} T s \frac{(1-e^{-\sigma T})}{\sigma T}\right]} \tag{3.32}$$

Here, p_s is the shock strength or the amplitude of the pressure waveform and s $(= p_s(0)/p_0)$ is the initial shock strength or the amplitude of the pressure waveform at the fan plane.

The non-dimensional time T (termed as 'time of flight') can be expressed in terms of the axial distance upstream of the fan by using kinematic relationships, as outlined by Morfey and Fisher [17]. Referring to figure 3.2, the axial Mach number of the shock (propagating with speed of sound c_0) relative to the axial inflow Mach number M_a is given by

$$M_u = sin\phi - M_a. \tag{3.33}$$

From figure 3.2, it is clear that

$$\phi + \beta + \mu = \pi. \tag{3.34}$$

In terms of Mach numbers M_a and M_{rel},

$$cos\beta = \frac{M_a}{M_{rel}}. \tag{3.35}$$

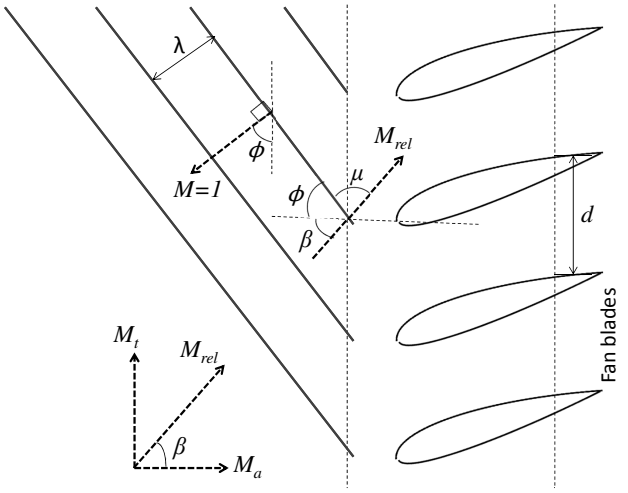

FIGURE 3.2: Shock waves traveling upstream of an ideal fan with speed of sound c_0

And from shock theory, the Mach angle μ is given by [17]

$$sin\mu = \frac{1}{M_{rel}}. \tag{3.36}$$

Using equations 3.34, 3.35 and 3.36, we get

$$cos\phi = \frac{1}{M_{rel}^2}\left[M_t - M_a\left(M_{rel}^2 - 1\right)^{1/2}\right] \tag{3.37}$$

$$sin\phi = \frac{1}{M_{rel}^2}\left[M_a + M_t\left(M_{rel}^2 - 1\right)^{1/2}\right] \tag{3.38}$$

If z is the axial distance traversed by the shock upstream of the fan and t is the time taken to travel this distance, then $z = (M_u c)t$, which on using equation 3.22, becomes

$$T = \frac{z}{\lambda M_u}. \tag{3.39}$$

From the figure 3.2, $\lambda = dcos\phi$ and $d = (\pi D)/B$, where D is the duct diameter. Hence, the inter-shock spacing λ is given by

$$\lambda = \frac{\pi D}{B} cos\phi. \tag{3.40}$$

Substituting equations 3.33, 3.37, 3.38 and 3.40 in equation 3.39, we get a linear relationship between T and z

$$T = \kappa z, \tag{3.41}$$

where

$$\kappa = \frac{B}{\pi D} \frac{M_{rel}^4}{\sqrt{M_{rel}^2 - 1}} \left[M_a \sqrt{M_{rel}^2 - 1} - M_t \right]^{-2}. \tag{3.42}$$

Note that in equation 3.42, only the magnitude of M_a should be used as its direction opposite to the direction of sound propagation has already been taken into account (figure 3.2). Substituting equation 3.41 in equations 3.31 and 3.32, we get the complete analytical expressions to predict the non-linear propagation of a regular saw-tooth type pressure waveform in hard-walled and acoustically lined intakes.

Non – linear propagation model in a hard – walled duct :

$$p_s(z) = \frac{p_0 s}{\left[1 + \frac{\gamma+1}{2\gamma} \kappa z s\right]} \tag{3.43}$$

Non – linear propagation model in an acoustically lined duct :

$$p_s(z) = \frac{p_0 s e^{-\sigma \kappa z}}{\left[1 + \frac{\gamma+1}{2\gamma} s \frac{(1 - e^{-\sigma \kappa z})}{\sigma}\right]} \tag{3.44}$$

3.5 Application of the analytical models to the non-linear propagation of rotor locked BPF tones

At high supersonic fan tip speeds, the rotor-locked BPF tones are strongly cut-on and have a high sound pressure levels (SPL) near the wall close to the fan. These high amplitude tones decay non-linearly on propagating upstream of the fan. In this section, equations 3.43 and 3.44 are applied to study the non-linear propagation of these tones in both hard-walled and acoustically lined ducts.

In equation 3.44, the linear attenuation rate σ is constant and so all the BPF harmonics are assumed to decay linearly at the same rate. In this study, the linear attenuation rate σ of the total pressure field is generally assumed be equivalent to the attenuation rate of the the first BPF mode (B,1). This is a reasonable assumption since the total pressure field of the saw-tooth waveform is generally dominated by the first BPF harmonic. Hence, σ in equation 3.44 can be evaluated as

$$\sigma = Real\left(\frac{ik_z}{\kappa}\right) = -\frac{k_{zi}}{\kappa}, \tag{3.45}$$

where $k_z(= k_{zr} + ik_{zi})$ is the axial wave-number of the least attenuated mode (B,1) in the acoustically lined section. The imaginary part (k_{zi}) of the axial wave-number is always negative for forward-propagating modes (propagating upstream of the fan). Since, both equations 3.43 and 3.44 are for a forward-propagating pressure waveform, the axial wave-number of the forward propagating mode (B,1) is used in calculating σ. However, the calculation of σ is not that straightforward for a realistic duct geometry as the axial wave-number of (B,1) cannot be easily determined. In that case, it is approximately determined from the far-field pressure field shapes of mode (B,1) in the hard-walled and lined configurations. This is detailed in chapter 4. Using equation 3.45 and the fact that $s = p_s(0)/p_0$, equations 3.43 and 3.44 can be modified as,

$$p_s(z) = \frac{p_s(0)}{\left[1 + \frac{\gamma+1}{2\gamma}\kappa\frac{p_s(0)}{p_0}z\right]} \tag{3.46}$$

$$p_s(z) = \frac{p_s(0)e^{k_{zi}z}}{\left[1 - \kappa\frac{\gamma+1}{2\gamma}\frac{p_s(0)}{p_0}\frac{(1-e^{k_{zi}z})}{k_{zi}}\right]} \tag{3.47}$$

Incase the total pressure field of the BPF tones is not entirely dominated by the 1st BPF mode, then the linear attenuation rate σ in equation 3.44 is determined from the resultant attenuation of the BPF tones summed up in an uncorrelated manner. This is explained in detail in chapter 5.

3.5.1 Non-linear adjustments to linear predictions

It can be clearly seen that in equations 3.46 and 3.47, the numerators denote the linear propagation models to predict the acoustic pressure field in hard walled and lined ducts respectively, and the denominators are the corresponding non-linear adjustments to the linear solutions. These equations however provide information about the amplitude of the pressure field at the duct wall but not its phase. But in order to predict the SPL at the duct wall, this information is sufficient. Hence, equations 3.46 and 3.47 can be rewritten in terms of SPL as,

$$SPL(z) = \underbrace{SPL(0)}_{\text{linear prediction}} \underbrace{- 20log_{10}\left[1 + \frac{\gamma+1}{2\gamma}\kappa\frac{p_s(0)}{p_0}z\right]}_{\text{non-linear adjustment}} \tag{3.48}$$

$$SPL(z) = \underbrace{SPL(0) + 8.69 k_{zi} z}_{\text{linear prediction}} \underbrace{- 20 log_{10}\left[1 - \kappa \frac{\gamma+1}{2\gamma} \frac{p_s(0)}{p_0} \frac{(1 - e^{k_{zi} z})}{k_{zi}}\right]}_{\text{non-linear adjustment}} \tag{3.49}$$

The first term on the right-hand side of the equation 3.48 is the SPL at the duct wall close to the fan (at z=0) or the source SPL at the wall and the second term is the non-linear attenuation term. In order words, the first term provides linear predictions in a hard-walled uniform cylindrical duct and the second term is the non-linear adjustment to the linear predictions.

Similarly, the first term on the right-hand side of the equation 3.49 is the SPL at the duct wall close to the fan (at z=0) or the incident SPL at the wall, the second term denotes linear attenuation due the acoustic lining and the third term denotes the non-linear attenuation. In order words, the first and the second term taken together provide linear predictions in lined sections of a uniform cylindrical duct and the final term is the non-linear adjustment to the linear predictions.

3.5.2 Application

Consider a uniform cylindrical duct which idealizes an intake duct of fan diameter D and length l as shown in figure 3.3. The acoustic liner starts very close to the fan. The length of the liner to the duct diameter is approximately 1:2. An incident mode (24,1) is injected at the fan plane, to simulate the rotor-locked BPF tone for a fan with 24 blades. The fan has 24 blades and is operating at sideline condition (M_a=0.55). The mean flow Mach number (M_a) is taken to be 0.55 which is typical of sideline condition. At this condition, the rotor-locked BPF mode (24,1) is strongly cut on and propagates non-linearly upstream of the fan. In this section, equations 3.48 and 3.49 are applied to predict the non-linear propagation of this mode.

Equation 3.48 is applied to the hard-walled sections of the duct. Equation 3.49 is applied in the lined section using the source level at the liner start predicted by equation 3.48. Figure 3.4 shows a comparison between the linear and non-linear predictions of axial SPL of the rotor-locked mode (24,1) inside the duct.

Figure 3.4 shows that the non-linear effects are significant close to the fan where the SPL is very high. When the source SPL at the duct wall is as low as 120dB, the non-linear effects are less significant and so the propagation of the rotor-locked mode can be predicted by using linear theory. Also at distances far away from the fan near the duct exit, the SPL at the duct wall reduces to pressure levels at which linear propagation can be assumed.

Figure 3.4 shows that the linear solutions always over predict the liner insertion loss when compared to the corresponding non-linear predictions. This clearly indicates that

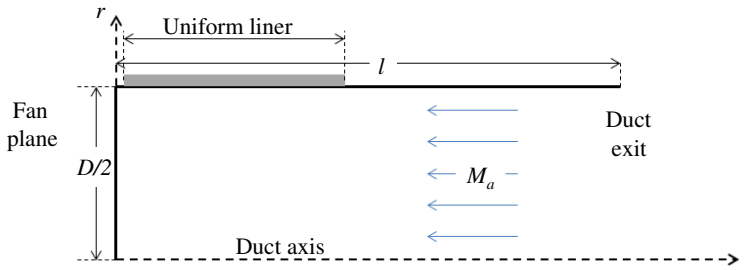

FIGURE 3.3: Sketch of a cylindrical duct of diameter D with uniform acoustic lining close to the fan

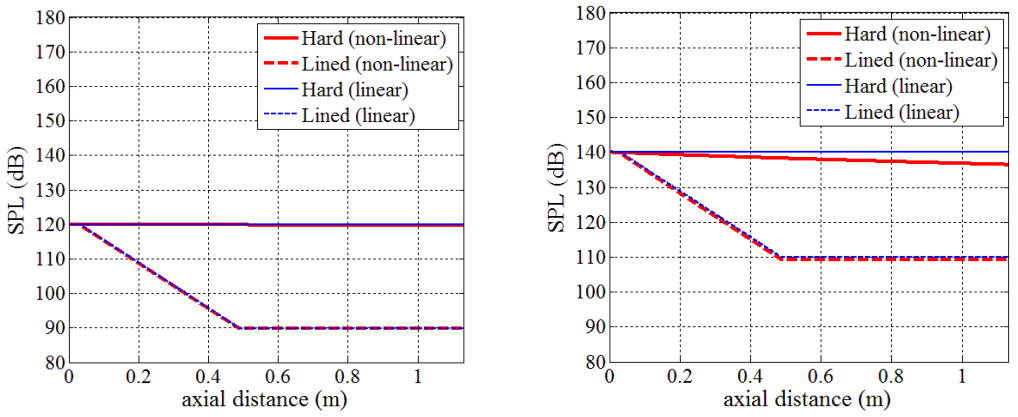

(a) 120 dB

(b) 140 dB

(c) 160 dB

(d) 180 dB

FIGURE 3.4: SPL of the rotor-locked BPF mode (24,1) at duct wall along the duct axis predicted by the analytical model at different source SPLs; blue: linear prediction, red: non-linear prediction

the non-linear propagation effects cannot be neglected in order to predict the correct liner attenuation of the acoustic pressure at high power settings.

3.6 Summary

This chapter provides a benchmark for all the non-linear predictions performed in this thesis. In this chapter, the analytical expressions derived by McAlpine and Fisher [19] to calculate the non-linear attenuation of a regular saw-tooth-type waveform with and without linear damping are revised. These expressions provide an understanding on how non-linear adjustments can be applied to the results predicted by linear models. The theory is then applied to predict the non-linear attenuation of the rotor-locked BPF mode at a high supersonic fan-tip speed and the results are compared to the corresponding linear predictions. The results indicate that the non-linear effects are significant close to the fan where the sound pressure levels are very high.

It must be notes that the non-linear model used in this thesis is based on some crude approximations. It neglects the importance of buzz-saw noise components in the noise spectrum thereby neglecting its influence on the attenuation of the BPF tones. Moreover, the model assumes that the shocks are localised at the tip of the fan blades whereas in practice the shocks have finite lengths along the span of the blades [60].

Chapter 4

Validation of CAA predictions for forward-arc fan noise

4.1 Introduction

Predicting Effective Perceived Noise Level (EPNL) at the engine design stage requires absolute values of SPL and directivities for all noise sources at the noise certification conditions. Using accurate Computational AeroAcoustics (CAA) predictions in place of measured data is highly beneficial since the latter is costly to acquire. Modern CAA methods are well developed for predicting propagation of sound on subsonic flows [9, 38]. They range from Helmholtz methods for irrotational flows, through Linearised Euler Equations (LEE) methods for sheared flows to full Euler and Navier-Strokes codes. In order to confidently use the computational methods for predicting fan noise propagation and radiation, validation against measured data is essential. However, such validations for well characterized sources and well defined liners is limited.

In this chapter, the far-field fan noise is predicted by using a commercial Finite/Infinite Element (FE/IE) CAA code ACTRAN/TM for rig and engine geometries of a typical HBR engine and the predictions are validated against measured far-field data. Fan noise sources are represented as a summation of high amplitude tones and multiple uncorrelated modes. By inferring the relative strengths of tones and multi-mode components from induct measurements and far-field directivities from hard-walled test data, the relative strengths of the source modes are obtained. Far-field predictions are performed for both hard-walled and lined configurations at the first BPF for five different engine speeds, and are compared to the measured far-field data. Since ACTRAN/TM cannot model the the non-linear propagation effects of high-amplitude tones at supersonic fan-tip speeds, a method to include such effects in the ACTRAN predictions is therefore described in this study. This is a more comprehensive study and an extension of the work reported by Astley *et al.* [61] and Achunche *et al.* [13].

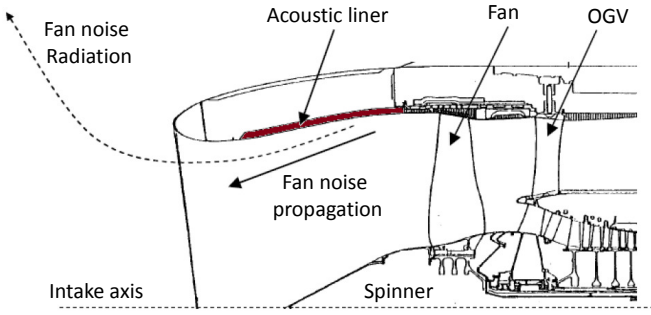

FIGURE 4.1: Propagation of fan noise through the intake and radiation into the forward-arc of the engine.

4.2 Literature Review

In the validation studies performed by Astley *et al.* [61] and Achunche *et al.* [13], a commercial FE/IE code ACTRAN/TM was used to model noise propagation and radiation from a turbofan rig intake at BPF, and the predictions were validated against measured far-field data. A similar validation against the measured engine data was also performed by Achunche in Chapter 7 of his thesis [62]. In these studies, the sources were represented as a multimodal component at subsonic fan-tip speeds, and a combination of multimodal content and a high amplitude rotor locked content at supersonic fan-tip speeds. An 'equal energy per mode' assumption was used for modelling the multimode content at different fan operating conditions. In-duct sound pressure level (SPL) measured at the transducer ring was used to calibrate the far-field predictions. At high supersonic fan-tip speed, a Frequency Domain Numerical Solution (FDNS) developed by McAlpine [15, 19, 55] was used to model the non-linear attenuation of the rotor-locked tones which improved the agreement with the far-field measurements.

In addition to noise predictions at BPF, Achunche [13] also performed fan broadband noise predictions at 50% fan speed and validated the results against the rig measurements. At certain frequencies, the 'equal energy per mode' assumption gives poor agreement with the measured far-field data. Therefore, a more complex power distribution over the azimuthal orders, derived from induct SPL measurements at the transducer ring, was used to define the noise source. This model significantly improved the accuracy of the far-field predictions.

Schuster *et al.* [63] performed a similar validation study using ACTRAN/TM to predict far-field fan noise at six different broadband frequencies at 55% engine speed. Multimodal predictions were produced using the traditional 'equal energy per mode' source

and also a more complex source distribution derived from in-duct measurements, similar to that of Achunche *et al*. [13]. However in modelling the latter source, an unequal power distribution in the radial orders was assumed for a given azimuthal order, with maximum power assigned to the first radial order. It was concluded that this source model provides improved predictions of the far-field directivity, particularly at shallow angles where the 'equal energy per mode' source over-predicts the far-field levels.

While the validation study performed by Schuster was limited to low engine speeds typical of approach, Lidoine *et al*. [64] also performed ACTRAN/TM predictions at cutback and sideline conditions and compared the results with fan rig test data. The source model was again derived from in-duct hard-walled measurements. Good agreement with the measurements was observed both for the hard-walled and lined configurations at approach and cutback conditions. However, an overestimation of the liner efficiency was observed at sideline condition due to non-linear propagation effects of the BPF mode, which is not taken into account by ACTRAN/TM.

Nark [65] performed CAA predictions at BPF at 54% and 87% engine speeds and compared them with measured far-field data. The prediction tool employed a parabolic approximation to the convected Helmhotz equation (based on potential mean flow). The radiation model was based on Ffowcs William Hawkings (FW-H) equation. The amplitude and phase of each source mode was randomly selected to take any value from 0-1 and 0-2π respectively. The agreement between the predicted and measured far-field SPL directivity was good at 54% speed. However at 87% speed, the agreement was not so good because of the uncertainty of source model at such speed and the possibility of non-linear propagation of the rotor-locked mode.

In this study, noise source models are derived from hard-walled in-duct and far-field measurements of SPL for rig and engine intakes. Far-field predictions obtained from ACTRAN/TM are validated with the measurements at BPF at five different fan speeds. Non-linear adjustments are applied to the linear ACTRAN predictions at high supersonic fan-tip speeds when linear propagation theory cannot be used confidently. In this study, all the in-duct and far-field measured data for both rig and engine intakes are referred from Achunche [13, 62].

4.3 Comparison between predicted and measured rig data

4.3.1 Intake rig

The intake rig used in the study is a 1/3rd scale model of a generic HBR engine with 24 fan blades and a diameter of about 1m [13]. Figure 4.2 shows the general set-up of the intake barrel. The transducer ring for in-duct measurements is located at the

transition casing between the cylindrical section of the intake and the baffle assembly.

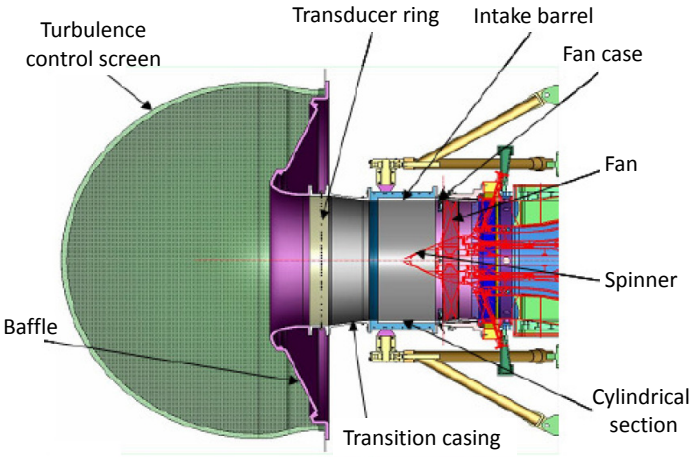

FIGURE 4.2: General experimental set-up of a 1/3rd model fan rig. [13]

4.3.2 Mode detection data

Figure 4.3 shows the variation of SPL with the azimuthal mode orders m and the fan speeds at 1BPF. The mode detection plot was obtained by decomposing the acoustic pressure measured at the transducer ring into different azimuthal mode orders m.

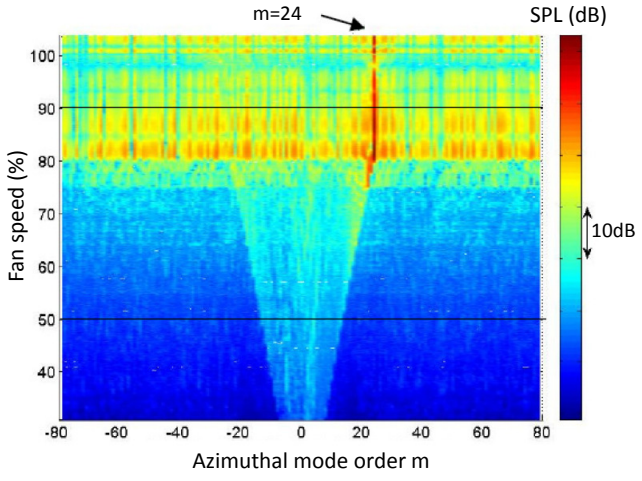

FIGURE 4.3: Mode detection plot at the 1BPF showing the variation of SPL with azimuthal modes and fan speed. [13]

When the fan speed is less than 80%, the distribution of SPL is fairly even over an increasing range of azimuthal mode orders corresponding to the cut-on modes at the

location of the transducer ring. However for fan speeds exceeding 80%, the rotor-locked 'm=24' mode cuts-on and and has a very high pressure amplitude. As a result, the SPL measured at the transducer ring is dominated by this mode at 80% and 90% fan speeds. Figure 4.4 shows the SPL of each azimuthal mode order measured at the transducer ring at 1BPF at five selected fan speeds. These fan speeds lie with the horizontal cut-outs of the plot shown in figure 4.3.

4.3.3 ACTRAN/TM model

In this study, far-field predictions will be performed at 1BPF at the selected fan speeds. The FE/IE tool ACTRAN/TM, detailed in chapter 2, is used within the shell code ANPRORAD to obtain the predictions. Figure 4.5 shows an example of a low frequency FE mesh for the rig intake generated by ANPRORAD. It is assumed that the rear portion of the nacelle does not affect the sound field in the forward-arc and therefore it is not represented in a realistic way.

4.3.4 Noise source model

Two types of source representation are used to model the fan noise source. In one of them, the modal intensity of the azimuthal mode orders are directly inferred from the in-duct or far-field hard-walled measurements. The other model is based on a more simpler representation of the noise source which consists of uncorrelated cut-on modes with equal energy in each mode and a single high-amplitude rotor locked mode (24,1). Both source models have the same total acoustic power at the fan plane. These are described in detail in the following sections.

4.3.5 Source representation at subsonic fan-tip speeds

At 50%, 60% and 70% speeds, the fan-tip speed is subsonic and the rotor locked mode m=24 is cut-off. The two source models that are used in ACTRAN/TM predictions at these speeds are denoted as A and B. Both sources are modelled as a multi-mode source consisting of all the cut-on modes at the fan plane. The intensities of the individual azimuthal mode orders of source A are directly inferred from the mode detection data shown in figures 4.4(a), 4.4(b) and 4.4(c).

ACTRAN/TM is intially run for a hard-walled intake with the source consisting of all the cut-on, incoherrent modes with unit intensity in each mode. The SPL predictions SPL_m^{uipm} for each azimuthal order m is obtained at the location of the transducer ring.

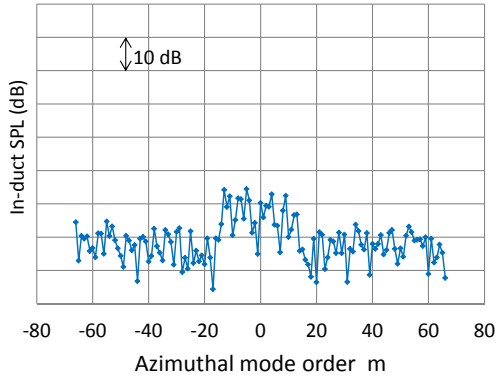

(a) 50% speed

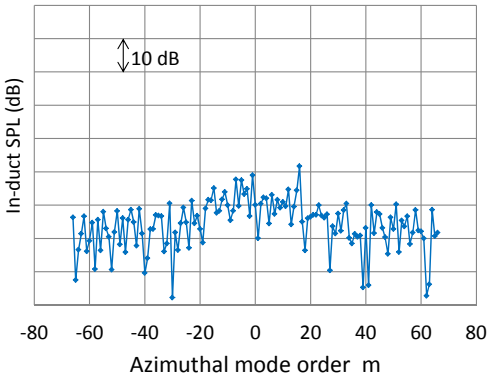

(b) 60% speed

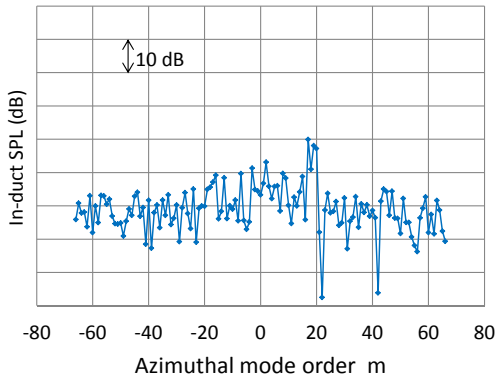

(c) 70% speed

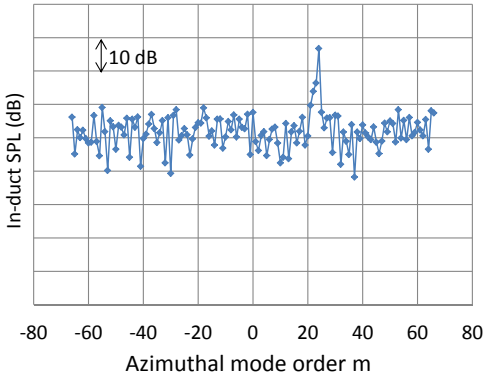

(d) 80% speed

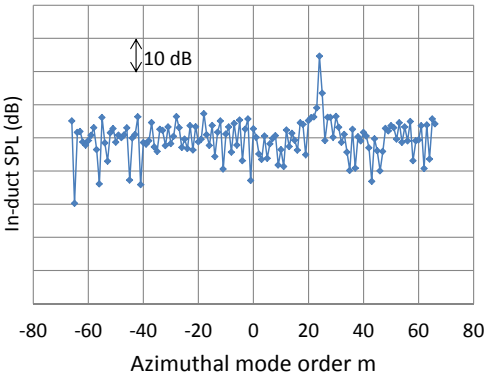

(e) 90% speed

FIGURE 4.4: Measured SPL of each azimuthal mode order at 5 selected fan speeds at 1BPF for fan rig test

By comparing SPL_m^{uipm} with the measured value SPL_m^M, the source intensity I_m^A of each azimuthal order m of source model A can be estimated by using the expression:

$$I_m^A = \frac{10^{SPL_m^M/10}}{10^{SPL_m^{uipm}/10}} * I_m^{uipm}, \tag{4.1}$$

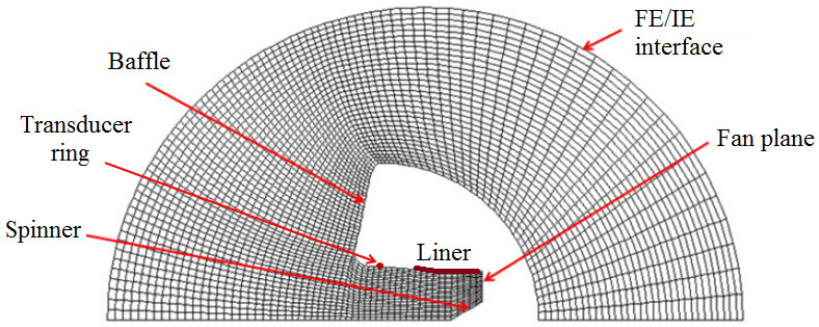

FIGURE 4.5: An example of a low-frequency ANPRORAD FE mesh for rig intake

where I_m^{uipm} is the total modal intensity of the azimuthal order m at the fan plane for an 'unit intensity per mode' source. It is assumed that all the cut-on radial orders for a given azimuthal mode order m has the same intensity. Source model A therefore predicts the same SPL distribution over the azimuthal modes at the duct wall at the location of the transducer ring as that of the measurements.

Source B, on the other hand, is a more simplified source model based on 'equal energy per mode' assumption, with the total source power equal to that of source A. Figures 4.6 shows an example of source model A and B at 50% fan speed.

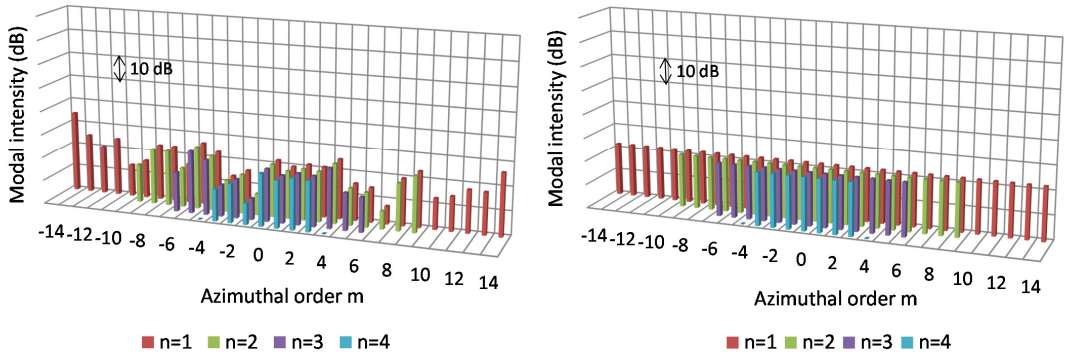

(a) Source A

(b) Source B

FIGURE 4.6: Source models at subsonic fan-tip speed (50% speed) for the rig geometry

4.3.6 Source representation at supersonic fan-tip speeds

At supersonic fan-tip speeds (80% and 90% fan speeds), the rotor locked mode m=24 is cut-on and has a very high amplitude as shown in figures 4.4(d) and 4.4(e). Due to the limitation of a dynamic range of 18.2dB in the measurements [62], only the SPL of

the high-amplitude azimuthal mode orders could be measured accurately. This means that the measured SPL for the rest of the cut-on modes at these speeds is unreliable. Therefore, the intensity of each azimuthal mode order at the source plane cannot be determined directly from the in-duct hard-walled measurements. Due to insufficient information of the energy content in all the cut-on azimuthal modes, a set of modified source models A' and B' are used at these speeds.

Source A' is modelled as an 'equal energy' multi-mode component plus the high amplitude modes. The high amplitude modes included in source model A' consists of modes m=22, m=23 and m=24 at 80% speed and modes m=24 and m=25 at 90% speed. The source intensities of these modes can be inferred directly from the in-duct measurements in the same way as performed for source A, by using equation 4.1.

The source strength of the 'equal energy' multi-mode component is however determined approximately from the hard-walled SPL measured by the far-field microphones over a range of 0^o to 20^o polar angles. The far-field SPL within this range has no contribution from the rotor-locked mode m=24 and the other high amplitude modes in its vicinity as they radiate at larger angles. The multi-mode component is therefore expected to dominate within this angular range, particularly those modes which radiate close to the duct axis. The sound power radiated from the hard-walled intake over the angular range of 0^o to 20^o polar angles is used to calibrate the multi-mode source. Therefore, the source intensity of the multi-mode component in the source model A' is determined by using the expression:

$$I^{A'}_{MM} = \frac{\int_{0^o}^{20^o} 10^{\left(\frac{SPL^M(\theta)}{10}\right)} \sin\theta d\theta}{\int_{0^o}^{20^o} 10^{\left(\frac{SPL^{uipm}(\theta)}{10}\right)} \sin\theta d\theta}, \tag{4.2}$$

where $I^{A'}_{MM}$ is the source intensity of each mode constituting the multi-mode (MM) component. $SPL^M(\theta)$ denotes the SPL measured at the far-field microphones spaced every $\Delta\theta$ and $SPL^{uipm}(\theta)$ denotes the SPL predicted at these locations by using 'unit intensity per mode' source ($I_{m,n} = 1$). The expression on the right-hand side of equation 4.2 is the ratio of the measured sound power radiated over the angular range of 0^o to 20^o and the predicted sound power for the 'unit intensity per mode' source in the absence of mean flow. (refer to equation C.8 of Appendix C for detail).

Source B', on the other hand, consists of a multi-mode component with the source intensity of each mode equal to $I^{A'}_{MM}$ and a single rotor-locked mode (24,1) superimposed on the multi-mode component. The excess energy in the high-amplitude modes of source A' is summed up and assigned only to the mode (24,1) in source model B'. If the second radial order of mode m=24 is cut-on, it is assigned the same source intensity as that in the rest of the cut-on modes (i.e., $I^{A'}_{MM}$), such that both the sources (A' and

B') have the same total source power. Figures 4.7 shows an example of source models A' and B' at 90% fan speed.

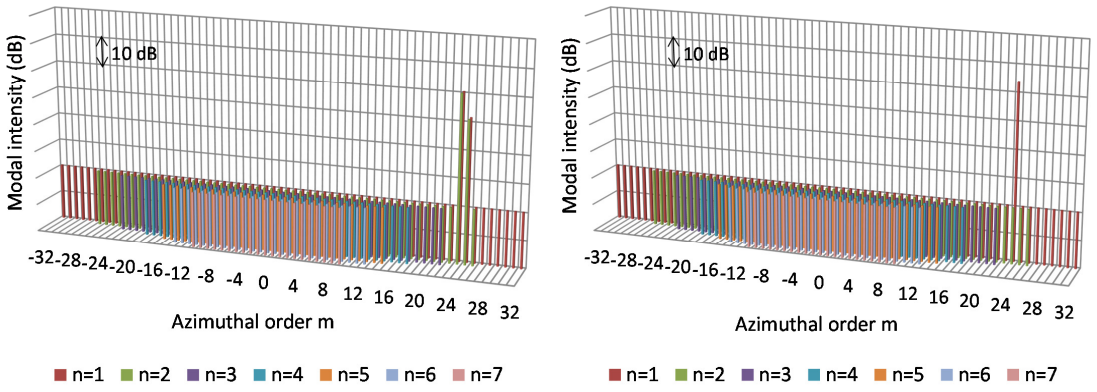

(a) Source A' (b) Source B'

FIGURE 4.7: Source models at supersonic fan-tip speed (90% speed) for the rig geometry

4.3.7 Comparison of predicted and measured field shapes

The source models presented in the previous section are used to obtain the far-field predictions for the hard-walled and uniformly lined configurations. The far-field SPL field shapes predicted by ACTRAN/TM at BPF at five different fan speeds are compared to the measurements as shown in figure 4.8 for hard-walled and lined configurations. The BPF (expressed in terms of Helmholtz number ka) and the mean flow axial Mach number at the fan are listed in table 4.1.

TABLE 4.1: The BPF and the fan-plane axial Mach number of the mean flow at different fan rig speeds

Fan speed (%)	50	60	70	80	90
BPF (ka)	15.4	18.6	21.9	25.1	28.5
Mach No.	0.23	0.30	0.37	0.44	0.55

Figures 4.8 shows that far-field predictions are in good agreement with the measurements at 50%, 60%, 70% and 80% speeds. Figures 4.8(a), 4.8(b) and 4.8(c) justify the usefulness of the simpler source models B based on 'equal energy per mode' assumption as it predicts similar far-field SPL directivities as that of source A.

At fan speeds above 80%, there is a sudden hump in the hard-wall SPL directivities between 40 to 90 degrees polar angles. This is due to the contribution from the

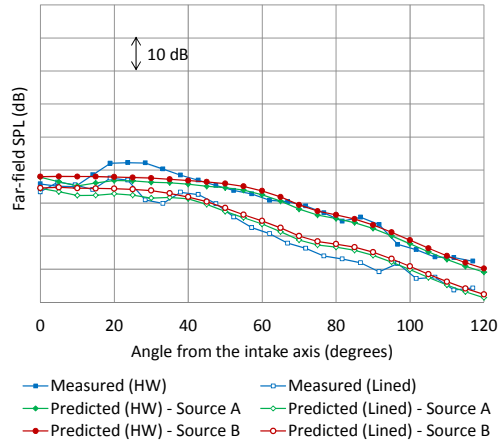

(a) 50% speed

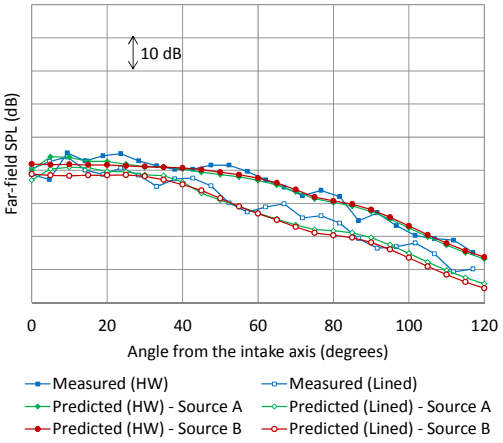

(b) 60% speed

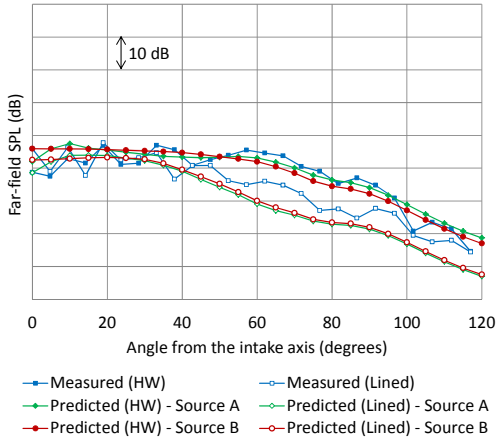

(c) 70% speed

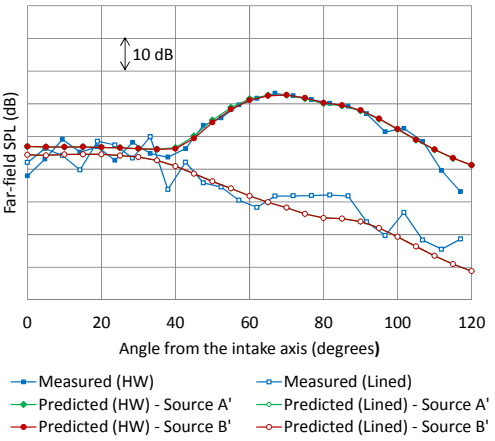

(d) 80% speed

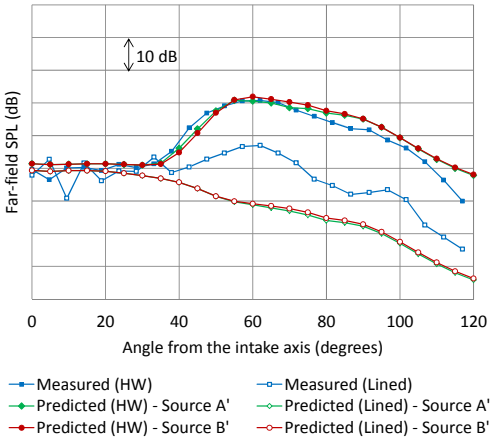

(e) 90% speed

FIGURE 4.8: Comparison between predicted and measured rig data

strongly cut-on rotor-locked mode m=24 and other high-amplitude modes near its vicinity, which radiate at these angles.

Figures 4.8(e) shows that the predictions at 90% speed are not in good agreement with the measurements for the lined configuration. The overall attenuation due to the liner is over predicted at higher polar angles. Since the rotor-locked mode m=24 dominates the sound pressure at these angles, the attenuation of this mode seems to be over-predicted. This may be due to the non-linear propagation effects in the high amplitude mode m=24, which are not modelled in ACTRAN/TM. This effect is however not significant at 80% fan speed because mode m=24 is just cut-on at the fan plane at this speed and is strongly attenuated by the liner. Therefore, good agreement with the measured data is obtained at 80% speed as the multi-mode component dominates far-field SPL in the lined case. At 90% speed, the m=24 mode is strongly cut-on and is less effectively attenuated by the liner and therefore it has a strong contribution to the far-field SPL. Hence, the non-linear propagation effects in this mode cannot be neglected at 90% speed and is taken into account in the next section.

4.3.7.1 Predicting the non-linear propagation of the rotor-locked mode m=24

The analytical non-linear propagation model described in chapter 3 is used to predict the correct liner attenuation of the rotor locked mode (24,1) at BPF at 90% fan speed. The SPL of the azimuthal mode order m=24 measured at the transducer ring is used to estimate the correct source SPL of the mode (24,1) by using the non-linear propagation model.

Determination of the linear attenuation rate of mode (24,1) in the lined section

In order to predict the non-linear propagation of mode (24,1) in the lined configuration by using equation 3.43, the linear attenuation rate of this mode in the lined section needs to be determined. Achunche [13] calculated this attenuation rate in an uniform cylindrical duct, neglecting the geometrical effects of the intake on the attenuation of mode (24,1). The mean flow Mach number prescribed at the source plane of the cylindrical duct was the same as that of the original rig intake. This resulted in the mass flow rate being different from the actual rate at the fan rig (due to presence of the spinner).

The linear attenuation rate of mode (24,1) evaluated by Achunche is however different from that predicted by ACTRAN/TM for the actual intake geometry. In order to investigate the reason behind this difference, the liner attenuation of mode (24,1) is predicted for the same intake without the spinner. Figure 4.9 shows the SPL contours of mode (24,1) predicted by ACTRAN/TM for the lined configuration with and without the spinner at 90% speed.

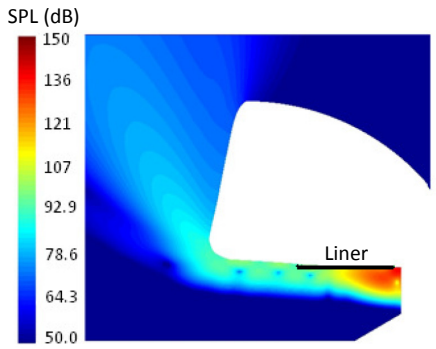

(a) Original intake geometry

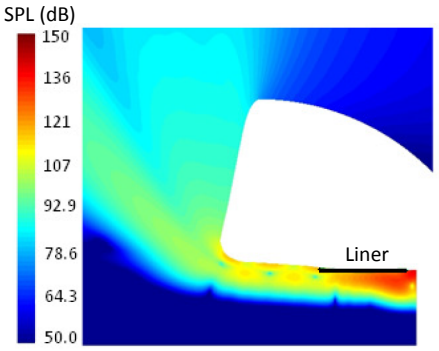

(b) Intake geometry without spinner, with same mean flow axial Mach number at the fan plane as the original intake

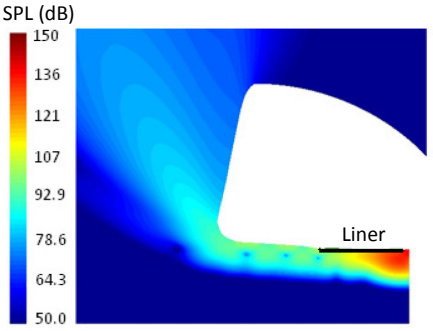

(c) Intake geometry without spinner, with same mass flow rate at the fan plane as the original intake

FIGURE 4.9: Contour plot of SPL of mode (24,1) at 1BPF (90% speed) for the lined configuration

Figures 4.9(a) shows the results for the original intake. Figure 4.9(b) show the SPL contour in the intake without the spinner when the same axial Mach number is prescribed at the fan as that of the original intake (M=0.55). It clearly indicates that the attenuation of mode (24,1) over the lined section is much less in the absence of the spinner. However, when the same mass flow rate is prescribed at the fan as that of the original intake (figure 4.9(c)), SPL contours of mode (24,1) is very similar to the original case.

Prescribing the same axial Mach number at the fan results in a much higher mean flow velocity at the acoustic liner as shown in figure 4.10(b). As a result, the mode (24,1) is more cut-on at the liner than the original case (figure 4.10(a)), and is therefore less effectively attenuated. Imposing the same mass flow rate at the fan however results in similar mean flow velocity at the liner as that of the original intake, as shown in figure 4.10(c). The mean flow axial Mach number at the fan plane in figure 4.10(c) is 0.45.

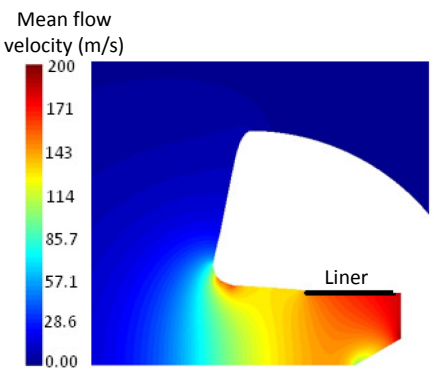

(a) Original intake geometry

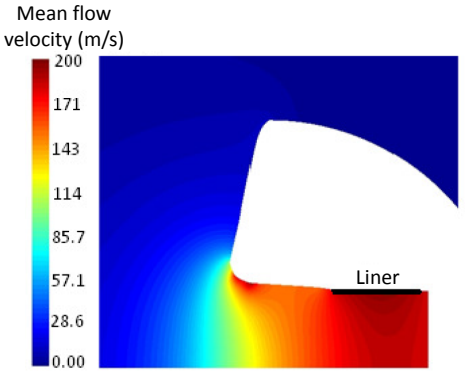

(b) Intake geometry without spinner, with same mean flow axial Mach number at the fan plane as the original intake

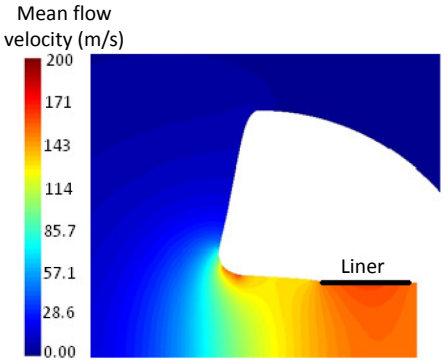

(c) Intake geometry without spinner, with same mass flow rate at the fan plane as the original intake

FIGURE 4.10: Contour of mean flow velocity at 90% speed

Figure 4.11 shows that the far-field SPL directivities of mode (24,1) predicted by ACTRAN/TM for the intake with and without the spinner. Figure 4.11(a) shows that the attenuation of mode (24,1) is under predicted by about 20 dB when the same intake geometry is used without the spinner and by prescribing the same Mach number at the fan plane (M=0.55). This is in agreement with the one estimated by Achunche by using the linear attenuation rate of mode (24,1) in a cylindrical duct. Figure 4.11(b) shows that the far-field attenuation of the mode (24,1) is well predicted when the mass flow rate prescribed at the fan is the same as that of the original intake.

The results therefore indicate that the procedure used by Achunche to determine the linear attenuation rate of mode (24,1) was not correct. In this study, the linear attenuation rate σ of the rotor-locked mode (24,1) is determined directly from ACTRAN/TM predictions by calculating the reduction in radiated sound power of mode (24,1) in the presence of the liner.

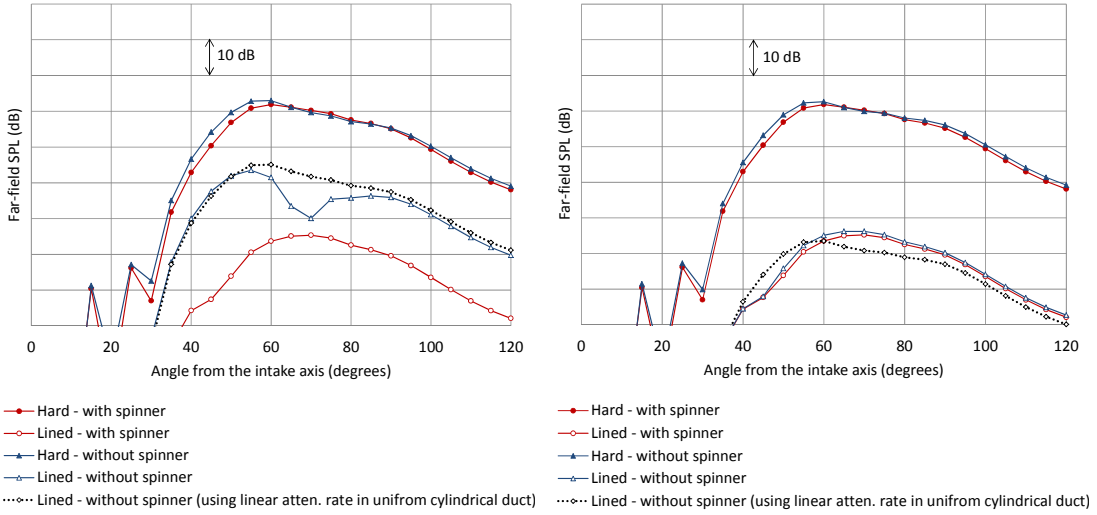

(a) same mean flow Mach number prescribed at the fan (b) same mass flow rate prescribed at the fan

FIGURE 4.11: Field shape of (24,1) mode in the far-field arc at 1BPF (90% speed) for hard-walled and lined configurations with and without the spinner

Non-linear adjustments to the far-field SPL predictions from ACTRAN/TM

Figure 4.12(a) shows the non-linear propagation of the rotor-locked mode (24,1) in both the hard-walled and the lined configurations, predicted by the non-linear analytical model. The correct source strength of mode (24,1) is predicted by equation 3.48, where the z corresponds to the location of the mode detection ring. $SPL(z)$ in equation 3.48 is, therefore, the SPL of mode (24,1) measured at the transducer ring, knowing which the SPL close to the fan ($z = 0$) can be estimated. The non-linear corrections at the end of the duct predicted by the analytical model (Δ_H for hard walled and Δ_L for lined cases) are applied to the far-field ACTRAN/TM predictions as shown in figure 4.12(b).

The implementation of the non-linear correction to the linear predictions by ACTRAN improves the agreement with the measurements. However, the agreement is not completely satisfactory for the lined configuration. It may be due to the fact that the application of this model is limited to uniform ducts, thereby ignoring the impact of the geometry and non-uniform flow effects on non-linear propagation of the rotor-locked mode. Moreover, the non-linear model neglects the buzz-saw noise component, thereby neglecting its interaction with the BPF tones.

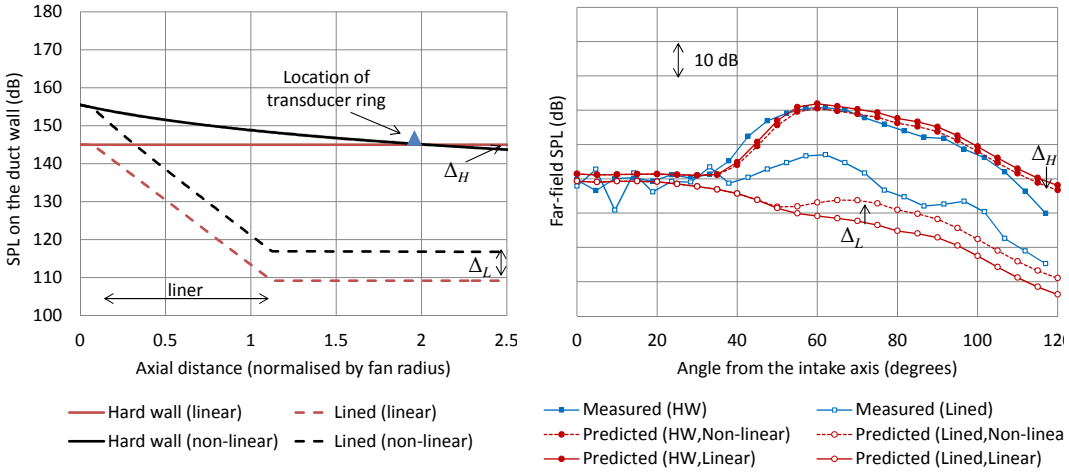

(a) SPL of mode (24,1) at the duct wall at BPF predicted by the non-linear analytical model

(b) Comparison between predictions and measured rig data at 90% speed (including non-linear adjustments)

FIGURE 4.12: Non-linear analysis at 90% speed for rig geometry

4.4 Comparison between predicted and measured engine data

4.4.1 Intake geometry and FE mesh

The experimental set-up for acquiring the noise test data for the static engine test performed at Rolls-Royce is detailed in Chapter 7 of reference [62]. Figure 4.13 shows one such experimental set-up for static noise test.

FIGURE 4.13: Experimental set-up for static noise test for a HBR turbofan engine

The intake is now a full-scale model of the HBR turbofan engine. The intake cowl is drooped downwards relative to the engine axis, to achieve the desired angle of attack when the aircraft operates. In order to accurately predict the geometrical effects due to the droop, a full 3D model of the intake including the exterior domain is required. Such

a model would however involve enormous computational cost and is impractical at the frequencies of interest. The intake geometry is therefore modelled by an equivalent axisymmetric intake.

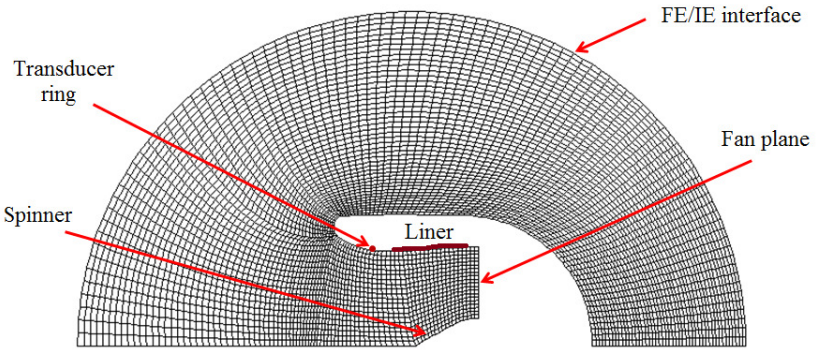

FIGURE 4.14: An example of a low-frequency ANPRORAD FE mesh for engine geometry

Figure 4.14 shows an example of a low frequency axisymmetric FE mesh for the engine intake generated by ANPRORAD. The far-field SPL directivities predicted by ACTRAN/TM on a arc ranging from 10^o to 120^o with centre along the duct axis, are compared with the measured engine test data.

4.4.2 Mode detection data

Figures 4.15 shows the SPL of each azimuthal mode order measured at the transducer ring at 1BPF at the five selected fan speeds.

As the intake is non-axisymmetric, the circumferential variation of the mean flow gets distorted. As a result of flow distortions, additional tones are generated at supersonic fan-tip speeds (80% and 90%) as the energy of rotor-locked mode m=24 gets scattered into adjacent azimuthal modes orders. This effect is clearly evident in figures 4.15(d) and 4.15(e).

4.4.3 Noise source model

Similar source representation as defined in section 4.3.4 is used. Since the source model is derived from hard-walled in-duct and far-field measurements, the effect of droop on the noise source definition is however retained in the axisymmetric analysis. Figures 4.16(a) and 4.16(b) show an example of source models A and B respectively, used for far-field predictions at 70% fan speed when the fan-tip speed is subsonic.

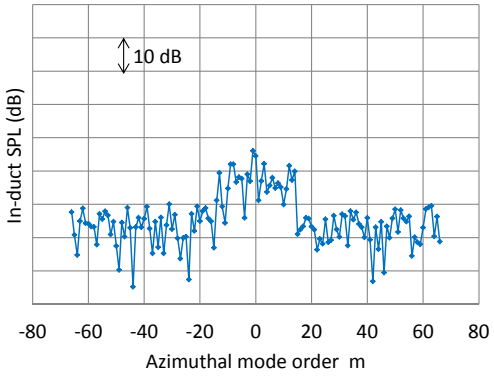

(a) 50% speed

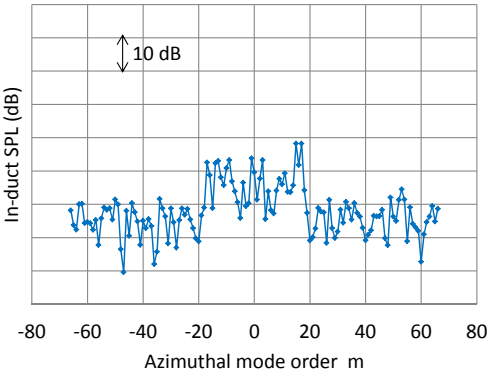

(b) 60% speed

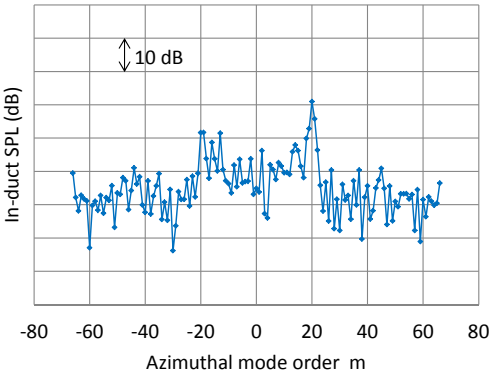

(c) 70% speed

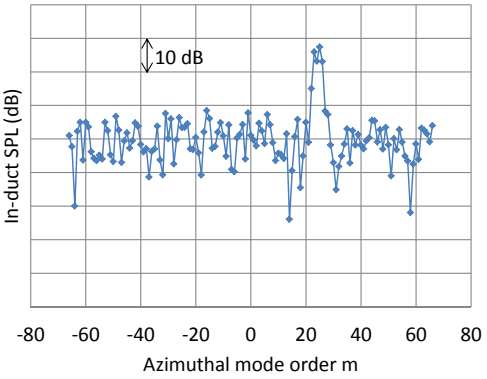

(d) 80% speed

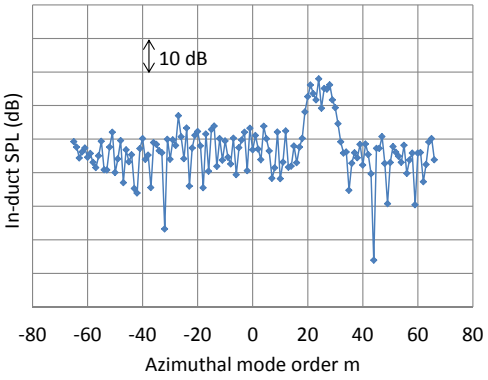

(e) 90% speed

FIGURE 4.15: Measured SPL of each azimuthal mode order at 5 selected fan speeds at 1BPF for engine test

At 80% speed, the high amplitude modes considered in modelling source A' in addition to rotor-locked mode m=24 are: m=22, m=23, m=25 and m=26. At 90% speed, the additional high amplitude modes range from: $19 \geq m \leq 23$ and $25 \geq m \leq 30$.

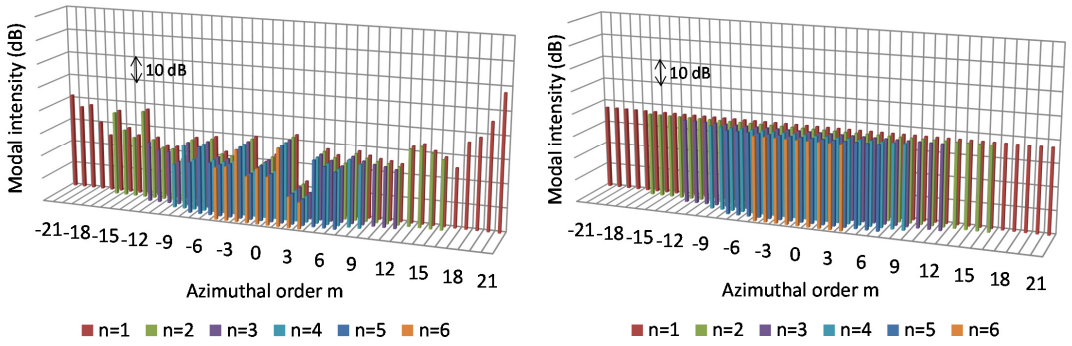

(a) Source A (b) Source B

FIGURE 4.16: Source models at subsonic fan-tip speed (70% speed) for the engine geometry

4.4.4 Comparison of predicted and measured field shapes

Figure 4.17 shows the comparison of the engine noise predictions with the measurements at the 1st BPF at the five different fan speeds (50%, 60%, 70%, 80% and 90% speeds).

Figure 4.17 shows that that the agreement between the predicted and measured far-field data for the engine test is not particularly as good as that obtained for the turbofan rig (section 4.3.7). This may be due to the fact that the 3D geometrical effects due to the intake droop is neglected in the current prediction. Moreover, the poor agreement with the measured far-field data at higher polar angles can be due to the presence of other noise sources like the noise from the exhaust, which is not modelled in the current study.

At 70% speed, the far-field directivity predicted by using source B gives a poor agreement with the measured data as shown in figure 4.17(c). The source model B seems to radiate greater acoustic power when compared to source A at 70% fan speed. This is because the mode m=21, which is just cut-on, dominates the total acoustic power of source A at the fan plane as evident from figure 4.16(a). Most of the energy in this mode is reflected back to the fan and therefore the total power radiated into the far-field is much less. This is not effectively modelled in source B as this source model is based on the 'equal intensity per mode' assumption at the fan plane.

At 80% fan speed, the overall agreement between the measured and the predicted field shapes is slightly better when the source model A' is used. This is because in source A' correct modal intensities are assigned to the high-amplitude modes whereas in source B', all the excess energy in these modes is assumed to be concentrated on the rotor-locked mode (24,1).

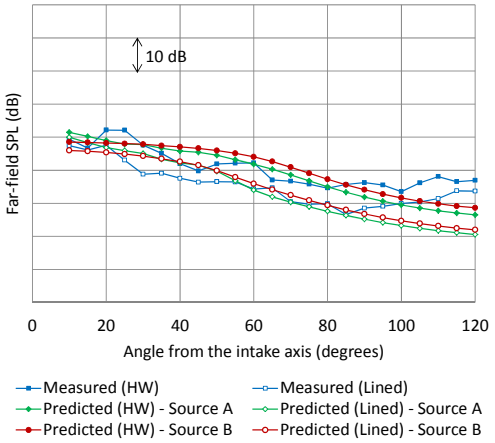

(a) 50% speed

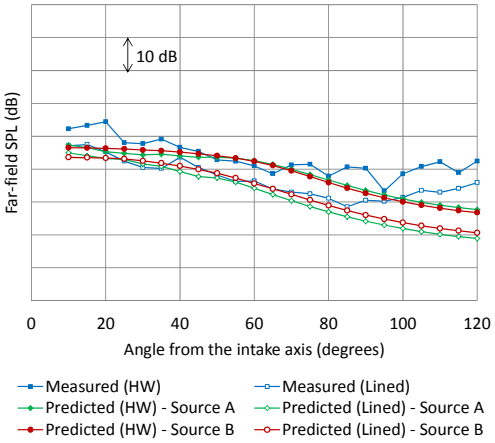

(b) 60% speed

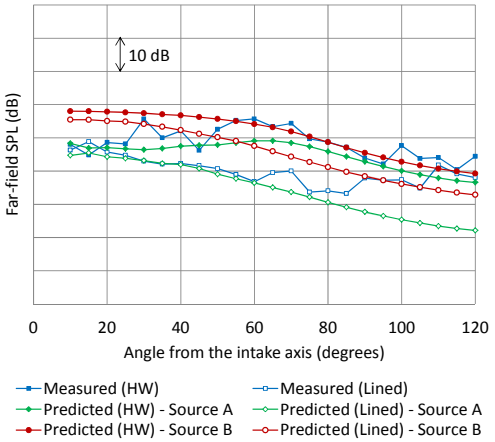

(c) 70% speed

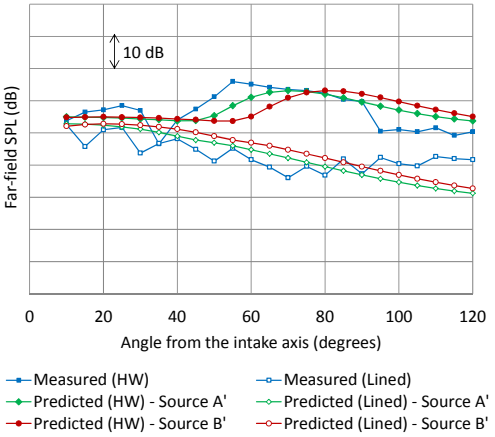

(d) 80% speed

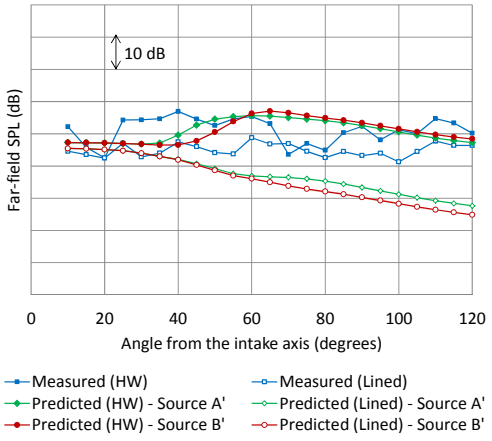

(e) 90% speed

FIGURE 4.17: Comparison between predicted and measured engine data

At 90% fan speed, the agreement between the measured and predicted field shapes for the lined configuration is not satisfactory, for both sources A' and B' (figure 4.17(e)). At this fan speed, though the rotor locked mode (24,1) has a high pressure amplitude at the

source plane, non-linear corrections applied to this mode does bring significant changes in the far-field field shapes for the lined configuration. This is because the (24,1) mode is strongly attenuated by the liner and the total far-field SPL is dominated by the multimode component. This shows that the non-linear effects are not the only reason for such discrepancies in far-field directivities for the current case. Such discrepancies could be due to the factors like 3D geometrical effects due to the droop, contamination of noise sources from the exhaust, etc.

4.5 Conclusions

In this chapter, the FE/IE code ACTRAN/TM used within the shell code ANPRO-RAD has been used to predict the far-field SPL field shapes for both the hard-walled and the lined configurations of an axisymmetric intake. These predictions have been validated against the measured far-field data for rig and engine intakes at the 1 BPF at different fan speeds. The following conclusions can be drawn from this study.

I. Fairly good far-field predictions can be obtained for intake fan noise at BPF at different fan speeds provided that the source modal content is correctly specified and if accurate impedance data of the acoustic liners are available.

II. Source A and A', which give a better representation of the source modal content than source B and B', gives slightly better predictions than the latter. This is particularly observed for cases when a nearly cut-on mode dominates the total source power. However in most of the cases, the usefulness of the often-used and a rather simplistic source model (B and B') is well justified

III. A methodology has been presented in this chapter to apply non-linear corrections to the ACTRAN/TM predictions for both hard-walled and lined configurations. In order to determine the non-linear corrections, the linear attenuation rate of the rotor-locked mode due to the liner is determined directly from the far-field predictions obtained by ACTRAN/TM, rather than calculating it for a uniform cylindrical duct with uniform mean flow, as suggested by Achunche [13]. The non-linear adjustments applied to the far-field predictions improves the agreement with the measurements, but only by a small amount.

IV. Better agreement with the measurements is observed for the rig predictions as compared to the engine predictions. This may be due to the fact the droop in the engine geometry was neglected in the current prediction model. Moreover, the measured far-field engine noise data includes the noise from the exhaust at higher polar angles which is not considered in the predictions.

Chapter 5

Automated optimisation of intake liners to reduce forward-arc fan noise

5.1 Introduction

Optimisation of liner performance plays an important role in designing low noise engines. The liner construction parameters like the porosity, thickness and the hole size of the porous sheets and the depth(s) of the honeycomb are the principal determiners of acoustic impedance and noise attenuation achieved by the liner. The performance of the liner also depends on the nature of source spectrum which is incident upon it. The selection of the physical liner parameters to optimise its impact on EPNL mainly depends on the impedance model to translate the physical liner parameters and the noise source which defines the modal content of the sound field.

In this chapter, intake liners are optimised to reduce fan noise radiated in the forward-arc of a turbofan engine at different engine conditions. The CAA tool used in this study is ACTRAN/TM which was validated against far-field measured data in the previous chapter. The practicability of embedding this CAA tool within automated optimisation schemes to optimise liners for realistic nacelle geometries and noise source spectra within industrially acceptable time-frames is investigated in this chapter.

5.2 Literature Review

A proper choice of optimisation technique and the cost functions is very essential in optimising acoustic liners to reduce community noise.

Lafronza [66–68] used an approximate evaluation of the Perceived Noise Level (PNL) [69] as a cost function to optimise liners within uniform duct geometries. A mode-matching propagation model was used to perform acoustic analysis and Response Surface Modelling (RSM) [70, 71] was used as an optimisation tool. RSM seeks to obtain a surrogate model of the cost function known as the response surface by performing calculations at a number of sample points in the design space generated by the Design of Experiments (DoE) technique [72]. It was this model which was searched instead of the real function by using a hybrid search of a global optimizer followed by a local search algorithm. This optimisation technique was used to optimise both uniform and axially segmented liners and proved to be capable of meeting industrial time constraints.

Law and Dowling [73] optimised liners for 'multi-mode' broadband source in uniform cylindrical and annular ducts. The total reduction in acoustic power per unit length of the liner was used as a cost function. A non-linear multi-variable optimisation algorithm 'fmincon' [74] available within MATLAB was used as an optimisation tool. The technique was mainly applied to optimise axially segmented liners to find the best combination of liner lengths collectively capable of addressing the input noise spectrum.

Copiello and Ferrante [75] used multi-objective genetic algorithm to optimise zero-splice liners in uniform cylindrical ducts. The in-duct liner attenuations were calculated analytically and thereafter, WienerHopf technique [29] was used to obtain the acoustic solution in the far-field. Effective perceived noise level (EPNL) [6] was used as a cost function in the optimisation study. It was shown that the multi-objective optimisation approach allowed optimisation of liners at different noise certification conditions at the same time.

Astley *et al*. [76] and Achunche *et al*. [77] used an automated liner optimisation procedure for uniform annular ducts. ACTRAN/TM was used within a propriety shell code 'B-induct' [78] to predict the acoustic transmission and absorption in a bypass duct. The code was integrated within a Rolls-Royce in-house optimisation suite 'SOFT' (Smart Optimisation For Turbomachinery) [79]. The acoustic power at the exit of the bypass duct was minimised by using a hybrid algorithm with Genetic Algorithm (GA) as a global optimizer followed by a gradient-based local optimizer. It was shown that there is an advantage of using segmented liners over uniform liners at low frequencies when very few propagating modes are present. This was also observed in the optimisation study reported by Lafronza [68].

Most of these liner optimisation studies were performed for uniform ducts, thereby neglecting the effects of realistic duct geometries on noise propagation. In this study, liner optimisation is performed for a realistic intake geometry to reduce radiated fan noise at approach and sideline conditions. Two fully-automated liner optimisation strategies are presented. One of them was proposed by Astley *et al*. [76] and the other

employs the optimisation toolbox in MATLAB. The feasibility of applying automated liner optimisation approaches for a realistic noise spectra is also investigated.

5.3 Liner model

The effectiveness of an acoustic liner depends critically on the acoustic impedance which it presents to the sound field in the intake. This in turn depends on the physical construction of the liner. In the current study, a single layer construction (figure 5.1) is used.

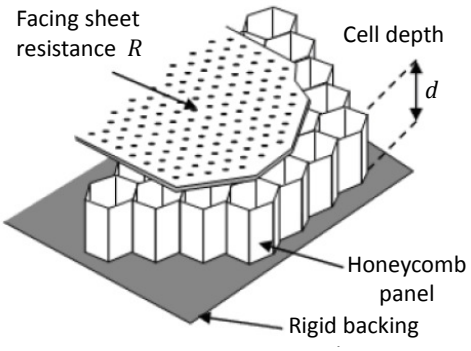

FIGURE 5.1: Single layer liner construction of resistance R and cell depth d

The non-dimensional impedance $z(= \mathbf{z}/\rho c)$ of the single layer liner is expressed as

$$z = R + i\chi = R + i\left(kl - \cot(kd)\right), \tag{5.1}$$

where R is the non-dimensional facing sheet resistance, d is the depth of the liner and $k(= \omega/c)$ is the free-field wave number and l is the mass intertance. The mass inertance (l) of the facing sheet is determined by [80]

$$l = \frac{[t_s + \epsilon(\sigma_h)d_h]}{\sigma_h}, \tag{5.2}$$

where t_s is the thickness of the sheet, d_h is the diameter of the holes on the sheet, σ_h is the % porosity (or the percentage open area) of the sheet and ϵ is the dimensionless end correction which depends on porosity σ_h and the grazing flow effects. The value of ϵ is always less than unity ($\epsilon < 1$). The non-dimensional resistance R of the facing sheet depends on an averaged grazing flow Mach number M over the lined surface [80], and is expressed as:

$$R = \frac{0.3M}{\sigma_h}. \tag{5.3}$$

For the purpose of this optimisation study, equation 5.2 is approximated to obtain a first order link between the inertance l and the non-dimensional resistance R. Therefore, by using equation 5.3 and assuming that $\epsilon(\sigma_h)d_h << t_s$, equation 5.2 can be approximated as:

$$l \approx \frac{t_s R}{0.3M}. \tag{5.4}$$

In the current study, the facing sheet thickness t_s is taken to be 0.95mm.

5.4 Noise source model

Fan noise is mainly composed of two noise components - (a) broadband noise and (b) tonal noise. Each of these noise components have been detailed in Chapter 1. The impact of an acoustic liner on each of these sources is generally quite different. In this study, independent acoustic analysis is performed for each source and the resulting sound fields are superimposed to give the overall attenuation in the far-field.

Broadband attenuations are computed for third octave band centre frequencies ranging from 250Hz to 5kHz. The broadband source is modelled as an ensemble of all the uncorrelated cut-on modes at the fan plane with equal acoustic power per mode at a given frequency.

Tone calculations are performed at BPF harmonics. BPF tone consists of a multi-mode 'interaction' component which is modelled in the same way as the broadband source. At a supersonic tip-speed, the rotor-locked single mode tones also exist which have a strong influence on the far-field directivity as seen in the previous chapter.

The noise source model used at different conditions in this chapter are detailed in Appendix A.

5.5 Optimisation study

ACTRAN/TM is used to obtain CAA predictions of far-field attenuation due to the liner. All the predictions are performed by using an axisymmetric intake. Computations are performed for each cut-on azimuthal mode order at each frequency for each source type in order to construct the total sound field radiated from the intake.

5.5.1 Cost function

The reduction in radiated sound power[1] due to the liner over an angular range $\theta_1 \rightarrow \theta_2$ is used as a cost function, i.e the quantity $\Delta PWL_{\theta_1 \rightarrow \theta_2}$, given by

$$\Delta PWL_{\theta_1 \rightarrow \theta_2} = 10log_{10}\left[\frac{\int_{\theta_1}^{\theta_2} \left|p^H(\theta)\right|^2 \sin\theta d\theta}{\int_{\theta_1}^{\theta_2} \left|p^L(\theta)\right|^2 \sin\theta d\theta}\right], \tag{5.5}$$

where p^H and p^L denote pressures on a far field spherical surface for the Hard and Lined cases respectively. Equation 5.5 is an approximate estimation for the reduction of the radiated power as it is determined in the absence of ambient flow. Moreover, this cost function can be considered a crude approximation to an EPNL contribution, providing a measure of liner attenuation over the angular range in the far-field. The use of more complex cost functions that approximate more closely an EPNL calculation does not materially affect the effort involved in the optimisation procedure and computational time. Therefore, no attempt is made to apply a subjective weighting to the attenuations or to simulate the time history element of an EPNL calculation. This is because the objective of the study is to illustrate and demonstrate the general features of liner optimisation procedure, rather than to provide a industrial template for its application.

Optimisations are performed at specific target frequencies and by integrating equation 5.5, weighted by a source spectrum over a range of frequencies.

5.5.2 Automated optimisation schemes

In this chapter, a fully automated optimisation approach is used to optimise intake liners in which the cost function is evaluated by generating and running CAA models in real time. Within the optimisation loop, acoustic computations are performed at each point in the liner design space by running ACTRAN/TM. In the current study, two automatic optimisation schemes are used to optimise intake liners and the total computational time in each scheme is compared. In both the schemes, a global search algorithm is followed by a local search algorithm, which drives the computation of the CAA solution at a sequence of points in the design space until convergence occurs. Genetic algorithm is used as a global search followed by a gradient based method to locate the optimum.

5.5.2.1 Scheme 1: Smart Optimisation For Turbomachinery (SOFT)

SOFT is a Rolls-Royce in-house optimisation code [79] which has an in-built library consisting of different optimisation algorithms. A proper choice of an optimisation

[1] Refer to Appendix C for the calculation of the radiated sound power

algorithm is necessary to perform liner optimisation within acceptable time frames. A study was conducted by Achunche in chapter 3 of his thesis [62] in which the different optimisation algorithms available with the SOFT were exploited to find a robust optimisation strategy. It was concluded that a hybrid search technique using the Adaptive Range Multiple objective Genetic Algorithm (ARMOGA) and Dynamic Hill Climbing (DHC) options in SOFT is most suitable for liner optimisation studies.

ARMOGA [81–83] is a genetic algorithm with a special ability to adapt the search region based on the best designs obtained from previous generations. It is also capable of performing multi-objective optimisation. In this optimisation technique, a set of designs called 'population' is iteratively transformed into a new population through mutation and cross-over processes as shown in figure 5.2(a). The blue dots constitute the initial population and the red dots constitute the new population generated by the old population. The performance of ARMOGA primarily depends on the population size and the number of generations (or transformations). Using a population consisting of about 50 design points, the algorithm converges to an optimum value after about 30-40 generations. As a result, if only ARMOGA is used for optimising the cost fuction, the optimisation process becomes highly time consuming. In this study, ARMOGA is therefore used as a tool to explore the entire design space rather than exploiting its capabilities as a global optimiser. The population size of 50-60 design points is used with only one generation. The best design point $\mathbf{x}$ obtained from the ARMOGA search is used as an initial value to the local search algorithm (DHC).

DHC [84] is used to locate the final optimum value. The algorithm maintains a list of $2n+2$ vectors if the number of design variables for the optimisation is n. Out of this set, n vectors form an orthogonal set and the other n are the negations of these vectors. The additional two vectors are functions of the direction moved by DHC in the last two iterations. DHC selects the vector of largest magnitude out of this set in each iteration to move in a particular direction. Starting from the initial point $\mathbf{x}$ (obtained from ARMOGA) and the vector $\mathbf{v}$, DHC evaluates the value of a cost function f at the point $\mathbf{x}+\mathbf{v}$ and compares it to the value f at $\mathbf{x}$. Supposing the cost function has to be maximised and if $f(\mathbf{x}+\mathbf{v}) > f(\mathbf{x})$, then $\mathbf{x}+\mathbf{v}$ becomes the new point and the process continues. But, if $f(\mathbf{x}+\mathbf{v}) < f(\mathbf{x})$, the magnitude of $\mathbf{v}$ is halved and the vector with the next largest magnitude is chosen for the next iteration. In this way the algorithm updates the magnitude of each vector in the set with the aim to get closer and closer to the optimum. The algorithm terminates if one of the chosen vectors has a magnitude equal to the minimum step size defined by the user. The final design point $\mathbf{x}$ obtained from the DHC is a point from which the function f cannot be further increased. Therefore, $\mathbf{x}$ becomes the optimium design point obtained from the hybrid search (ARMOGA+DHC). The search process of DHC is shown in figure 5.2(b).

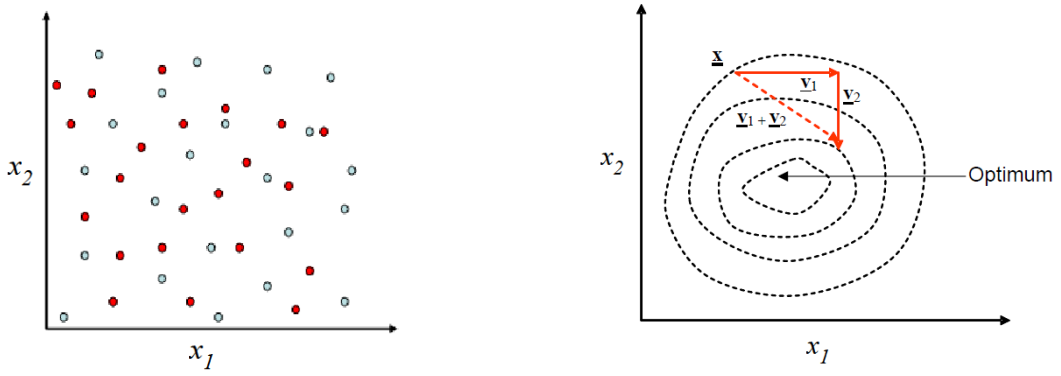

(a) ARMOGA (b) DHC

FIGURE 5.2: Search space for the SOFT optimisation [76]

5.5.2.2 Scheme 2: Optimisation toolbox 'Optimtool' in MATLAB

The optimisation toolbox 'Optimtool' available in MATLAB has several optimisation algorithms out of which Genetic Algorithm (GA) and 'fmincon' are chosen in order to perform a hybrid search similar to scheme 1. GA is used to scan the design space and to provide the starting point for 'fmincon' to locate the optimum.

In MATLAB, 'fmincon' is used instead of DHC because the latter is not available in the optimisation library of 'Optimtool'. The algorithm 'fmincon' is a non-linear multi-objective gradient-based method which uses 'trust-region reflective' algorithm [74]. The algorithm requires a gradient vector $\mathbf{g}$ and a Hessian matrix $\mathbf{H}$ at each iteration evaluated at a design point $\mathbf{x}$. The nature of the cost function f in the neighbourhood of the point $\mathbf{x}$ is approximately modelled using these gradient matrices. This approximate model is called 'trust-region' and it reflects the behaviour of the actual function f in the neighbourhood of point $\mathbf{x}$. If the aim is to maximise the cost function, a design point $\mathbf{x_{new}}$ at which the 'trust-region' reaches the maximum value is obtained. If $f(\mathbf{x_{new}}) > f(\mathbf{x})$, then $\mathbf{x_{new}}$ becomes the new point and the process continues. The tolerance value ($|f(\mathbf{x_{new}}) - f(\mathbf{x})|$) is calculated at each iteration and the process terminates when the tolerance value is equal to the minimum value specified by the user (10^{-6} by default).

The gradient vector $\mathbf{g}$ and the Hessian matrix $\mathbf{H}$ is evaluated automatically by 'fmincon' if the analytical expression of the cost function is known. In the current study, the cost function is evaluated numerically using ACTRAN/TM and therefore these matrices have to be provided externally by the user at each iteration. If the cost function is denoted by $f(x,y)$, then the gradient vector $\mathbf{g}$ and Hessian matrix $\mathbf{H}$ are expressed as

$$\mathbf{g} = \begin{Bmatrix} \frac{\partial f}{\partial x} \\ \frac{\partial f}{\partial y} \end{Bmatrix} \tag{5.6}$$

$$\mathbf{H} = \begin{bmatrix} \frac{\partial^2 f}{\partial^2 x} & \frac{\partial^2 f}{\partial x \partial y} \\ \frac{\partial^2 f}{\partial y \partial x} & \frac{\partial^2 f}{\partial^2 y} \end{bmatrix} \tag{5.7}$$

The single and double derivatives in equations 5.6 and 5.7 are evaluated numerically using finite difference scheme (central difference approximation), as shown below.

$$\frac{\partial f}{\partial x} = \frac{f(x+h, y) - f(x-h, y)}{2h} \tag{5.8}$$

$$\frac{\partial f}{\partial y} = \frac{f(x, y+k) - f(x, y-k)}{2k} \tag{5.9}$$

$$\frac{\partial^2 f}{\partial^2 x} = \frac{f(x+h, y) - 2f(x, y) + f(x-h, y)}{h^2} \tag{5.10}$$

$$\frac{\partial^2 f}{\partial^2 y} = \frac{f(x, y+k) - 2f(x, y) + f(x, y-k)}{k^2} \tag{5.11}$$

$$\frac{\partial^2 f}{\partial x \partial y} = \frac{\partial^2 f}{\partial y \partial x} = \frac{f(x+h, y+k) - f(x+h, y-k) - f(x-h, y+k) + f(x-h, y-k)}{4hk} \tag{5.12}$$

Here, h and k are the small changes in x and y respectively. Both $\mathbf{g}$ and $\mathbf{H}$ are evaluated and fed into 'fmincon' externally by a separate MATLAB script. Therefore, in each iteration a total of nine CAA evaluations of the cost function need to be performed as shown in figure 5.3.

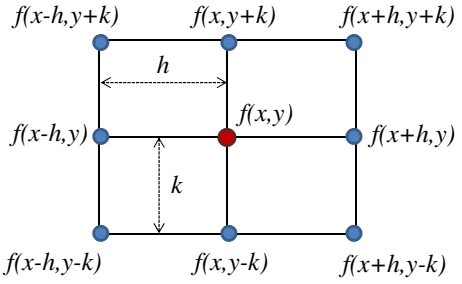

FIGURE 5.3: Grid showing the points where the CAA evaluations are performed at each iteration in 'fmincon' (red dot: actual design point)

5.6 Optimisation of intake liners for broadband noise at approach condition

In this section, optimisation of the intake liner is performed for an equal energy broadband source at an approach condition (refer to Appendix A for details on the source model and engine condition). Figure 5.4 shows the intake geometry and liner position used in the study which are taken from an axi-symmetrized model of an HBR intake used for various liner studies in the European Commission 5th Framework programme SILENCE(R)[2] [85]. The geometry and the liner location are very similar to the generalised configuration shown in figure A.1 of Appendix A.

The far-field attenuations are predicted over an angular range of 40^o to 90^o. Therefore, θ_1 and θ_2 in equation 5.5 are fixed to 40^o and 90^o respectively. This angular range is taken from the lip liner optimisation study in SILENCE(R) [85]. Ideally, the liners should be optimised to minimise EPNL as a cost function but in this study a simple cost function is used, as described in section 5.5.1. It is therefore reasonable to consider this range of polar angles for the assessment of the forward-arc radiated noise towards the ground from the engine at approach condition.

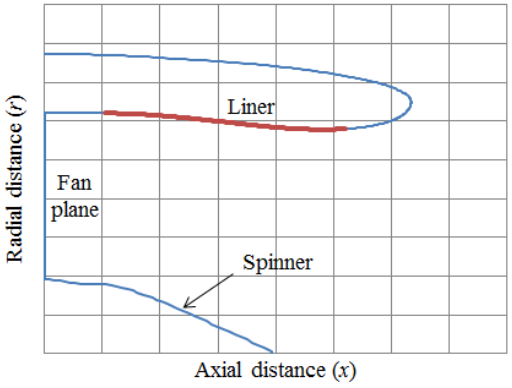

FIGURE 5.4: Intake geometry and liner position

5.6.1 High frequency approximation

The requirement of finer mesh resolutions for acoustic evaluations at very high frequencies makes the computation very expensive. In this study, an approximation is used to reduce the computational cost for acoustic evaluations at high frequencies. It is assumed that the sound field behaves more or less like a diffused field at very high

[2] `http://www.xnoise.eu/fileadmin/user_upload/Projects/SILENCER_FinalExecutivePublishableSummary-1.pdf`

frequencies as large number of modes are incident at the fan plane [86, 87]. In such cases, an equivalent simulation can be performed at a lower frequency but by using the liner impedance corresponding to the frequency of interest. This approximation is termed as High Frequency Approximation (HFA) in the current study.

The frequency above which HFA is applied is chosen by comparing the far-field SPL directivities predicted at this frequency with those at higher frequencies in the considered frequency range. Figure 5.5 shows a comparison of the far-field SPL directivities predicted at two high frequencies (3150Hz and 5kHz) with the equivalent predictions performed at 2kHz. A single layer liner of resistance $2\rho c$ and 74mm cell depth is used in the lined configuration with the liner impedance calculated at the actual frequencies.

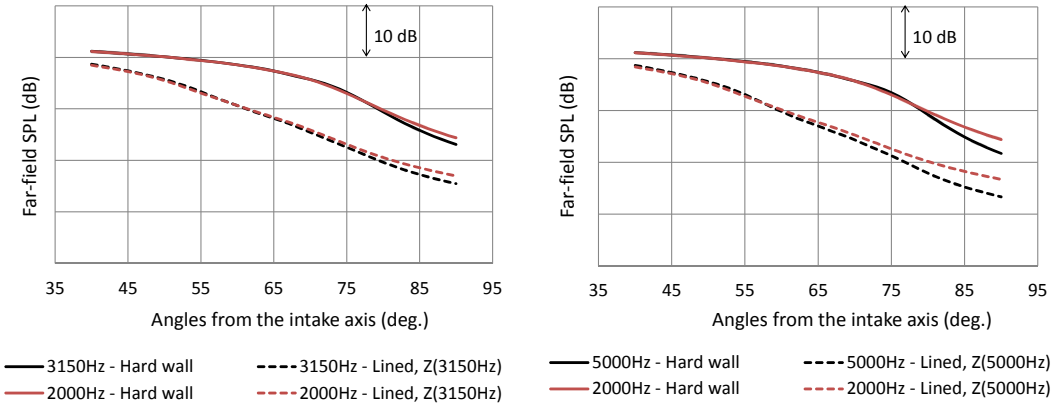

(a) 3150Hz

(b) 5000Hz

FIGURE 5.5: High frequency approximation to predict the far-field SPL directivities for hard walled and lined cases for frequencies greater than 2 kHz at approach condition

Figure 5.5 shows that the far-field predictions at 3150Hz and 5kHz have a close agreement with the equivalent predictions performed at 2kHz. A frequency of 2kHz is therefore chosen in the current optimisation study at approach condition above which HFA is applied. This particular choice of frequency is not governed by any strict rule and therefore one might consider applying this approximation at a frequency higher than 2kHz (say 2500Hz) or a lower frequency as long as the predicted far-field directivities have a close agreement with those predicted at the higher frequencies. The total computational time at this frequency also needs to be considered while making this choice. A total of 537 modes are cut-on at the fan plane at 2kHz and therefore it is reasonable to assume that the sound field behaves like a diffused field above this frequency.

The method of choosing the frequency above which HFA is applied is also explained later in this chapter when liner optimisation is performed at sideline condition where

two frequencies are initially chosen for HFA and separate liner optimisations are performed to investigate the difference in the results.

5.6.1.1 Results: Scheme 1

Figure 5.6 shows the result of SOFT optimisation of the intake liner with respect to its construction characterized by liner depth d and facing sheet resistance R at a target frequency of 2 kHz. The liner depth d and the resistance R are restricted to lie within the range [5mm, 75mm] and [0, $5\rho c$] respectively.

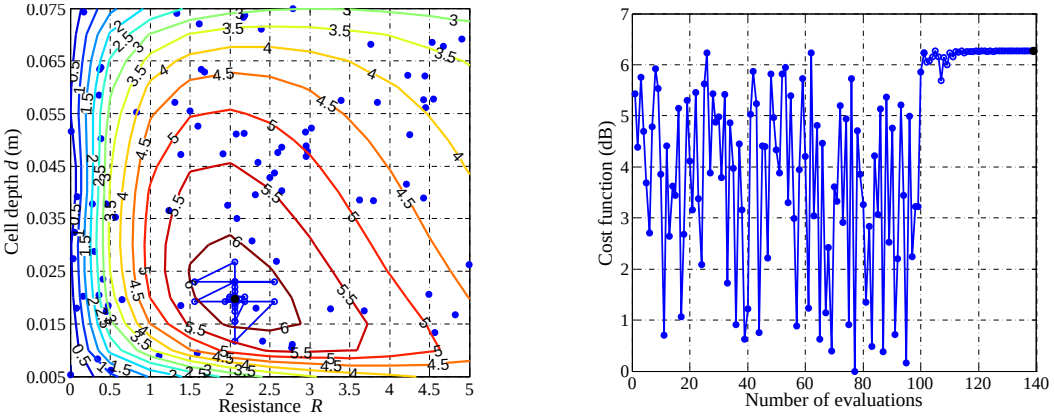

(a) GA points (solid circles) and DHC path (hollow circles) superimposed on pre-computed contours of the cost function in the R-d design space

(b) Value of cost function ($\Delta PWL_{40^o \to 90^o}$) versus the number of evaluations

FIGURE 5.6: SOFT Optimisation of $\Delta PWL_{40^o \to 90^o}$ at 2kHz at approach condition, characterized by liner resistance R and cell depth d

TABLE 5.1: Optimisation results at 2kHz at approach condition

Resistance R (non-dimensional)	2.06
Cell depth (in meter)	0.0197
Maximum attenuation	6.28
No. of evaluations (SOFT)	138
CPU time (SOFT)	14hr 10min 41sec
No. of evaluations (Contours)	165
CPU time (Contours)	16hr 56min 13sec

Figure 5.6(a) indicates the evaluation points in the R-d design space. One hundred points generated by GA are shown as solid circles. The population size in ARMOGA is set to 50 with 1 generation. The subsequent DHC path is indicated by the sequence of hollow circles. The results are superimposed on an independently computed contours of the cost function in the R-d design space. This acts as a check for the results obtained

by SOFT optimisation. Clearly, the optimum obtained by SOFT is consistent with contours.

Figure 5.6(b) shows the value of the cost function at each evaluation. The black solid circle indicates the final optimum value. Figure 5.6(b) shows a clear break between the relatively random GA phase and the deterministic DHC portion of the process. A total of 138 evaluations in SOFT are needed to converge to the optimum. Since an axisymmetric model is used, each evaluation at this frequency involves multiple ACTRAN calculations at different azimuthal orders. A cumulative total of about 14 hours of CPU time was required for the entire process in SOFT, as listed in table 5.1. It takes more take to calculate the contours as the number of ACTRAN evaluations is greater. The job was executed on an Intel (R) Core 2 Duo processor of 3.00GHz clock speed and 4.00GB RAM (Windows XP 32-bit Operating system).

When the cost function $\Delta PWL_{\theta_1 \to \theta_2}$ is integrated over the frequencies, we get:

$$\Delta PWL_{f_1 \to f_2, \theta_1 \to \theta_2} = 10log_{10} \left[\frac{\int_{f_1}^{f_2} \int_{\theta_1}^{\theta_2} \left| p^H(\theta, f) \right|^2 \sin\theta d\theta df}{\int_{f_1}^{f_2} \int_{\theta_1}^{\theta_2} \left| p^L(\theta, f) \right|^2 \sin\theta d\theta df} \right]. \tag{5.13}$$

In the current study, the broadband noise source model consists of equal energy in each $1/3^{rd}$ octave band, with all the energy concentrated at its centre frequency. Integration of cost function over frequency is therefore approximately implemented by summing up the cost functions calculated at the centre frequencies of the 1/3rd octave bands which lie within the considered frequency range (250Hz - 5kHz). The equation used in the optimisation study is, therefore, expressed as:

$$\Delta PWL_{250Hz \to 5kHz, \theta_1 \to \theta_2} = 10log_{10} \left[\frac{\sum_{f=250Hz}^{5kHz} \int_{\theta_1}^{\theta_2} \left| p^H(\theta, f) \right|^2 \sin\theta d\theta}{\sum_{f=250Hz}^{5kHz} \int_{\theta_1}^{\theta_2} \left| p^L(\theta, f) \right|^2 \sin\theta d\theta} \right], \tag{5.14}$$

where f corresponds to the centre frequencies of the 1/3rd octave bands in the frequency range 250Hz - 5kHz. The SOFT optimisation for the same configuration when the cost function is integrated over fourteen 1/3 octave frequencies ranging from 250Hz to 5kHz by using equation 5.14, is shown in Figure 5.7. On the left, a maximum liner depth of 75mm is specified and on the right, the maximum liner depth is halved to 37.5mm. It is clear in figure 5.7 that the contours contain much more information than simply the location of the global optimum. The computational time increases considerably when the optimisation is performed for a range of frequencies. The optimisation process takes approximately 5 days on a single processor as shown in table 5.2. This however is at the limit of what is currently acceptable in an industry context.

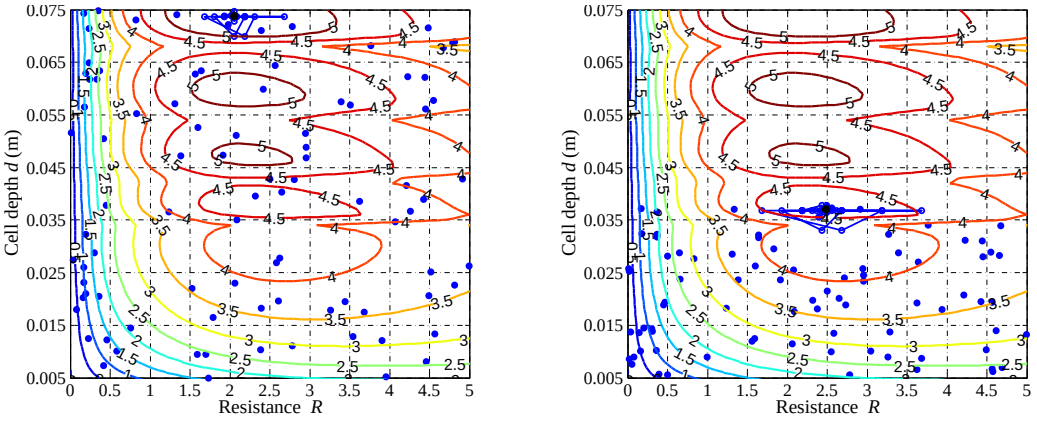

(a) Permissable range of d : 0-75mm

(b) Permissable range of d : 0-37.5mm

FIGURE 5.7: SOFT optimisation results of $\Delta PWL_{40^o \rightarrow 90^o}$ integrated from 250Hz to 5kHz at approach condition, characterized by liner resistance R and cell depth d. GA points (solid circles) and DHC path (hollow circles) superimposed on pre-computed contours of the cost function in the R-d design space.

TABLE 5.2: Optimisation results of cost function ($\Delta PWL_{40^o \rightarrow 90^o}$) integrated over the frequency range of 250Hz to 5kHz at approach condition

Comparison	**0-75mm depth**	**0-37.5mm depth**
Resistance R (non-dimensional)	2.057	2.49
Cell depth (in meter)	0.0738	0.0373
Maximum attenuation	5.455	4.76
No. of evaluations (SOFT)	130	139
CPU time (SOFT)	108hr 12min 3sec	113hr 45min 8sec
No. of evaluations (Contours)	165	165
CPU time (Contours)	137hr 26min 10sec	137hr 26min 10sec

5.6.1.2 Results: Scheme 2 (compared with scheme 1)

The results obtained from the SOFT optimisation scheme and the MATLAB optimisation toolbox are compared for the cases mentioned in previous section.

Tables 5.3 and 5.4, show that the optimisation results produced by both the methods are in good agreement. Figures 5.8(a) and 5.8(b) show the corresponding MATLAB optimisation results for figures 5.6(a) and 5.7(a) respectively.

The tables 5.3 and 5.4 show that the optimisation Scheme 2 is more time consuming than scheme 1. This is because while performing the local optimisation using 'fmincon' in scheme 2, nine separate CAA evaluations are performed at every iteration to calculate the Hessian and gradient matrices (figures 5.3). It takes the same amount of time to populate the design space using GA but the local optimisation performed by 'fmincon' in scheme 2 consumes more time than that used in SOFT (DHC).

In this section, greater number of GA evaluations are performed as compared to the previous section when optimising the liner over the frequency range. More seeding of the design space ensures a proper starting point for the local optimiser and is done especially for 'fmincon' in MATLAB optimisation which takes more time than DHC to converge to the optimum value. A population size of 60 and 2 generations are therefore used both in ARMOGA (SOFT) and GA (MATLAB). This is the reason why 210 evaluations are required in SOFT (table 5.4) to reach the optimum value as compared to 130 evaluations (table 5.2) in the previous section, although they solve the same problem.

TABLE 5.3: Comparison between the optimisation results of SOFT and MATLAB at 2kHz frequency at approach condition

Comparison	**SOFT**	**MATLAB**
Resistance R (non-dimensional)	2.06	2.09
Cell depth (in meter)	0.019	0.019
Maximum attenuation	6.28	6.27
No. of evaluations	138	235
CPU time	14hr 10min 41sec	23hr 35min 6sec

TABLE 5.4: Comparison between the optimisation results of SOFT and MATLAB for a frequency range of 250Hz to 5kHz at approach condition

Comparison	**SOFT**	**MATLAB**
Resistance R (non-dimensional)	2.06	2.06
Cell depth (in meter)	0.0738	0.0738
Maximum attenuation	5.455	5.456
No. of evaluations	210	306
CPU time	177hr 46min 15sec	253hr 30min 8sec

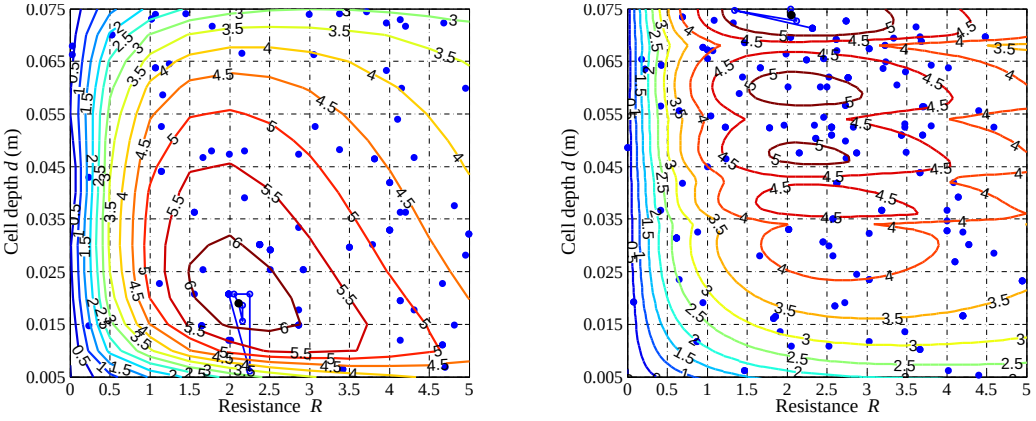

(a) $\Delta PWL_{40^o \to 90^o}$ at 2kHz

(b) $\Delta PWL_{40^o \to 90^o}$ integrated from 250Hz to 5kHz

FIGURE 5.8: Results of MATLAB optimisation of intake liner at approach condition. GA points (solid circles) and 'fmincon' path (hollow circles) superimposed on pre-computed contours of the cost function in the R-d design space.

5.6.2 Frequency characteristics of liner attenuation

In this section, the overall performance of liners optimised by using SOFT at four specific frequencies is compared to that of the two liners optimised over the whole frequency range but with different constraints on liner depth (maximum depths of 75mm and 37.5mm respectively). An optimisation is performed at 250Hz, 1kHz, 2kHz and 5kHz to determine the optimal liner construction at these frequency. The performance of these liners are then assessed over a wide range of frequencies as sown in figure 5.9. The optimal liner depths at these frequencies are predicted to be 75mm, 55mm, 19.7mm and 71.6mm respectively when a maximum depth of 75mm is specified. The optimal liner depth when the cost function is integrated over the considered frequency range (250Hz - 5KHz) is 73.8mm and 37.3mm if the maximum cell depths are constrained to 75mm and 37.5mm respectively. Performance curves for both these liners are denoted as A and B respectively in figure 5.9. Also shown is the performance of an ideal liner obtained by using the optimal values of resistance and reactance at each frequency. This liner denotes the maximum attainable attenuation. The difficulty in realizing such a liner is that the optimal impedances at each frequency require different liner depths and facing sheet resistances and cannot therefore be achieved in practice. This curve represents the best that one could possibly achieve. It coincides at 1.0 kHz with the liner optimised for this frequency, and at 2 kHz for the liner optimised for 2 kHz, and so on. At the lower frequencies (250 Hz for example) this property no longer holds because the liner optimised for this particular frequency is still constrained in the current exercise by a maximum cell depth of 75 mm and the 'ideal' impedance at this frequency corresponds to a larger value.

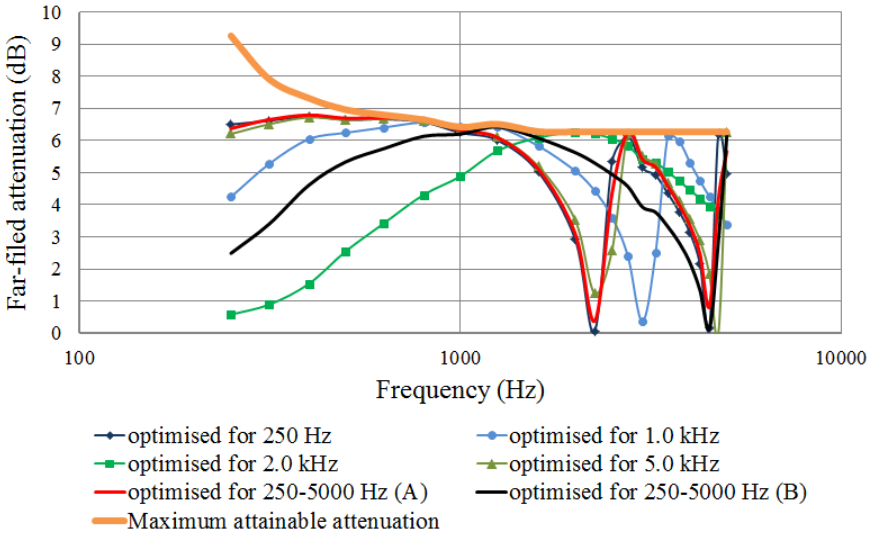

FIGURE 5.9: Overall performance of liners optimised by using SOFT

One cannot read a great deal into the results shown in figure 5.9 except to observe that the current optimisation produces results at specific target frequencies which are consistent with the ideal curve.

The selection of a liner which is effective in some sense over the whole frequency range is by no means a straightforward task. At certain frequencies, the attenuation predicted by the optimised liners drop down to a very low value close to 0dB. This is because of the fact that at some frequencies the liner reactance becomes infinitely large (due to -cot(kd) dependence) and the liner starts to behave as a hard-wall. This behaviour is well expected for a single-layer liner model as the acoustic performance of these liners is strongly dependent on the cell depth. When the liner cell depth is close to half of the acoustic wavelength, the absorption is minimum as the reactance reaches an infinitely large value. The frequencies at which the absorption is minimum are called anti-resonant frequencies of the liner. Conversely, when the cell depth is close to a quarter of the wavelength, the absorption is maximum as the reactance tends to 0. Such frequencies are called resonant frequencies of the liner when the liner performance is maximum.

5.7 Optimisation of intake liners for a typical noise spectra at sideline condition

The optimisation at the approach condition was conducted for a multi-mode 'broadband' source. A more realistic liner optimisation task should also take into account the contributions from tone sources. This increases the total number of CAA predictions due to these extra noise sources thereby increasing the total optimisation time. In this section, liner optimisation is performed at sideline condition for a noise source spectrum consisting of both broadband and BPF tone components. The source model, condition and the intake configuration are detailed in Appendix A.

Liner optimisation is initially performed for individual noise sources independently and then for the total source spectrum by combining all the sources together. The frequency range considered in this study is 250Hz to 5kHz. The cost function is the same as used previously (equation 5.5). An angular range of 0^o to 120^o is considered to predict the noise levels in the far-field at sideline condition. There is however no specific reason for not choosing the previous angular range of 40^o to 90^o used at approach condition. The liner optimisation study at approach was used as a comparison with a semi-automated liner optimisation strategy [38] which used the same intake, liner location and engine conditions as SILENCE(R). But, the current optimisation study at sideline condition is a stand-alone study and therefore a much wider range of polar angles is considered.

5.7.1 High frequency approximation

The high frequency approximation strategy detailed in section 5.6.1 is reused in the current study to reduce the computational cost at high frequencies. In Figure 5.10, the far-field SPL directivities at three high frequencies (2000Hz, 3150Hz and 5000Hz) are compared to their equivalent predictions at relatively low frequencies (800Hz and 1000Hz). A single layer liner of resistance $1.5\rho c$ and 5.5mm cell depth is used in the lined configuration. The liner impedance is however calculated at the actual frequencies when an equivalent acoustic computation is performed at a low frequency. Figure 5.10 shows that equivalent predictions at both 800Hz and 1kHz provides good agreement with the predictions performed at the actual frequencies, with 1kHz being slightly better.

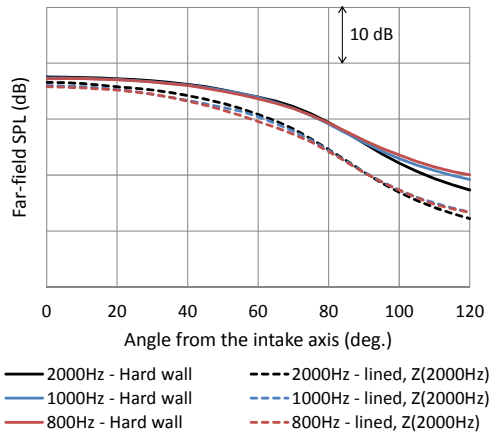

(a) 2000Hz

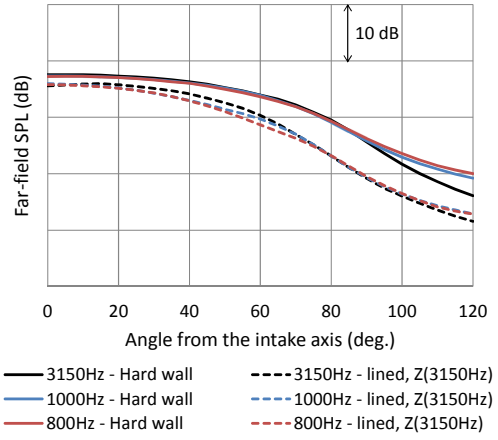

(b) 3150Hz

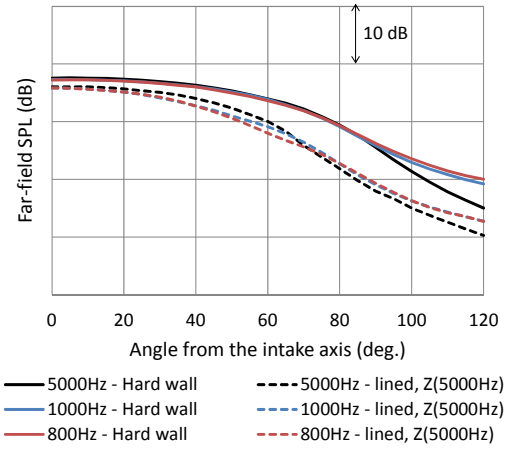

(c) 5000Hz

FIGURE 5.10: High frequency approximation to predict the far-field SPL directivities for hard walled and lined cases for some high frequencies at sideline condition

5.7.2 Liner optimisation for broadband source

An 'equal energy' broadband spectrum is used in the study with a source PWL of 125dB allocated to each 1/3rd octave band. The contours of the cost function integrated over 1/3rd octave band centre frequencies in the range 250Hz to 5kHz is shown in figure 5.11. The contours are plotted at 0.5dB intervals against liner resistance R and cell depth d.

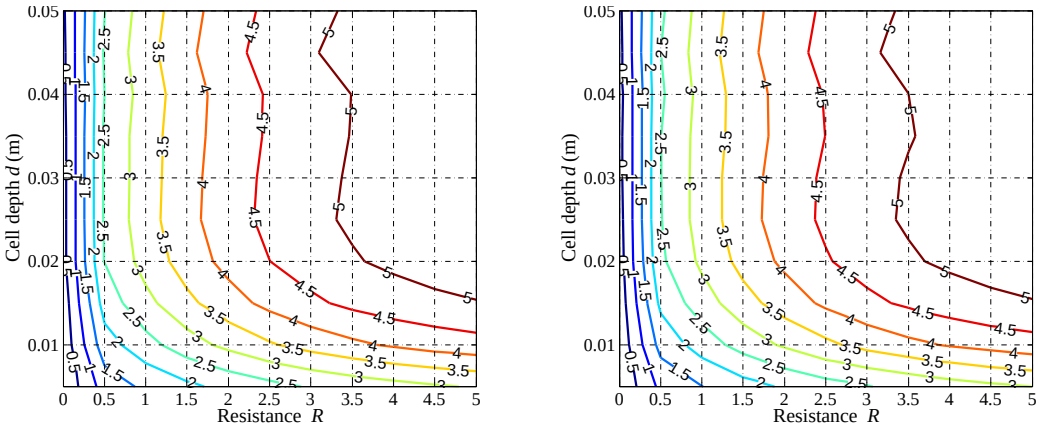

(a) HFA above 800Hz

(b) HFA above 1kHz

FIGURE 5.11: Contours of $\Delta PWL_{0^o \rightarrow 120^o}$ integrated from 250Hz - 5kHz plotted against non-dimensional liner resistance R and cell depth d at sideline condition

The contours in figure 5.11 indicate that a high resistance liner ($R > 3.5$) with cell depth greater than 20mm is required to achieve 5dB noise attenuation when only broadband source is considered in the noise spectrum.

Figure 5.11(a) and 5.11(b) are produced by applying HFA above 800Hz and 1kHz respectively. The computation was performed on an Intel (R) Quad-Core processor of 3.00GHz clock speed and 16 GB RAM (Windows XP 64-bit Operating system). A total of 110 ACTRAN/TM simulations is required to produce these contours in figure 5.11. The total CPU time required to produce figure 5.11(a) and 5.11(b) by using axisymmetric parallelism [39] on four processors are approximately 40 and 62 hours respectively. There is hardly any difference in the results obtained for the both the cases but less computational time is required when higher frequency ACTRAN/TM calculations are performed at 800Hz, as expected. It is therefore reasonable to apply HFA above 800Hz in the liners optimisations performed in the remaining part of this chapter.

5.7.3 Liner optimisation for BPF tones

Only the first three BPFs in table A.2 of Appendix A are considered in this study as the rest lies outside the considered frequency range (250Hz to 5kHz). The noise source

at BPF consists of the single mode (SM) rotor-locked component and the multi-mode (MM) component. The source PWL of these individual components at BPFs are listed in table A.2. The acoustic computation for the multi-mode source is performed at 800Hz with the liner impedance calculated at the exact BPF. The use of this assumption was well justified in sections 5.7.1 and 5.7.2. The contours of the cost function against liner resistance R and cell depth d produced independently for SM and MM noise components at first three BPFs are shown in figure 5.12, 5.13 and 5.14.

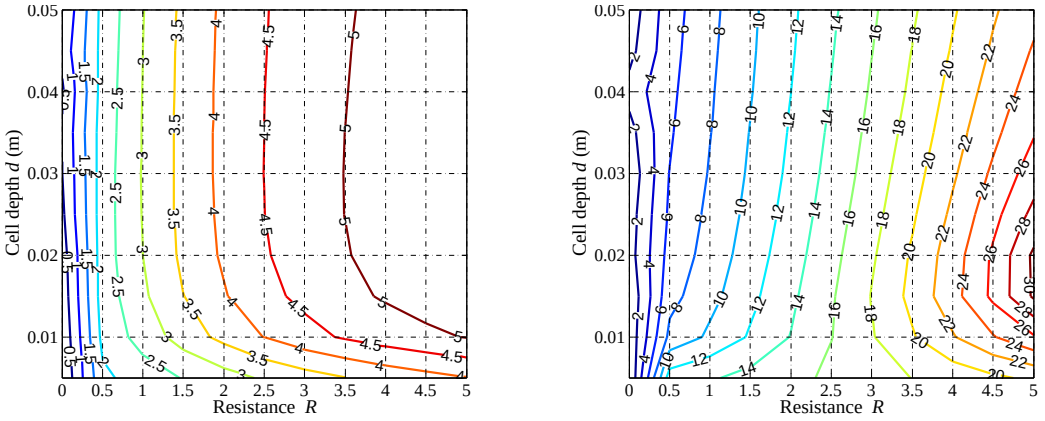

(a) MM component - HFA (800Hz)

(b) SM component - mode (24,1)

FIGURE 5.12: Contours of $\Delta PWL_{0^o \to 120^o}$ plotted against non-dimensional liner resistance R and cell depth d for MM and SM noise components at 1st BPF at sideline condition

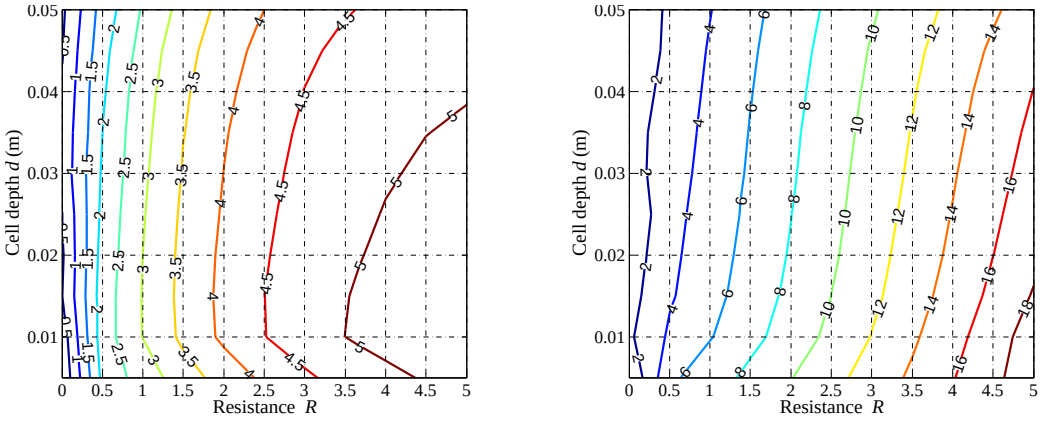

(a) MM component - HFA (800Hz)

(b) SM component - mode (48,1)

FIGURE 5.13: Contours of $\Delta PWL_{0^o \to 120^o}$ plotted against non-dimensional liner resistance R and cell depth d for MM and SM noise components at 2nd BPF at sideline condition

Figure 5.12, 5.13 and 5.14 shows that a maximum of about 5dB attenuation can be obtained for the MM noise source within the considered limit of liner resistance R and cell depth d. The SM noise sources can however be attenuated to a much greater

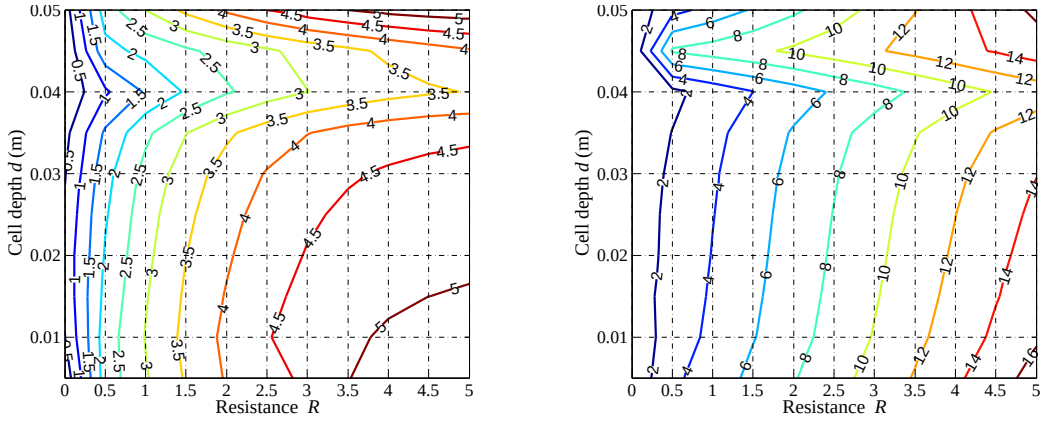

(a) MM component at 3 BPF - HFA (800Hz)

(b) SM component at 3 BPF - mode (72,1)

FIGURE 5.14: Contours of $\Delta PWL_{0^o \rightarrow 120^o}$ plotted against non-dimensional liner resistance R and cell depth d for MM and SM noise components at 3$^{\text{rd}}$ BPF at sideline condition

extent. Liner attenuation is the greatest for the SM noise component at the 1$^{\text{st}}$ BPF ($\sim$ 30dB) and it decreases at higher BPF harmonics.

The total number of grid points in the R-d design space at which ACTRAN/TM computations are performed is the same as that used in the previous section. It takes about $3\frac{1}{2}$ hours to produce the contours in figure 5.12(a), 5.13(a) and 5.14(a) and it remains the same for all the BPFs since the computation is performed at 800Hz instead of actual frequencies. The time required to produce the contours for the SM components however depends on the computational time at the frequency of interest. It takes approximately 1, 2 and 3 hours respectively to produce the contours for the SM components at first three BPFs.

Figure 5.15 shows the contours of $\Delta PWL_{0^o \rightarrow 120^o}$ for the total noise source at the first three BPFs. This is obtained by combining the individual SM and MM noise components at BPFs with their respective source strengths, listed in table A.2. The results indicate that the attenuation is dominated by the SM components at all the BPFs. This is because the SM tones have significantly greater source strengths than their corresponding MM components. As a result of this, the far-field SPL directivity of SM component still protrudes over the MM component at the individual BPFs even when an efficient liner is used. This is evident in figure 5.16, where the liner used for prediction at all the three BPFs has a resistance of $5\rho c$ and cell depth of 15mm.

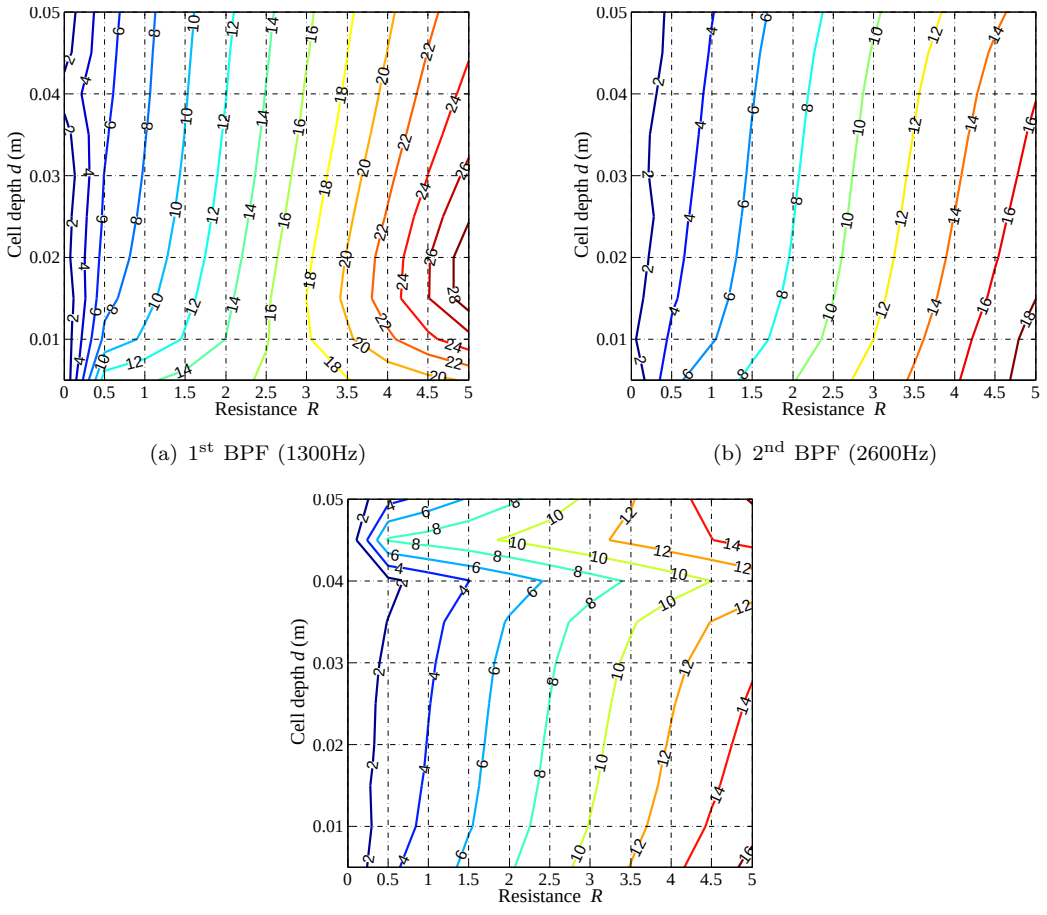

(a) 1st BPF (1300Hz)

(b) 2nd BPF (2600Hz)

(c) 3rd BPF (3900Hz)

FIGURE 5.15: Contours of $\Delta PWL_{0^o \rightarrow 120^o}$ plotted against non-dimensional liner resistance R and cell depth d for the total noise source at the first three BPFs at sideline condition

5.7.4 Liner optimisation for the total noise spectrum - Broadband and BPF tones

In this section, the intake liner is optimised over the entire source spectrum by combining the individual sources with their respective source strengths, and integrating over the considered frequency range. Two different methods are used to combine the individual sources which are illustrated in table 5.5. They differ only in the acoustic computation of the MM components at BPFs. The acoustic computation for the MM sources at BPFs are performed at 800Hz in both the methods. However in method B, the liner impedance is calculated at the centre frequency of the 1/3rd Octave band which contains the BPF instead of calculating it at the exact BPF which is done in method A. The attenuation of all the other sources are predicted in the same way as described in the previous sections. In other words, no additional effort is required to compute the attenuation of the MM components at BPFs in method B as the data

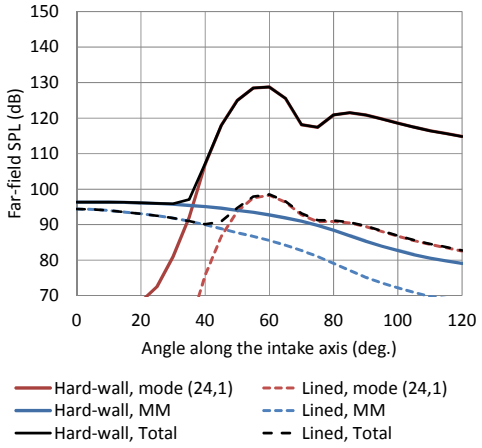

(a) 1st BPF (1300Hz)

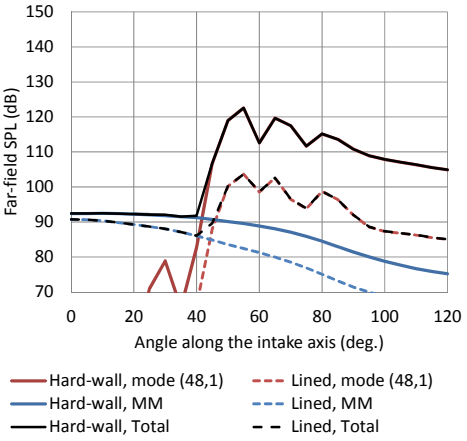

(b) 2nd BPF (2600Hz)

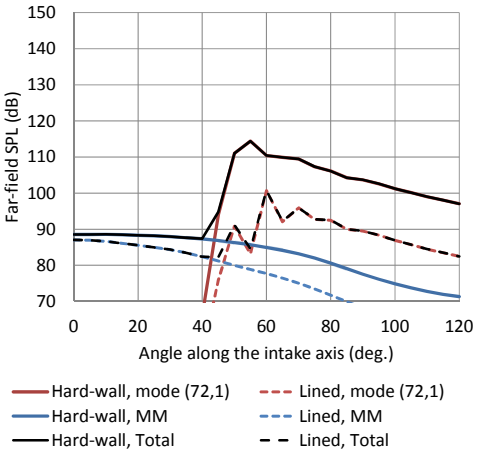

(c) 3rd BPF (3900Hz)

FIGURE 5.16: Far-field SPL directivities for hard-wall and uniformly lined (R=5, d=15mm) configurations at the first three BPFs at sideline condition

can be obtained from the broadband computation. Therefore, this method will significantly reduce the total computation time over the entire noise spectrum for the combination of different sources.

Figure 5.17 shows the contours of $\Delta PWL_{0^o \rightarrow 120^o}$ produced for the entire source spectrum over the considered frequency range by using method A and B. The grid resolution in the R-d design space used to produce these contours is the same as used in the previous sections, which involves a total of 110 ACTRAN/TM evaluations. Figure 5.17 indicates that there is hardly any difference in the contours produced by the two methods but it takes approximately 3 days to produce figure 5.17(a) as compared 2 days in producing figure 5.17(b). This clearly justifies the usefulness of method B.

Figure 5.17 shows that the results are once again dominated by the SM components at BPFs. However in all the predictions done so far, the propagation of the rotor-locked

TABLE 5.5: Methods to combine the individual noise sources over the entire frequency range at sideline condition

Method A	Acoustic computation of the MM components at BPFs is performed at 800Hz but the liner impedance is calculated at the exact BPFs. (as done in section 5.7.3)
Method B	Acoustic computation of the MM components at BPFs is performed at 800Hz but the liner impedance is calculated at the centre frequency of the 1/3rd Octave band which contains the BPF.

SM components was considered to be linear. Non-linear propagation effects however cannot be ignored at such conditions. Therefore, the correct overall attenuation for the source spectrum is predicted in the next section by considering the non-linear effects in the SM components at BPFs.

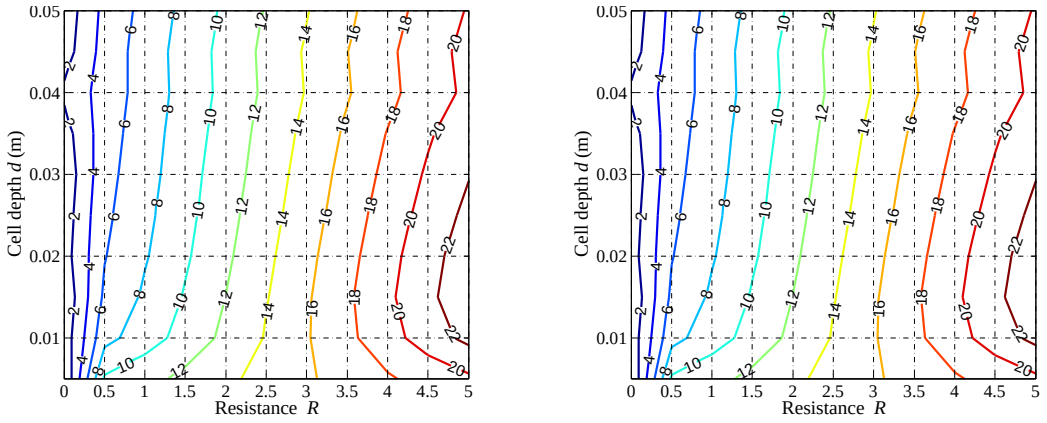

(a) Method A

(b) Method B

FIGURE 5.17: Contours of $\Delta PWL_{0^o \rightarrow 120^o}$ plotted against non-dimensional liner resistance R and cell depth d for the entire source spectrum over the considered frequency range

5.7.4.1 Non-linear adjustments to ACTRAN/TM predictions

The non-linear analytical model detailed in chapter 3 is again used in this study to predict the non-linear attenuation of the rotor-locked SM tones at BPFs. This model is based on the attenuation of a regular saw-tooth waveform which is a superposition of all the rotor-locked BPF tones. Since only the first three BPFs are considered in this study, the SM tones at these BPFs are combined incoherently and the non-linear model is applied to this combined source. Non-linear propagation effects are assumed to be insignificant in other sources due to their relatively low source levels.

The Source SPL of the SM tones at first three BPFs are added incoherently to obtain the total source SPL as expressed in equation 5.15. To predict the non-linear attenuation in the lined case, the absorptive term σ in equation 3.44 is determined from the linear attenuation of the combined SM source predicted by ACTRAN/TM.

$$SPL^{Source}_{TOTAL} = 10log_{10}\left(10^{\frac{SPL^{Source}_{(24,1),1BPF}}{10}} + 10^{\frac{SPL^{Source}_{(48,1),2BPF}}{10}} + 10^{\frac{SPL^{Source}_{(72,1),3BPF}}{10}}\right) \quad (5.15)$$

Figure 5.18(a) shows the axial plot of SPL at the duct wall predicted by the analytical model for the hard-walled and lined cases. The corresponding linear solutions and are also included in this figure. These results are used to adjust the linear far-field predictions by ACTRAN/TM. This is illustrated in figure 5.18(b). The non-linear corrections in SPL values at the duct wall predicted by the analytical model are directly applied to correct the far-field directivities of the combined SM source predicted by ACTRAN/TM.

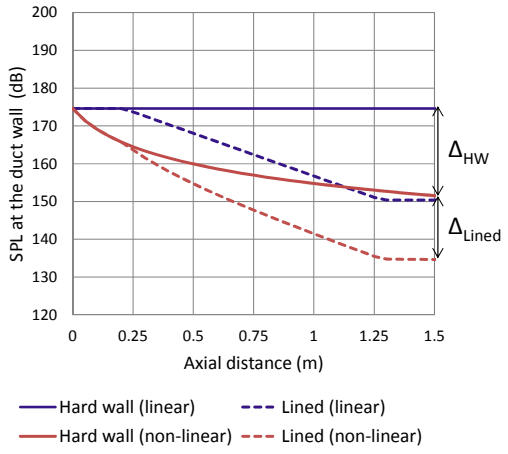

(a) SPL at the duct wall along the duct axis predicted by the non-linear model

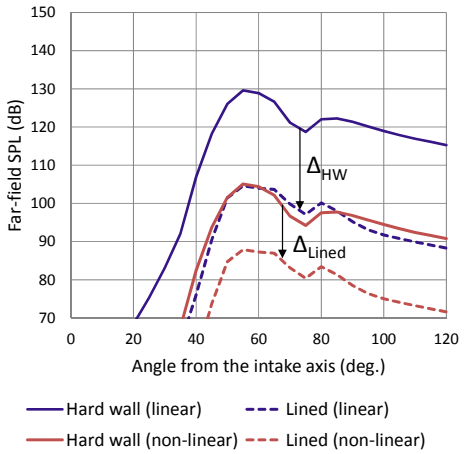

(b) Non-linear adjustments applied to the far-field directivities predicted by ACTRAN/TM

FIGURE 5.18: Methodology to apply non-linear adjustments to the linear far-field predictions by ACTRAN/TM by using the results obtained by the analytical non-linear propagation model

The correct liner attenuations are obtained at grid points in the *R-d* design space by using this methodology and the contours in figure 5.17 are reproduced to obtain the contours in figure 5.19. Again, there is hardly any difference between the results predicted by using methods A and B. Figure 5.19 indicates that the total attenuation decreases substantially due to non-linear propagation effects in the SM tones.

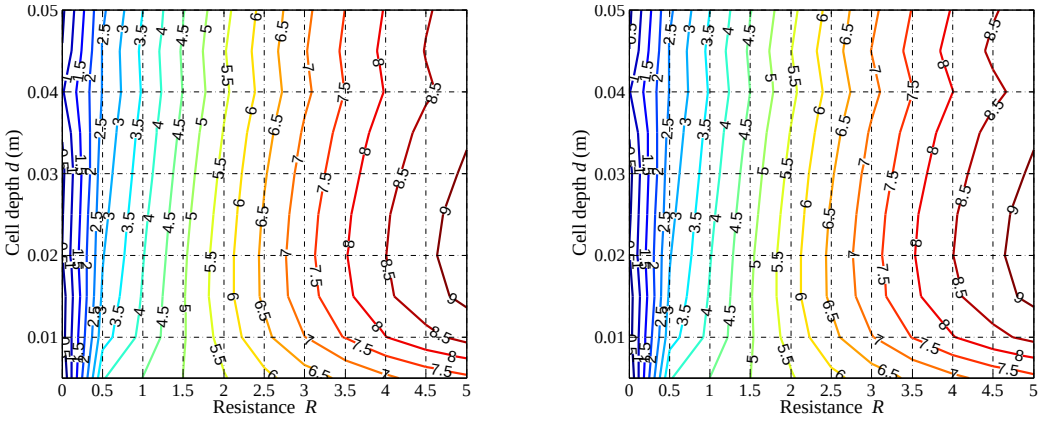

(a) Method A

(b) Method B

FIGURE 5.19: Contours of $\Delta PWL_{0^o \to 120^o}$ plotted against non-dimensional liner resistance R and cell depth d for the entire source spectrum over the considered frequency range including non-linear adjustments to SM tones at BPF

Figure 5.20 and table 5.6 show the SOFT optimisation results when the automated optimisation strategy is applied to figure 5.19(b). A maximum attenuation of 9.2dB is achieved when the optimal liner of resistance $5\rho c$ and cell depth of 20.6mm is used.

Figure 5.21 shows the far-field directivities for the total noise spectrum. The optimal liner selected by the SOFT optimisation is used in the lined configuration. The corresponding linear solutions by ACTRAN/TM are also included in figure 5.21. The attenuation drops down by about 14dB when non-linear propagation effects are included in the prediction.

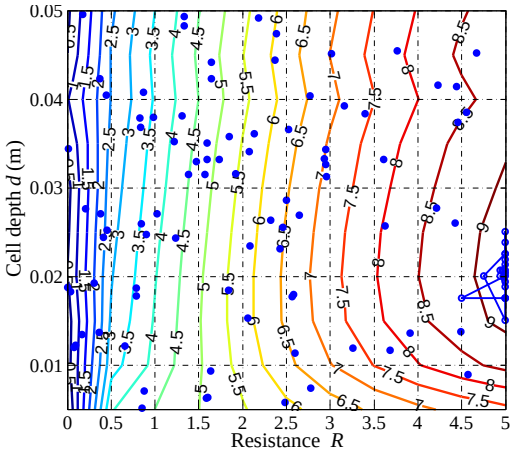

FIGURE 5.20: SOFT optimisation results of $\Delta PWL_{0^o \to 120^o}$ characterized by liner resistance R and cell depth d for the entire source spectrum over the considered frequency range (Method B) at sideline condition. GA points (solid circles) and DHC path (hollow circles) superimposed on pre-computed contours of the cost function in the R-d design space.

TABLE 5.6: Results of SOFT optimisation of the intake liner for the total source spectrum over the considered frequency range at sideline condition (Method B)

Resistance R (non-dimensional)	5.0
Cell depth (in meter)	0.0206
Maximum attenuation	9.20
No. of evaluations	126
CPU time	85hr 41min 25sec

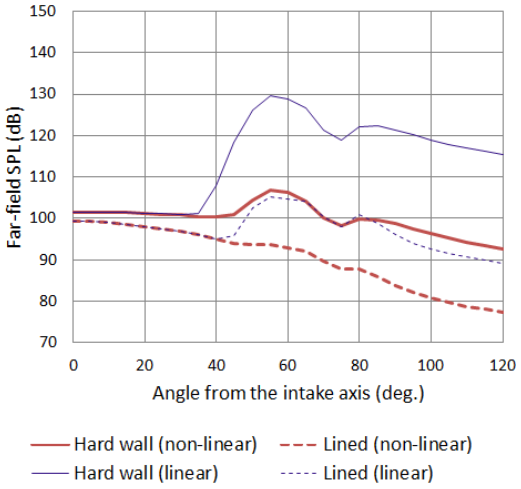

FIGURE 5.21: Far-field SPL directivity of the total noise source at sideline condition; the optimal liner selected by SOFT is used in the lined configuration

5.8 Comparison of the results with the benchmark optimisation studies of Lafronza

The intake liner optimisation study presented in this chapter can be compared to the benchmark examples of Lafronza [66] in which liners where optimised for a uniform circular duct idealizing an intake geometry. Lafronza also used only two design variables to specify the acoustic impedance, namely, the face-sheet resistance and the liner cell depth. An approximate evaluation of PNL was used as a cost function and the frequency spectrum was limited to 150Hz to 7500Hz (18 one-third octave bands). An 'equal-energy' multi-mode source model was used at the approach condition. At the sideline condition, the noise source consisted of both the multi-mode component and the single-mode BPF tones.

The optimisation results of Lafronza indicated the requirement of high resistance liners (R typically greater than 5) at sideline condition. However, at approach condition, the optimum value of the resistance was predicted to be less than 4. These are in good agreement with the optimisation results presented in the current study. The optimum

liner cell depths computed at the approach condition are however quite different between the two studies. The optimum cell depth predicted in the current study is much greater than that predicted by Lafronza. This may be because of the fact that unlike Lafrona, no subjective weighting is applied to the attenuations calculated at different frequencies as the main purpose of this study is to demonstrate the feasibility of the automated optimisation methods for realistic intakes rather than to provide an industrial template for their application. Moreover, the implementation of such weighting does not materially affect the computational effort involved in the procedure. The optimum cell depth predicted by both the studies for the total noise source at sideline condition however lie within a comparable range of 0.01-0.02m. Both the studies indicate that the total liner attenuations at high fan speeds are dominated by that of the BPF tones.

A direct comparison of optimum liner impedances and the attenuations with Lafronza's results is however not possible as the duct geometry, liner extents and the engine conditions are not exactly the same. Therefore, it is difficult to comment on the impact of the geometry and flow effects on the optimisation results. However, by referring to the study presented in the previous chapter, it can be pointed out that the attenuations of nearly cut-on high amplitude rotor locked modes are affected by the geometry and the flow. As these modes propagate along the duct wall, the flow variations along the liner becomes very important in order to correctly predict the liner attenuation.

5.9 Conclusions

An automated liner optimisation procedure involving realistic (axisymmetric) geometry and flow has been attempted for the first time at two different engine conditions. Earlier liner optimisation studies involved only uniform circular and annular ducts. The study demonstrates the feasibility of integrating CAA codes within automated optimisation schemes to optimise the performance of liners in realistic intakes on industrial time scales.

Two different automated liner optimisation has been presented in this chapter schemes to reduce radiated fan noise in the forward-arc of a turbofan engine. These schemes were initially demonstrated at approach condition to optimise intake liners for 'equal energy' broadband spectrum. Identical results were obtained from both the schemes. However, the MATLAB optimisation scheme took longer processing time due to larger number of CAA evaluations required by the local search algorithm 'fmincon'. The performance of some optimal liners was also investigated over the considered frequency range and was compared to the maximum attainable attenuation at each frequency. The performance of the optimised liners were predicted to be relatively low when compared to an 'ideal' liner at low frequencies.

Intake liners were also optimised for a more realistic noise spectrum at sideline condition. The noise spectrum consisted of broadband noise and tones at the harmonics of BPF. The contours of ΔPWL as a function of the liner design parameters were produced for the individual noise components as well as for total noise spectrum. Nonlinear adjustments were applied to ACTRAN/TM predictions to correctly determine the attenuation of rotor-locked tones. SOFT optimisation strategy was used to optimise the intake liner for the total noise spectrum at sideline condition. The results indicate the need for a high resistance liner at such conditions.

The results confirm the feasibility of applying automated liner optimisation approaches for realistic intake geometries and realistic noise spectra at different noise certification conditions. The optimisation process requires the execution of a large number of individual CAA analysis, especially when optimisation is performed for a range frequencies and for all the noise sources. The cumulative process-time, however, lies with the acceptable limit in industrial practice.

The optimisation study presented in this chapter was limited to single-layer liners in which only two design parameters (resistance R and cell depth d) were used in the optimisation. In industrial applications, however, double-layer liners are commonly used and the optimisation of such liners would involve more than two parameters (for instance, facing sheet and septum resistance and the cell depths of the two layers). The number of design parameters in liner optimisation would further increase if more than one liner is optimised simultaneously, as in the case of segmented liners. The automated optimisation schemes used in this study which employ genetic algorithm followed by a local search (DHC or 'fmincon'), however, do not have a restriction on the number of design parameters used in the optimisation. This was demonstrated by Achunche [62] who used the SOFT optimisation strategy to optimise segmented liners in an annular duct. As the total optimisation time increases with the number of design parameters, applying such schemes for realistic intake geometries and noise spectrum would be a time consuming process. However, it can be possible to achieve industrially acceptable time scales with such optimisation schemes by employing coarse parallelization and multi-threading which would reduce the computational cost. An alternative solution to this problem would also be to use Response Surface Methods (RSM) in which a surrogate model of the real cost function is deduced by the use of design of experiments (DoE) and it is this approximate function which is optimised instead of the real cost function.

Chapter 6

Liner damage study - analytical asymptotic model

6.1 Introduction

Traditional installations of turbofan intake liners have acoustically 'hard' axial splices between liner segments for ease of fabrication and assembly. The splices scatter energy from the rotor-locked tones into adjacent azimuthal orders for which the liner is less effective, thereby degrading the liner performance [88, 89]. The significance of this 'splice effect' has led to the adoption of 'zero-splice' liners in many current turbofan engines. However, damage can occur to such liners in service. The extent to which local impedance changes due to liner repairs reduce the effectiveness of the zero-splice design then becomes an issue when determining how much damage is acceptable before noise certification levels are compromised.

In this chapter, the acoustic effect of liner damage or repair on the total noise attenuation achieved by a zero-splice liner is assessed. An analytical asymptotic model is used to generate benchmark solutions for subsequent full numerical calculations done in chapter 7. The effect of the size and location of the hard patch on the performance of the liner is assessed by using this asymptotic model. The incident field consists of a rotor-locked BPF tone for a fan operating condition in which fan-tip speed is supersonic. The method gives an estimate of the scattered field based on linear theory. However at such operating conditions, non-linear propagation effects of the rotor-locked mode cannot necessarily be neglected (as discussed in chapter 3). In section 6.4 of this chapter, a new procedure is presented in which a nonlinear correction is applied to the results obtained from the linear model.

6.2 Literature Review

Computational studies of acoustic scattering and absorption in ducts with circumferentially varying liners were first performed some 30 years ago [90, 91]. These were constrained by the computational resource available at that time and could deal only with simple liner configurations at low frequencies. More recent computational studies include both Finite Element (FE) [89] and Boundary Element (BE) [92] models which deal with more realistic frequencies. While most of these studies deal only with splices, Gabard and Astley[25] applied a numerical FE mode matching technique to study the effects of hard patches in zero-splice liners for incident azimuthal mode numbers which were still somewhat short of the values required to represent the rotor-locked tone at Blade Passing Frequency (BPF) in realistic intakes.

In parallel with the above numerical approaches, a semi-analytical model for splice scattering, which was originally devised by Cargill [93], has subsequently been extended and implemented by Tester *et al.* [88, 94]. In this model which is computationally much less demanding than numerical approaches, the scattered field is expressed in terms of sources generated by the incident field only and propagated by a Green's function derived for a peripherally uniform liner. Good agreement has been demonstrated for splice predictions obtained from Cargill's model when compared to a three-dimensional FE analysis [94]. Tester [95] further extended this model by using the mode amplitudes predicted by Cargill model at the exit plane as input to ACTRAN/TM to obtain the far-field directivity of each hard-wall mode by using an axi-symmetric model. The prime advantage of the Cargill model is that it provides a key for rapid evaluations of modal scattering.

The analytical code modified and extended by Tester as Cargill code [96] is used in this chapter to perform a parametric study of the acoustic effects of liner damage to the performance of zero-splice liners.

6.3 The liner patch problem

In this study, it will be assumed that any portion of the liner which has been repaired due to damage will be ineffective in absorbing sound. A repaired portion of the liner will therefore be modelled by an acoustically 'hard' patch. This is a conservative assumption which represents the worst outcome from a liner repair.

6.3.1 Prediction tool

The prediction tool used in this study is the Cargill code [96] developed by Tester. It is an analytical asymptotic model which predicts the scattering of a single incident mode

by an axial hard splice. In this model, which is computationally less demanding than numerical approaches, the scattered field is expressed in terms of sources generated by the incident field only and is propagated by a Green's function derived by Rienstra and Tester [88] for a circumferentially uniform liner with uniform mean flow. The model is based on Kirchhoff's approximation which assumes that the total area of the splices is very small compared to the total lined area. By applying this approximation, the scattered field is expressed as an integral over the total spliced area with the integrand featuring only the incident field and the Greens function. The Cargill code solves the following equation to compute the scattered field in the presence of a hard splice of area A_s [93, 96]:

$$p_s(x,r,\theta) = \int_{A_s} p_0(x_0,r_0,\theta_0)\frac{1}{ik}\left(ik - M_x\frac{\partial}{\partial x_0}\right)^2 \frac{G(x,r,\theta|x_0,r_0,\theta_0)}{Z}dA, \tag{6.1}$$

where p_0 is the incident pressure field, k is the free-field acoustic wavenumber ($=\omega/c$), M_x is the Mach number of the uniform axial mean flow, Z is the specific acoustic impedance of the liner. It is assumed that $p_s << p_0$ to derive equation 6.1 [93, 96]. $G(\mathbf{x}|\mathbf{x_0})$ is a Green's function derived for a circumferentially uniform liner with a uniform mean flow [88]. The coordinate $\mathbf{x_0}$ in $G(\mathbf{x}|\mathbf{x_0})$ corresponds to the location of the sources which, in this case, is located along the hard splice.

Consider a uniform circular duct of radius a having an acoustic liner of length L with a hard splice of angular width $\delta\theta_s$ located at a azimuthal angle θ_s. Since the sources are located along the hard splice, $r_0 = a$. Therefore for a coordinate system with its origin at the centre of the lined section, equation 6.1 can be re-written as:

$$p_s(x,r,\theta) = \int_{-L/2}^{x}\int_{\theta_s}^{\theta_s+\delta\theta_s} p_0(x_0,a,\theta_0)\frac{1}{ik}\left(ik - M_x\frac{\partial}{\partial x_0}\right)^2 \frac{G(x,r,\theta|x_0,a,\theta_0)}{Z}ad\theta_0 dx_0. \tag{6.2}$$

The Cargill model solves equation 6.2 to predict the scattered field in the lined section with a hard splice running all the way throughout the length of the liner. The above expression for pressure is then matched to the hard-walled solutions at the hard-lined interface by using the mode-matching conditions of Astley [25] to predict the total pressure field inside the duct. Anechoic boundary condition is applied at the end of the duct by constraining all the reflected mode amplitudes to zero.

Tester further modified the code to predict the scattering from a 'hard patch'. This modification involves a technique to model the hard patch without making any implicit changes to the Cargill formulation. In order to model a hard patch, a finite length of the duct segment with a single splice is modeled by using Cargill's theory. This length is equal to the axial length of the hard patch and the width of the patch is equal to

the width of the splice. This is illustrated in figure 6.1. A uniformly lined section with the same liner impedance as that of the spliced section is placed upstream and downstream of the hard patch, and the scattered field which is calculated in the spliced section is matched to solutions in the adjacent uniformly lined sections by using the mode-matching conditions of Astley [25]. A hard-walled section is required at the fan plane and at the highlight to facilitate the imposition of the incident pressure field in terms of hard-walled duct modes and the anechoic boundary condition respectively. An unwrapped version of the resulting duct wall is shown as figure 6.1.

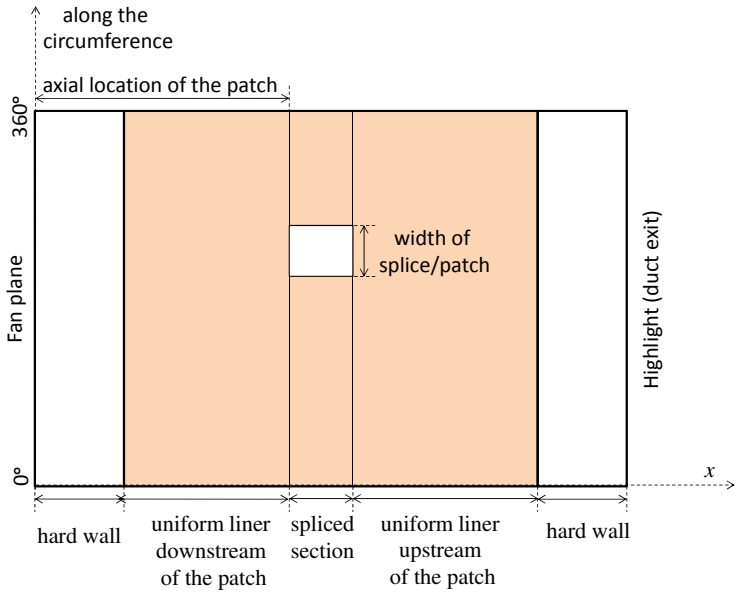

FIGURE 6.1: An unwrapped figure of a uniform cylindrical duct to describe the modeling of a hard patch in Cargill code

It is important to note that Cargill code (version 13) can only deal with circular ducts with uniform mean flow. Moreover, if the Cargill model is used to predict the scattering caused by large patches or thick splices, the results may be questionable as the model is based on Kirchhoff's approximation.

6.3.2 Intake geometry, source and conditions

Figure 6.2 shows the intake model used in this study, which is a uniform cylindrical duct of fan radius $a = 0.64$m. A uniform zero-splice liner starts at a short distance upstream of the fan face. The ratio of the liner length to fan diameter is of the order 1:2. The Mach number of the mean flow is denoted by M_x.

The engine operating conditions used in the study are listed in table 6.1. The fan-tip speed is supersonic at all these conditions. The BPF at these conditions are listed in

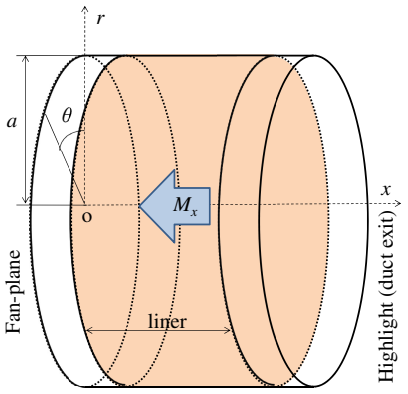

FIGURE 6.2: A uniform cylindrical intake with a uniform zero-spliced lining used for Cargill predictions; M_x is the mean flow axial Mach number

TABLE 6.1: Conditions used in the hard patch study

Cases	BPF (ka)	M_x	Resistance (ρc)	Reactance (ρc)
1	25.5	-0.41	1.78	-0.40
2	27.0	-0.45	2.10	-0.45
3	28.6	-0.49	2.24	-0.41

table 6.1 in terms of Helmholtz number ka. In all the cases presented here, an incident mode $(24, 1)$ is used to characterise the BPF tone for a fan with 24 blades. The specific resistance and reactance of the acoustic liner used in each case is also listed in table 6.1.

6.3.3 Results

In the current study, The effects of the size and the location of a hard patch are investigated for different conditions listed in table 6.1. The patch is always assumed to be square shaped. The general effects of a hard patch on the axial attenuation of the incident mode (24,1) is shown in figure 6.3. The modal power levels (PWLs) of the different azimuthal mode orders are expressed relative to the source PWL of the incident mode (24,1) and is plotted against the axial distance along the duct. In the Cargill code, the acoustic power is determined by using Morfey's [97] definition of the acoustic intensity. Morfey showed that if one used his definition, the acoustic power would be conserved in an irrotational mean flow. Therefore, it can be argued that this definition which is used in the Cargill code may not provide an accurate measure of the modal PWL in the lined section of the duct where Myers [43] 'slip wall' liner boundary condition is specified.

Figure 6.3 shows that in the absence of the patch, modal scattering does not occur and the rotor-locked mode is effectively attenuated by the liner, approximately by 50dB relative to the source level. However in the presence of a patch, the power of the

incident mode (24,1) is scattered into other azimuthal orders which are not attenuated by the liner as much as the mode (24,1). Hence, the total exit PWL increases by about 20dB.

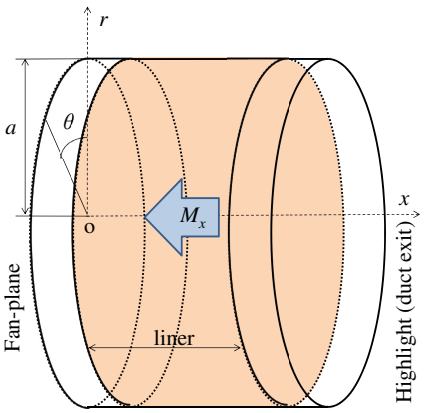

(a) Uniformly lined

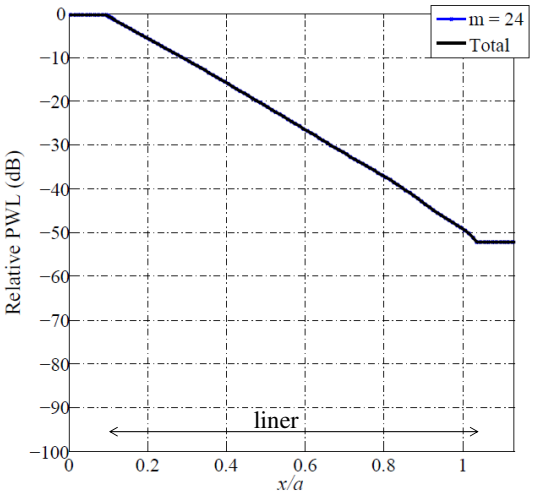

(b) Cargill predictions for (a)

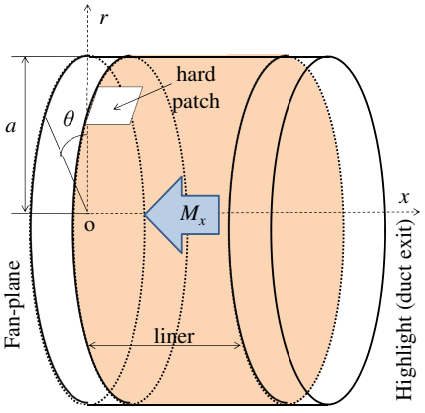

(c) Lined with a hard patch

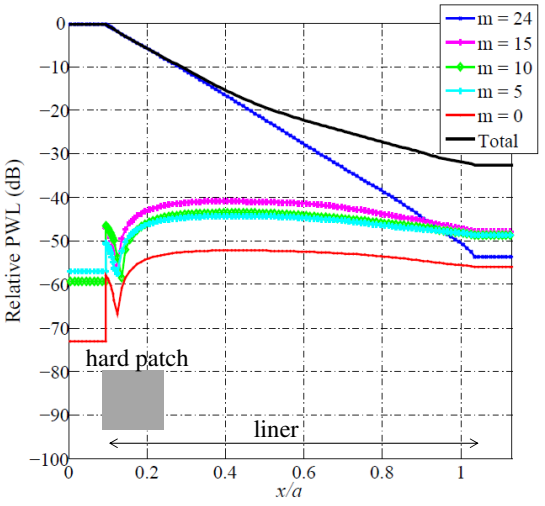

(d) Cargill predictions for (c)

FIGURE 6.3: Modal PWL (relative to the in incident) along the duct axis with and without a hard patch at the liner start at frequency $ka = 27.0$

As the rotor-locked mode (24,1) generated at the fan reaches the lined section, some power is reflected back towards the fan but most of it is transmitted which is in turn scattered by the patch into a number of modes. The original mode (24,1) and the scattered modes are again partially reflected and transmitted into the hard-wall section upstream of the liner (near the duct exit). This transmitted power is then radiated from the duct exit into the far-field, which will not be modelled in the current study. Only few of the scattered modes are shown in figure 6.3.

It is important to note that the PWL of the incident and the scattered field shown in figure 6.3 is the PWL of both the forward and backward propagating modes summed up over all the radial modes cut-on at BPF for a particular azimuthal order.

6.3.3.1 Results at different frequencies

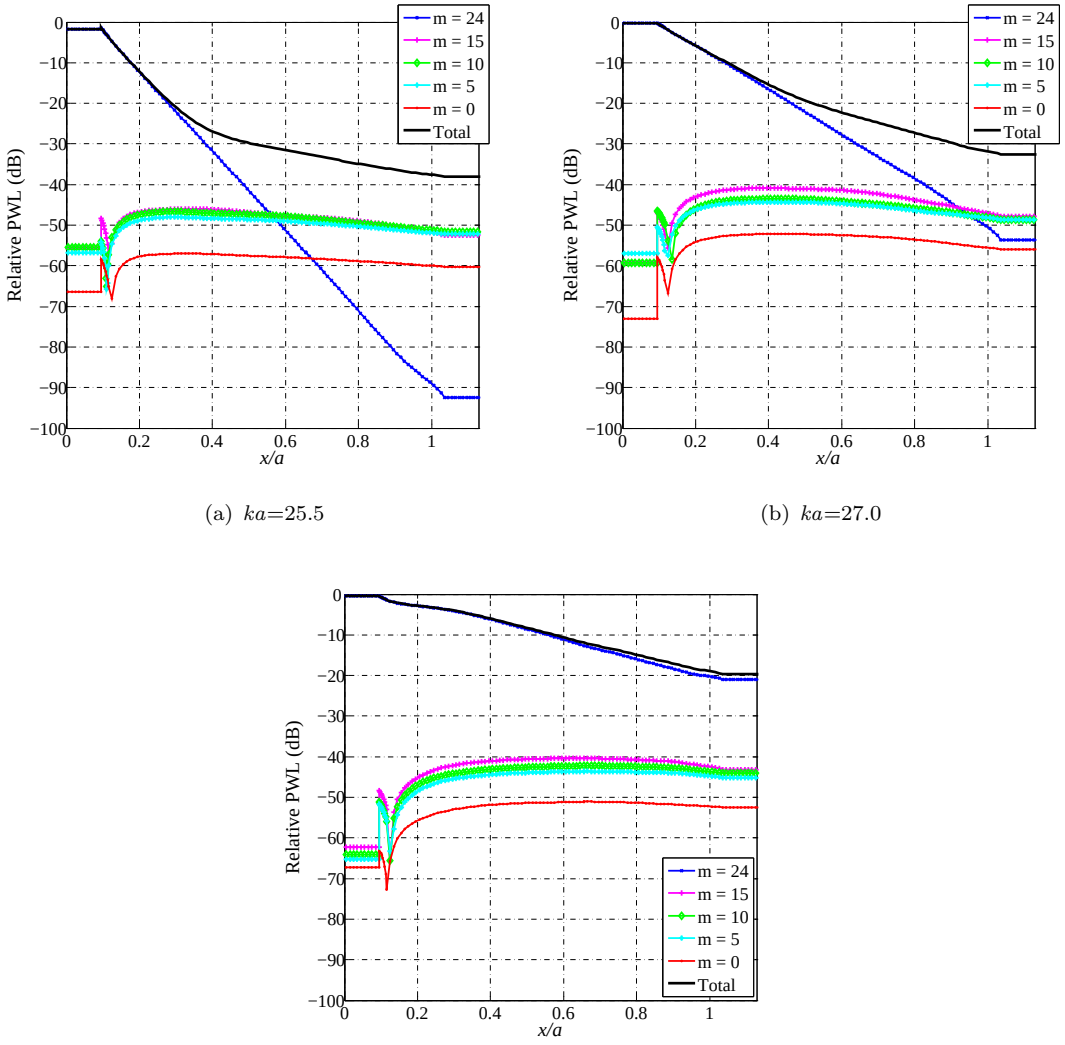

(a) ka=25.5

(b) ka=27.0

(c) ka=28.6

FIGURE 6.4: Modal PWL along the duct axis at different frequencies for a hard patch of width 8.9% of the duct circumference located at the start of the liner

The dependance of the patch effect on different frequencies (or conditions) listed in table 6.1 for a large patch of width 8.9% of the duct circumference located at the start of the liner is shown in figure 6.4. Modal power and total power along the duct axis are plotted in the same format as in figure 6.3.

At ka=25.5, the mode (24,1) is nearly cut-on and is heavily attenuated by the liner. The PWL at the duct exit is then dominated by the scattered modes.

At ka=27.0 however the mode (24,1) is more cut-on and less attenuated. The power in the incident mode and the scattered modes at the highlight is then more evenly balanced, although the scattered modes still dominate the overall transmitted power.

At ka=28.6, the mode (24,1) is strongly cut-on and quite poorly attenuated. The transmitted power at the the exit is then dominated by the original tone and unchanged by the patch.

Case 2, when ka=27.0, is the most interesting of these cases. The contributions to the transmitted power from the incident and scattered components are then comparable in magnitude. In the remainder of this chapter we focus on this particular condition.

6.3.3.2 Results for different patch sizes

Results are presented in figure 6.5 for four different patch widths. Condition 2 is considered (ka=27.0) in the analysis. The patch is located close to the fan to maximise the scattering effect. The acoustic power distribution over the azimuthal modes at the duct exit is shown in figure 6.6.

Figure 6.5 shows that when the patch width increases from 1.6% to 3.8% of the duct circumference, there is a significant increase in the total PWL at the duct exit as the power in the scattered modes increases. However, the increase in total PWL at the duct exit slows down for the larger patches. If the patch size is increased further, the total PWL at the duct exit is expected to increase as the total lined area decreases resulting in less noise attenuation. A patch width of 100% of the duct circumference corresponds to an intake configuration without a liner for the current case and therefore the total PWL relative to the incident level would be zero at the duct exit.

The results presented in this section is, however, subject to validation of Kirchhoff's approximation used in the Cargill model which assumes that the area of the hard patch (or splice) is very small as compared to the total lined area. Therefore, the accuracy of these Cargill results, especially for larger patches, will be tested in the next chapter when these predictions will be compared to that obtained from the CAA tool ACTRAN/TM.

Figure 6.6 shows that the acoustic power at the exit is distributed over wide range of azimuthal mode orders for the smaller patches. As the patch size increases the power distribution over mode orders become more complex and shows a specific pattern against the azimuthal order. A similar pattern was was also observed by Gabard and Astley [25]. Such a pattern seems to occurs when the patch width exceeds the circumferential wavelength of the incident mode (24,1).

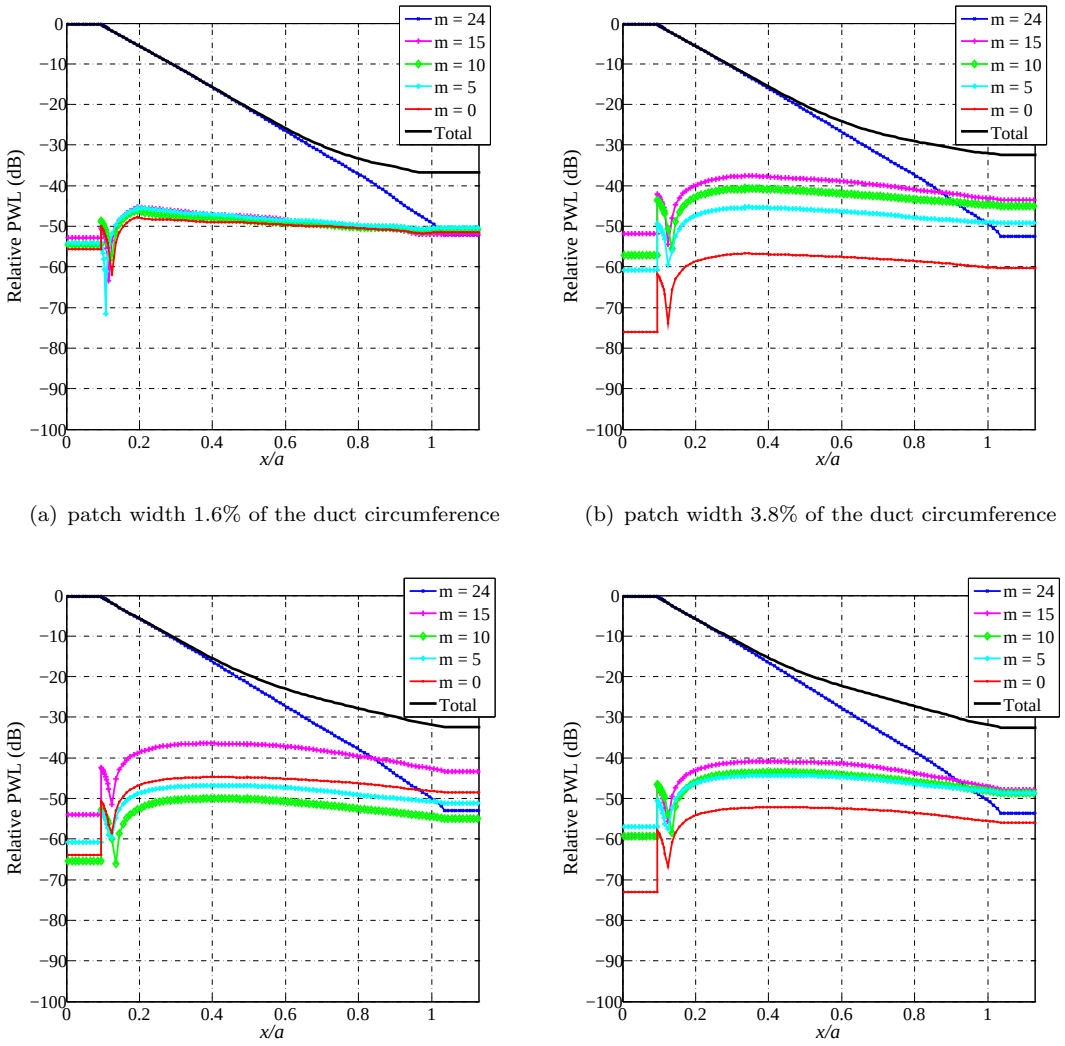

(a) patch width 1.6% of the duct circumference

(b) patch width 3.8% of the duct circumference

(c) patch width 6.4% of the duct circumference

(d) patch width 8.9% of the duct circumference

FIGURE 6.5: Modal PWL along the duct axis for different patch sizes at the liner start location at ka=27.0

6.3.3.3 Results for different locations of the patch

Figure 6.7 shows the results for four different patch locations relative to the liner at ka=27.0. A patch width 3.8% of the duct circumference is chosen in the current analysis. These plots indicate that the detrimental effects of the patch is greatest when it is located closest to the fan, as one would expect.

6.4 Non-linear adjustments to Cargill predictions

The study performed in previous section (section 6.3) was based on the Cargill's analytical model of scattering which is a linear model. The propagation of the rotor-locked

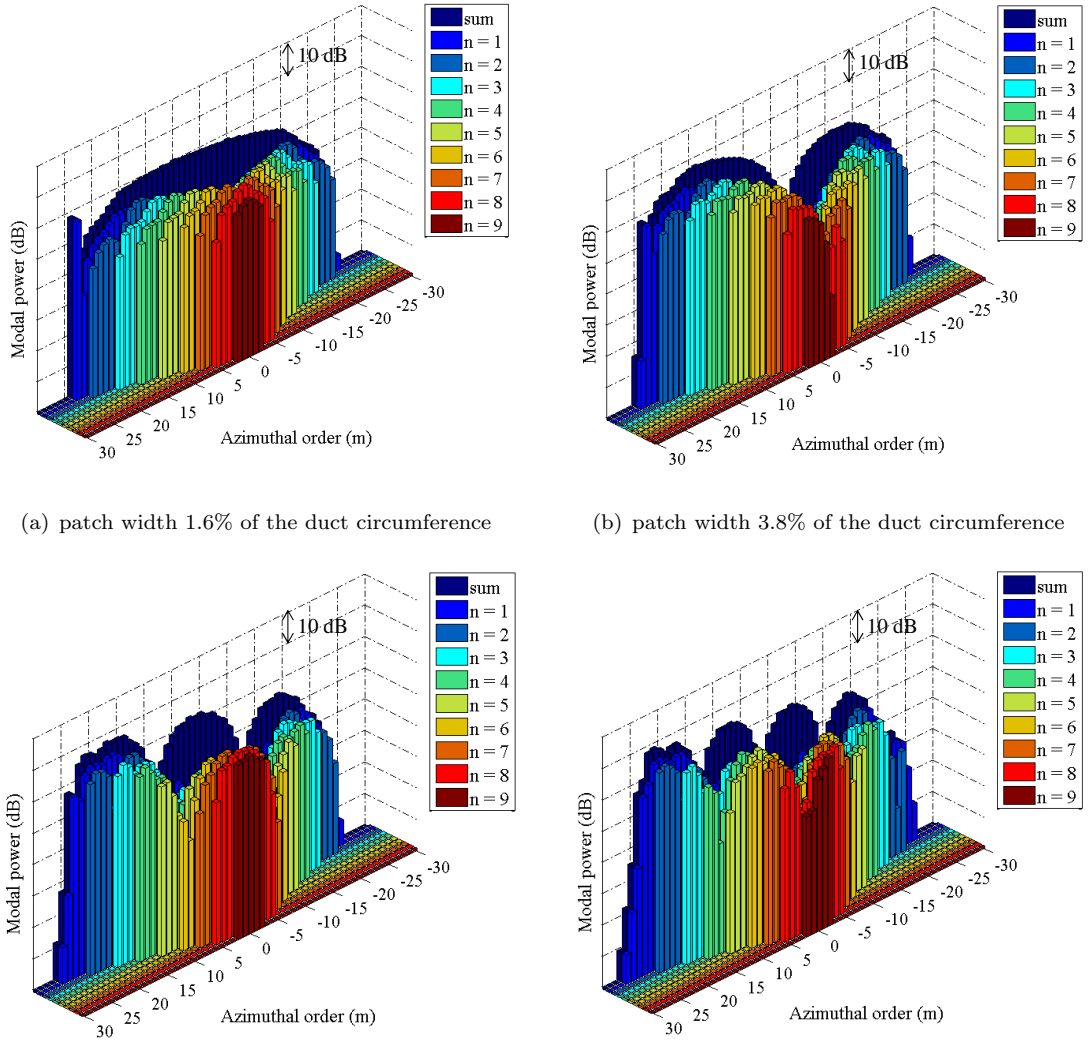

(a) patch width 1.6% of the duct circumference

(b) patch width 3.8% of the duct circumference

(c) patch width 6.4% of the duct circumference

(d) patch width 8.9% of the duct circumference

FIGURE 6.6: Modal PWL at the duct exit at ka=27.0 for different patch sizes at the start of the liner

mode (24,1) at condition 2 cannot be predicted by using linear theory as it generally has a very high amplitude at such conditions. An adjustment is therefore applied to the linear result by using the analytical model of non-linear attenuation detailed in chapter 3.

6.4.1 Assumptions

The methodology which is used to implement non-linear adjustments to the results obtained from Cargill code, invokes the following assumptions:

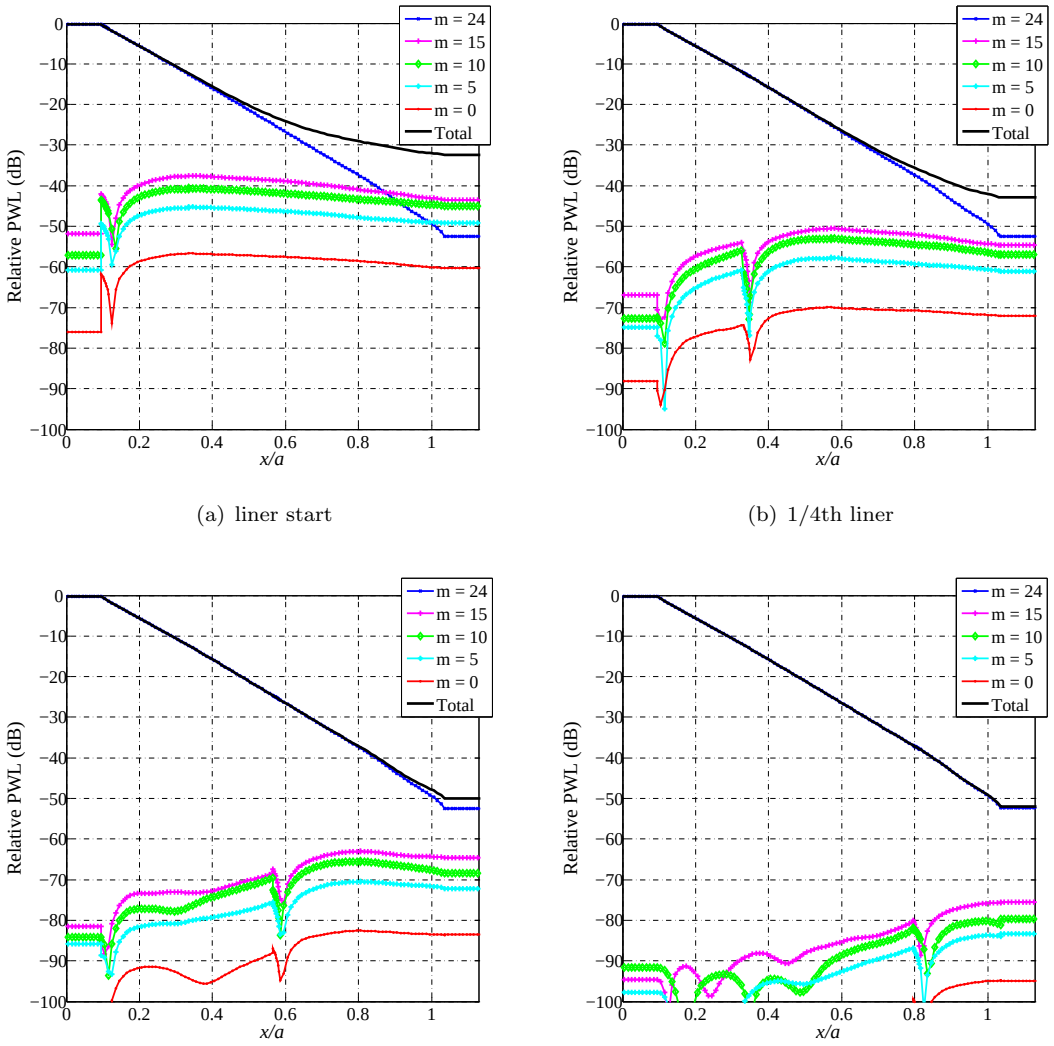

(a) liner start

(b) 1/4th liner

(c) 1/2 liner

(d) liner end

FIGURE 6.7: Modal PWL along the duct axis for different patch locations relative to the liner for a patch width 3.8% of the duct circumference at ka=27.0

6.4.1.1 Non-linear effects are dominant only in the rotor-locked incident field

It can observed from the linear results presented in section 6.3 that the PWL of the scattered modes are about 40 dB below the incident PWL, when the hard patch is located very close to the fan. As the distance of the patch from fan increases, the PWL in the scattered field drops down further. Since non-linear effects are pronounced only at high source strengths, it is reasonable to assume that the non-linear effects in the scattered modes are almost negligible. Therefore, the non-linear model described in section 3.5 is only applied to predict the non-linear propagation of the rotor-locked mode (24,1). The absorptive term σ in equation 3.44 is determined from the linear

attenuation rate of the rotor-locked incident mode (24,1) predicted by the Cargill model.

6.4.1.2 Negligible reflection of the rotor-locked mode (24,1)

The non-linear model is applicable only for shock waves propagating purely in one-dimensional manner in one particular direction (section 3.5). Hence, the model can only be used to predict the non-linear attenuation of forward propagating mode (24,1) (propagating upstream of the fan). The theory is not applicable for the reflected mode (24,1). In practice when the rotor-locked mode is strongly cut-on at the fan plane at high supersonic fan-tip speeds, the reflection of this mode is very small. It is therefore reasonable to assume that there is negligible reflection of this mode.

6.4.1.3 Scattering occurs pre-dominantly at the start of a hard patch

In order to apply non-linear adjustment to the patch-scattered modes, it is assumed that all the scattering occurs at the start of the patch. The PWL of the scattered modes is therefore dropped down by an amount equal to the difference in SPL of the incident mode between the linear and non-linear predictions calculated by using the non-linear model at the start of the patch.

It is important to note that the difference in SPL predicted at the wall is used to correct the PWLs. This is because PWL cannot be calculated directly from the non-linear model as the model predicts the acoustic pressure only at the duct wall. Therefore, it can be considered as a crude assumption and could only be applicable for modes which propagate along the duct wall like the rotor-locked mode (24,1) in this case. Since most of the acoustic power in this mode is concentrated at the duct wall, it is assumed that the change in PWL of mode (24,1) due to non-linear effects is approximately equal to the change in SPL predicted by the model. Finally, the drop in PWL of this mode due to non-linear effects calculated at the start of the patch is used to correct the PWLs of the scattered modes.

6.4.2 Results

Figure 6.8 is a reproduction of figure 6.5(b) which includes the non-linear propagation effects at different source amplitudes of the incident mode (24,1). By using the methodology and the assumptions stated in the previous section, corrected axial distributions of modal power are obtained for a range of incident pressure amplitudes varying from 150dB to 180dB.

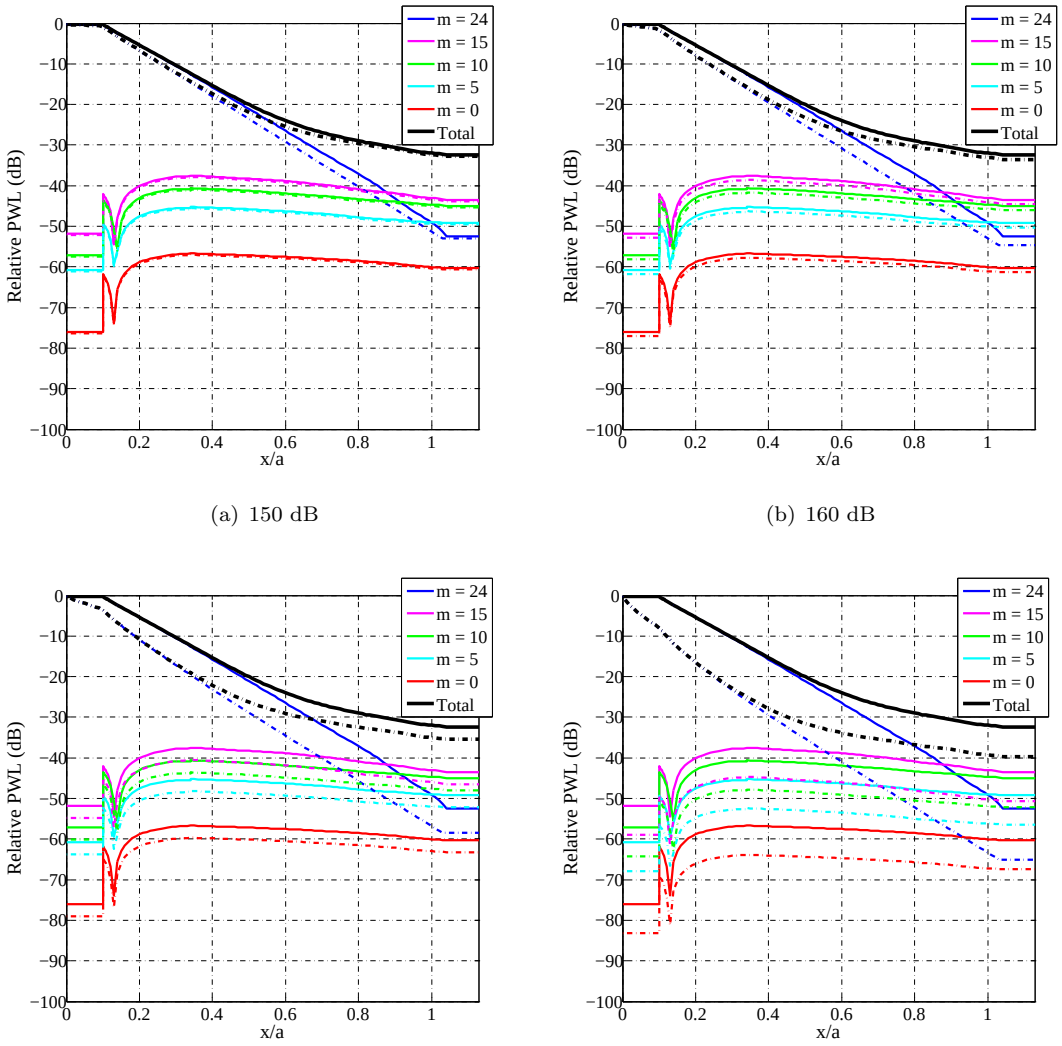

(a) 150 dB

(b) 160 dB

(c) 170 dB

(d) 180 dB

FIGURE 6.8: Modal PWL along the duct axis for a patch width of 3.8% of the duct circumference at liner start at ka=27.0 for different SPLs of the rotor-locked incident mode (24,1) at the duct wall close to the fan; linear prediction (solid line) and non-linear predictions (broken lines)

Figure 6.8 clearly indicates that the non-linear effects cannot be neglected, especially at high source amplitudes, as it affects the PWL of the incident and the scattered modes. However, it is interesting to note that the difference in the total PWL at the duct exit for a liner configuration with a patch relative to the uniformly lined configuration remains almost constant for different incident pressure amplitudes.

Figure 6.9 shows the relative sound power level (PWL) at the duct exit as a function of the patch width. The patch width is represented in terms of the percentage of the duct circumference. In figure 6.8, the modal PWL was expressed relative to the incident PWL but in figure 6.9, the reference value is the hard-walled case including non-linear adjustment. A patch width of zero corresponds to the uniformly lined configuration.

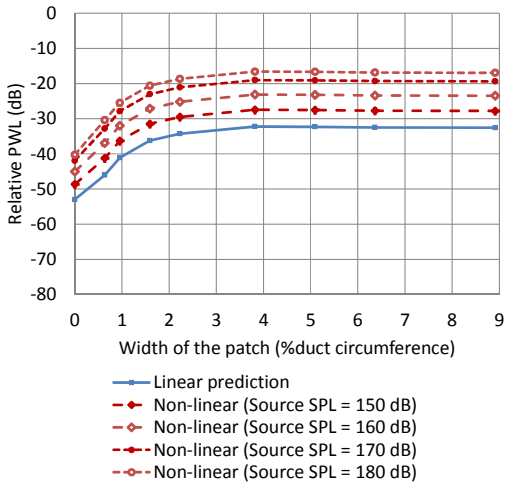

FIGURE 6.9: Relative sound power level (PWL) predicted by the Cargill model at the duct exit plotted against patch width

Figure 6.9 shows that the size of the patch directly affects the liner insertion loss, thereby affecting the liner performance. The liner insertion loss decreases with the size of the hard patch. However, the effects of larger patches on the liner performance seem to be less significant which may be because of the limitations of Cargill model to predict the acoustic effects of larger patches as it is based on Kirchhoff's approximation. The accuracy of the results shown in figure 6.9, will be tested in the next chapter when the predictions will be compared to ACTRAN/TM.

Figure 6.9 shows that non-linear effects degrade the liner insertion loss quite significantly. For an incident pressure amplitude of 180dB at the fan plane, the liner insertion loss decreases by about 15dB compared to the linear predictions. This indicates that the non-linear effects become more important as the SPL of the rotor-locked incident mode (24,1) at the duct wall close to the fan increases, as discussed in chapter 3.

6.5 Conclusions

The Cargill asymptotic model, with or without a non-linear adjustment, provides an efficient and fast tool for predicting the scattered field due to a hard patch in a zero-splice liner. The above statement is subject to validation that Kirchhoffs approximation, on which the code is based, is indeed accurate for these problems, and especially for larger patch sizes. It is therefore important to validate the results obtained from Cargill code with an efficient CAA tool like ACTRAN/TM, which is done in the next chapter.

Subject to this proviso, the results presented in section 6.3.3 throw some light on the effects of hard patches on the acoustics of a lined intake. They indicate that the size of the patch affects scattering and thus the effectiveness of the liner. Moreover, as one

might expect, the proximity of the patch to the fan plane increases the power of the scattered modes and hence reduces the effectiveness of the liner.

Finally in section 6.4, a methodology to implement non-linear adjustments to the Cargill predictions was discussed. The results clearly indicate that non-linear effects cannot be neglected at high source amplitudes of the rotor-locked mode.

Chapter 7

Liner damage study - computational models

7.1 Introduction

In the previous chapter, an analytical asymptotic model Cargill code was used to perform a preliminary study to assess the acoustic effect of damage in a zero-splice liner. The model provided an efficient and a rapid method for predicting the scattered field in the presence of liner patches. While the solutions were obtained relatively quickly as compared to a full numerical analysis, the use of 'Cargill' method means that the internal duct geometry has to be represented as a uniform cylindrical duct with a uniform mean flow. Moreover, the Cargill model is derived by assuming that the patch (or splice) width is small compared to a characteristic acoustic wavelength.

The objective of the current study is to simulate the acoustic effects of damage and repair to a zero-splice liner in a realistic intake geometry by using a computational model. The effects of the extent and the location of the damage on the overall performance of the liner is assessed. In addition to in-duct analysis, the acoustic effects of liner damage on far-field noise attenuation is also investigated. Initially, a numerical study is presented for a uniform cylindrical intake and the results are compared to the asymptotic Cargill solutions. The computational analysis is then applied to geometries representing a realistic intake with non-uniform mean flow, and the results obtained from different intake models are compared with each other.

At supersonic fan-tip speed, a method to account for non-linear propagation effects by using the analytical model described in chapter 5 is proposed and is applied to the linear numerical solutions.

7.2 Intake Models

Three intake models of increasing geometrical complexity are used to represent the axi-symmetric intake. These are shown figures 7.1(a), 7.1(b) and 7.1(c). The fan radius a and the extent of the acoustic liner have been referred from the previous chapter.

In case of model 1, the intake is represented by a uniform cylindrical duct of radius a, with a uniform mean flow of Mach number M_x. In model 2, the intake is represented by a non-uniform duct of a more realistic internal geometry and includes a spinner. Beyond the highlight of the intake, the acoustic domain of model 2 is represented by a uniform cylindrical hard-wall extension. Anechoic boundary conditions are assumed at the exit plane in both the methods. Both these models is used to perform in-duct analysis. In model 3, the full internal and external geometry of the nacelle is modeled to study the far-field acoustic radiation. In case of models 2 and 3, the mean flow within the intake is non-uniform and is calculated independently by using a compressible mean flow solver. Like the previous chapter, liner damage is again modelled by an acoustically 'hard' patch of square shape.

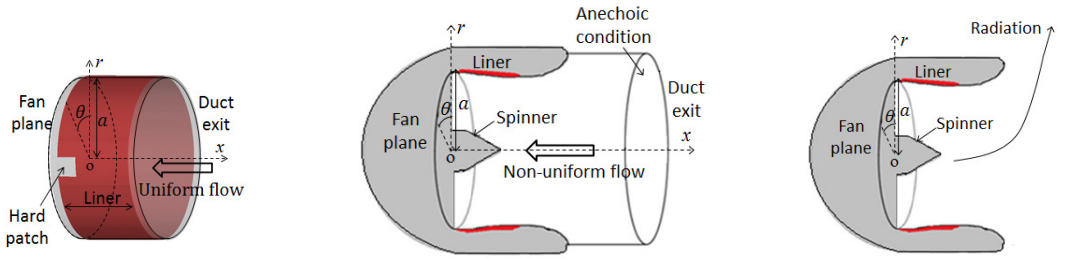

(a) Model 1 (b) Model 2 (c) Model 3

FIGURE 7.1: Intake models

7.3 The Computational model

The CAA code ACTRAN/TM is used to model the effects of the hard patch. A three dimensional (3D) model of the intake is needed in order to represent scattering from a liner patch. The FE mesh for the intake models are generated by using Gmsh [98], a 3D FE grid generator with a build-in CAD engine and post-processor. By using key geometric data in coordinate form, the intake geometry is created by using B-spline interpolation. The resulting 3D domain is then meshed by using Gmsh and the resulting FE model is imported into ACTRAN/TM. Quadratic tetrahedral or pentahedral elements are used.

(a) Uniformly lined

(b) Lined with a hard patch

FIGURE 7.2: Liner configurations used in the study

7.4 ACTRAN predictions for intake model 1

The acoustic effect of the hard patch on liner performance is assessed by comparing the transmitted sound power with and without the patch. Figures 7.2(a) and 7.2(b) show the two configurations for model 1; the first represents a uniformly lined case and the second a lined intake with a square hard patch.

The engine condition and the liner impedance is the same as that used in the previous chapter (Case 2 in table 6.1). Typically, the engine condition corresponds to the 'cutback' or 'sideline' noise certification points for a large turbofan engine. The incident field again consists of the rotor-locked mode (24,1) injected at the fan plane with a unit intensity.

Figures 7.3(a) and 7.3(b) show the two different meshes generated for the ACTRAN calculations. Figure 7.3(a) shows a fully-unstructured mesh generated throughout the entire duct volume by using tetrahedral elements. Figure 7.3(b) shows a mesh generated by extruding a transverse unstructured cross-sectional mesh in the axial direction (x). The extruded mesh consists of pentahedral (prismatic) elements. Both meshes have a resolution of 4 quadratic elements per wavelength. An axi-symmetric unstructured mesh of the same resolution was also generated and will be used to validate the results obtained from the 3D meshes for the uniformly lined configuration. This is shown in figure 7.4

7.4.1 Results for the uniformly lined case

Results are presented as axial plots of computed Sound Pressure Level (SPL) on the duct wall. Figures 7.5(a) and 7.5(b) show the SPL on the duct wall at four azimuthal angles at 0^o, 90^o, 180^o and 270^o. Results are shown for the unstructured mesh and the extruded mesh respectively. The results for the ACTRAN/TM axi-symmetric model (figure 7.4) are also shown. Figures 7.5(a) and 7.5(b) show that the acoustic pressure

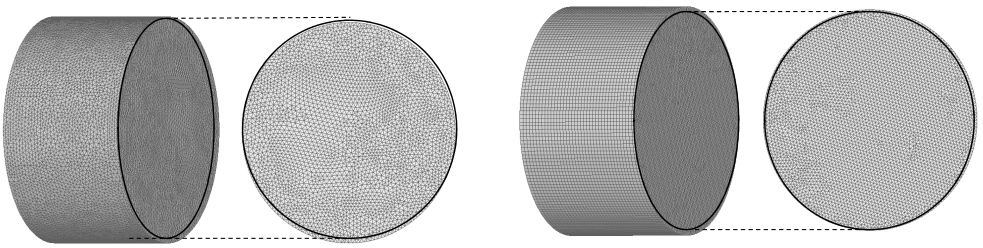

(a) Unstructured mesh (b) Extruded mesh

FIGURE 7.3: 3D meshes used for ACTRAN calculations (mesh resolution: 4 quadratic elements per wavelength)

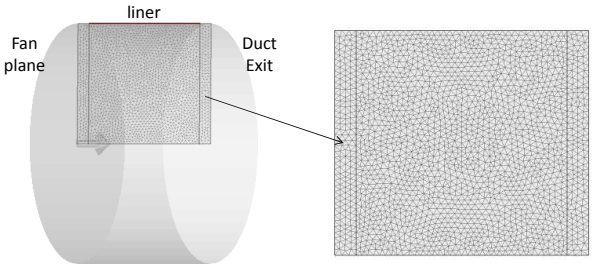

FIGURE 7.4: Axi-symmetric mesh to simulate the uniformly lined case

decays linearly along the duct in the lined section as expected. The incident mode, which is just cut-on, is heavily attenuated by the liner and the acoustic pressure at the wall drops approximately by 53dB over the length of the liner.

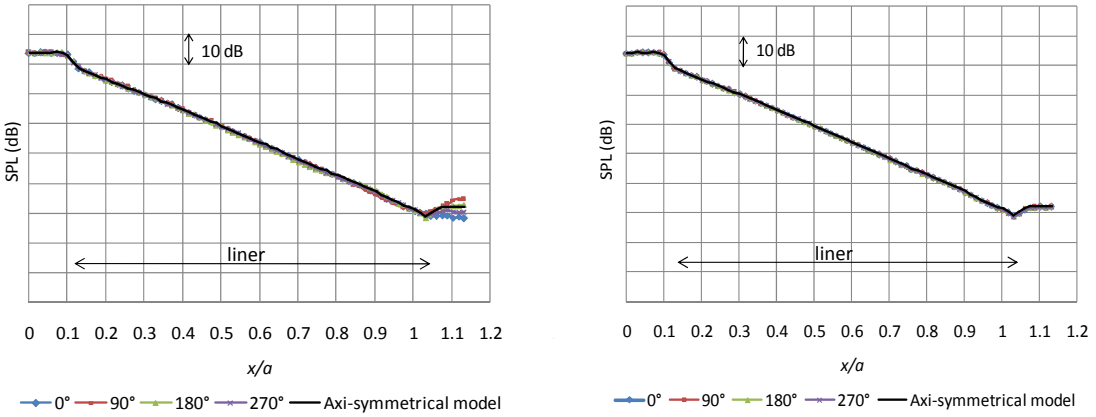

(a) ACTRAN results for unstructured mesh (b) ACTRAN results for extruded mesh

FIGURE 7.5: SPL on the duct wall along the duct axis for the uniformly lined case

The axi-symmetric solution is regarded as a reference solution since any mesh effects due to the transverse mesh are absent in the axi-symmetric problem. In figure 7.5(a),

there is some scatter in the predicted SPL at the four azimuthal locations near the duct exit. However, for the extruded mesh (figure 7.5(b)), good convergence is obtained and the results are in agreement with the axi-symmetric model. The reason for the discrepancy lies in the greater numerical 'scattering' which occurs in the fully unstructured mesh. This is evident in figures 7.6, 7.7 and 7.8.

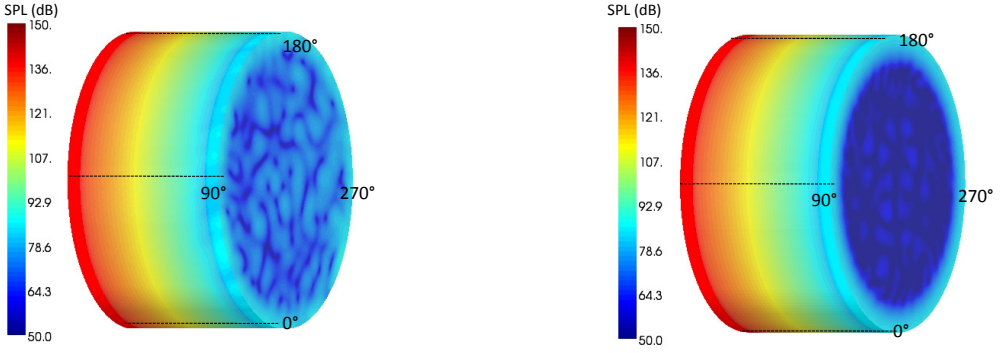

(a) ACTRAN results for unstructured mesh

(b) ACTRAN results for extruded mesh

FIGURE 7.6: Contour plot of SPL on the surface of the duct for the uniformly lined case

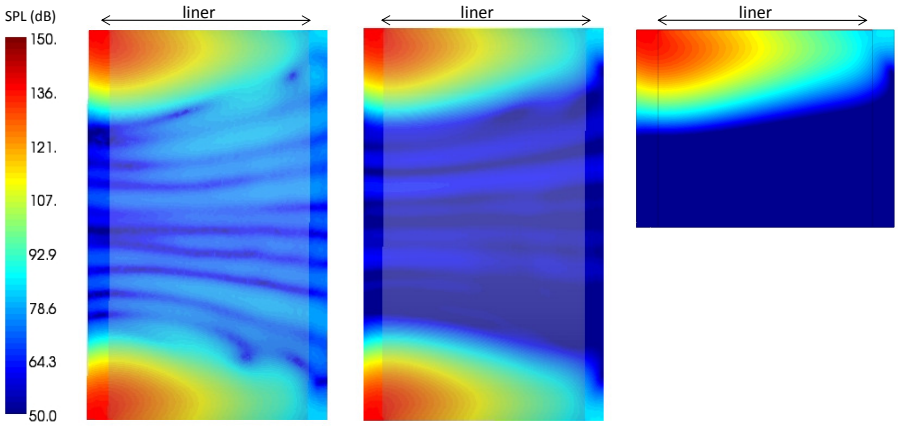

FIGURE 7.7: Contour plot of SPL along the $x-y$ plane for the uniformly lined case obtained by using the unstructured mesh (left), extruded mesh (middle) and the axi-symmetric mesh (right)

Figures 7.6 and 7.7 show contours of SPL on the surface of the model, and on a cross-section through the axis. The contours should be azimuthally symmetric but transverse scattering by the mesh is evident on the exit plane in figure 7.6, and inside the duct in figure 7.7. This effect is reduced when the extruded mesh is used, which is structured in the axial direction. As noted before, no numerical scattering is produced by the axi-symmetric mesh.

Scattered modal intensities at the exit plane are shown in figure 7.8. Here, the results obtained by using a lower mesh resolution of 3 quadratic elements per wavelength are also included, for both the unstructured mesh and the extruded mesh. Since the geometry and the liner are azimuthally symmetric, all scattering into modes other than m=24 is spurious and due to the mesh. The drop in the level of the scattered field as the mesh is refined is evident, as is the benefit of using the extruded mesh.

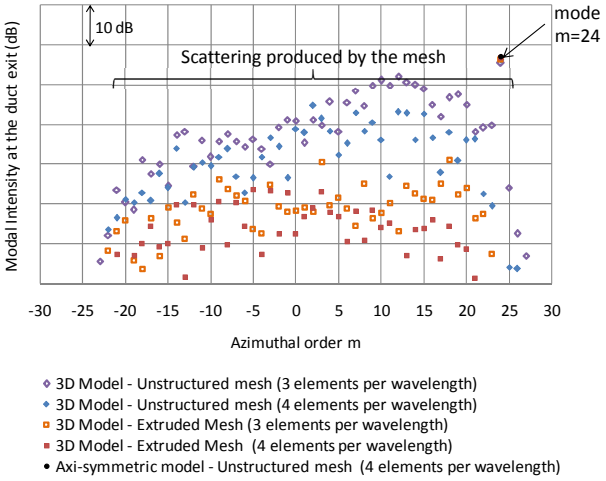

FIGURE 7.8: Modal intensity (in dB) at the duct exit

The level of the mesh scattered modes provides a numerical 'noise floor' when applying this type of model to cases where large axial attenuation by the liner is present. Returning to figure 7.5(b), it is clear that the spurious mesh scattering does not contaminate the solution at the end of the liner when the extruded mesh is used. However, this is not the case for the fully unstructured mesh (figure 7.5(a)). In assessing the effect of the patch, both meshes will be used. The attenuation will be significantly lower for the case with a hard patch and convergence to a common value will be evident when using the unstructured and the extruded meshes except for very small patches. This provides a measure of the adequacy of the resolution of both meshes.

7.4.2 Results for a lined intake with a hard patch

Figures 7.9(a) and 7.9(b) show the variation of SPL on the duct wall along the duct axis at four azimuthal angles at every 90^o for the lined configuration with a square hard patch of width 1.6% and 3.8% of the duct circumference respectively. For a large turbofan engine with a fan diameter approaching 3m, these are equivalent to square patches of width approximately 15cm and 36cm respectively. The hard patch is located at the 90^o azimuthal location at the start of the liner, as shown in figure 7.2(b). Figures 7.9(a) and 7.9(b) show that the SPL at the duct exit increases in the presence

of the hard patch when compared to the uniformly lined configuration. However, there is a considerable variation with azimuthal location. For example, the SPL at the duct exit at 90^o is much lower compared to the other azimuthal locations. The SPL on the patch itself increases, as one would expect, since the acoustic pressure is not attenuated locally on the patch which is acoustically 'hard'.

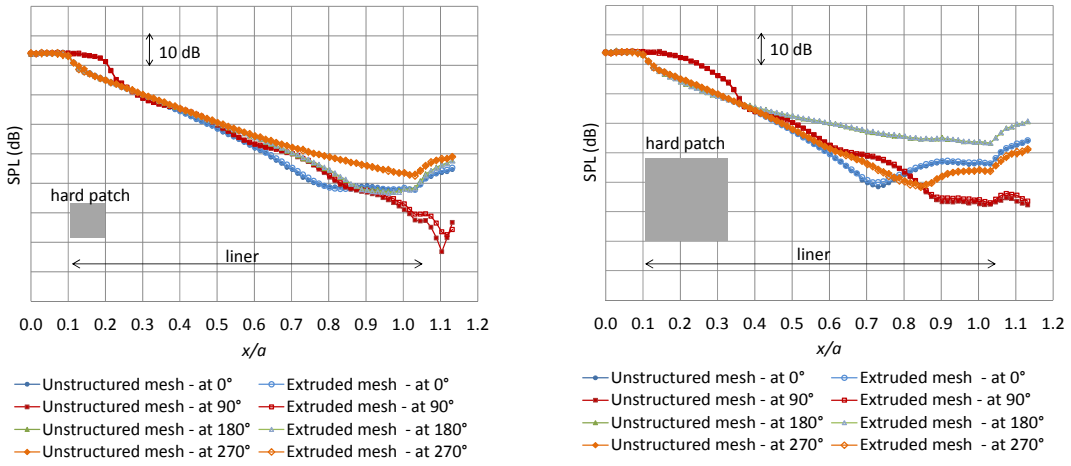

(a) patch width 1.6% of the duct circumference

(b) patch width 3.8% of the duct circumference

FIGURE 7.9: SPL on the duct wall along the duct axis; hard patch located at 90^o azimuthal location at the start of the acoustic liner

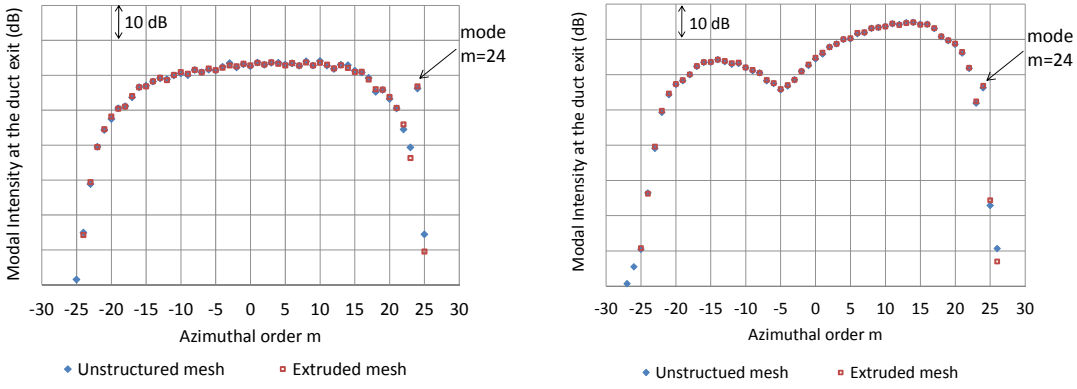

(a) patch width 1.6% of the duct circumference

(b) patch width 3.8% of the duct circumference

FIGURE 7.10: Modal intensity (in dB) at the exit plane for a lined intake with a hard patch

Figures 7.10(a) and 7.10(b) show the modal intensities at the duct exit for the two patch sizes of figures 7.9(a) and 7.9(b). In this case and in contrast to the uniformly lined case of figure 7.8, the incident mode (24,1) is legitimately scattered into other azimuthal orders due to the presence of the patch. The modal intensities in the scattered modes increases with patch size and exceed the power of the incident (24,1) mode, thereby increasing the total transmitted power at the duct exit.

Figures 7.9 and 7.10 confirm that the results obtained by using the unstructured mesh and the extruded mesh yield results which are in good agreement. This indicates that for these hard patches, the numerical scattering produced by the mesh has an insignificant effect on the results. That is to say, the numerical 'noise floor' is well below the solution generated by the 'patch-scattered' tones.

7.4.2.1 The effect of patch size on noise attenuation

Figure 7.11 shows the contour plot of SPL on the surface of the duct and the exit plane for a sequence of patch sizes ranging from very small (<1% of duct circumference) to very large (approaching 9% of duct circumference). The patch is located at the start of the liner. Figure 7.11 indicates that the acoustic pressure is hardly attenuated on the hard patch itself. It also indicates that a larger patch produces greater modal scattering, thereby degrading liner performance. The SPL contours at the exit plane indicate that the scattering of the rotor-locked (24,1) mode produces a significant azimuthal directivity.

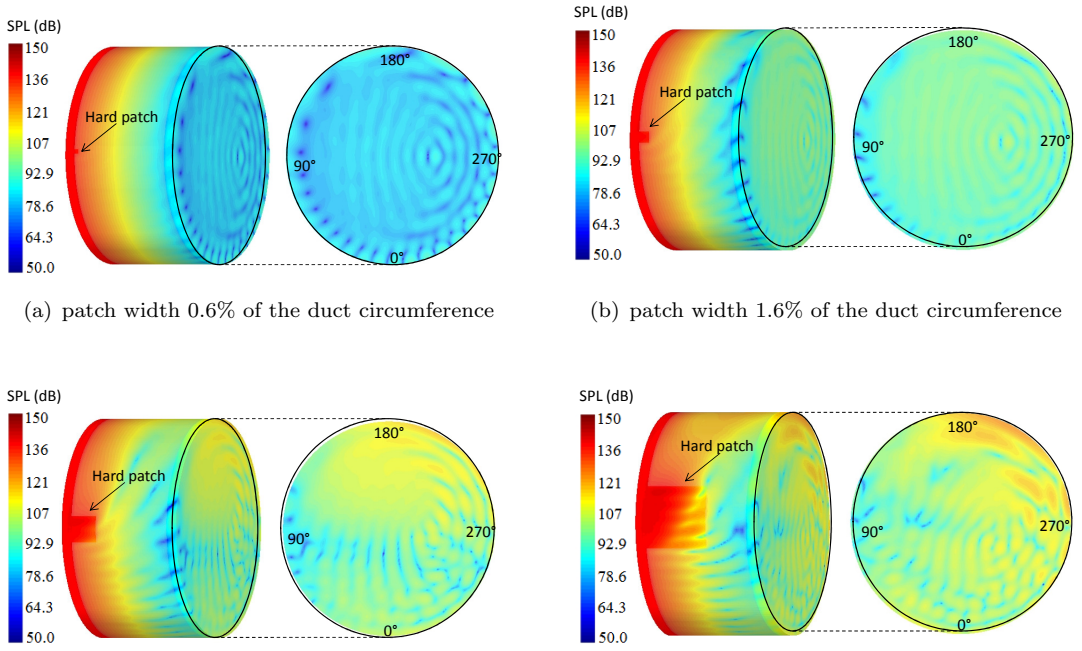

(a) patch width 0.6% of the duct circumference

(b) patch width 1.6% of the duct circumference

(c) patch width 3.8% of the duct circumference

(d) patch width 8.9% of the duct circumference

FIGURE 7.11: Contour plot of SPL on the duct surface and on the exit plane for a lined configuration with a square hard patch of different sizes located at the start of the liner

In figure 7.12, the relative sound power level (PWL) at the duct exit is plotted against patch width. The reference in this case is the hard-wall configuration. The width of the square hard patch is represented as a percentage of the duct circumference (figure 7.12(a)) and as a percentage of circumferential wavelength of the rotor-locked

(24,1) mode (figure 7.12(b)). A patch width of zero corresponds to the uniformly lined configuration. The data from the ACTRAN/TM axi-symmetric model corresponding to this case is included for completeness. The figure shows good agreement between the results obtained for the unstructured mesh and the extruded mesh to predict the patch effect. The PWL increases rapidly for patch widths less than 2% of the duct circumference (or patch widths less than 50% of the circumferential wavelength of the incident mode). When the patch size is increased further, the increase in PWL becomes less rapid.

The relative PWL would continue to increase if the patch width is increased further beyond our considered limit of 9% of the duct circumference as the total area of the acoustic liner would decrease. The relative PWL would eventually reach 'zero value' when the width of the patch is 100% of the duct circumference as this would correspond to a configuration with no acoustic liner.

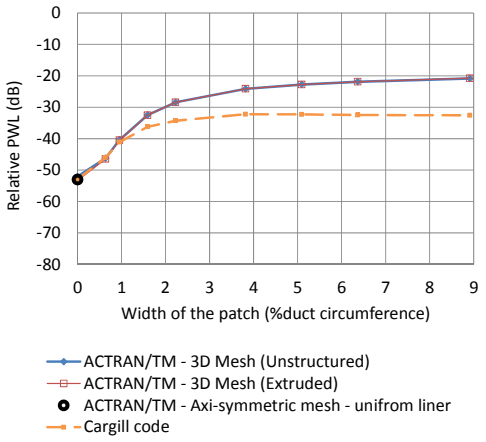

(a) patch width in terms of percentage of the duct circumference

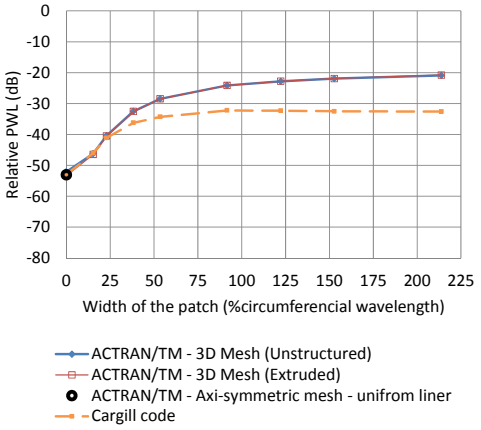

(b) patch width in terms of percentage of the circumferential wavelength

FIGURE 7.12: Relative PWL (in dB) at the duct exit for a lined intake with a hard patch located at the start of the liner

7.4.2.2 Comparison to asymptotic solutions

In figure 7.12, the computed results are also compared to the Cargill predictions. The agreement between ACTRAN/TM and the Cargill prediction is good for patch widths smaller than 1% of the duct circumference (25% of the circumferential wavelength of the incident mode). However, the Cargill formulation under predicts the effect of larger patches. This is consistent with the Kirchhoff approximation upon which the Cargill formulation is based which assumes that the width of the patch/splice is small compared to the duct circumference and to the circumferential wavelength of incident

mode. These data indicate that Cargill prediction can be applied with confidence only to very small patches.

7.4.2.3 The effect of patch location on noise attenuation

Figure 7.13 shows a contour plot of SPL on the duct surface and the exit plane for two different patch locations. A patch width of 3.8% of the duct circumference is used. In figure 7.13(a), the patch is located at one quarter of the distance along the liner and in figure 7.13(b) it is located at the mid-point.

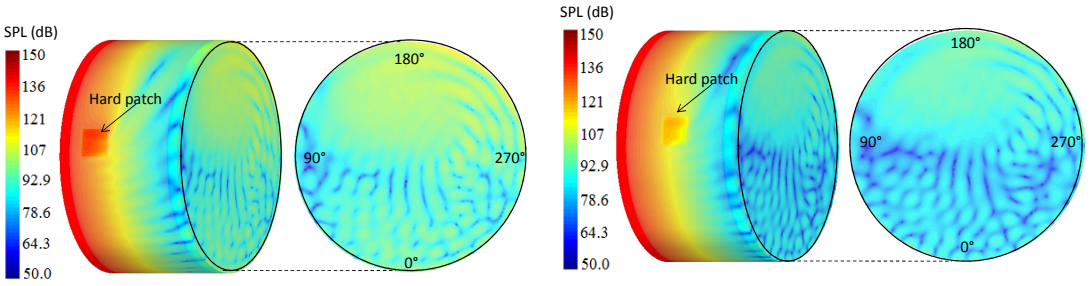

(a) 1/4th liner (b) 1/2 liner

FIGURE 7.13: Contour plot of SPL on the duct surface and on the exit plane for different locations of a square hard patch of width 3.8% of the duct circumference

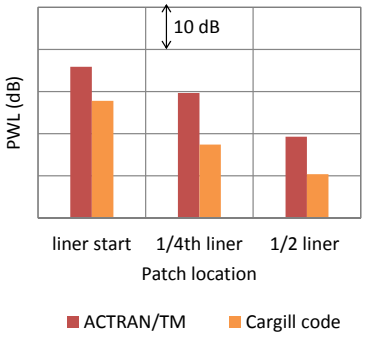

FIGURE 7.14: PWL at the duct exit for different locations of a hard patch of width 3.8% of the duct circumference

Figure 7.14 shows PWL at the duct exit for different patch locations and the results are compared to those obtained from the Cargill analysis. The effect of the patch on noise attenuation is most pronounced when the patch is located at the start of the liner. The width of the patch is greater than 1% of the duct circumference, and the agreement with the Cargill prediction is again quite poor at all patch locations.

7.4.2.4 Non-linear adjustments to the ACTRAN predictions

The results presented in previous sections were obtained by assuming linear propagation. Equations 3.43 and 3.44 are used as the basis for non-linear adjustments to the linear predictions obtained by ACTRAN/TM. The same assumption stated in section 6.4 is considered in this study.

The absorptive term σ in equation 3.44 is determined from the linear attenuation rate of the rotor-locked incident mode (24,1) predicted by the ACTRAN/TM axi-symmetric model.

Figure 7.15(a) shows the axial plot of SPL of the rotor-locked incident mode (24,1) at the duct wall predicted by the analytical model. The numerators in the expressions on the right-hand side of equations 3.43 and 3.44 correspond to the linear solutions, and are also included in figure 7.15(a). Solid lines therefore correspond to the hard-wall case with and without non-linear adjustments. Broken lines correspond to the uniformly lined case with and without non-linear effects.

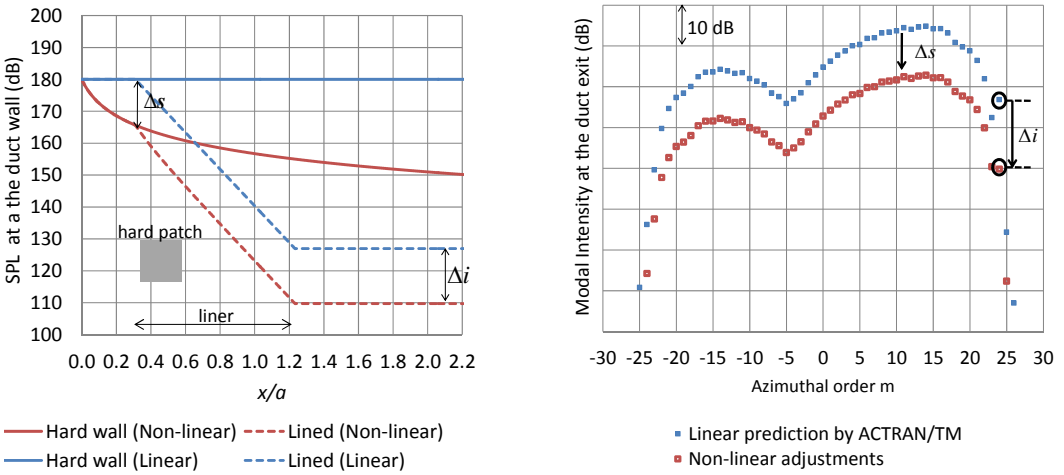

(a) SPL of (24,1) mode at the duct wall along the axis predicted by the analytical model

(b) Non-linear corrections applied to the ACTRAN/TM predictions of patch scattering

FIGURE 7.15: Methodology to apply non-linear adjustments to the linear prediction by ACTRAN/TM for intake model 1 by using the results obtained by the analytical non-linear propagation model

These results are used to adjust the linear predictions of patch scattering by ACTRAN/TM. This is illustrated in figure 7.15(b). It is assumed that the non-linear corrections in SPL values at the duct wall predicted by the analytical model can be applied directly to correct the modal intensity values predicted by ACTRAN/TM. The modal intensities of the scattered modes at the exit plane are therefore adjusted by an amount Δs equal to the difference in SPL of the incident mode between the linear and non-linear predictions calculated at the start of the patch. This is based on the

assumption that scattering occurs at the start of the hard patch. It is then assumed that the non-linear attenuation of the BPF tone over the rest of the liner is the same as for the uniformly lined case, and that the 'patch scattered' modes are not affected by non-linear effects. Figure 7.15(a) shows that the linear theory over predicts the wall pressure amplitude of the incident mode (24,1) at the duct exit by an amount Δi. Therefore, the modal intensity of the incident mode at the exit plane predicted by ACTRAN/TM is adjusted by the amount Δi as shown in figure 7.15(b). By using the corrected modal intensities of the azimuthal modes, the actual PWL at the exit plane is computed. In order to predict the non-linear effects, the actual locations of the liner and the highlight have been referred from that of the realistic intake geometry (model 2), used in the next section.

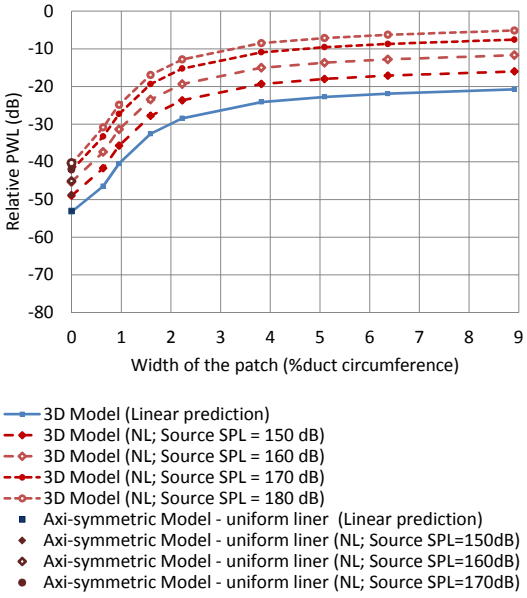

FIGURE 7.16: Non-linear adjustments applied to the results obtained by ACTRAN/TM to investigate the patch effect

Figure 7.16 shows the effect of including a non-linear adjustment to the linear solutions obtained from ACTRAN/TM and presented in figure 7.12. A patch location at the start of the liner is considered as it has the worst effect on noise attenuation. By using the methodology and the assumptions stated above, the corrected PWL at the duct exit for different patch sizes are obtained. The results are plotted for a range of incident pressure amplitudes varying from 150dB to 180dB. The reference value for the relative PWL is once again the hard-walled case but including the adjustment for non-linear attenuation. The plots show that non-linear effects degrade the liner insertion loss as the relative PWL increases. For an incident pressure amplitude of 180dB at the fan plane, non-linear attenuation increases the relative PWL by about 15dB compared to the linear predictions. However, the difference in PWL for a given

patch size relative to the uniformly lined configuration remains almost constant for different incident pressure amplitudes.

7.5 ACTRAN predictions for intake model 2

Intake model 2 (shown in figure 7.17(a)) is a more detailed representation of a realistic intake geometry with non-uniform mean flow profile inside the duct (figure 7.17(b)). The mean flow is computed using a compressible Euler flow solver by prescribing constant axial velocity at the fan plane ($M_x = 0.45$) and a parallel flow at the duct exit.

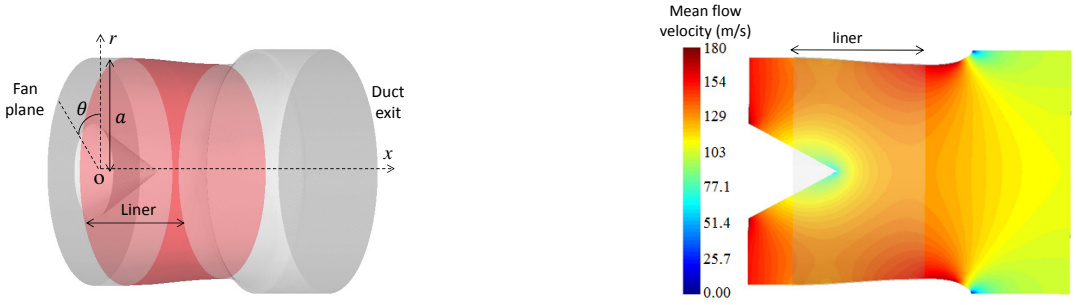

(a) Intake model

(b) Cross-sectional view of mean flow

FIGURE 7.17: Intake model 2 with a cross-sectional view of the mean flow profile inside the duct

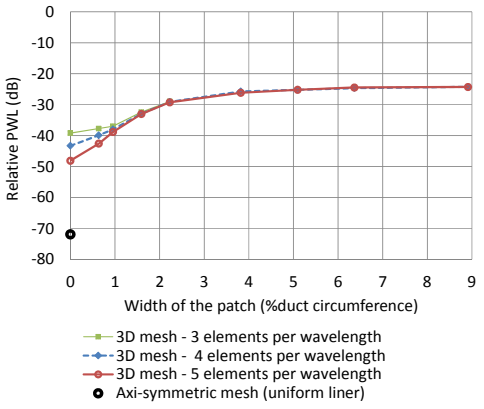

(a) Unstructured FE mesh

(b) ACTRAN/TM results for different mesh resolutions

FIGURE 7.18: Unstructured FE mesh over the intake model and ACTRAN/TM results for different mesh resolutions

The extruded mesh used in the case of intake model 1 is difficult to generate when dealing with the duct geometry of model 2. However, it is clear from results predicted in the previous section that ACTRAN/TM predictions obtained from the extruded and

the fully-unstructured meshes are in good agreement when predicting the patch effect, except for very small patches where the attenuation is large (>50dB say) in which case the numerical 'noise floor' intrudes into the true solution. For patch sizes of practical interest however, the unstructured mesh can be used with confidence. Figure 7.18(a) shows an unstructured FE mesh with a resolution of 5 quadratic elements per wavelength which has been used in an ACTRAN/TM computation of model 2. Results obtained from this mesh for different patch sizes are compared to those obtained by coarser meshes in figure 7.18(b) and convergence is observed, as anticipated, for patch widths above 1% of the duct circumference.

7.5.1 Results

7.5.1.1 The effect of patch size on noise attenuation

The source, liner impedance and engine condition are the same as were used for intake model 1. Figure 7.19 shows the contour plot of SPL on the surface of the duct and on the exit plane for two different patch sizes with the patch located at the 90^o azimuthal location at the start of the liner. The SPL at the exit plane has a similar azimuthal directivity as observed for intake model 1 (figure 7.11). The acoustic wave shifts in a direction diametrically opposite to the patch (270^o azimuthal location) for the smaller patch. For the larger patch however, the acoustic power seems to be maximum in the quadrant between 180^o and 270^o.

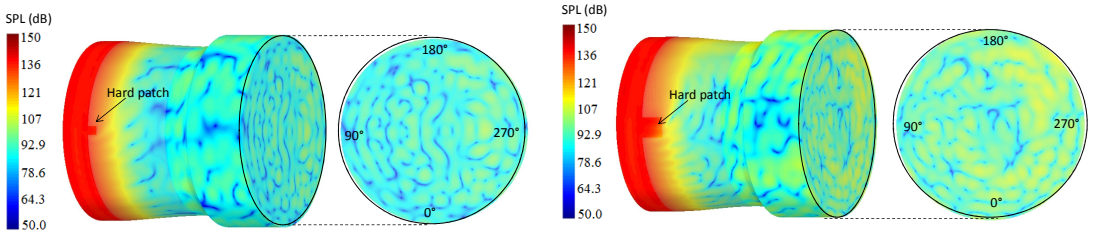

(a) patch width 1.6% of the duct circumference (b) patch width 3.8% of the duct circumference

FIGURE 7.19: Contour plot of SPL on the duct surface and on the exit plane for a lined configuration with a hard patch of different sizes, located at the start of the liner

Figure 7.20 shows plots of relative PWL at the duct exit plotted against the width of the hard patch as a percentage of the duct circumference. A patch width of zero corresponds to the uniformly lined configuration for which the predictions from an axi-symmetric model are included. The results obtained for model 2 are compared to those from model 1. For the uniformly lined case, the liner attenuation of the incident mode predicted by the axi-symmetric model is 71dB in model 2. This cannot be resolved by the ACTRAN/TM 3D model which again has a numerical 'noise floor' at about 50dB

below the incident field. In practice, such large attenuations are largely of academic interest since they are unlikely to be realized due to the presence of other noise sources such as the interaction and distortion tones. In the presence of a hard patch of widths greater than 1% of duct circumference, the relative PWL for the patches lie within the region where numerical results are not contaminated by mesh scattering. Predictions for both the intake models follow a very similar trend. Neglecting the values predicted for patch widths smaller than 1% of the duct circumference where results may be contaminated by numerical scattering, the patch effect predicted for intake model 2 is somewhat less than that for model 1, by up to 5dB for very large patches. This indicates that the effect of a hard patch may be less pronounced when a realistic intake geometry is used in the prediction.

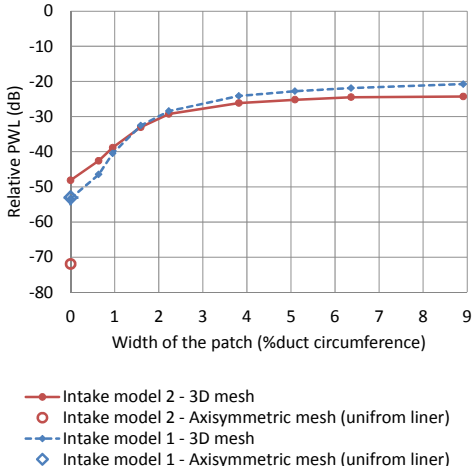

FIGURE 7.20: Relative PWL (in dB) at duct exit for a lined intake with a hard patch located at the start of the liner

7.5.1.2 The effect of patch location

In figure 7.21(a), a contour plot of SPL is shown on the duct surface and on the exit plane when the patch is located at one quarter of the distance along the liner. The patch width is 3.8% of the duct circumference. In figure 7.21(b), a plot of PWL at the duct exit is shown for different patch locations and the results are compared with that of intake model 1. The ACTRAN results obtained by using both the intake models show a similar trend, with the PWL being highest when the patch is located at the start of the liner.

7.5.1.3 Non-linear adjustments to ACTRAN results

Figure 7.22 shows the effect of applying the non-linear adjustment to the linear solutions obtained for the more realistic geometry, that is model 2. The patch is located at

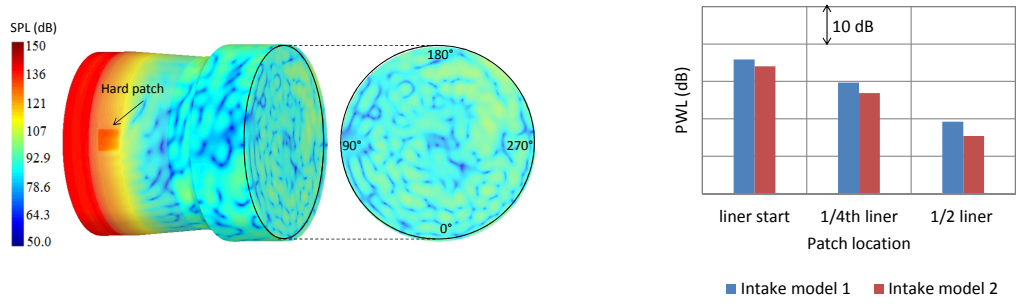

(a) SPL contours for patch location at 1/4th of the liner

(b) PWL at duct exit for different patch locations

FIGURE 7.21: Effect of patch location on noise attenuation

the start of the liner. For the current intake model, the linear attenuation rate σ of the rotor-locked incident mode (24,1) is determined by the corresponding ACTRAN/TM axi-symmetric model.

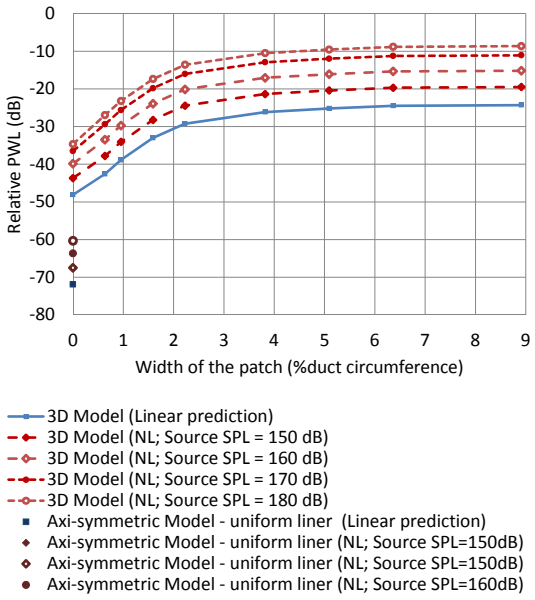

FIGURE 7.22: Non-linear adjustments applied to the results obtained by ACTRAN/TM to investigate the patch effect in intake model 2

Figure 7.22 shows that as in model 1, non-linearity accentuates the effect of the patch and that at supersonic fan-tip speeds, non-linear effects cannot be neglected. The relative increase in PWL at duct exit for different incident pressure amplitudes is similar to that predicted for intake model 1 (figure 7.16). This is not entirely surprising since the non-linear adjustment applied to ACTRAN/TM results for a patch located at the start of the liner is strongly influenced by non-linear attenuation of the incident

mode in the hard-wall section just upstream of the fan, which is the same for both the intake models.

7.6 Prediction of far-field SPL directivity by using intake model 3

The acoustic impact of hard patches on far-field noise attenuation is investigated in this section. Prediction of the far-field noise radiation by using a full 3D model of the intake including the exterior domain involves enormous computational cost and is impractical at the frequency of interest. An alternate procedure is therefore implemented in this study to predict the far-field noise levels by using equivalent axisymmetric models. This involves the following steps -

I. Predict the modal amplitudes of the transmitted modes $\{B_{mn}\}$ at the duct exit by using the 3D in-duct model (model 2) as shown in figure 7.23(a).

II. Identify the source amplitudes $\{A_{mn}\}$ in an equivalent axisymmetric in-duct model shown in figure 7.23(b) which results in the same modal amplitudes at the duct exit predicted in step I. This needs to be done for each azimuthal mode cut-on at the fan plane.

III. Predict the radiated field for the equivalent source modes by using an axisymmetric model including external domain as shown in figure 7.23(c).

IV. Add the radiated sound pressures of all the azimuthal mode orders at different polar angles in a correlated manner to obtained the total far-field solution.

In order to compute the source modal amplitudes $\{A_{mn}\}$ of the cut-on radial modes for a particular azimuthal mode m by using the axisymmetric intake model shown in figure 7.23(b), the following system of equations need to be solved

$$\{B_{mn}\} = [T]\,\{A_{mn}\} \tag{7.1}$$

or

$$\begin{Bmatrix} B_{m1} \\ B_{m2} \\ . \\ . \\ . \\ B_{mN_1} \end{Bmatrix} = \begin{pmatrix} T_{11} & T_{12} & T_{13} & . & . & . & T_{1N_2} \\ T_{21} & T_{22} & T_{23} & . & . & . & T_{2N_2} \\ . & . & . & . & . & . & . \\ . & . & . & . & . & . & . \\ . & . & . & . & . & . & . \\ T_{N_1 1} & T_{N_1 2} & T_{N_1 3} & . & . & . & T_{N_1 N_2} \end{pmatrix} \begin{Bmatrix} A_{m1} \\ A_{m2} \\ . \\ . \\ . \\ A_{mN_2} \end{Bmatrix}, \tag{7.2}$$

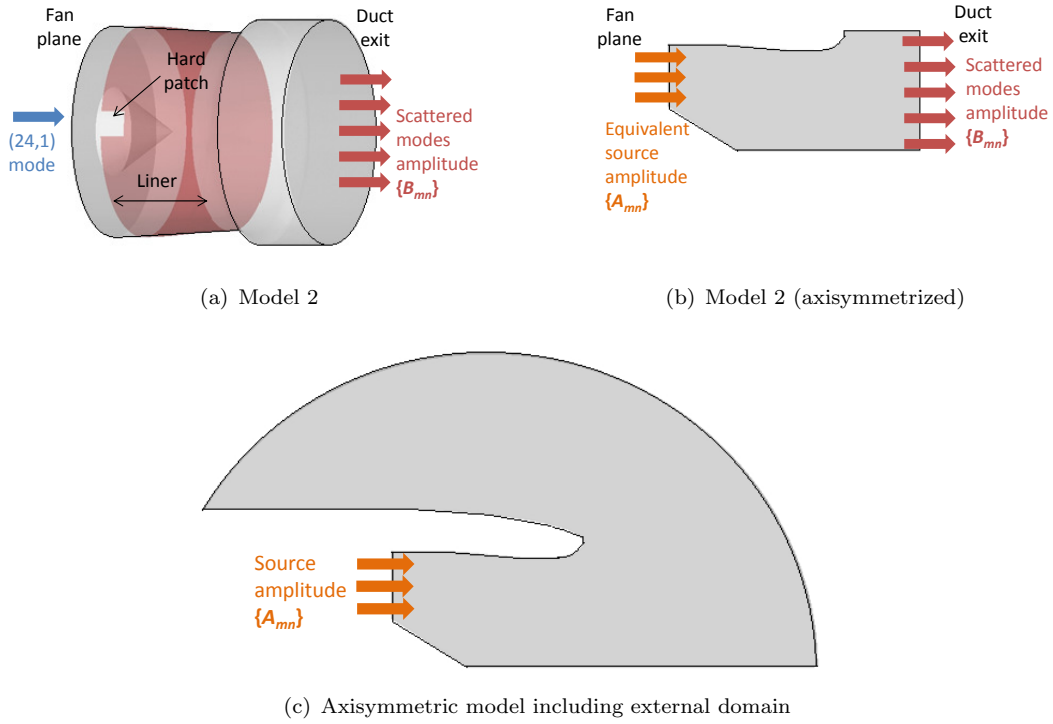

(a) Model 2

(b) Model 2 (axisymmetrized)

(c) Axisymmetric model including external domain

FIGURE 7.23: Methodology to predict far-field SPL directivity for a lined intake with a hard patch

where N_1 and N_2 are the number of radial modes cut-on at the fan plane and the duct exit respectively of intake model 2 for the azimuthal mode m. The modal amplitudes $\{B_{mn}\}$ are known from the predictions obtained by using the 3D in-duct model (model 2). $[T]$ is the transfer matrix in which each term represents the contribution from each source mode independently to the resulting modal amplitudes at the duct exit. For instance, T_{ij} is the modal amplitude of mode (m,i) predicted by using the equivalent axisymmetric model (figure 7.23(b)) by injecting only the mode (m,j) of unit amplitude at the source plane. The matrix $[T]$ can therefore be determined easily.

The transfer matrix $[T]$ is not necessarily a square matrix. Therefore, there are three possible cases -

I. If $N_2 = N_1$, $[T]$ is square matrix and exact solution is obtained

II. If $N_2 > N_1$, the system of equations is over-determined and the solution is obtained by using a least squares technique

III. If $N_2 < N_1$, the system is under-determined and a basic solution is obtained with at most N_2 non-zero components.

These operations are already incorporated in the MATLAB function 'mldivide' [74].

Figures 7.24 and 7.25 show the unstructured mesh and mean flow profile in the FE domain. The mean flow is computed using a compressible Euler flow solver by prescribing constant axial velocity at the fan plane ($M_x^{FAN} = 0.45$) and in the far-field ($M_x^{FF} = 0.25$).

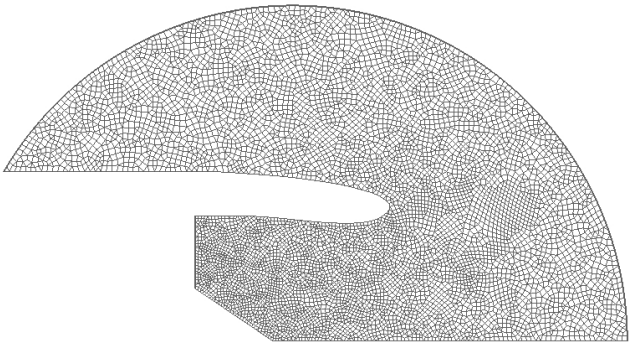

FIGURE 7.24: Unstructured FE mesh

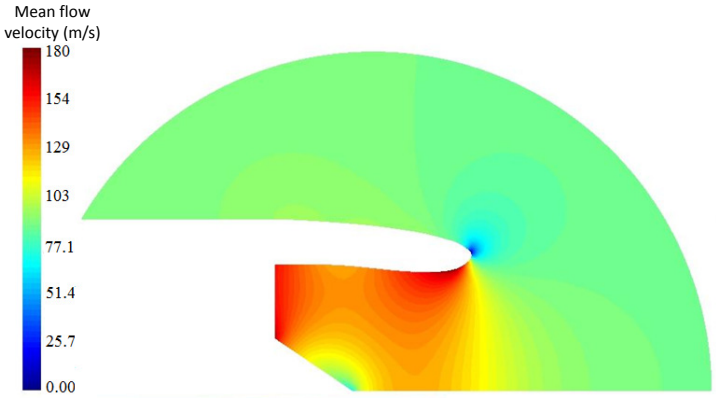

FIGURE 7.25: Mean flow profile in the FE domain

7.6.1 Results

7.6.1.1 The effect of interaction/distortion tones

It was assumed so far that only the rotor-locked mode (24,1) is incident at the fan plane but in practice, the noise source at BPF also consists of the interaction or distortion tones. In this study, these tones are modelled as the multimode component consisting of all the cut-on modes at the fan plane with equal energy in each mode.

Figure 7.26 shows the modal intensity of the different azimuthal modes at the source plane and the duct exit of intake model 2 when the 'equal-energy' multimode source

is incident. The figure illustrates that the attenuation of the multimode component is merely affected even in the presence of a very large hard patch. This shows that a hard patch has insignificant effect on the attenuation of the multimode component. Therefore, in all far-field predictions performed in this study, it is assumed that the presence of the patch does not effect the far-field directivity of the multimode component.

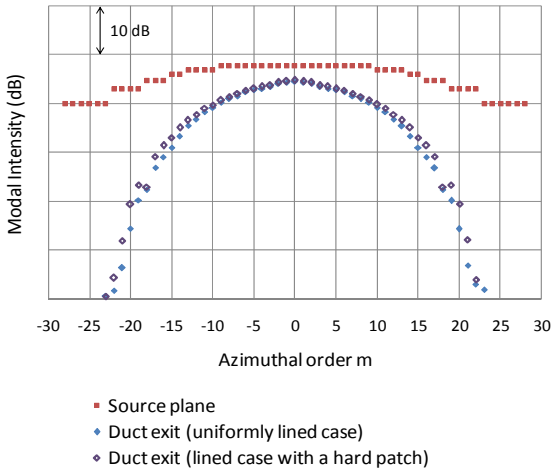

FIGURE 7.26: Effect of the hard patch of width 8.9% of the duct circumference in intake model 2 on the attenuation of the MM component

The far-field SPL directivities at BPF for the two sources - rotor-locked mode and the multimode component are shown separately in figure 7.27. The rotor-locked mode m=24 has a very amplitude at the considered fan speed and therefore it protrudes above the floor set by the multimode component by an amount Δ for the hard walled configuration. The protrusion Δ mainly depends upon the condition at which the fan is operating. The total far-field SPL for the hard walled case is therefore dominated by the multimode component at lower polar angles and by the rotor-locked mode at higher angles. In the presence of the liner, the rotor-locked mode is strongly attenuated but the multimode component is less well attenuated and therefore the total far-field SPL is dominated by the latter.

Figure 7.28 shows the effect of the protrusion of mode (24,1) above the multimode component on the far-field SPL directivity for the lined intake with a hard patch of width 1.6% of the duct circumference. The patch is located at the start of the liner at 90^o azimuthal angle. The far-field directivities are plotted at four azimuthal angles at every 90^o. The results are compared to that of the hard-walled and the uniformly lined intakes. The far-field SPL is the highest at 270^o azimuthal angle which is consistent with the results previously obtained from intakes models 1 and 2. Figure 7.28 clearly indicates that the effect of the hard patch is more pronounced when the protrusion of rotor-locked mode above the multimode component increases.

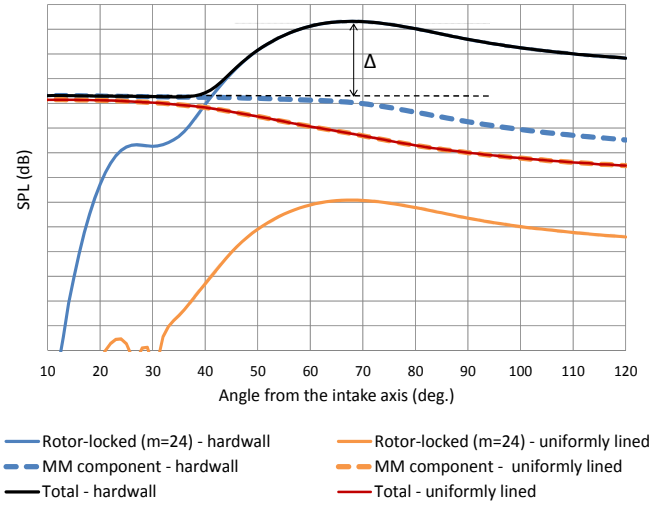

FIGURE 7.27: Predicted far-field SPL directivity of the rotor-locked mode (24,1) and the multimode (MM) component; Δ is the protrusion of mode (24,1) above the floor set by the MM component.

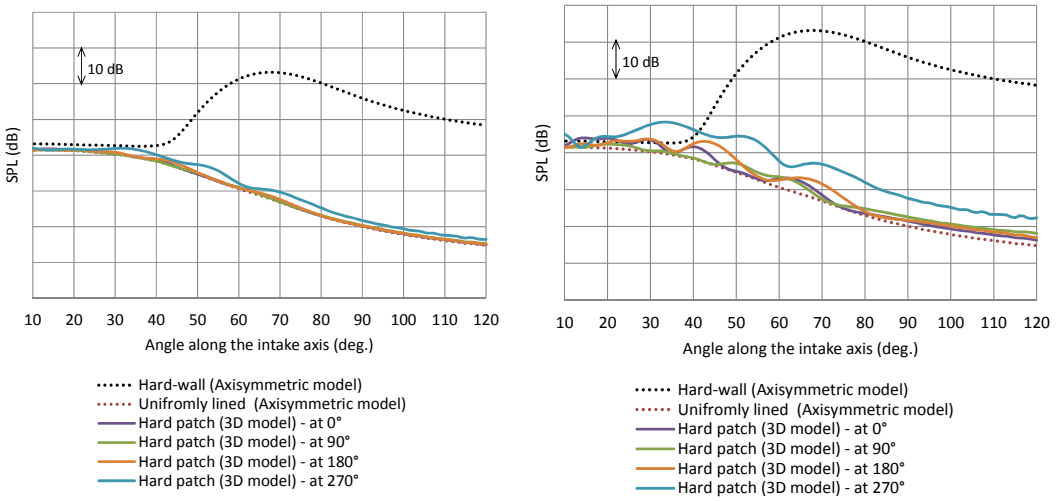

(a) 20dB protrusion

(b) 30dB protrusion

FIGURE 7.28: Effect of the hard patch of width 1.6% of the duct circumference on far-field directivity for different protrusions of the mode (24,1) above the MM component

7.6.1.2 The effect of patch size on far-field directivity

The effect of different patch sizes on the noise radiated into the far-field from the turbofan intake is illustrated in figure 7.29. The patch is again assumed to be located at the start of the liner where its impact is the greatest, and at 90^o azimuthal location. The quantity ΔSPL is the net increase in SPL when compared to the uniformly lined

configuration. Figure 7.29 shows the plot of ΔSPL over the surface of a hemisphere of very large radius in the far-field with its center coinciding with the duct axis.

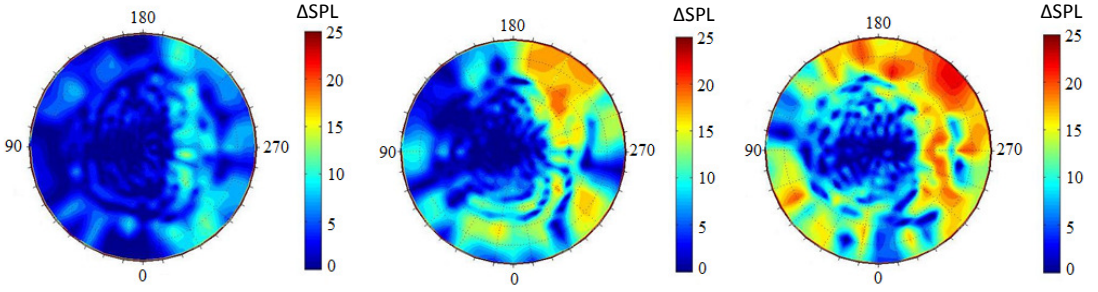

(a) 1.6% width (b) 3.8% width (c) 8.9% width

FIGURE 7.29: Effect of patch width (in terms of % of the duct circumference) on the far-field directivity for 30dB protrusion of mode (24,1)

Figure 7.29 shows that the radiated noise increases with the size of the hard patch, as one would expect. For the smaller patch (1.6% width), the far-field SPL is highest in the direction diametrically opposite to the patch location (90^o azimuthal location). For larger patches, however, the far field SPL is highest between 180^o to 270^o. This far-field directivity pattern is also consistent with the pattern of the SPL contours at duct exit obtained from the simpler intake models (models 1 and 2) but the cause of such noise directivity patterns is still not clear.

7.6.1.3 Non-linear adjustments to the ACTRAN predictions

The methodology which is implemented to apply non-linear adjustments to the linear far-field predictions by ACTRAN/TM is based on the same assumptions as stated in section 6.4. Non-linear effects are again assumed to be dominant only in the rotor locked mode (24,1). Figure 7.30(a) shows the axial plot of SPL of mode (24,1) at the duct wall predicted by the analytical model. The linear attenuation rate σ of the rotor-locked mode (24,1) is the same as that in intake model 2. The solid lines show in figure 7.30(a) are the non-linear predictions for hard walled and uniformly lined intakes and the dotted lines are the corresponding linear predictions.

These results are used to adjust the far-field directivities predicted by ACTRAN/TM. This is illustrated in figure 7.30(b). The non-linear corrections in SPL values at the duct exit predicted by the analytical model is directly applied to correct the levels of the far-field directivities for the different configurations.

Figure 7.31(a) and 7.31(b) show the corrected far-field SPL directivities at 270^o azimuthal location for incident pressure amplitudes of 160dB and 180dB respectively. The corresponding linear predictions are shown in dotted lines. The results are presented for a patch width of 1.6% of the duct circumference located at the start of

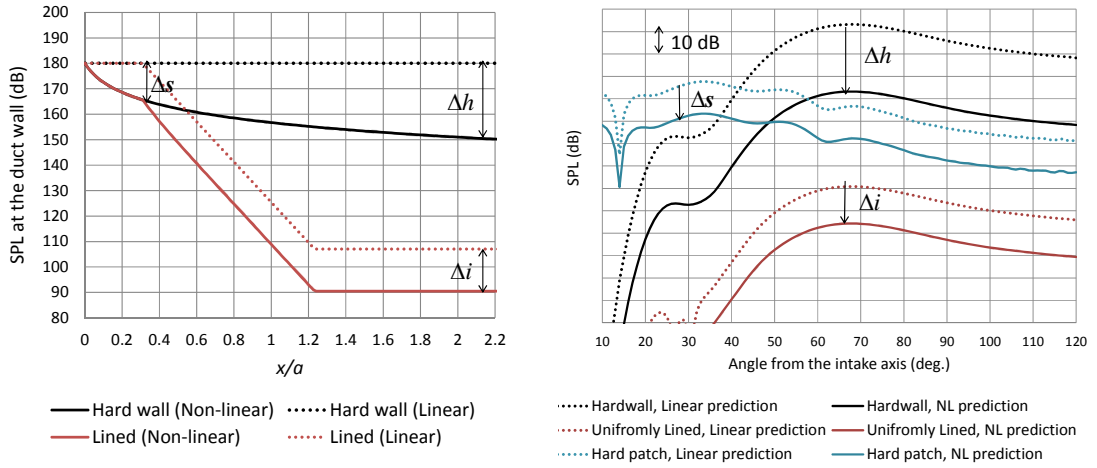

(a) SPL of (24,1) mode at the duct wall along the axis predicted by the analytical model

(b) Non-linear corrections applied to the ACTRAN/TM far-field predictions

FIGURE 7.30: Methodology of applying non-linear adjustments to the far-field prediction by ACTRAN/TM by using the results obtained by the analytical non-linear propagation model

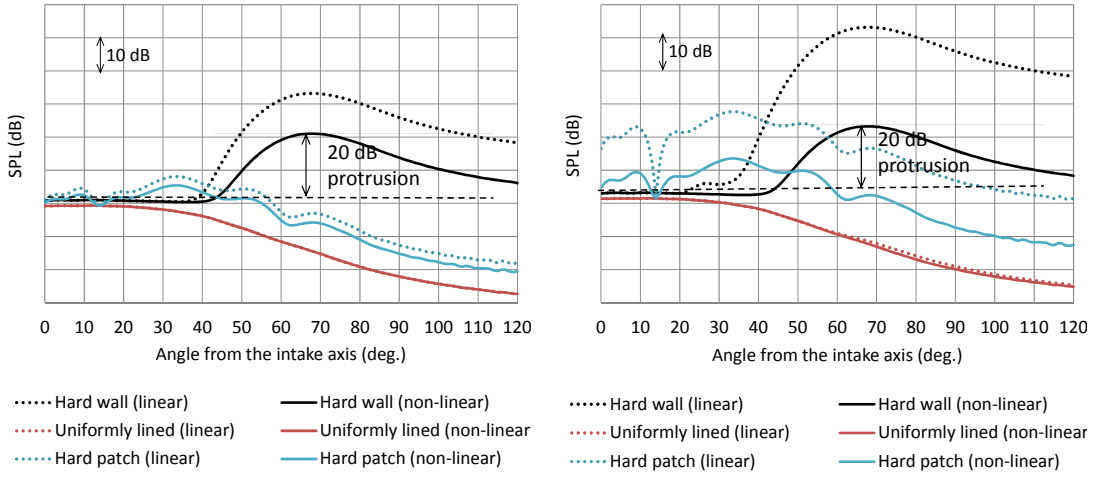

(a) 160dB

(b) 180dB

FIGURE 7.31: Non-linear adjustments applied to the far-field results obtained by ACTRAN/TM at different source levels of rotor-locked mode (24,1)

the liner at 90^o azimuthal location. The protrusion of the rotor-locked mode (24,1) is 20dB and is determined with respect to the non-linear predictions. Comparing Figure 7.31 with figure 7.28, it is clear that the non-linear effects increases the effect of the hard patch on far-field SPL. This effect is more significant at high pressure amplitudes (180dB in the present case).

7.7 Conclusions

In this study, ACTRAN/TM has been used to predict the effects a hard patch on noise attenuation by a zero-splice liner. A uniform cylindrical intake is used initially to demonstrate the acoustic effects of the patch and to compare the results with a semi-analytical asymptotic model. Good agreement is observed between the two prediction tools for patch widths smaller than 1% of the duct circumference, but the asymptotic code under predicts the effect of the larger patches.

The same computational approach is then applied to a realistic intake geometry with non-uniform mean flow. Both in-duct and far-field analysis is performed. The results obtained from different models are consistent with each other. This justifies the conservative use of simpler intake models to study the patch effect on zero-splice liners. The impact of the hard patch is, however, slightly less pronounced when realistic intake geometry and mean flow are taken into consideration.

The interactions or distortion tones have also been included in the noise source along with the rotor locked tones. These are modelled as 'equal energy' multimode component. The results indicate that the attenuation of these tones is merely effected by the hard patch. When the multimode component is also included in the noise source, the effect of the patch is more pronounced when the protrusion of the rotor-locked mode above the multimode component is larger.

The results presented in this study throw light on the effect of the size and the location of hard patches on the acoustics of a lined intake. They indicate, as one might expect, that larger patches have more detrimental effects on the performance of a zero-splice liner. Moreover, the proximity of the patch to the fan plane increases the power of the scattered modes, thereby reducing the effectiveness of the liner.

In this study, non-linear corrections have also been applied to the linear results obtained by ACTRAN/TM. Like the previous chapter, the results again indicate that non-linear effects cannot be neglected in predicting the effect of hard patches when the fan is operating at high power settings.

Chapter 8

Acoustic analysis of liners for fan blade instabilities

8.1 Introduction

Most components in an engineering problem are susceptible to self-exited vibrations when subjected to high speed air flows, which in turn interact with the unsteady mean flow resulting in coupled instabilities [99]. This phenomenon is known as flutter. In turbomachinery applications, flutter is generally associated with the blades of fan, compressors and low-pressure turbines. It occurs when the blades absorb energy from the interacting fluid and start to vibrate in an unsteady manner, causing damage to the fan. It is therefore very important to consider the effects of flutter in the development of improved turbofan engines, especially when thin, slender and flexible fan blades are used.

Fan flutter is mainly influenced by factors such as blade mistuning, mean flow distortions, pylon effects and acoustic properties of the intake duct [99]. This study focuses on the last factor. Variation in the duct cross-sectional area and impedance discontinuities in presence of acoustic liners may result in large acoustic reflections which interact with the fan causing the fan blades to flutter (shown in figure 8.1). The impact of these reflections on the fan blades depends on the amplitude and phase of the reflected modes. A high amplitude reflected mode and/or a reflected mode in phase with the fan vibration is more likely to render the fan blade unstable.

Achunche, in chapter 8 of his thesis [62], investigated the effects of different intake geometries on fan flutter. The analysis was performed in hard-walled intakes using the axisymmtric version of ANPRORAD to predict the reflected mode amplitude and phases. This chapter is a continuation of the work performed by Achunche [62]. In this

chapter, the acoustic impact of different liners on flutter is investigated. The study aims to find optimum liner(s) capable of reducing fan flutter.

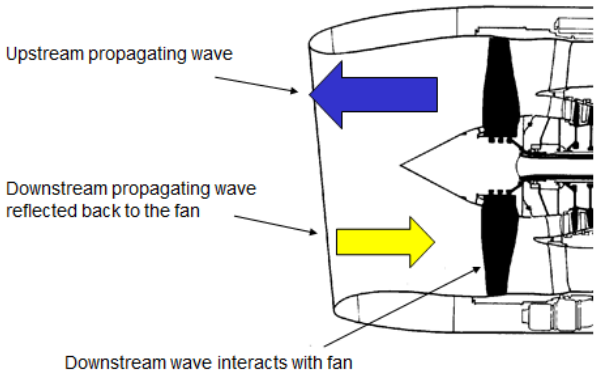

FIGURE 8.1: Fan flutter caused from the interaction of reflected modes with the fan blades in a turbofan intake

8.2 Literature Review

Flutter is an area which links unsteady aerodynamics with structural dynamics. The prediction of such a phenomenon has proven to be a difficult task over the years. In most of the flutter investigations performed by the authors in the past [100–102], the fluid and the structure was analysed separately linked via the surface pressure. The governing equations for the two analysis were solved separately and the structural motion caused by the unsteady flow of the fluid was used as a boundary condition.

Vahdati *et al.* [99] also treated fan blade response and the intake acoustic domain as separate entities in the analysis of fan flutter in a turbofan intake. It was shown that the fan blades start to flutter when there is both frequency and shape match between the pressure perturbation due to the vibration and rotation of the fan and an acoustic mode in the intake. The frequency ω of the pressure perturbation due to fan rotation and blade vibration is given by $\omega = \omega_N + \text{ND}*\Omega$, where ω_N is the natural frequency of the first vibrating mode of the fan, ND is the number of nodal diameter of the vibrating mode in which the fan is vibrating and Ω is the fan rotational speed. The first vibrating mode of the fan corresponds to 1ND. From the flutter calculations of Vahdati *et al.* [99], it was concluded that the unstable modes have growing time histories, whereas the stable ones have decaying ones. It was observed that 2ND and 3ND vibration modes are very unstable (shown in figure 8.2) at low frequencies. The instability of these vibration modes are exacerbated when they interact with the (2,1) and (3,1) acoustic modes. Vahdati *et al.* concluded that flutter occurred each time the

frequency ω of pressure perturbation due to fan rotation and blade vibration matched the cut-on frequencies of the individual modes.

Achunche [62] used ACTRAN/TM within a shell code ANPRORAD to predict the amplitude and the phase of the reflected flutter modes 2ND (or (2,1)) and 3ND (or (3,1)) (figure 8.2) at the fan plane. In his study, the effects of the intake geometry on flutter were investigated. It was concluded that the acoustic reflections in a rig intake with the flare is smaller than that of a scaled flight intake as the geometrical expansion into the surroundings of the former is more gradual to ensure lesser reflections from the highlight.

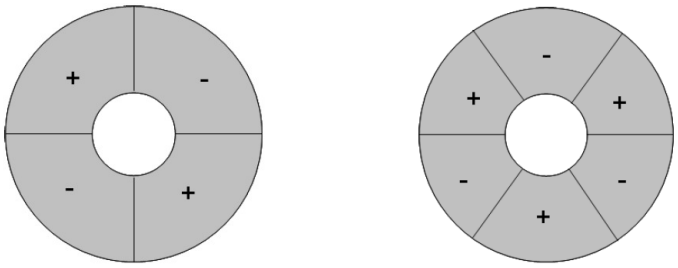

(a) 2ND (b) 3ND

FIGURE 8.2: Unsteady pressure patterns generated by 2ND and 2ND vibration modes of the fan [62]

8.3 Acoustic analysis of different liner configurations for fan-flutter

In this study, the impact of different intake liner configurations on flutter are investigated using ACTRAN/TM [39] within the shell code ANPRORAD (both axisymmetric and 3D version). Like Achunche [62], the reflection coefficients of the reflected modes (2,1) and (3,1) are predicted at the fan plane, having prescribed incident modes (2,1) and (3,1) respectively at this plane. The predictions are performed over a range of fan speeds (66%-83%) at low frequencies in the vicinity of the cut-on frequencies of the modes (2,1) and (3,1) for a static engine condition (no ambient flow).

8.3.1 Liners with hard axial splices

In this section, an axisymmteric rig intake with a fan diameter of about 0.8m (figure 8.3(a)) is used. The intake has a double degree of freedom (DDOF) liner with two hard axial splices 180^o apart. The liner impedance is shown in figure 8.3(b) where R is the non-dimensional resistance and χ is the non-dimensional reactance. These

values are the predicted impedance for the DDOF liner used in the rig test performed at Rolls-Royce plc. and was provided by the industry to investigate its impact on fan-flutter. The impact of the splice widths on flutter is also investigated in this study.

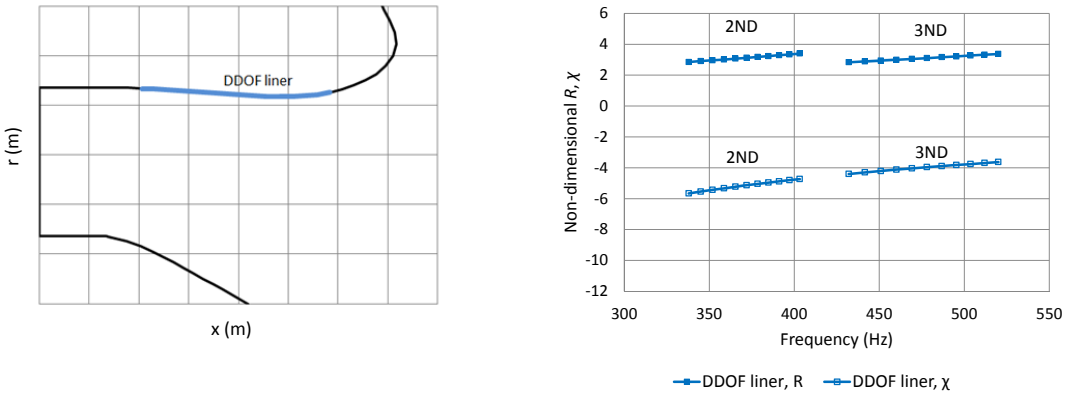

(a) Intake geometry

(b) Liner impedances

FIGURE 8.3: Intake geometry and liner impedances for modes 2ND (2,1) and 3ND (3,1) used for spliced liner configuration

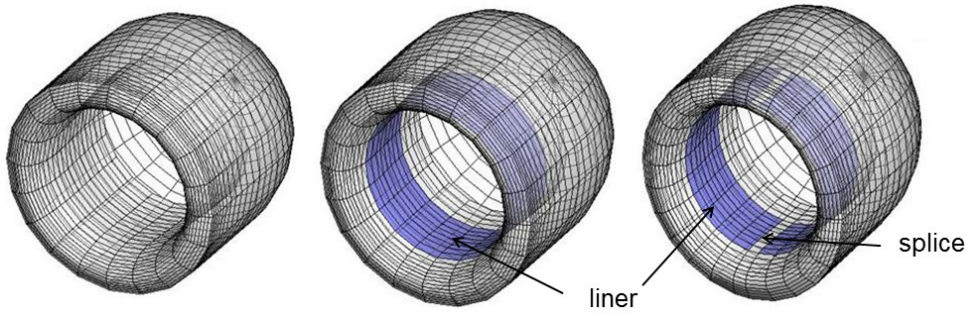

FIGURE 8.4: ANPRORAD 3D mesh over the nacelle; hard-wall (left), fully lined (middle) and spliced liner (right)

It is important to note that the liner impedance in figure 8.3(b) for flutter modes 2ND and 3ND are not for a single engine condition. In fact, the Mach number varies with frequency and the relationship between the Mach number and frequency is not the same for both the flutter modes. Moreover, the impedances themselves are independent of the mode orders 2ND or 3ND. These operation points at which the impedance is specified lie in the vicinity of flutter bite, that is, when the natural frequency of the

first vibrating mode of the fan matches with the cut-off frequency of the flutter modes at the fan (see figure 13 of reference [99]).

8.3.1.1 Results

The effects of the spliced liner on flutter is compared with hard-walled and uniformly lined configurations. Figure 8.4 shows the ANPRORAD 3D mesh over the intake nacelle for the three configurations used in the study. Figures 8.5(a) and 8.5(b) show the amplitude of the reflected modes (2,1) and (3,1) respectively relative to that of the incident modes of same order. Figures 8.6(a) and 8.6(b) show the respective phases of these modes.

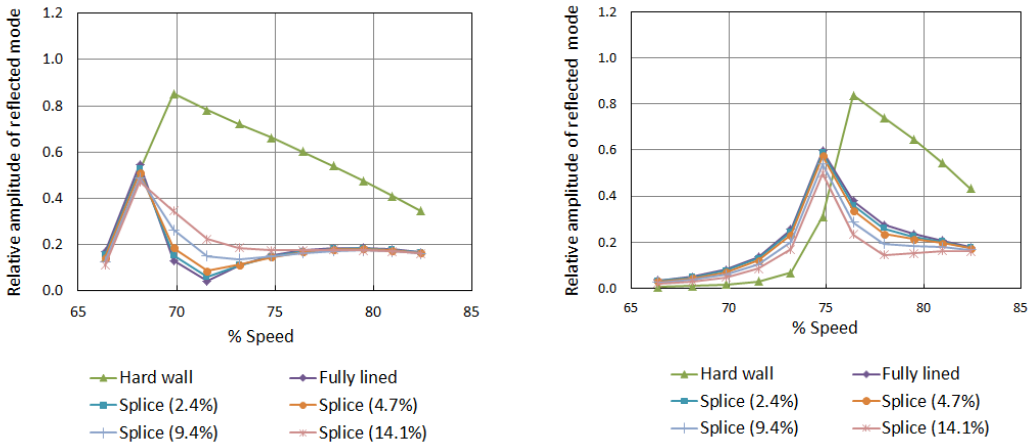

(a) Reflected (2,1) mode

(b) Reflected (3,1) mode

FIGURE 8.5: Relative amplitude of the reflected modes for a hard-walled, fully-lined and spliced intake (splice width represented in terms of % of the duct circumference at the fan plane)

In figures 8.5(a) and 8.5(b), the amplitude of reflected (2,1) and (3,1) modes for the hard-wall configuration is greatest at about 70% and 76% fan speeds. This is because at these fan speed respectively, the incident modes (2,1) and (3,1) are nearly cut-on at the fan plane and therefore most of the energy in these mode gets reflected back. As the fan speed increases, the mode becomes more cut-on and less energy is reflected back.

In figures 8.5(a) and 8.5(b), the peaks in the reflection coefficient seem to be different for the hard and lined configurations. It is important to understand that these are not the actual peaks where the reflected amplitude attains the maximum value within the considered range of engine speeds. This is because ACTRAN/TM simulations are performed at fixed interval points within this range and therefore the actuals peaks can be missed out. However, by performing some extra predictions near the maximum value of reflection coefficient, it is found that the peak amplitudes for the hard and the

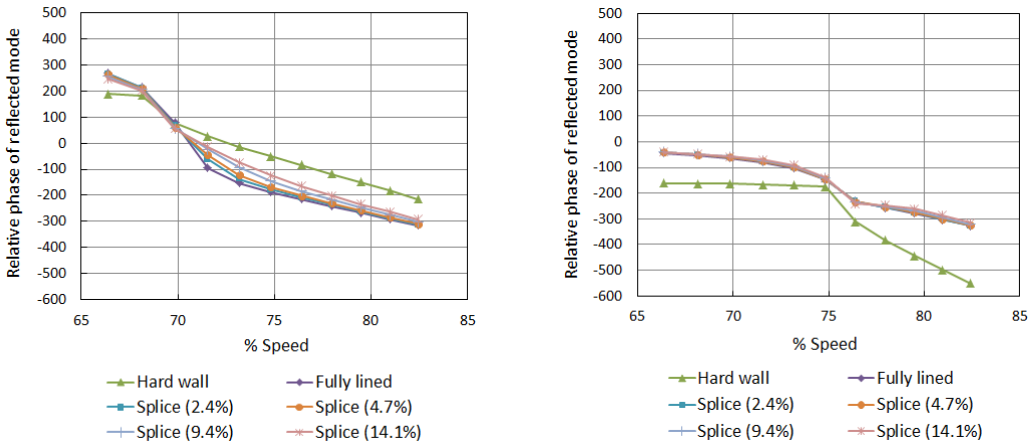

(a) Reflected (2,1) mode

(b) Reflected (3,1) mode

FIGURE 8.6: Relative phase of the reflected modes for a hard-walled, fully-lined and spliced intake (splice width represented in terms of % of the duct circumference at the fan plane)

lined cases occur at the same operation point and the values are slightly higher than those shown in these plots.

In the uniformly lined case, the reflected amplitude drops down when the mode is cut-on since most the of the energy in these modes is absorbed by the liner. A wider splice seems to increase the amplitude of reflected mode (2,1) at higher speeds but on the other hand, it reduces the amplitude of reflected mode (3,1). However, the effect of splices on the reflection coefficients can be considered to be small when compared to the uniformly lined case.

In figures 8.6(a) and 8.6(b), a much larger scale of angular range is used to represent the relative phases. This is because it is assumed that the variation of the relative phase of the reflected flutter mode with the engine speed is continuous. If the scale of the phase plots is limited to 360^o, the relative phase will look discontinuous and it will be difficult to know if it is 'after one complete rotation' or 'after two rotations' and so on.

Figures 8.6(a) and 8.6(b) indicate a linear variation in the relative phase of the reflected modes against fan speed for different configurations when the modes are cut-on at the fan plane.

8.3.2 Axially segmented liners

In this section, a slightly different axisymmteric rig intake is used with same fan diameter. The intake has an axially segmented liner with 25% of the liner close to the fan

being a liner tuned at a low frequency and rest 75% being a community noise liner (figure 8.7(a)). The liners used in the study are shown in table 8.1. The liner impedance of the all the liners is shown in figure 8.7(b), where R and χ are the non-dimensional resistance and reactance respectively.

TABLE 8.1: Segmented liner configurations used for flutter analysis

Liner configuration	1st segment (close to the fan) - 25% of liner	2nd segment - 75% of liner
1	low resistance ($\sim$ 0.5) deep liner	community noise liner
2	high resistance ($\sim$ 2.5) deep liner	community noise liner

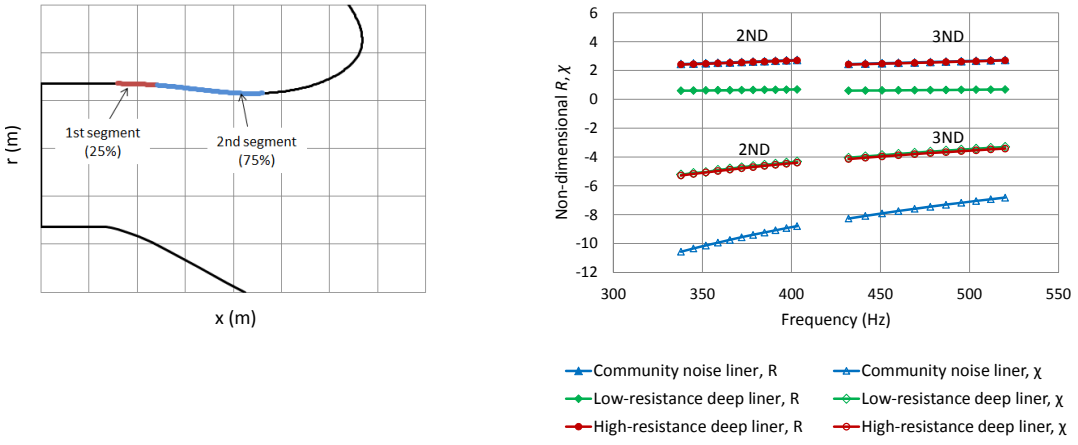

(a) Intake geometry

(b) Liner impedances

FIGURE 8.7: Intake geometry and liner impedance used for segmented liner configuration

8.3.2.1 Results

The effects of the segmented liner configurations 1 and 2 on flutter is again compared with hard-walled and uniformly lined cases. The community noise liner is used in the uniformly lined case. Figures 8.8(a) and 8.8(b) show the amplitude of the reflected modes (2,1) and (3,1) respectively relative to that of the incident modes of same order. Figures 8.9(a) and 8.9(b) shows their respective phases.

Figure 8.8(a) shows that the segmented liner configuration 2 (with a high resistance deep liner in 1st segment) performs better in reducing the amplitude of the reflected mode (2,1). Figure 8.8(b) shows large reflection of (3,1) mode at the fan plane for the segmented configuration 1. The peak amplitude of the reflected mode (3,1) however drops down in case of configuration 2. The results indicate that the performance of the

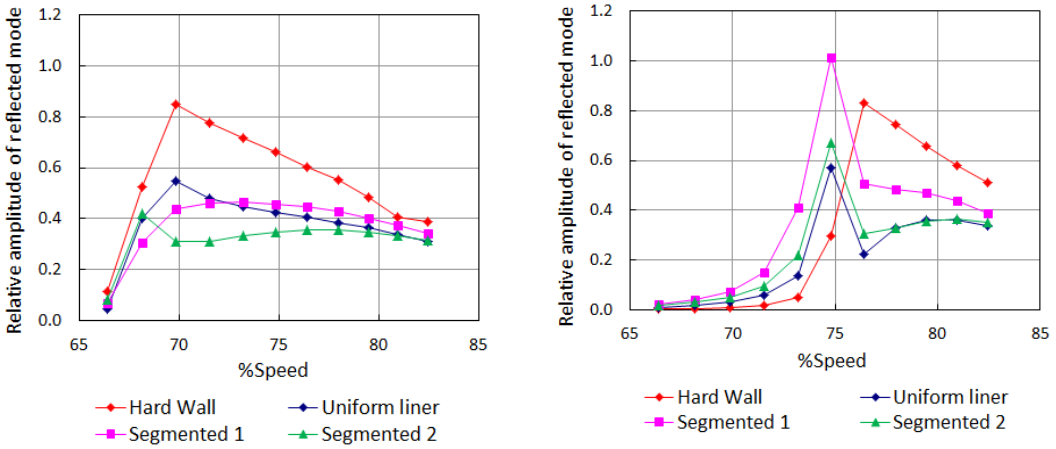

(a) Reflected (2,1) mode

(b) Reflected (3,1) mode

FIGURE 8.8: Relative amplitude of the reflected modes for a hard-walled, uniformly lined and segmented liner configurations 1 and 2

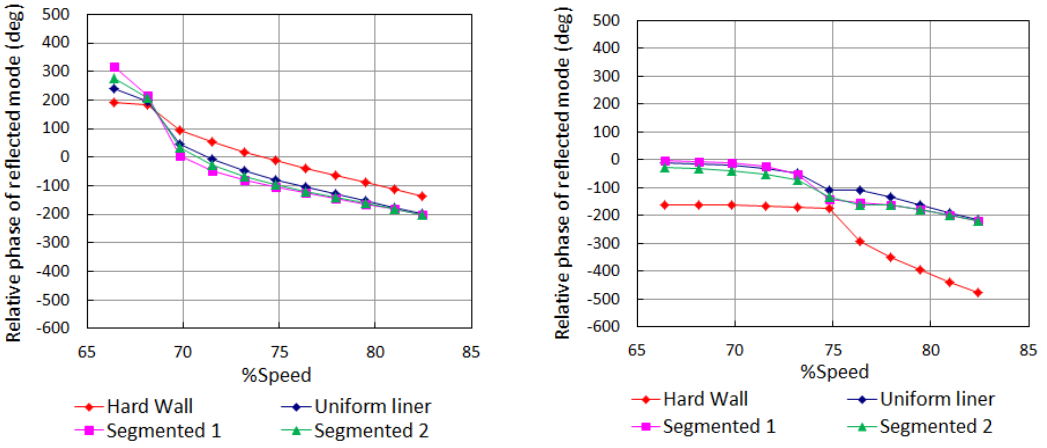

(a) Reflected (2,1) mode

(b) Reflected (3,1) mode

FIGURE 8.9: Relative phase of the reflected modes for a hard-walled, uniformly lined and segmented liner configurations 1 and 2

segmented liner configuration 2 is better than configuration 1 in reducing the acoustic reflections but shows no significant benefit over the uniformly lined case.

Like the spliced liner configuration, the linear variation in phase of the reflected modes relative to the incident is also observed both for configurations 1 and 2 at both sides of the cut-off cut-on transition. (figure 8.9(a) and 8.9(b))

8.3.3 Circumferentially varying liners

In this section, the same intake is used as that of the previous section. The intake has an axially segmented liner with two segments of equal lengths. The first segment constitutes the community noise liner used in the previous section and has circumferentially uniform lining. The second segment has a liner with variable circumferential extent (figure 8.10(a)). The segmented liner configurations used in the study are shown in table 8.2. The liner impedances of the all the liners are shown in figure 8.10(b), where R and χ are the non-dimensional resistance and reactance respectively.

TABLE 8.2: Segmented liner configurations with second segment having variable circumferential extent

Liner configuration	1st segment (close to the fan) - 50% of liner (fully lined)	2nd segment - 50% of liner (partially lined)
A	community noise liner	low R ($\sim$ 0.2) shallow liner
B	community noise liner	high R ($\sim$ 2.5) deep liner

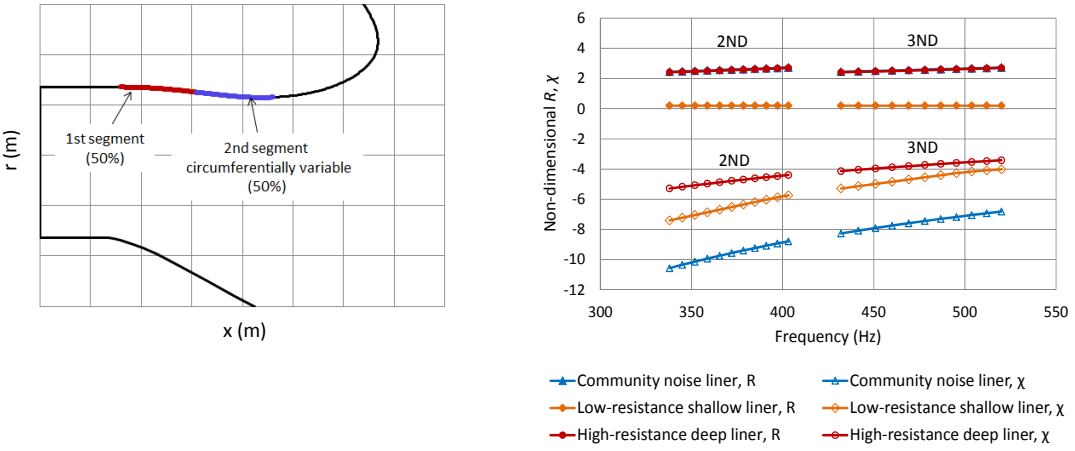

(a) Intake geometry

(b) Liner impedances

FIGURE 8.10: Intake geometry and liner impedance used for segmented liner configurations with second segment having variable circumferential extent

8.3.3.1 Results

In this study, the effects of different circumferential extents in the second liner segment on the reflected modes (2,1) and (3,1) are investigated. Figure 8.11 shows the ANPRORAD 3D mesh over the intake nacelle for four different liner extents. Figures 8.12(a) and 8.12(b) show the amplitude of the reflected modes (2,1) and (3,1)

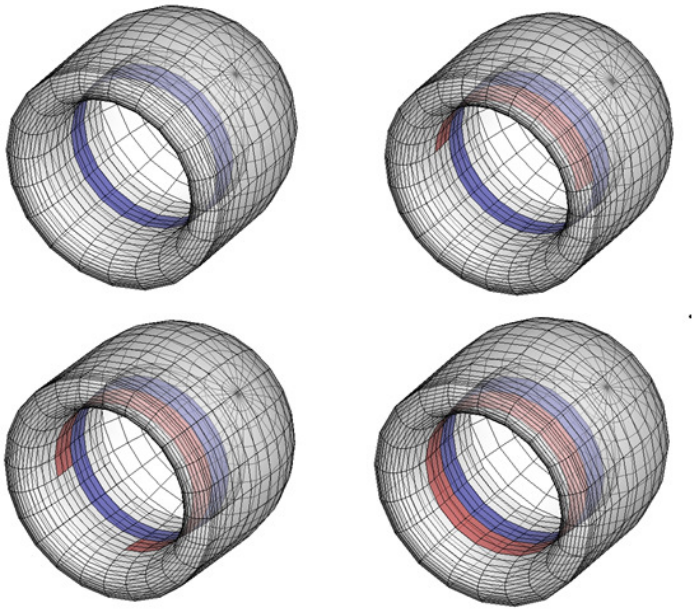

FIGURE 8.11: ANPRORAD 3D mesh over the nacelle; 2nd segment - 0^o lined (top left), 180^o lined (top right), 285^o lined (bottom left) and 360^o lined (bottom right)

respectively relative to that of the incident modes of same order, for configuration A. Figures 8.13(a) and 8.13(b) show the respective phases of these modes. Figures 8.14 and 8.15 show similar plots for configuration B.

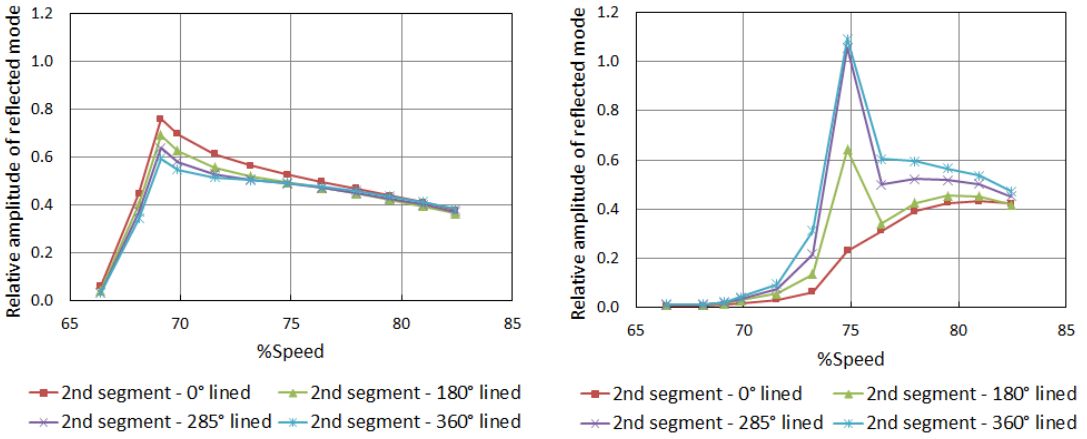

(a) Reflected (2,1) mode

(b) Reflected (3,1) mode

FIGURE 8.12: Relative amplitude of the reflected modes for configuration A

Figures 8.12 and 8.14 show that a low resistance liner in the segment close to fan (configuration A) reduces the reflection of mode (2,1) but increases the reflection of mode (3,1) compared to the case the second segment is unlined. A high resistance

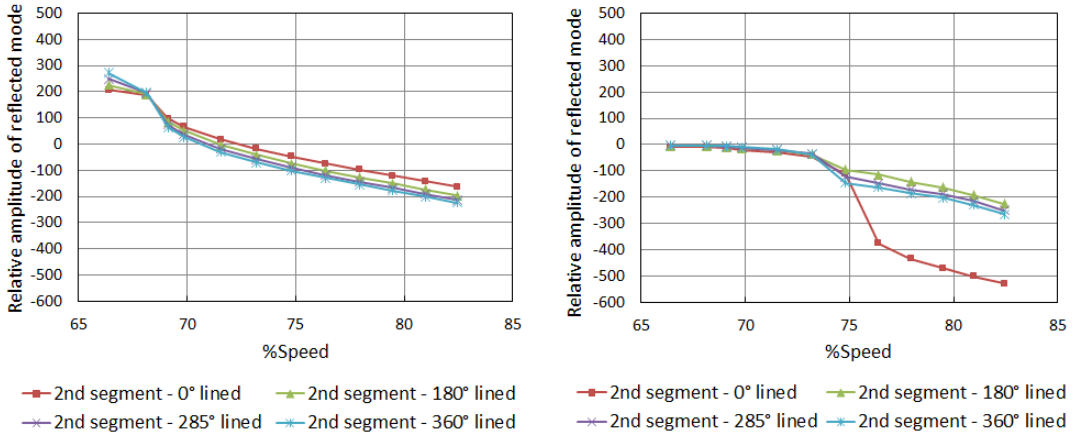

(a) Reflected (2,1) mode

(b) Reflected (3,1) mode

FIGURE 8.13: Relative phase of the reflected modes for configuration A

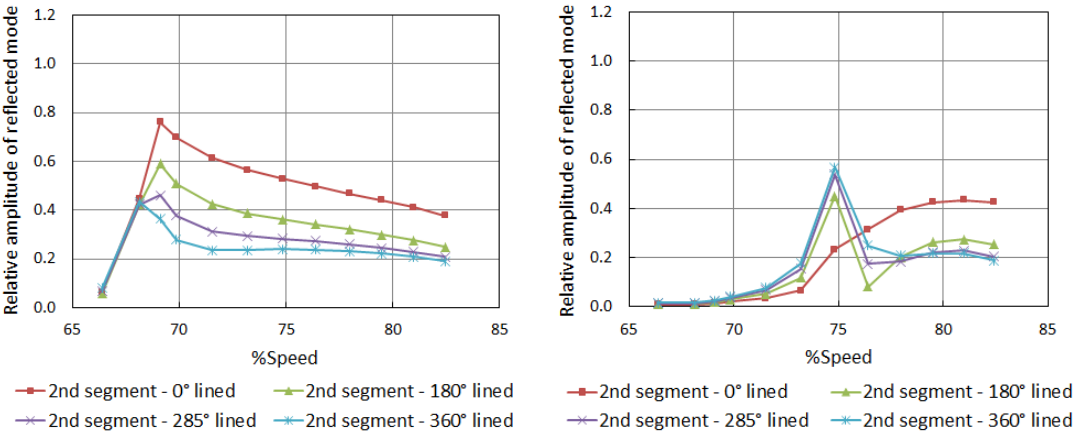

(a) Reflected (2,1) mode

(b) Reflected (3,1) mode

FIGURE 8.14: Relative amplitude of the reflected modes for configuration B

liner again proves to be effective in reducing the peak amplitude of the reflected mode (3,1). It can also be concluded from figures 8.12 and 8.14 that the increase in the circumferential coverage of the lined area reduces the reflection of mode (2,1) but increases that of mode (3,1).

8.4 Automatic optimisation of intake liner for flutter

In this section, the objective is to find liner constructions which can effectively reduce the modal amplitudes of the reflected modes (2,1) and (3,1) over a range of engine speeds with the aim to minimise fan flutter. The 'SOFT' optimisation technique,

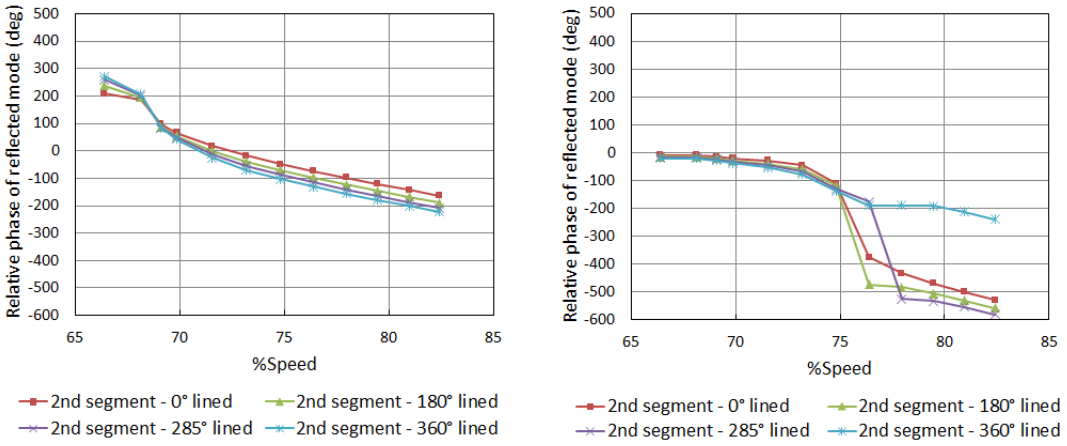

(a) Reflected (2,1) mode

(b) Reflected (3,1) mode

FIGURE 8.15: Relative phase of the reflected modes for configuration B

demonstrated in chapter 5, is used to identify the optimum liner impedance to minimise the reflected modal amplitude within the non-dimensional $R - \chi$ design space. The global optimiser ARMOGA is followed by the gradient-based local search DHC. Here, the cost function is the amplitude of the reflected modes (2,1) or (3,1) relative to the incident amplitude of the same mode order. The intake geometry and the liner configuration is the same used in section 8.3.2 (figure 8.7(a)). The liner of which the impedance will be optimised is 25% of the intake liner closer to the fan (1st segment) and the community noise liner is applied over remaining 75% of lined area.

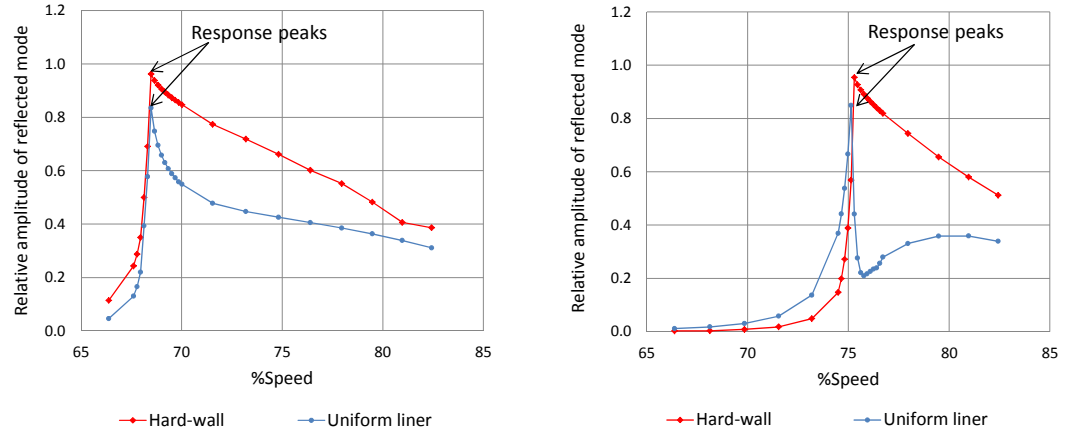

(a) Reflected (2,1) mode

(b) Reflected (3,1) mode

FIGURE 8.16: Reflected modal amplitude relative to incident modal amplitude in hard-walled and uniformly lined intake

Figures 8.16(a) and 8.16(b) show the modal amplitudes of the reflected modes (2,1) and (3,1) respectively against the engine speeds in the hard-walled intake and the uniformly

lined intake with the community noise liner. These results are the same as shown in figures 8.8(a) and 8.8(b) with some extra ACTRAN evaluations near the response peaks. The optimisation study is performed at the response peaks of the reflected modes (2,1) and (3,1), as indicated in figures 8.16(a) and 8.16(b) respectively. These are particularly on the either side of the cut-on/cut-off transition of the modes at the fan plane. The optimum impedance values of the liner obtained from the optimisation study are translated into some DDOF liner models and the acoustic impact of these liners on flutter are investigated over the considered engine speeds.

8.4.1 Optimisation results

Figures 8.17 and 8.18 shows the optimisation results for the reflected modes (2,1) and (3,1) respectively, at engine speeds corresponding to the response peak of the reflected modal amplitudes shown in figure 8.16. These engine speeds are particularly on the either side of the cut-on/cut-off transition of the modes. Therefore, at one of the engine speeds the mode is just cut-off at the fan plane while at the other it is just cut-on. The SOFT results are superimposed on the independently computed contour plots. Table 8.3 illustrates that the SOFT optimisation results and the total time consumed for the current cases.

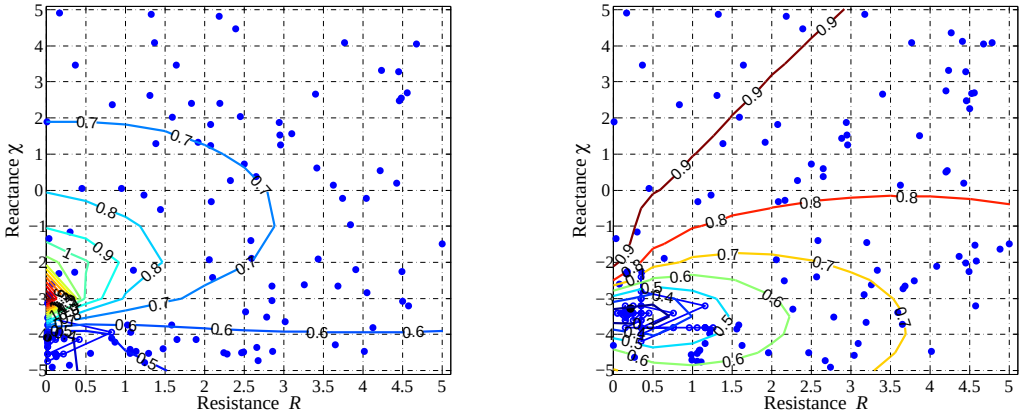

(a) mode (2,1) cut-off

(b) mode (2,1) cut-on

FIGURE 8.17: SOFT optimisation results of the relative amplitude of the reflected mode (2,1) at engine speeds close to the mode cut-on/cut-off transition. SOFT search points are superimposed on the independently computed contours of reflected modal amplitude against liner resistance and reactance; Blue dots are global search points, blue lines are local search paths. Engine speeds (frequencies) at which the mode is just cut-off and just cut-on are shown.

Figures 8.17 and 8.18 show that the results obtained by the SOFT opmtimisation and the contour plots are consistent. The contours clearly provide much more information of the design space than simply the location of the global optimum. The trends shown

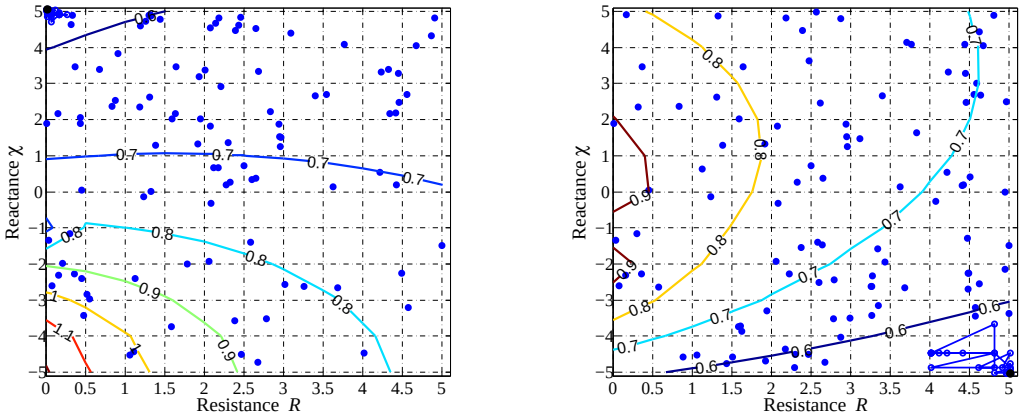

(a) mode (3,1) cut-off

(b) mode (3,1) cut-on

FIGURE 8.18: SOFT optimisation results of the relative amplitude of the reflected mode (3,1) at engine speeds close to the mode cut-on/cut-off transition. SOFT search points are superimposed on the independently computed contours of reflected modal amplitude against liner resistance and reactance; Blue dots are global search points, blue lines are local search paths. Engine speeds (frequencies) at which the mode is just cut-off and just cut-on are shown.

TABLE 8.3: SOFT optimisation results at engine speeds near the cut-on/cut-off transition of reflected modes (2,1) and (3,1)

Comparison	mode (2,1) (cut-off)	mode (2,1) (cut-on)	mode (3,1) (cut-off)	mode (3,1) (cut-on)
Resistance R	0.02	0.22	0.02	5.01
Reactance χ	-4.08	-3.28	5.05	-5.03
Reflected modal amplitude (relative to incident)	0.30	0.26	0.58	0.54
No. of evaluations	134	146	124	126
CPU time	46min 51sec	51min 15sec	49min 38sec	50min 39sec

in contour maps are very different depending on if the mode is cut-off or cut-on at the fan plane. It is therefore not straightforward task to find a liner impedance value with which the reflected modal amplitude of the flutter modes at these engine speeds can be well reduced.

In figures 8.17(a) and 8.18(a), the relative amplitudes of the reflected (2,1) and (3,1) modes exceed unity as these modes are strongly reflected back at the fan-plane. In figures 8.17(a) and 8.18(a), the mode (2,1) and (3,1) are respectively cut-off at the fan-plane and are very close to becoming cut-on. However, there are locations further along the duct where the mode nearly cuts-on due to changes in geometry and mean flow and most of the energy is reflected back due to sudden changes in liner impedances. The results indicate that this happens when 25% of liner close to the fan (which is being optimised) has a very low resistance (close to 0) as compared to $R \sim 2.5$ of the community noise liner which cover the rest 75% of the total liner length.

8.4.1.1 Selection of optimal liners

The optimum liner parameters identified by SOFT optimisation are very different at engine speeds corresponding to the response peaks indicated in figure 8.16. An alternative procedure is therefore introduced to select the optimal liners. For selecting the liner parameters effective to reduce reflected modal amplitudes of the flutter modes over the considered range of engine speeds, the following steps are taken.

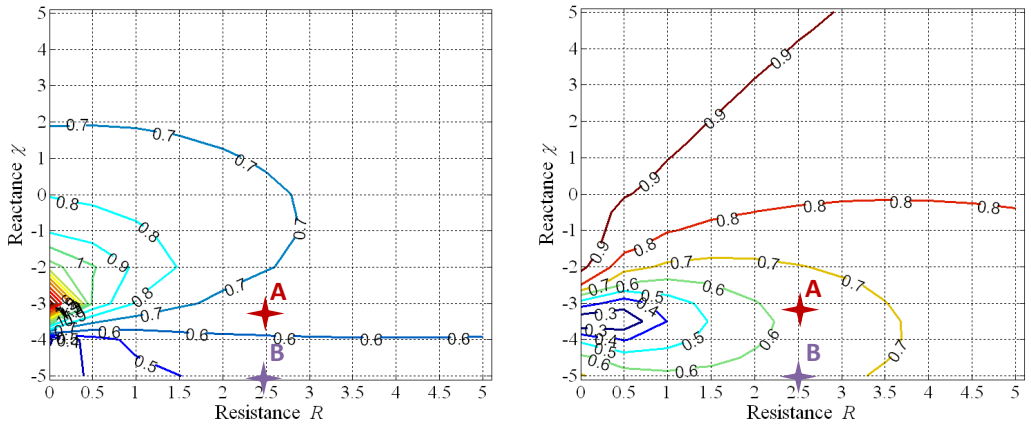

(a) mode (2,1) cut-off (b) mode (2,1) cut-on

FIGURE 8.19: Contour plots of reflected modal amplitude of mode (2,1) against liner resistance and reactance at engine speeds close to the mode cut-on transition. The markers show the selected liners (A and B).

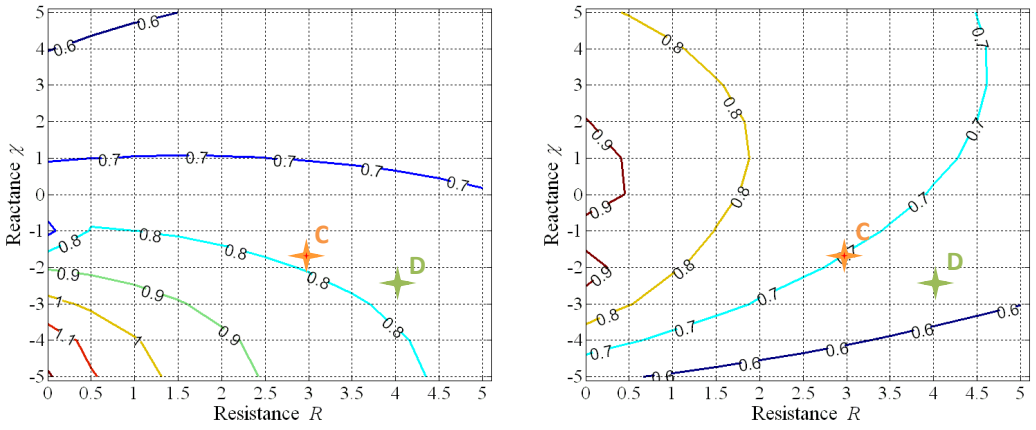

(a) mode (3,1) cut-off (b) mode (3,1) cut-on

FIGURE 8.20: Contour plots of reflected modal amplitude of mode (3,1) against liner resistance and reactance at engine speeds close to the mode cut-on transition. The markers show the selected liners (C and D).

I. Select a combination of liner resistance R and reactance χ with which the reflected modal amplitude does not exceed a certain value (0.7 for mode (2,1) and 0.8 for

mode (3,1)) on the both sides of response peak. The selected combinations of liner resistance R and reactance χ are shown by markers in figures 8.19 and 8.20.

II. Assuming a DDOF liner model, select the liner parameters (cell depths, facing sheet, septum resistance etc.) which will have the impedance value close to the liner selected in step I.

III. Predict impedance of the selected liners for the considered range of engine speed (for combinations of Mach number and frequency). The impedance of the selected liners is shown in figure 8.21

IV. Apply the impedance to the 1st segment (25%) while the 2nd segment (75%) having community noise liner, and predict the modal amplitudes of the reflected modes (2,1) and (3,1) by running individual ACTRAN analyses.

V. Compare the relative responses for the selected liners with baseline configurations (hard-wall and uniform liner).

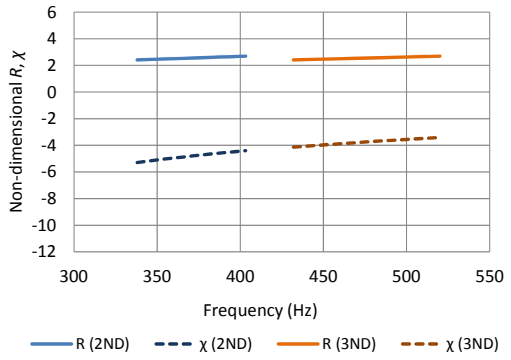

(a) Liner A ($R \sim 2.5$, 60mm cell depth)

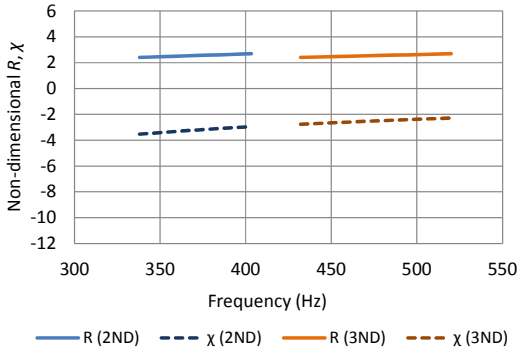

(b) Liner B ($R \sim 2.5$, 90mm cell depth)

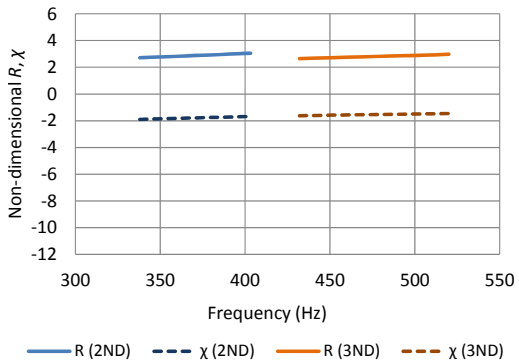

(c) Liner C ($R \sim 3$, 200mm cell depth)

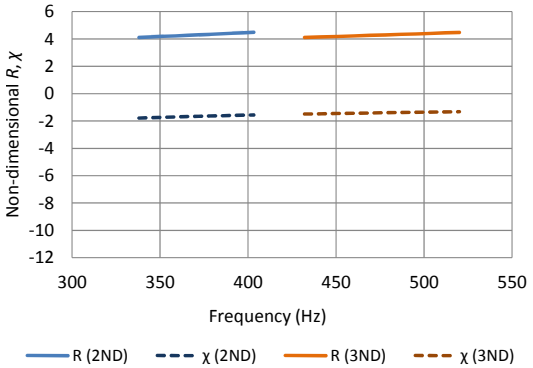

(d) Liner D ($R \sim 4.5$, 200mm cell depth)

FIGURE 8.21: Predicted impedance of selected liners against frequency

8.4.1.2 Predictions for the selected liners

The liners selected in the previous section are used in conjunction with community noise liner to predicted the amplitudes of the reflected modes (2,1) and (3,1) at the fan plane, for the considered range of engine speeds. The results are compared with the hard-walled and the uniformly lined cases. The reflected modal amplitudes predicted for modes (2,1) and (3,1) are shown in figures 8.22(a) and 8.22(b) respectively.

Figures 8.22(a) and 8.22(b) indicate a difficulty in reducing the peak level of reflected modal amplitude for both modes (2,1) and (3,1), especially mode (3,1). The band width of the peak however varies depending on the liner. The peak of the reflected amplitude of mode (2,1) can be reduced to the value smaller than 0.7 while it is difficult to find a liner which does the same for mode (3,1).

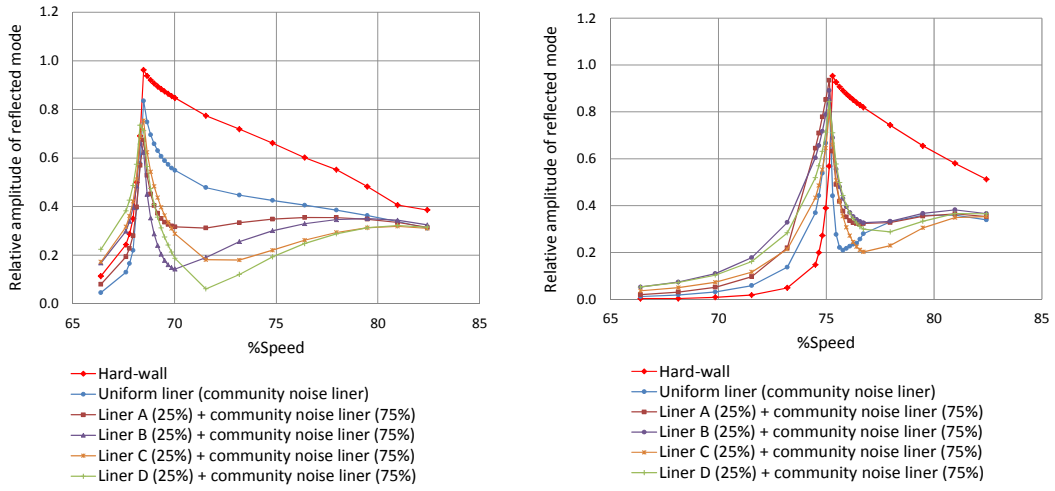

(a) Reflected (2,1) mode

(b) Reflected (3,1) mode

FIGURE 8.22: Reflected modal amplitudes predicted for segmented liner configurations with selected liners (25%) and community noise liner (75%)

8.5 Conclusions

The reflections of acoustic modes which enhance fan blade instabilities in different intake liner configurations have been predicted by using ACTRAN/TM within the shell code ANPRORAD 3D. The effects of different liner configuration on the 2ND (2,1) and 3ND (3,1) flutter modes were investigated. The conclusions from this study can be summarized as below.

8.5.1 Effect of intake liner splices

The amplitude and phase of the reflected wave at the fan in a lined intake with two splices was compared to that when the intake is uniformly lined. The influence of the width of the splice was also investigated. As the splice width increases the magnitude of reflection of flutter mode (2,1) decreases while that of mode (3,1) increases. However, the effect of typical liner splices on the amplitude and phase of the reflected flutter wave at the fan, and hence the effect on flutter, is predicted to be small.

8.5.2 Effect of axially segmented liners

The effects of axially segmented liners (25% length closer to the fan with deep liner and 75% length with community noise liner) on the reflected wave was investigated. This configuration performs better than the uniform liner in reducing the amplitude of the reflected flutter mode, although in some cases the reflected mode amplitude can increase when the mode just cuts on. The peak amplitude of the reflected modes can be reduced significantly if the deep liner has a slightly higher resistance than the community noise liner.

8.5.3 Effect of circumferentially varying liners

The impact of the circumferential extent of liner on flutter was also investigated. The results indicate that a smaller circumferential coverage of the liner decreases the amplitude of the reflected mode (2,1), but increases for the reflected mode (3,1). But whether the liner configuration is beneficial or disadvantageous compared to the uniformly lined case depends greatly on the liner impedances. High resistance liners again prove to be effective in reducing the amplitude of the flutter modes.

8.5.4 Liner optimisation for fan-flutter

Optimisations are conducted at engine speeds corresponding to response peaks of the reflected flutter modes. Several DDOF liners have been selected for reducing reflected modal amplitudes of these modes at the fan plane over the considered range of engine speeds when the selected liners are used in conjunction with the community noise liner in the axially segmented liner configuration. The liner selection influences the peak amplitude of mode (2,1) and also the bandwidth of both (2,1) and (3,1) modes, but does not change very much the peak amplitude of the mode (3,1). It is however important to consider the impact of a liner selected for fan flutter on the reduction of community noise and to ensure that the penalty is acceptable.

Chapter 9

Conclusions and Future work

9.1 Overall conclusions

The work presented in this thesis is motivated by the need to predict the performance of acoustic liners in modern turbofan intakes to reduce community noise and low-frequency acoustic reflections which trigger fan-blade instabilities. Such predictions provide a key to optimising liners and developing improved liner designs. However, any damage or repair to the liner has a potential to compromise the effectiveness of the liner. Therefore, the effects of damage/repair on liner performance have also been investigated in this thesis to determine the acceptable limit.

This thesis also presents novel methodologies for predicting sound propagation and attenuation in acoustically lined intake ducts and radiation to the far field by exploiting the commercial CAA code ACTRAN/TM. This code is based on FE formulation for the acoustic velocity potential and is computationally less expensive when compared to alternative CAA methods based on full Euler and Navier-Stokes codes. It cannot however model the non-linear propagation effects which cannot be neglected at supersonic fan-tip speeds. In this thesis, these effects have been taken into account by using an analytical non-linear propagation model and subsequent adjustments were applied to the linear ACTRAN/TM predictions at no additional computational cost.

In order to confidently use the prediction method, the far-field SPL predictions obtained from ACTRAN/TM have been validated against rig and engine test data at different fan speeds both for hard-walled and lined configurations. Two different noise source models have been used to represent fan noise at BPF. One of them used a complex distribution of acoustic power in the azimuthal modes with individual levels inferred from hard-walled in-duct and far-field measurements, while the other was based on the conventional 'equal energy per mode' assumption. The study justified the validity of 'equal energy per mode' assumption to model the noise source as the results

obtained from the both the source models had a good agreement. This simple representation of the noise source was subsequently used in rest of the thesis. Non-linear adjustments applied to the ACTRAN/TM predictions at supersonic fan-tip speeds slightly improved the agreement with the measured far-field SPL directivities. Good overall agreement with measured data indicated that the prediction method can predict the performance of intake liners with sufficient fidelity to be used for liner optimization studies.

An automated liner optimisation strategy was presented by running ACTRAN/TM within SOFT or MATLAB optimisation suite. The optimisation technique involved a global GA search followed by a local search algorithm. Intake liners were optimised to reduce forward-arc fan noise at approach and sideline conditions, both for broadband and tone noise sources. The results indicated the benefit of using high resistance liners when the engine is operating at sideline condition. It was also shown that the liner insertion loss for the combined noise source at sideline condition is dominated by that of the BPF tones when linear propagation was assumed. The insertion loss however dropped when the non-linear effects were considered in the prediction. This indicated that such effects cannot be neglected at high power settings. The study demonstrated the feasibility of applying an automated approach to optimise liners in realistic turbofan intakes and for well-defined noise sources within industrially acceptable timescales.

Liner damage/repair, however, degrades the performance of optimised liners and therefore the acoustic impact of the size and the location of these liner patches on the performance of a zero-splice liner was investigated. It was shown that larger patches have more detrimental effects on the performance of a zero-splice liner. Moreover, the proximity of the patch to the fan increases scattering, thereby reducing the effectiveness of the liner. The predictions were initially made by using an asymptotic model for in-duct analysis in a uniform cylindrical duct. Though the model provided a fast tool to predict the patch-scattered modes, it suffered from the limitation of Kirchhoff's approximation. Numerical predictions by using ACTRAN/TM were later performed to validate the results and to extend the study in realistic intakes. The effects of patches on far-field noise directivities were also investigated by using ACTRAN/TM. The detrimental effects of liner patches on far-field noise attenuation increases with the protrusion of the rotor-locked BPF mode above the multi-mode noise component as observed in the far-field SPL directivity. Non-linear adjustments to the linear results were found to increase the patch effect further.

Finally, the acoustic impact of intake liners to reduce fan-blade instabilities occurring at low frequencies have been investigated. The interaction of the high-amplitude reflected flutter modes with the fan blades is an important factor to determine these instabilities. It was shown that high resistance liners perform better in reducing the amplitude of the reflected flutter modes. An optimisation study to reduce the acoustic reflections of the flutter modes was also conducted. The study indicated that it was difficult to reduce

the peak amplitudes of the reflected flutter modes by a large amount. Moreover, the impact of these optimised lines on community noise must also be taken into account.

If the results and the discussions from all the chapters are drawn together, it can be concluded that in order to design an optimal intake liner for all engine conditions, it is important to assess its impact on community noise especially at high frequencies and fan-blade instabilities at low frequencies. It is however difficult to find a liner which is capable of addressing both the problems because high resistance deep liners which perform better in reducing fan-flutter might not be a good option for suppressing community noise. Therefore, a compromise needs to made taking into consideration that the penalty is acceptable in accordance with the key requirements of the engine manufacturers. Liner damage/repair has a potential to degrade liner performance and therefore it is also important to consider their impact on noise attenuation by the liner. Larger patches lying closer to fan causes greater model scattering thereby degrading the noise suppressing capability of the liner. The patch effect further increases with the amount of protrusion of the rotor-locked BPF tone above the broadband noise floor in the noise spectrum. Last but not the least, the study also indicates the importance of considering non-linear propagation effects in the prediction in order to accurately calculate the liner insertion loss at high fan speeds.

9.2 Recommendations for future work

The work reported in this thesis opens the door to many questions and possible further improvements to the methods used in the study to predict the performance of intake liners at different engine speeds. One of the important areas of extending this work is to improve the method for predicting the non-linear propagation effects at high fan speeds. Though the current analytical model provides a quick tool to compute the non-linear attenuation of the BPF tones and can be easily used for adjusting ACTRAN/TM results, the model does not take into account the buzz-saw noise components at supersonic regime. This can be considered as weakness of the model as the presence of other EO tones in the spectrum can modify the non linear propagation of the BPF tones. The model also assumes that the shocks are located at the fan blade tips which is questionable as in practice the shocks have finite width along the blade span.

This analytical model was also used in this thesis to predict the correct source SPL of the rotor-locked BPF mode by using the hard-walled measurements from the transducer ring located at the throat of the intake duct. This can be considered to be a sensitive approach because no matter what the source SPL is, the shock waves would end up with more or less the same SPL at the wall at distances further away from the fan. This highlights the importance of having measurements close to the fan so

that the correct source level can be measured directly rather than determining it from the measurements at the transducer ring. A useful extension of the work presented in chapter 4 would be to validate the far-field predictions with measurements by using the measured source levels in the predictions rather than inferring them from the measurements near the throat.

Acoustic liners in realistic intake geometries were optimised in this thesis to reduce community noise and low-frequency acoustic reflections. However, these optimisation studies were performed separately. In future, it would be interesting to investigate the feasibility of performing automated multiple-objective liner optimisation to simultaneously reduce community noise (low frequencies for cabin noise and high frequencies for community noise) and low-frequency acoustic reflections which trigger fan-blade instabilities.

Moreover, liner optimisation was performed with respect to single layer liner construction characterized by liner resistance and reactance (or liner cell depth). The next step in this direction would be to extend the automated optimisation approach for more complex liner constructions like DDOF liners which involves more than two liner parameters. When the number of design variables increases, the total optimisation time also increases and therefore it would be necessary to employ more complex search algorithms to obtain the results within acceptable time frames. The use of response surfaces rather than evaluating the cost function explicitly could be considered as an option for optimisation studies when more design parameters are included.

When liners are optimised for a range of frequencies and for different noise sources, the total optimisation time increases drastically. Although the cummulative process time currently lies within acceptable industrial time limits, there is always a need for efficient coarse parallelisation and multi-threading as the key to more extensive use of the automated liner optimization technique, especially when non-axisymmetric intake models are used.

In this thesis, the impact of hard patches on liner performance was investigated by using an asymptotic model and ACTRAN/TM. The next step is to compare these predictions with the measurements to test the accuracy of the results obtained to date. Moreover, it is also essential to investigate the importance of second liner discontinuity and the associated impact of liner patches with different aspect ratios.

Appendix A

Generic intake and noise spectra for liner optimisation study

The generic intake geometry and the generalised noise source spectra used in the liner optimisation study in chapter 5 are presented in this appendix.

A.1 Intake geometry

Figure A.1 shows the axisymmetric version of a generic intake of a HBR turbofan engine. The fan diameter D is assumed to be 2.4m. The acoustic liner starts at a distance of 0.21m from the fan plane. The total liner length is $0.45 * D$. The MATLAB script used to generate the intake geometry and the position of the liner is shown below.

```
% GENERIC INLET GEOMETRY
clear all
clc

% Input Coordinates
%--------------------------------

x = [0.501792114695 1.24521072797;
-0.00358422939068 1.24521072797;
-0.462365591398 1.22222222222;
-0.802867383513 1.1877394636;
-1.08243727599 1.12643678161;
-1.18996415771 1.06896551724;
-1.19713261649 1.01915708812;
-1.15053763441 0.973180076628;
```

```
-1.0394265233 0.938697318008;
-0.910394265233 0.931034482759;
-0.720430107527 0.942528735632;
-0.390681003584 0.984674329502;
0 1;
0.3 1; % dummy node
0.3 0.298850574713; % dummy node
0 0.298850574713;
-0.0931899641577 0.27969348659;
-0.204301075269 0.275862068966;
-0.321428571429 0.232824427481;
-0.489285714286 0.145038167939;
-0.731182795699 0];
% x and y coordinates
y = x(:,2); x = -x(:,1);

% Use spline function to generate nacelle geometry
%————————————————————

nacelle = [spline(0:13,x(1:14,1),0:0.1:13) ; spline(0:13,y(1:14,1),0:0.1:13) ];
% find relevant data - exclude dummy nodes
for g = 1:length(nacelle)
if nacelle(1,g) < 0 && nacelle(2,g) <= 1.1
junk(:,g) = nacelle(:,g);
else
n(:,g) = nacelle(:,g);
end
end
% remove zeros
x_info = find(n(1,:)); y_info = find(n(2,:));
if length(x_info) >= length(y_info)
nacelle = n(:,x_info);
else
nacelle = n(:,y_info);
end

% Use spline function to generate spinner geometry
%————————————————————

s2 = (x(15:21)+abs(min(x(15:21))))*100;
spinner = [spline(s2,x(15:21,1),0:0.1:max(s2));spline(s2,y(15:21,1),0:0.1:max(s2))];
% find relevant data - exclude dummy nodes
for g = 1:length(spinner)
```

```
if spinner(1,g) >= 0
s(:,g) = spinner(:,g);
end
end
% remove zeros
x_info = find(s(1,:)); y_info = find(s(2,:));
if length(x_info) >= length(y_info)
spinner = s(:,x_info);
else
spinner = s(:,y_info);
end
spinner(:,733) = [0.731182795699;0];

% Generate fan face
%------------------------------

fan_y = 0.298850574713:(1-0.298850574713)*1e-3:1;
fan_x = zeros(1,length(fan_y));

% Redefining the geometry
%-------------------------------

% The fan radius is 1.2m
fan_x = fan_x'*1.2;
fan_y = fan_y'*1.2;
liner = zeros(length(nacelle(1,end-34:end-2)),2);

nacelle = nacelle'*1.2;
spinner = spinner'*1.2;
nacelle(:,1) = nacelle(:,1)+0.123;
spinner(:,1) = spinner(:,1)+0.123;
liner(:,1) = nacelle(end-34:end-2,1);
liner(:,2) = nacelle(end-34:end-2,2);

% plot generic inlet geometry
%------------------------------

figure
% plot nacelle
plot(nacelle(:,1),nacelle(:,2),'Linewidth',1.5); hold on;
% plot liner position
plot(liner(:,1),liner(:,2),'-r','Linewidth',3);
% plot fan plan
plot([fan_x(1) fan_x(1)+0.123],[fan_y(1) fan_y(1)],'Linewidth',1.5);
plot([fan_x(end) fan_x(end)+0.123],[fan_y(end) fan_y(end)],'Linewidth',1.5);
```

```
plot(fan_x,fan_y);
% plot spinner
plot(spinner(:,1),spinner(:,2),'Linewidth',1.5);
% plot axis
grid on
set(gca,'Fontsize',16,'Ylim',[0 2],'YTick',[0:0.2:2])
set(gca,'Fontsize',16,'Xlim',[0 2],'XTick',[0:0.2:2])
xlabel('x (m)');
ylabel('r (m)');
print(gcf,'-depsc','Generic_nacelle') hold off

clear g junk n s s2 x_info y_info

% End of the Script
%————————————————————————
```

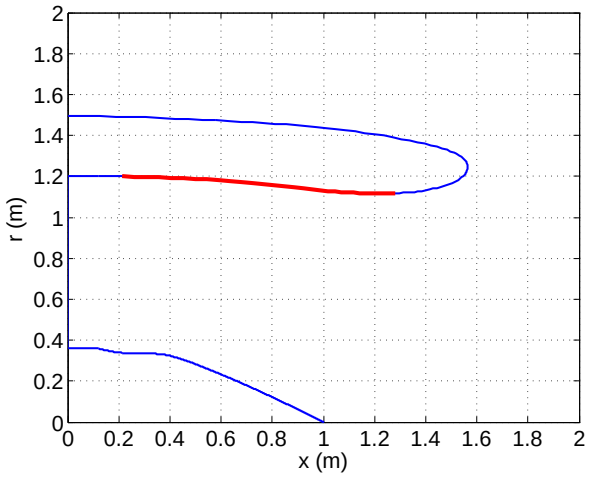

FIGURE A.1: Intake geometry; acoustic liner indicated in red

A.2 Specifications at different engine conditions

The specifications used in the optimisation study at different noise certification points (approach, cutback and sideline) are listed in table A.1. The total (or stagnation) speed of sound is $340m/s$ and the total fluid density is $1.23Kg/m^3$.

A.3 Noise Source Spectra

In the fan noise source model, only the broadband noise and the Blade Passing Frequency (BPF) tones are included. Buzz-saw tones (engine order tones) which exist at

TABLE A.1: Specifications at the engine conditions

Engine condition	BPF(Hz)	Fan-plane Mach No.	Ambient Mach No.
Approach	700	0.22	0.25
Cutback	1050	0.45	0.25
Sideline	1300	0.55	0.25

supersonic fan-tip speeds are not included.

The broadband noise is represented as an ensemble of uncorrelated modes with equal power in each third octave frequency band, and an equi-partition of acoustic power between all cut on modes for a given frequency. All the power in the third octave band is assumed to be concentrated at its centre frequency. The broadband noise for the approach condition has power level of 120dB (re 10^{-12}) in each third octave band. For both the cutback and sideline conditions the broadband noise has a power level of 125dB (re 10^{-12}) in each third octave band.

The fundamental BPF f_{1BPF} is given as the product of the number of blades B (taken to be 24) and the shaft rotation frequency Ω_s in Hz (i.e. $f_{1BPF} = B\Omega_s$). Harmonics of the BPF f_{BPF} occur at n*BPF, where n is a positive integer. The BPF tones consist of a multi-mode component and a single-mode component. The multi-mode component consists of all cut-on modes with equal power in each mode, while the single mode component consists of a single rotor-locked mode of azimuthal order $n * B$, and first radial order. The single mode component exists only at supersonic fan-tip speeds, and therefore it exists only during the sideline condition. The multi-mode power level for the approach condition (PWL_{MM_A}) and the cutback condition (PWL_{MM_C}) are given by

$$PWL_{MM_A} = -0.006 * f_{BPF} + 134.0 \tag{A.1}$$

and

$$PWL_{MM_C} = -0.003 * f_{BPF} + 140.0 \tag{A.2}$$

respectively. The multi-mode (MM) and single-mode (SM) power levels at the sideline condition are respectively given by

$$PWL_{MM_S} = -0.003 * f_{BPF} + 138.0 \tag{A.3}$$

and

$$PWL_{SM_S} = -0.006 * f_{BPF} + 172.5 \tag{A.4}$$

The power levels (PWL) for the BPF harmonics at all three conditions are listed in table A.2 and shown in figures A.2(a), A.2(b) and A.2(c). A frequency range of 50Hz-10kHz is considered to present the generic noise spectra.

TABLE A.2: Power levels of MM and SM sources at the first 7 BPF harmonics at different engine conditions

Approach	MM	Cutback	MM	Sideline	MM	SM
f_{BPF}(Hz)	PWL(dB)	f_{BPF}(Hz)	PWL(dB)	f_{BPF}(Hz)	PWL(dB)	PWL(dB)
700	129.8	1050	136.8	1300	134.1	164.7
1400	125.6	2100	133.7	2600	130.2	156.9
2100	121.4	3150	130.5	3900	126.3	149.1
2800	117.2	4200	127.4	5200	122.4	141.3
3500	113.0	5250	124.3	6500	118.5	133.5
4200	108.8	6300	121.1	7800	114.6	125.7
4900	104.6	7350	117.9	9100	110.7	117.9

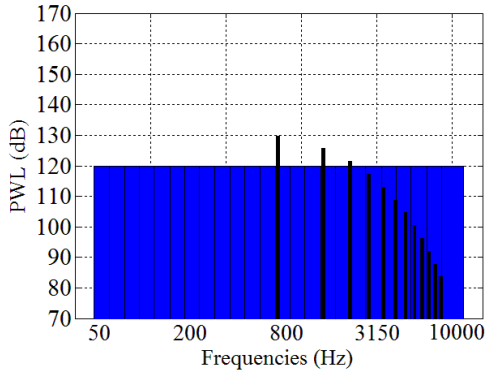

(a) Approach

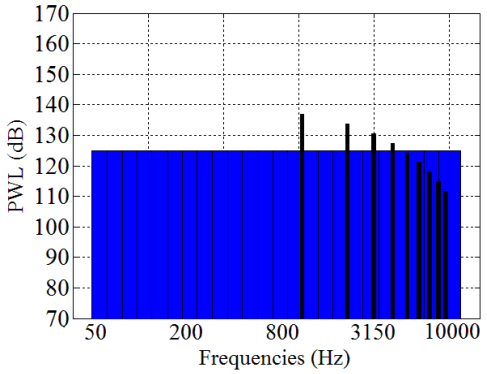

(b) Cutback

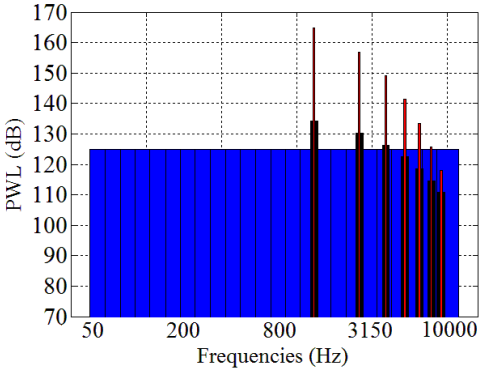

(c) Sideline

FIGURE A.2: Hard-wall spectra at different engine conditions; blue: broadband, black: MM component and red: SM component of BPF tones

Appendix B

Determination of the infinite element order for intake predictions

ACTRAN/TM uses FE/IE model to solve the acoustic problem in an unbounded domain, as discussed in chapter 2. It is very important to choose an appropriate IE order and the centre of the IE domain for an accurate representation of the acoustic field at large distances from the sources. Spurious acoustic reflections at the FE/IE interface may occur for low IE orders. However, high IE orders may significantly increase the number of degrees of freedom of the problem thereby increasing the computational cost. It is therefore essential to identify an appropriate order by performing a few test cases prior to launching a large number of simulations [39]. In this appendix, a convergence study for the far-field solutions obtained by ACTRAN/TM is performed to propose some general rules to determine an optimal IE order for typical intake predictions

Figure B.1 shows the ACTRAN/TM predictions of the far-field SPL directivities of BPF modes for different IE orders. Sideline engine condition mentioned in Appendix A is used in this convergence study. The same FE mesh is used when computations are performed at a particular frequency. Tables B.1 and B.2 show the Number of Degrees Of Freedom (NDOF), the time consumed and the total memory required to perform the acoustic computations at 1BPF (1300Hz) and 5BPF (6500Hz) respectively for different IE orders.

Figure B.1 clearly indicates that ACTRAN/TM computations at high frequency require higher IE orders to obtain accurate far-field solutions. It is difficult to establish a rule of thumb to determine the optimal IE order for intake predictions and therefore the selection is entirely based on the convergence of far-field noise directivities. The total computational cost and time should also be taken into account while determining the order. Figure B.1 shows that the far-field SPL directivities converges for IE

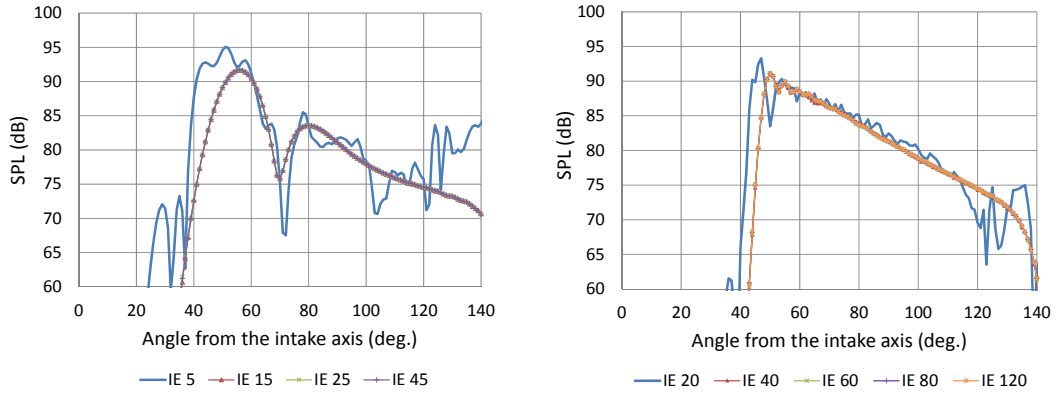

(a) mode (24,1) at 1BPF (1300Hz)

(b) mode (120,1) at 5BPF (6500Hz)

FIGURE B.1: The effect of IE order on the far-field SPL directivity of the BPF modes at sideline condition

TABLE B.1: Investigation of NDOF, total time consumed and memory required for ACTRAN/TM computation at 1BPF (1300Hz) for different IE orders

IE order	NDOF	Computation time (sec)	Memory required (MB)
5	37,652	12	177
15	41,068	14	197
25	44,255	15	234
45	50,574	23	364
70	58,723	50	627

TABLE B.2: Investigation of NDOF, total time consumed and memory required for ACTRAN/TM computation at 5BPF (6500Hz) for different IE orders

IE order	NDOF	Computation time (sec)	Memory required (MB)
20	816,74	365	4,016
40	979,354	422	4,381
60	1,043,554	649	5,949
80	1,095,654	731	7,274
120	1,139,854	2006	10,899

orders greater than 15 for 1300Hz and 40 for 6500Hz. These can therefore be chosen as optimal IE orders for the current cases.

Figure B.2 and B.3 shows a comparison of ACTRAN/TM predictions of the absolute value of the acoustic pressure in the FE domain for a low IE order and the chosen IE order (15 and 40 for 1300Hz and 6500Hz respectively). The solutions are clearly contaminated by spurious reflections from the FE/IE interface for lower IE orders.

The IE order also depends on the size of the FE domain. If the FE domain is small then a higher IE order must be used to accurately represent the acoustic field at large

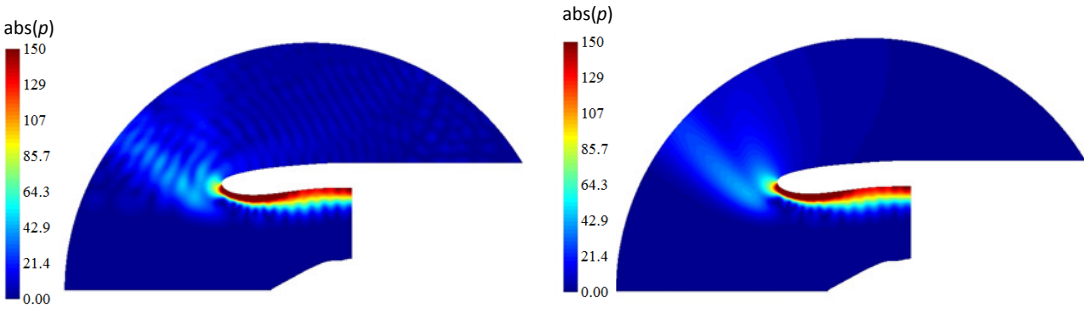

(a) IE order 5 (b) IE order 15

FIGURE B.2: Absolute value of acoustic pressure of mode (24,1) at 1BPF (1300Hz) in the FE domain

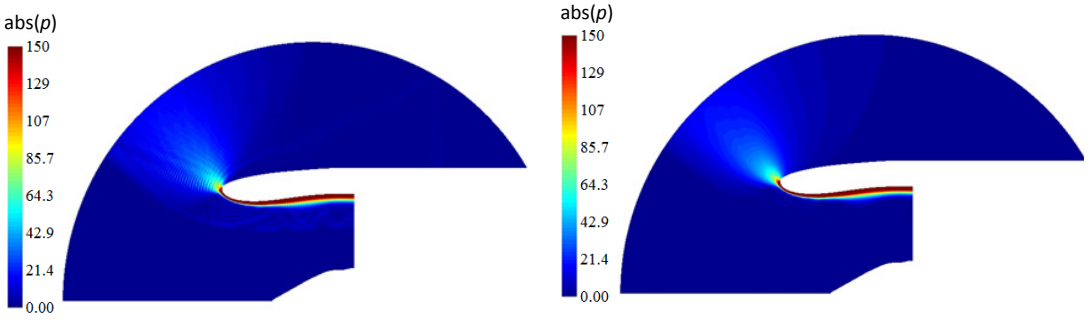

(a) IE order 20 (b) IE order 40

FIGURE B.3: Absolute value of acoustic pressure of mode (120,1) at 5BPF (6500Hz) in the FE domain

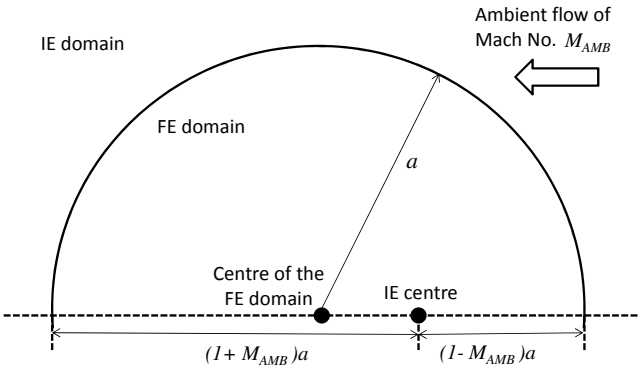

FIGURE B.4: Location of the IE centre with respect to the centre of the FE domain of radius a

distances from the sources. Conversely, if the FE domain is larger then a relatively low IE order can be used. The convergence criterion for infinite elements are detailed in reference [39].

The centre of the IE domain should also be specified very carefully in ACTRAN/TM. The IE centre should coincides with the centre of the FE domain if there is no ambient flow. In case of ambient flow, the location of IE centre depends on the ambient flow Mach Number M_{AMB}, as shown in figure B.4.

Appendix C

Sound power on a spherical surface enclosing an acoustic source

Consider an acoustic source enclosed by a spherical surface S of radius R as shown in figure C.1. The total sound power W over the surface S is given by

$$W = \int_S \mathbf{I} \cdot \hat{n} dS \tag{C.1}$$

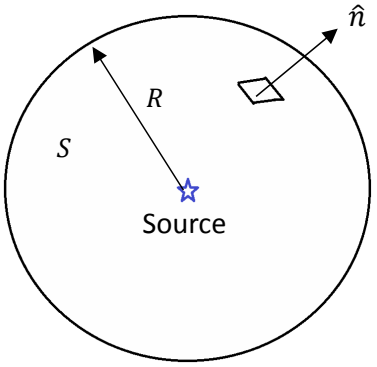

FIGURE C.1: An acoustic source enclosed inside a spherical surface S, where $\hat{n}$ is the unit normal to surface S

where $\mathbf{I}$ is the acoustic intensity travelling across the surface and $\hat{n}$ is the unit normal to the surface. Equation C.1 can therefore be rewritten as

$$W = \int_S I_r dS \tag{C.2}$$

where I_r is the radial component of the acoustic intensity $\mathbf{I}$. The elemental surface dS can be expressed as

$$dS = 2\pi R^2 sin\theta d\theta \tag{C.3}$$

where θ is the polar angle as shown in figure C.2. On substituting equation C.3 in equation C.2, the total radiated sound power W becomes

$$W = 2\pi R^2 \int_{\theta_1}^{\theta_2} I(\theta) sin\theta d\theta \tag{C.4}$$

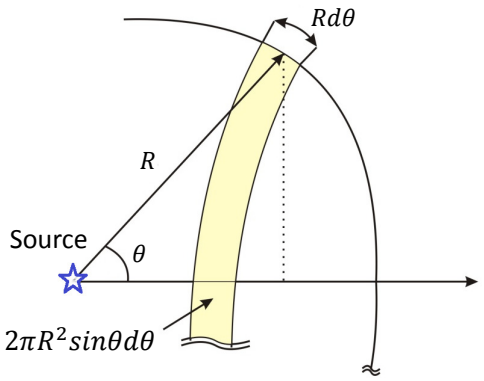

FIGURE C.2: Calculation of area of annular surface element dS

In equation C.4, the acoustic power is calculated on the spherical surface over an angular range $[\theta_1, \theta_2]$. Assuming a plane wave in the absence of flow, the time-averaged acoustic intensity $I(\theta)$ can be written

$$I(\theta) = \frac{|p(\theta)|^2}{2\rho_0 c_0} \tag{C.5}$$

where ρ_0 and c_0 are the fluid density and speed of sound respectively. On substituting equation C.5 in equation C.4, the total radiated sound power W becomes

$$W = \frac{\pi R^2}{\rho_0 c_0} \int_{\theta_1}^{\theta_2} |p(\theta)|^2 \, sin\theta d\theta \tag{C.6}$$

Therefore, the radiated sound PWL can be expressed as

$$PWL = 10log_{10}\frac{W}{W_{ref}} = 10log_{10}\left(\frac{\pi R^2}{\rho_0 c_0 W_{ref}} \int_{\theta_1}^{\theta_2} |p(\theta)|^2 \, sin\theta d\theta\right) \tag{C.7}$$

where W_{ref} is the reference power. In terms of SPL (reference value p_{ref}), equation C.7 can be rewritten as

$$PWL = 10log_{10}\frac{W}{W_{ref}} = 10log_{10}\left(\frac{\pi R^2 p_{ref}^2}{\rho_0 c_0 W_{ref}}\int_{\theta_1}^{\theta_2} 10^{\frac{SPL(\theta)}{10}} sin\theta d\theta\right) \tag{C.8}$$

Equation C.7 (or equation C.8) is used in this thesis to calculate the total sound power radiated from turbofan intakes into the far-field. For a series of pressure measurements over a far-field arc with microphones spaced every $\Delta\theta$, the integrals in equation C.8 can be approximately evaluated by using Trapezoidal rule.

Bibliography

[1] International Civil Aviation Organisation, "Volume 1: Aircraft noise," in *Annex 16 to the Convention on International Civil Aviation: Environmental Protection*, 5th ed., July 2008.

[2] C. Hodge, "Quiet aircraft design and operational characteristics," in *Aeroacoustics of flight vehicles: Theory and practice, volume 2: Noise control*, pp. 383–413, (H. Hubbard, ed.), 1991.

[3] *The Jet Engine*, ch. Environmental Impact, pp. 54–64. Rolls-Royce plc, 2005.

[4] P. Arguelles, J. Lumsden, M. Bischoff, D. Ranque, P. Busquin, S. Rasmussen, B. Droste, P. Reutlinger, R. Evans, R. Robins, W. Kroll, H. Terho, J. Lagardere, A. Wittlov, and A. Lina, "Meeting society's needs and winning global leadership," in *European Aeronautics: A vision for 2020*, January 2001.

[5] R. J. Astley, A. Agarwal, K. R. Holland, P. F. Joseph, R. H. Self, M. G. T. Smith, R. Sugimoto, and B. J. Tester, "Predicting and reducing aircraft noise," in *14th International Congress on Sound and Vibration*, July 2007.

[6] M. J. T. Smith, *Aircraft Noise*. Cambridge University Press, 2004.

[7] R. J. Astley, "Propulsion system noise - turbomachinery," in *The Encyclopedia of Aerospace Engineering (Richard Blockley and Wei Shyy)*, John Wiley and Sons, 2010.

[8] L. Bertsch, W. Dobrzynskiy, and S. Guerinz, "Tool development for low-noise aircraft design," in *14th AIAA/CEAS Aeroacoustics Conference (29th AIAA Aeroacoustics Conference)*, May 2008. AIAA 2008-2995.

[9] R. J. Astley, "Numerical methods for noise propagation in moving flows, with application to turbofan engines," *Acoustical Science and Tecnology*, vol. 246, pp. 63–69, 2009.

[10] L. Enghardt, A. Holewa, and U. Tapken, "Comparison of different analysis techniques to decompose a broad-band ducted sound field in its mode constituents," in *13th AIAA/CEAS Aeroacoustics Conference (28th AIAA Aeroacoustics Conference)*, May 2007. AIAA 2007-3520.

[11] C. R. Lowis, *In-duct measurement techniques for the characterisation of broadband aeroengine noise.* PhD thesis, Institute of Sound and Vibration Research, University of Southampton, UK, July 2007.

[12] C. R. McAleer, *Predicting fan noise propagation in aeroengine bypass ducts.* EngD Thesis, Institute of Sound and Vibration Research, University of Southampton, UK, March 2009.

[13] I. Achunche, R. J. Astley, R. Sugimoto, and A. J. Kempton., "Prediction of forward fan noise propagation and radiation from intakes," in *15th AIAA/CEAS Aeroacoustics Conference*, May 2009. AIAA 2009-3239.

[14] D. M. Nark and M. G. Jones, "Broadband liner optimisation for the source diagnostic test fan," in *18th AIAA/CEAS Aeroacoustics Conference*, June 2012. AIAA 2012-2195.

[15] A. McAlpine and M. J. Fisher, "On the prediction of "buzz-saw" noise in aero-engine inlet ducts," *Journal of Sound and Vibration*, vol. 248, pp. 123–149, 2001.

[16] R. Sugimoto, P. Murray, and R. J. Astley, "Folded cavity liners for turbofan engine intakes," in *18th AIAA/CEAS Aeroacoustics Conference (33rd AIAA Aeroacoustics Conference)*, June 2012. AIAA 2012-2291.

[17] C. L. Morfey and M. J. Fisher, "Shock-wave radiation from a supersonic ducted rotor," *The Aeronautical Journal of the Royal Aeronautical Society*, vol. 74, pp. 579–585, 1970.

[18] M. J. Fisher, B. J. Tester, and P. J. G. Schwaller, "Supersonic fan tone noise prediction," in *4th AIAA/CEAS Aeroacoustics Conference*, June 1998. AIAA 98-2249.

[19] A. McAlpine and M. J. Fisher, "On the prediction of "buzz-saw" noise in acoustically lined aero-engine inlet ducts," *Journal of Sound and Vibration*, vol. 265, pp. 175–200, 2003.

[20] W. Eversman, "Theoretical models for duct acoustics propagation and radiation," in *Aeroacoustics of flight vehicles: Theory and practice, volume 2: Noise control*, pp. 101–163, (H. Hubbard, ed.), 1991.

[21] J. M. Tyler and T. G. Sofrin, "Axial flow compressor noise studies," *SAE transactions*, vol. 70, pp. 309–332, 1962.

[22] P. M. Morse and K. U. Ingard, *Theoretical acoustics.* McGraw-Hill, 1986.

[23] C. J. Brooks, *Prediction and control of sound propagation in turbofan engine bypass ducts.* EngD Thesis, Institute of Sound and Vibration Research, University of Southampton, UK, September 2007.

[24] A. McAlpine, R. J. Astley, V. J. T. Hii, N. J. Baker, and A. J. Kempton, "Acoustic scattering by an axially-segmented turbofan inlet duct liner at supersonic fan speeds," *Journal of Sound and Vibration*, vol. 294, pp. 780–806, 2006.

[25] G. Gabard and R. J. Astley, "A computational mode-matching approach for sound propagation in three-dimensional ducts with flow," *Journal of Sound and Vibration*, vol. 315, pp. 1103–1124, 2008.

[26] E. J. Rice, "Multimodal far-field acoustic radiation pattern using mode cut-off ratio," *AIAA Journal*, vol. 16, no. 9, pp. 906–911, 1978.

[27] E. J. Rice, "Modal propagation angles in ducts with soft walls and their connection with supressor performance," in *5th AIAA Aeroacoustics Conference*, May 1979. AIAA 79-0624.

[28] G. Gabard and R. J. Astley, "Theoretical model for sound radiation from annular jet pipes: Far- and near-field solutions," *Journal of Fluid Mechanics*, vol. 549, pp. 315–341, 2005.

[29] R. Munt, "The interaction of sound with a subsonic jet issuing from a semi-infinite cylindrical pipe," *Journal of Fluid Mechanics*, vol. 83, no. 4, pp. 609–640, 1977.

[30] S. Rienstra, "Acoustic radiation from a semi-infinite annular duct in a uniform subsonic mean flow," *Journal of Sound and Vibration*, vol. 94, no. 2, pp. 267–288, 1984.

[31] S. Lidoine, H. Batard, and A. Delnevo, "Acoustic radiation modelling of aero-engine intake, comparison between analytical and numerical methods," in *7th AIAA/CEAS Aeroacoustics Conference*, May 2001. AIAA 2001-2140.

[32] R. J. Astley and W. Eversman, "Wave envelope and infinite element schemes for fan noise radiation from turbofan inlets," *AIAA Journal*, vol. 22, no. 12, pp. 1719–1726, 1984.

[33] R. J. Astley, G. J. Macaulay, J.-P. Coyette, and L. Cremers, "Three-dimensional wave-envelope elements of variable order for acoustic radiation and scattering. part i. formulation in the frequency domain," *Journal of the Acoustical Society of America*, vol. 103, no. 1, pp. 49–63, 1998.

[34] W. Eversman, "Mapped infinite wave envelope elements for acoustic radiation in a uniformly moving medium," *Journal of Sound and Vibration*, vol. 224, no. 4, pp. 665–687, 1999.

[35] V. Ahuja, Y. Ozyoruk, and L. N. Long, "Computational simulations of fore and aft radiation from ducted fans," in *6th AIAA/CEAS Aeroacoustic Conference*, June 2000. AIAA 2000-1943.

[36] N. Chevaugeon, J. F. Remacle, X. Gallez, P. Ploumhans, and S. Caro, "Efficient discontinuous galerkin methods for solving acoustic problems," in *11th AIAA/CEAS Aeroacoustic Conference*, May 2005. AIAA 2005-2823.

[37] R. Leneveu, B. Schiltz, J. Manera, and S. Caro, "Parallel dgm scheme for lee applied to exhaust and bypass problems," in *13th AIAA/CEAS Aeroacoustics Conference*, May 2007. AIAA 2007-3510.

[38] R. J. Astley, R. Sugimoto, and P. Mustafi, "Computational aero-acoustics for fan duct propagation and radiation. current status and application to turbofan liner optimisation," *Journal of Sound and Vibration*, vol. 330, no. 16, pp. 3832–3845, 2011.

[39] Free Field Technologies, Louvain-la-Neuve, *ACTRAN 12.1 users' manual*, 2012.

[40] F. Fahy, *Foundation of Engineering Acoustics*. Elsevier Academic Press, 1st ed., 2001.

[41] L. E. Kinsler, A. R. Frey, A. B. Coppens, and J. V. Sanders, *Fundamentals of Acoustics*. John Wiley and Sons, 2000.

[42] W. Eversman, "The boundary condition at an impedance wall in a non-uniform duct with potential mean flow," *Journal of sound and vibration*, vol. 246, pp. 63–69, 2001.

[43] M. K. Myers, "On the acoustic boundary condition in the presence of flow," *Journal of Sound and Vibration*, vol. 71, no. 3, pp. 429–434, 1980.

[44] B. A. Finlayson, *The method of weighted residuals and variational principles*. London Academic Press, 1977.

[45] R. J. Astley, "Infinite elements for wave problems: A review of current formulations and an assessment of accuracy," *International journal of numerical methods in engineering*, vol. 49, pp. 951–976, 2000.

[46] R. J. Astley, "Infinite elements," in *Computational methods for acoustics problems*, pp. 37–65, Saxe-Coburg Publications (F. Magoules), 2008.

[47] R. J.Astley and J.-P. Coyette, "The performance of spheroidal infinite elements," *International Journal for Numerical Methods in Engineering*, vol. 52 (12), pp. 1379–1396, 2001.

[48] N. Tsuchiya, *Inlet shell users manual*. (ISVR, University of Southampton, UK), June 2005.

[49] R. Sugimoto, *Multi-m (provisional) ver. 0.1 : Shell code for dealing with multiple azimuthal modes with using Anprorad intake models*. (ISVR, University of Southampton, UK), February 2008.

[50] S. Laldjee, *PHOENIX Manual v0.4*. (ISVR, University of Southampton, UK), May 2012.

[51] D. G. Crighton, "Model equations of nonlinear acoustics," *Annual Reviews of Fluid Mechanics*, vol. 11, pp. 11–33, 1979.

[52] A. D. Pierce, *Acoustics - An Introduction to Its Physical Principles and Applications*. McGraw Hill, 1981. pp. 566-606.

[53] M. F. Hamilton and D. T. Blackstock, *Nonlinear acoustics*. Academic Press, 1998. pp. 14-32.

[54] D. T. Blackstock, *Fundamentals of Physical Acoustics*. John Wiley & Sons., 2000. pp. 84-91.

[55] A. McAlpine, M. J. Fisher, and B. J. Tester, "Buzz-saw noise: A comparison of measurement with prediction," *Journal of Sound and Vibration*, vol. 290, no. 3-5, pp. 1202–1233, 2006.

[56] J. S. Mendousse, "Nonlinear dissipative distortion of progressive sound waves at moderate amplitudes," *Journal of Acoustical Society of America*, vol. 25, no. 1, pp. 51–54, 1953.

[57] I. Rudnick, "On the attenuation of a repeated sawtooth shock wave," *Journal of Acoustical Society of America*, vol. 25, no. 5, pp. 1012–1013, 1953.

[58] E. Houghton and P. Carpenter, *Aerodynamics for Engineering Students*. Butterworth-Heinemann Publications, 5th ed., 2003. pp. 68-95.

[59] J. D. Anderson, *Fundamentals of aerodynamics*. McGraw Hill, 3rd ed., 2001. pp. 47-111.

[60] R. Fernando, Y. Druon, R. Marchiano, and F. Coulouvrat, "A nonlinear computational method for the propagation of shock waves in aero-engine inlets towards a new model for buzz-saw noise prediction," in *15th AIAA/CEAS Aeroacoustics Conference (30th AIAA Aeroacoustics Conference)*, May 2009. AIAA 2009-3238.

[61] R. J. Astley, I. Achunche, and R. Sugimoto, "Validation of CAA prediction of noise radiated from turbofan intakes," in *16th International Congress on Sound and Vibration*, July 2009.

[62] I. M. Achunche, *Acoustic optimisation and prediction of sound propagation in turbofan engine ducts*. EngD Thesis, Institute of Sound and Vibration Research, University of Southampton, UK, December 2009.

[63] B. Schuster, L. Lieber, and A. Vavalle, "Optimisation of seamless inlet liner using an emperically validated prediction method," in *16th AIAA/CEAS Aeroacoustic conference*, June 2010. AIAA 2010-3824.

[64] S. Lidoine and B. Caruelle, "Fan noise radiation from intake: comparisons between FEM predictions and fan rig test measurements with flare," in *12th International Congress on Sound and Vibration*, July 2005.

[65] D. M. Nark, "Assessment of radiated fan noise prediction capabilities using static engine test data," in *17th AIAA/CEAS Aeroacoustics Conference*, June 2011. AIAA 2011-2807.

[66] L. Lafronza, *Computer-aided liner optimization for fan noise propagation and radiation.* PhD thesis, Institute of Sound and Vibration Research, University of Southampton, UK, December 2007.

[67] L. Lafronza, A. McAlpine, A. J. Keane, and R. J. Astley, "Computer-aided liner optimisation for broadband noise," in *10th AIAA/CEAS aeroacoustics conference*, May 2004. AIAA 2004-3029.

[68] L. Lafronza, A. McAlpine, A. J. Keane, and R. J. Astley, "Response surface method optimization of uniform and axially segmented duct acoustics liners," *Journal of Aircraft*, vol. 43, no. 4, pp. 1089–1102, 2006.

[69] U.S. Dept. of Transportation, Federal Aviation Administration, *Noise Standard: Aircraft Type and Airworthiness Certification.* Advisory Circular AC36-4C, July 2003. pp. 102-113.

[70] G. Box and N. Draper, *Empirical Model-Building and Response Surfaces.* John Wiley and Sons, 1987.

[71] A. J. Keane and P. B. Nair, *Computational approaches for aerospace design: the pursuit of excellence.* John Wiley and Sons, 2005.

[72] R. Fisher, *The Design of Experiments.* Oliver and Boyd, 1935.

[73] T. R. Law and A. P. Dowling, "Optimisation of annular and cylindrical liners for mixed exhaust aeroengines," in *13th AIAA/CEAS Aeroacoustics Conference*, 2007.

[74] MathWorks, *Matlab R2012a Help Manual.* Massachusetts, USA, March 2012.

[75] D. Copiello and P. Ferrante, "Multi-objective optimization of "true" zero-splice liners for aero-engine intakes," in *15th AIAA/CEAS Aeroacoustics Conference*, May 2009. AIAA 2009-3107.

[76] R. J. Astley, I. M. Achunche, R. Sugimoto, and A. J. Kempton, "Automatic liner optimisation for bypass ducts," in *Euronoise*, October 2009.

[77] I. M. Achunche, R. J. Astley, R. Sugimoto, and A. J. Kempton, "Liner optimisation for a uniform bypass duct using b-induct and soft," in *Aerodynamic Design and Optimisation Seminar (ADOS)*, Derby, UK, September 2008.

[78] R. Sugimoto, *B-induct users manual, shell program for ACTRAN induct analysis for bypass ducts.* (ISVR, University of Southampton, UK), November 2004.

[79] S. Shahpar, "Soft, a new design and optimisation tool for turbomachinery," in *Evolutionary methods for design, optimisation and control*, (K. Giannakoglou and D. Tsahalis and J. Periaux and K. Papailiou and T. Fogarty, eds.), CIMNE, Barcelona, 2002.

[80] R. E. Motsinger and R. Kraft, "Design and performance of duct acoustic treatment," in *Aeroacoustics of flight vehicles: Theory and practice, volume 2: Noise control*, pp. 165–205, (H. Hubbard, ed.), 1991.

[81] D. Goldberg, *Genetic Algorithms in Search, Optimization and Machine Learning.* Addison-Wesley, 1989.

[82] D. Sasaki, "Armoga - an efficient multi-objective genetic algorithm," tech. rep., Genome Exploration Research Group, RIKEN Genomic Sciences Center, RIKEN Yokohama Institute, Yokohama, Japan, 2005.

[83] D. Sasaki and S. Obayashi, "Efficient search for trade-offs by adaptive range multi-objective genetic algorithms," *Journal of aerospace computing, information and communication*, vol. 2, pp. 44–64, 2005.

[84] D. Yuret and M. de la Maza., "Dynamic hill climbing: overcoming the limitations of optimization techniques," in *Proceedings of the 2nd Turkish symposium on artificial intelligence and neural networks*, June 1993. pp. 254-260.

[85] J. A. Hamilton and R. J. Astley, "Mid frequency theoretical optimisation of an intake lip liner for T700 static tests," tech. rep., SILENCE(R) : Work Package 1.2, Task 3, 2002.

[86] A. J. Kempton and M. G. Smith, "Ray-theory predictions of the sound radiated from realistic engine intakes," in *7th AIAA Aeroacoustics Conference*, October 1981. AIAA 81-1982.

[87] A. J. Kempton, "Ray-theory and mode-theory predictions of intake-liner performance: A comparison with engine measurements," in *8th AIAA Aeroacoustics Conference*, April 1983. AIAA 83-0711.

[88] B. J. Tester, C. J. Powles, N. J. Baker, and A. J. Kempton, "Scattering of sound by liner splices: a kirchhoff model with numerical verification," *AIAA Journal*, vol. 44, pp. 2009–2017, 2006.

[89] A. McAlpine and M. C. M. Wright, "Acoustic scattering by a spliced turbofan inlet duct liner at supersonic fan speeds," *Journal of Sound and Vibration*, vol. 292, no. 3-5, pp. 911–934, 2006.

[90] W. Watson, "Noise suppression characteristics of peripherally segmented duct liners." NASA TP-1904, 1981.

[91] R. J. Astley, N. Walkington, and W. Eversman, "Transmission in flow ducts with peripherally varying liner," in *6th AIAA Aeroacoustics Conference*, June 1980. AIAA 80-1015.

[92] A. McAlpine, M. Wright, H. Batard, and S. Thezelais, "Finite/boundary element assessment of a turbofan spliced intake liner at supersonic fan operating conditions," in *9th AIAA/CEAS aeroacoustics conference*, May 2003. AIAA 2003-3305.

[93] A. M. Cargill, "Scattering from joins between liners in intake ducts with application to br710 buzz-saw noise," report TSG0688, Rolls-Royce, Derby, UK, 1993.

[94] B. Tester, N. Baker, A. Kempton, and M. Wright, "Validation of an analytical model for scattering by intake liner splices," in *10th AIAA/CEAS Aeroacoustics Conference*, May 2004. AIAA 2004-2906.

[95] B. J. Tester and L. D. Mercato, "Far-field directivity of rotor-locked tones radiated from fan intakes with spliced liners for different intake shapes with flow," in *12th AIAA/CEAS Aeroacoustics Conference*, May 2006. AIAA 2006-2456.

[96] B. J. Tester, *User guide version 2 : Cargill for liner splice scattering (code version 13).* (ISVR, University of Southampton, UK), 2009.

[97] C. L. Morfey, "Acoustic energy in non-uniform flows," *Journal of Sound and Vibration*, vol. 14, no. 2, pp. 159–170, 1971.

[98] C. Geuzaine and J. F. Remacle, *Gmsh: a three-dimensional finite element mesh generator with built-in pre- and post-processing facilities (Version 2.5.0).* Free Software Foundation, Inc., Boston, USA, 2010.

[99] M. Vahdati, A. I. Sayma, C. Breard, and M. Imregun, "Computational study of intake duct effects on fan flutter stability," *AIAA Journal*, vol. 40, no. 3, pp. 408–418, 2002.

[100] Z. Yun and Y. Hui, "Coupled fluid-structure flutter analysis of a transonic fan," *Chinese Journal of Aeronautics*, vol. 24, no. 3, pp. 258–264, 2011.

[101] J. G. Marshall and M. Imregun, "A review of aeroelasticity methods with emphasis on turbomachinery applications," *Journal of Fluids and Structures*, vol. 10, no. 3, pp. 237–267, 1996.

[102] M. Imregun, "Prediction of flutterstability using aeroelastic response functions," *Journal of Fluids and Structures*, vol. 9, no. 5, pp. 419–434, 1995.